FACULTY OF BIOSCIENCE ENGINEERING
DEPARTMENT OF MICROBIAL AND MOLECULAR SYSTEMS
CENTER FOR SURFACE CHEMISTRY AND CATALYSIS: CHARACTERIZATION AND APPLICATION TEAM
Celestijnenlaan 200F - box 2461
B-3001 HEVERLEE, BELGIUM
lisa.geerts@kuleuven.be
www.biw.kuleuven.be

Lisa Geerts

MODEL PLATINUM CATALYSTS

February 2020

KU LEUVEN

ARENBERG DOCTORAL SCHOOL
FACULTY OF BIOSCIENCE ENGINEERING

Model Platinum Catalysts

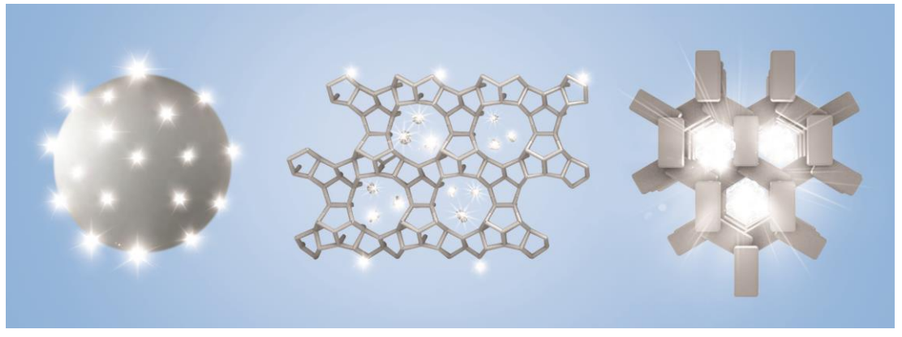

Lisa Geerts

Supervisors:
Prof. Johan Martens
Dr. Sreeprasanth Pulinthanathu Sree

Dissertation presented in partial fulfilment of the requirements for the degree of Doctor of Bioscience Engineering
February 2020

MODEL PLATINUM CATALYSTS

Lisa GEERTS

Supervisor(s):
Prof. Johan A. Martens
Dr. Sreeprasanth Pulinthanathu Sree

Members of the Examination Committee:
Prof. Christophe Courtin, Chairman
Prof. Maarten Roeffaers
Prof. Christophe Detavernier
Prof. Sara Bals
Prof. Jin Won Seo
Dr. Céline Chizallet

Dissertation presented in partial fulfilment of the requirements for the degree of Doctor of Bioscience Engineering

February 2020

Doctoraatsproefschrift nr. 1624 aan de faculteit Bio-ingenieurswetenschappen van de KU Leuven

Uitgegeven in eigen beheer, LISA GEERTS, HEVERLEE

Acknowledgements

The past four years have been an intense and enriching journey. Throughout the whole process towards this PhD thesis, I have received a great deal of support and guidance. I would like to thank all the people who guided me out of my comfort zone to reach this major point in my professional and personal life.

First, I would like to express my sincerest gratitude to my promotor, Prof. Johan Martens for giving me the opportunity to start this research project. I feel privileged that I could be a part of his research group, that lies close to his heart. He believed in my capacities in all stages of the work and without his guidance, the thesis would not be in its current form. I am very grateful for the scientific discussions, creative ideas and critical feedback. He has been a true mentor and I will certainly take his advice with me in the future. I also wish to thank my co-promoter, Dr. Sreeprasanth Pulinthanathu Sree. It has been an honor to be his first PhD student. He has taught me invaluable insights about the scientific details of this project, but beyond that, I appreciate his enthusiastic encouragement and heart-warming support. His advice, not only in academic sense, has given me great confidence. Thank you for mentoring me throughout the PhD and beyond.

I am deeply grateful to all members of the jury for agreeing to participate in the defense of this thesis. I would like to thank Prof. Maarten Roeffaers, Prof. Sara Bals and Prof. Christophe Detavernier, for their perspective and inspiring suggestions over the years. I also want to thank the two external members of the examination committee, Prof. Jin Won Seo and Dr. Céline Chizallet. Thank you for the commitment and evaluation of the PhD. I also wish to thank the chairman Prof. Christophe Courtin. I feel honored that you all have accepted to be on my committee.

Although only a few names are mentioned on the cover, I have received support and help from a large number of people that are not credited there. I would like to express my appreciation to Prof. Christine Kirschhock. I want to thank her for taking the time for discussing results, for assistance with images and for baking cake at the team buildings. A success factor in this PhD project is my colleague, Gina Vanbutsele. I greatly appreciate her assistance and advice in the lab, particularly for the hydroisomerization reactions. I would also like to thank Dr. Vinodchandran Chandrasekharan Nair, Dr. Sambhu Radhakrishnan and Dr. Eric Breynaert for their scientific and technical assistance with NMR. In particular, I would like to thank Vinod and Sambhu for being helpful and giving advice.

During this PhD project I had the opportunity to work with excellent collaborators. I am grateful for the people at EMAT at the University of Antwerp with whom I was involved for advanced (S)TEM and electron tomography. Thank you in particular for Alexander Skorikov, Prof. Thomas Altantzis and Prof. Sara Bals. I also want to thank Dr. Ranjith K. Ramachandran, Dr. Jolien Dendooven and Prof. Christophe Detavernier from the CoCooN research group at Ghent University. They helped enormously with ALD research samples and gave good advice for the papers. I would also like to give special thanks to Prof. Jin Won Seo for teaching me how to use the electron microscope, for her time and for her help with the interpretation of the results. I also want to thank Dr. Frederik Ceyssens and Prof. Robert Puers from ESAT with whom I was involved for the replica microelectrodes.

This doctoral work was done in the frame of a project supported by Research Foundation Flanders (G0A5417N). I want to thank Prof. Vladimir Galvita from LCT at Ghent University and Prof. Denis Constales from ELIS at Ghent University for their contribution to this project.

Another part of my work was dedicated to NiFe clusters for the oxygen evolution reaction. For this project, I worked with Dr. Salvatore Cosentino, Dr. Ting-Wei Liao, Anupam Yadav, Dr. Didier Grandjean and Prof. Peter Lievens from the Laboratory of Solid-State Physics and Magnetism and Pin-Cheng Lin and Prof. Lino M. C. Pereira from Institute for Nuclear and Radiation Physics at KU Leuven. In the frame of this project, I could visit ESRF in Grenoble, which was an experience I highly enjoyed. I wish to thank them all for the nice collaboration.

I also want to acknowledge the students I collaborated with: Charlotte Van Ammel, Hannelore Geerts-Claes, Julie Vermeersch and Joyce Claesen. It has been a pleasure to work with you. Many thanks also to Loes Verheyen, Wauter Wangermez, Dirk Dom, Stef Usé and Werner Wouters for organizing the lab and giving advice. They ensured that lab work ran smoothly. I also wish to mention Birgit Van Deynse, Inge Devos, Ines Jossa and Lieve Pollentier for their kind support with administrative tasks.

I also wish to thank Tom Bosserez and Jan Rongé for their useful advice and entrepreneurial spirit, especially in the first phase of the project. I am also grateful for all the other wonderful colleagues I shared an office with: Gino Heremans, Christos Trompoukis, Brecht Vallaey, Robin Peeters, Barbara Thijs and Hanne Imbrechts. Thank you for the scientific suggestions and fun work breaks. I count myself lucky to be surrounded with you.

I enjoyed working in the group of Prof. Martens and wish to express my sincere gratitude to all colleagues of the group. Andreas and Michiel, thank you for the nice

chats and the pep talk. I also thank Maarten, Sam, Elke, Niels, Rien, Sara, Pieter-Jan, Heleen and the "new generation" Charlotte, Lore, Ewoud, Karel, Nick, Lander, Hannah and Tim. Many thanks also to all the other colleagues at Chem&Tech for providing a good atmosphere and for the corridor chats. In particular, I wish to thank my friend Dorien Kerstens for all the nice moments and conversations we shared over the years. I would also like to thank Dr. Chen Zhou for her assistance with STEM.

I also would like to say a heartfelt thank you to my family and friends. Thank you for listening, for challenging my thinking, for parties, city trips, game nights,… The friendship is highly appreciated. In particular, I want to say a big thank you to my boyfriend Wout who has been by my side throughout this process and contributed both directly and indirectly. I am truly thankful for having him in my life and am looking forward to what life still holds for us. I also want to thank my parents Magy and Ivan and my sister Lauren. Their unconditional love and stimulation towards personal development are priceless. Mama and papa, I can't say thank you enough for giving Lauren and me such a warm home. I also appreciate all the opportunities that you have given me. I know you believe in me and want the best for me. Lauren, even though we see each other less than we used to, on whatever continent you are, I can feel the warm support and friendship in Leuven.

Abstract

Platinum is used by many industries because of its exceptional catalytic activity, electrochemical properties and corrosion resistance. It is widely used as a catalyst in the chemical production, in fuel cell and electrolyser electrodes and in sensors for analytical and medical applications. Catalysts are key to face grand technological challenges in the fields of energy and environmental protection and to ensure a sustainable supply of chemicals and materials.

Catalysts are shaped in many ways. Due to the high cost of platinum, most efforts are directed towards maximizing the exposed surface area in order to increase the utilization of the platinum itself and thus to reduce the Pt loadings. This is conventionally achieved through reducing the size of the Pt particles to the nanoscale by dispersing them on porous high surface area supports. For some specific applications, and especially electrocatalysis and molecular sensing, unsupported nanostructured platinum architectures, combining high exposed surface area with electric conductivity, are needed.

Understanding kinetic data by relating it with structural and compositional properties is essential for rational design of new catalysts. Gaining scientific insight when using industrial catalysts is very difficult because of the complexity and heterogeneous nature of such materials. They often contain a combination of phases that can vary in bulk and surface structure, particle size, shape, chemical composition, defects, impurities, promotors and interactions among the different phases. Usually supports themselves are also irregular with a heterogeneous surface. Characterization is inherently challenging for these catalysts and the active site is ill-defined. This complexity has been the driving force for many researchers to use model catalysts. Many model studies have been previously reported using single crystals or Pt particles on planar supports. Yet, examples of well-characterized 3D Pt model catalysts were only scarcely reported.

The primary focus of this thesis was on the synthesis and characterization of generic 3D model platinum catalysts that can be used in kinetic investigations of many types of reactions under practically relevant reaction conditions. Compared to planar model catalysts, the structural complexity of such 3D model catalyst systems is more closely related to the industrial catalysts.

A first model system was prepared by using a monodisperse, spherical alumina support to reduce the complexity. Spherical alumina particles with a particle size of about 1 μm were synthesized by a chemical precipitation method. Using 2D and 3D electron

microscopy and ^{27}Al solid-state NMR, the core-shell structure of the particles was fully characterized. The spherical alumina particles were then decorated with uniform Pt nanoparticles (~1 nm) using the strong electrostatic adsorption method. To establish its relevance as a model catalyst, the Pt alumina catalyst was combined with erionite zeolite having comparable morphology to generate a bifunctional catalyst. The suitability of such a physical mixture with a well-characterized Pt model catalyst was demonstrated in the hydroisomerization-hydrocracking of n-decane.

The potential of atomic layer deposition (ALD) of platinum for creation of model catalysts was investigated. ALD could even be used to introduce acid sites next to platinum performing bifunctional catalysis with zeolites. Plasma-enhanced ALD of Ga_2O_3 (Ga-ALD) was performed on COK-14, an all-silica zeolite that lacks acid sites. After ALD, metal sites were introduced via Pt incipient wetness impregnation. Using electron microscopy, Pt nanoparticles were found to be preferentially located on the edges of the COK-14 plates. The optimum proximity between the Ga acid and Pt metal sites resulted in high activity and selectivity surpassing other large pore zeolites. To understand the potential of ALD for introducing metal sites in a zeolite, Pt-ALD was performed on ZSM-5 zeolite, which resulted in finely dispersed Pt nanoparticles of 1-2 nm. The hydroisomerization experiments confirmed Pt-ALD to be an adequate method for introducing metal sites on aluminosilicate zeolites. This work demonstrates how ALD-tailored materials can help in understanding the relationship between structure and performance.

The final model system was a continuous unsupported platinum catalyst with an open and porous structure. The structure was prepared using the hard templating concept, consisting of filling the pores of a mesoporous template followed by removal of the template. Pt-ALD was chosen for depositing Pt in the pores and Zeotile-4 was selected as the template. By using Pt-ALD, the replica structure could be created over micrometer distances. Such larger structures are valuable in electrode and sensor applications. The structure was studied in detail with electron microscopy and tomography. The applicability was demonstrated in the electrocatalytic hydrogen evolution reaction (HER). Furthermore, the suitability of the structure for use in biomedical sensors was demonstrated.

Samenvatting

Platina wordt door veel industrieën gebruikt vanwege zijn uitzonderlijke katalytische en elektrochemische eigenschappen en corrosiebestendigheid. Het wordt vaak verwerkt in katalysatoren voor de chemische productie, in elektroden voor brandstof- en elektrolysecellen en in sensoren voor analytische en medische toepassingen. Katalysatoren zijn van cruciaal belang om grote technologische uitdagingen op het gebied van energie en milieubescherming het hoofd te bieden en om op een duurzame manier chemicaliën en materialen te maken.

Er in een grote verscheidenheid aan katalysatoren. Vanwege de hoge kostprijs van platina wordt vaak betracht het blootgestelde oppervlak te maximaliseren. Dit wordt gedaan om de efficiëntie van het platina zelf te verhogen, zodat minder metaal nodig is. Meestal wordt dit bereikt door de grootte van de Pt-partikels te verkleinen tot nanoschaal door ze te verdelen over poreuze dragers met een groot oppervlak. Voor sommige specifieke toepassingen, met name elektrokatalyse en moleculaire detectie, worden ook continue fijnverdeelde platina nanostructuren zonder drager ontwikkeld. Zij combineren een groot specifiek oppervlak met elektrische geleidbaarheid.

Inzicht in kinetische data en het verband met structurele en compositionele eigenschappen is essentieel voor het rationeel ontwerpen van nieuwe katalysatoren. Dit is echter erg moeilijk bij het gebruik van industriële katalysatoren vanwege de complexiteit en de heterogeniteit van dergelijke materialen. Ze bevatten vaak een combinatie van fasen die kunnen variëren in bulk- en oppervlaktestructuur, deeltjesgrootte, morfologie, chemische samenstelling, defecten, onzuiverheden, promotors en interacties tussen de verschillende fasen. Vaak zijn de dragers zelf ook onregelmatig met een heterogeen oppervlak. Karakterisering is inherent uitdagend voor deze katalysatoren en de actieve site is slecht gedefinieerd. Deze complexiteit is voor veel onderzoekers de drijfveer geweest om modelkatalysatoren te gebruiken. Er zijn reeds eerder modelstudies gerapporteerd op basis van *single crystals* of Pt-partikels op vlakke dragers. Voorbeelden van goed gekarakteriseerde 3D Pt-modelkatalysatoren zijn schaars.

De primaire focus van dit proefschrift lag op de synthese en karakterisering van generieke 3D model platina katalysatoren, die gebruikt kunnen worden in kinetische studies van verschillende soorten reacties onder praktisch relevante reactieomstandigheden. De structurele complexiteit van dergelijke 3D modelkatalysatoren is in vergelijking met vlakke modelkatalysatoren nauwer verwant met de industriële variant.

Om de complexiteit te verminderen werd het eerste modelsysteem gemaakt met behulp van een monodisperse sferische drager. Sferische aluminapartikels met een deeltjesgrootte van 1 μm werden gesynthetiseerd met een chemische precipitatiemethode. Met behulp van 2D- en 3D-elektronenmicroscopie en ^{27}Al vaste stof NMR werd de kern-schil structuur van de partikels volledig gekarakteriseerd. De sferische aluminapartikels werden vervolgens gebruikt als drager voor uniforme Pt-nanopartikels (~ 1 nm) die met behulp van de sterke elektrostatische adsorptiemethode werden afgezet. Om de relevantie als modelkatalysator te bewijzen, werd de Pt/alumina katalysator gemengd met erioniet-zeoliet partikels met een vergelijkbare morfologie om een bifunctionele katalysator te creëren. De geschiktheid van een dergelijk fysisch mengsel met een goed gekarakteriseerde Pt-modelkatalysator werd aangetoond in de hydroisomerisatie-hydrokraking van n-decaan.

Het potentieel van atoomlaagdepositie (ALD) van platina voor het creëren van modelkatalysatoren werd onderzocht. ALD zou zelfs kunnen worden gebruikt om zure sites te introduceren naast platina dat bifunctionele katalyse met zeolieten uitvoert. Plasma-versterkte ALD van Ga_2O_3 (Ga-ALD) werd uitgevoerd op COK-14, een zeoliet die geheel uit silica bestaat en geen zure sites heeft. Na ALD werd de metaalfunctie geïntroduceerd via Pt capillaire impregnatie. Met behulp van elektronenmicroscopie bleek dat de Pt-nanopartikels zich bij voorkeur op de randen van de COK-14-platen hadden afgezet. De optimale nabijheid tussen de zure en metallische sites resulteerde in een hoge activiteit en selectiviteit die andere zeolieten met grote poriën overtreft. Om het potentieel van ALD voor het introduceren van de metaalfunctie in een zeoliet te begrijpen, werd Pt-ALD uitgevoerd op een ZSM-5-zeoliet. Dit resulteerde in fijn verdeelde Pt-nanopartikels van 1-2 nm. De hydroisomerisatie experimenten bevestigden dat Pt-ALD een geschikte methode is voor het introduceren van metaalplaatsen op aluminosilicaatzeolieten. Dit werk laat zien dat op maat gemaakte ALD materialen nuttig zijn om het verband tussen structuur en performantie te leggen.

Het laatste modelsysteem was een continue Pt-katalysator met een open en poreuze structuur. De structuur werd vervaardigd met het harde matrijs concept dat bestaat uit het vullen van de poriën van een mesoporeuze matrijs, gevolgd door het verwijderen van de matrijs. Pt-ALD werd gekozen voor afzetten van Pt in de poriën en Zeotegel-4 werd gekozen als matrijs. Door gebruik te maken van Pt-ALD kon de replicastructuur over micrometerafstanden worden vervaardigd. Dergelijke grotere structuren zijn nuttig in elektrode- en sensortoepassingen. De structuur werd tot in detail bestudeerd met elektronenmicroscopie en tomografie. De toepasbaarheid werd gedemonstreerd in de elektrokatalytische waterstofevolutiereactie (HER). Verder werd de geschiktheid van de structuur voor gebruik in biomedische sensoren aangetoond.

List of abbreviations

ALD	Atomic Layer Deposition
BF	Bright-Field
EDX	Energy-dispersive X-ray spectroscopy
fcc	Face-centered cubic
(HA)ADF	(High-Angle) Annular Dark-field
HER	Hydrogen Evolution Reaction
(HR-)SEM	(High Resolution) Scanning Electron Microscopy
MAS NMR	Magic Angle Spinning Nuclear Magnetic Resonance
MR	Membered Rings
SEA	Strong Electrostatic Adsorption
SMSI	Strong Metal–Support Interaction
(S)TEM	(Scanning) Transmission Electron Microscopy
TGA	Thermogravimetric analysis
UHV	Ultra-High Vacuum
XRD	X-Ray Diffraction

List of symbols

Symbol	Meaning	Unit
δ_{iso}	Isotropic chemical shift	ppm
C_Q	Quadrupolar coupling constants	MHz
η_Q	Asymmetry parameter	/

Table of contents

Introduction

Platinum (Pt) is a rare element with distinctive physical and chemical properties that are useful for many industries. The average content in the earth crust amounts to only 0.005 g/t, which is reflected in its high price.[1] In marketing, "platinum" products are generally associated with wealth, prestige and exclusivity: *e.g.* platinum credit cards, platinum music awards, platinum memberships to hotels or airlines, *etc.*[2] Yet, more than a prestige symbol, the platinum metal itself is indispensable in many applications for modern life. Well-known examples include automotive catalysts for exhaust purification, sensors in medical devices and electrodes in fuel cells.[3–5] It is also used in jewels, electronics, laboratory equipment and for trading and investment.[1,2]

In heterogeneous catalysis, platinum holds a special place. It can catalyze both oxidizing and reducing reactions. It is resistant to corrosion, unaffected by most acids and alkalis, thermally stable and electrically conductive.[2,5–7] Pt is used in numerous oxidation and (de)hydrogenation reactions providing useful chemicals and consumer products such as pharmaceuticals, fertilizers, gasoline and plastics.[3–6] Faced with grand concerns in the fields of energy and environmental protection, there is continued interest to develop improved catalysts for a sustainable supply of these products. The primary goal in catalyst development is to create catalysts that selectively form desired products at high reaction rates and that are stable under operating condtions.[8,9] However this is a challenging task.

Due to the high cost of platinum, most efforts are directed towards decreasing the platinum loading through maximizing the exposed surface area. This is conventionally achieved through reducing the size of the Pt nanoparticles by dispersing them on porous high surface area supports.[10–12] Popular supports in catalysis are metal oxides, activated carbons and zeolites.[13] However for use in some specific applications, usually where electron transport or biocompatibility is important, unsupported nanostructured high-surface area platinum catalysts are developed.[14–16]

Typical catalysts have a very complex structure. They can contain a combination of phases that can vary in bulk and surface structure, particle size, shape, chemical environment, defects, impurities, promotors and interactions with the support. Usually supports themselves are also irregular with a heterogeneous surface.[17–19] This chemical and structural complexity was found to be imperative for the reactivity. Frequently, the performance could be improved by optimizing physical properties such as particle size and shape or chemical properties such as the nature of the support materials.[12,17]

The criterion for evaluation of the catalyst's utility is often the performance (activity and selectivity) in a catalytic reactor, which is quantified and interpreted in terms of reaction kinetics.[20] The basis for deriving reaction kinetics is the sequence of elementary steps that occur during a catalytic cycle.[8,21,22] The steps of a catalytic cycle are[8,20,22,23]:

1) Diffusion of reactants from bulk fluid phase to the external surface of the porous catalyst particle.

2) Intraparticle diffusion of the reactants into the catalyst pores.

3) Adsorption of reactants onto the active sites on the surface.

4) Chemical reaction on the surface of the catalyst.

5) Desorption of products from catalyst surface.

6) Intraparticle diffusion of the products to the external surface of the catalyst particle.

7) Diffusion of the products from the external particle surface to the bulk of the fluid.

Each step can be rate limiting for the overall reaction process. In addition, heat transfer can have large effects, especially for exo- or endothermic reactions.[8,20,22,23] The term microkinetics is used when step 3-5 are used in reaction kinetics studies. They incorporate the basic surface chemistry of the reaction at a molecular level in absence of heat- and mass-transfer limitations.[21] Steps 1, 2 and 6,7 involve physical transport, according to well-known diffusion laws. In cases where these steps are included, the term macrokinetics is used.[8,22,23] The nature of the catalyst can strongly affect each of these steps. Kinetic models are important to consider, but are not the subject of this doctoral research.

To improve catalysts by rational design, a fundamental understanding of the link between the microscopic structure of the catalyst and the reaction kinetics is crucial. From a fundamental point of view, however, the structural heterogeneity of the catalyst implies a variety of possible active sites. The typical metal catalyst is too complex and nonuniform to be useful for elucidation of the most meaningful structure–function correlations. Besides the inherent difficult surface structure characterization of these catalyst materials,[12,18,24] experimental data are not readily interpretable. The individual contributions of each type of influencing parameter cannot be distinguished in the measured total activity. In addition, multicomponent diffusion and adsorption in the porous support and the presence of temperature gradients could complicate interpretation of changes in kinetic experiments significantly.[12,18,25,26]

To surmount these difficulties, systematic investigations with model catalysts are performed where the complex technical catalyst is substituted by a more simplified well-defined catalyst. The term model catalyst implies that a complex catalyst is substituted by a more simplified system that alleviates variations in particle size, shape and irregular defect structures of high surface area systems.[27,28] By excluding these variations, the complexity can be significantly reduced.[27,28] A wide range of model systems with different levels of complexity has been previously reported. They range from single crystals to well-defined nanoparticles on planar and 3D supports. Each model system has limitations and the level of complexity should be adjusted according to the needs and purpose of the study.[25] Traditionally single crystal surfaces were studied with surface science techniques. A shortcoming of this approach is the so-called pressure and materials gap.[10,25,29–31]

The pressure gap originates from the discontinuity in pressure between model and real reaction conditions. Surface science studies are usually performed under ultrahigh-vacuum (UHV) conditions to eliminate surface contamination. Moreover many techniques such as electron spectroscopies demand high vacuum conditions.[10] However today, several surface sensitive techniques that work in a wide range of pressures are available as reviewed by others.[10,24,28,30,32,33] The materials gap is used to indicate that single crystal surfaces lack the complexity needed to study some important aspects, *e.g.* particle size or support interaction, of the catalytic performance.[30] In order to resolve this, models with increased complexity were developed. They were mainly nanoparticles on planar supports.[10,30,33] These two-dimensional model catalysts are advantageous because surface science analytical tools can, due to the planarity, still be applied.[30,33] These studies have conveyed many important insights for understanding the catalytic performance *e.g.* structure sensitivity and promotor effects.[17,31] They have contributed significantly to our understanding of catalysts at the atomic/molecular level: namely how catalyst structure influences elementary processes at the active sites.

However the planar model catalysts are far away from the analogous industrial catalyst. The heterogeneous nature of technical catalysts impedes direct transfer of insights gained with ideal perfect surfaces to real world surfaces.[17,31] Furthermore they cannot be tested in realistic reactor setups. On this level, features associated with the 3D structure of the catalyst (*e.g.* pore structure, distribution active Pt nanoparticles on support) and its packing in the reactor can have large effects on the catalyst performance. It is also important to take heat and mass transfer effects into account.

Hence, in addition to atomic/molecular level investigations with planar model systems having well-defined surfaces, these concepts should be validated at the engineering/reactor level using 3D model catalysts. 3D model systems should be

developed and tested in realistic reactor conditions for meaningful kinetic data for practical applications.

Objectives

The primary focus of the doctoral project was on creating a new group of 3D models for platinum catalyst systems that can be tested at the reactor level. They are useful for several types of reactions in realistic conditions. The objectives of this work are synthesis, characterization, and subsequent catalytic reaction studies, both with supported and unsupported model catalysts. In this doctoral study, '3D model' refers to the entire catalyst system, thus including platinum and the support if one is used.

To be eligible as a 3D model system, the model should have low structural complexity with a high degree of uniformity regarding the support structure as well as the supported active particles. Ideally, all the properties such as support structure, particle size, shape, surface structure and location of the particles can be controlled and well-characterized.[34–36] In this research, electron microscopy plays an important role. Several electron microscopy techniques, among other characterization methods, are extensively used for imaging of the model catalysts. They provide useful information on crystallographic structure, size, size distribution, shape and organization of the Pt nanoparticles on the support, which is essential for understanding in model catalytic studies.[37,38]

Outline of the thesis

This dissertation is divided in 4 chapters. Chapter 1 reviews Pt model catalyst systems and presents the background and motivation of this research. The aim is to review the materials that have been used as Pt model catalysts and to show the insights that have been gained with these systems. In the first part, the complexity of heterogeneous catalysis is discussed by describing technical catalyst designs and parameters exerting influence on the performance. In the second part, common model catalyst systems, including the synthetic routes, are described. A key conclusion is that only a few examples of well-characterized 3D Pt model catalysts, that can be tested in realistic reactor conditions, were reported. Chapters 2-4 contain experimental work addressing synthesis and characterization of different 3D Pt model catalysts for various catalytic reactions.

Chapter 2 contains the most simple 3D model catalyst: the support is spherical and dense. It was chosen to focus on alumina spheres, because alumina is a popular catalyst support material. 2D and 3D electron microscopy and ^{27}Al magic angle spinning

nuclear magnetic resonance spectroscopy contributed significantly in revealing the structure of the alumina particles. Using the strong electrostatic adsorption method, Pt nanoparticles were deposited on the support. To establish its relevance as a model catalyst, the Pt alumina catalyst was combined with erionite zeolite having comparable morphology to generate a bifunctional catalyst and tested for the hydroconversion of n-decane.

In chapter 3, the potential of atomic layer deposition (ALD) for creation of model catalysts is demonstrated. ALD is a self-limited growth method which relies on sequential reactions of gas phase precursor molecules and a co-reactant with a solid surface, resulting in the consecutive depositions of (sub)monolayers. Due to the self-limiting surface nature of the surface reactions, ALD enables exact thickness control and exceptional conformality.[39] ALD can be applied to deposit thin films of a wide range of materials such as oxides, nitrides, sulfides and metals on various supports.[19,39–45] Furthermore, a large amount of different elements can be grown by ALD.[46] In addition, due to a nucleation-controlled growth mechanism of noble metals, ALD can be applied to deposit uniform metal nanoparticles with atomic level control of the size.[40] Moreover, in comparison with "line-of-sight" deposition techniques such as cluster beam deposition or physical vapor deposition, ALD is, due to the self-saturating nature of the reactions, capable to conformally deposit metal nanoparticles in porous structures with large depth to width ratio.[40,47,48] Another advantage of ALD is that the processes can be optimized for high-purity of the deposited material, without contaminants and ligands.[49–51] ALD has become a mainstream deposition tool in microelectronics.[46] Recently, it has, due to its benefits, also been considered as a promising versatile tool for atomic scale tailoring of catalyst properties towards specific requirements for enhanced performance.[19,47,52,53]

A great deal of earlier work on ALD been carried out to understand the mechanisms, to find new materials and processes and to explore if ALD is well-suited for creation of functionality in nanostructures.[19,39,41,47,53–55] In this work, the feasibility of ALD for introducing gallium acid and Pt metal sites in zeolites was evaluated and the resulting tailored catalysts were used as bifunctional catalysts in the hydroconversion of n-decane. There exist many ways to introduce gallium and metal on supports, however depositions of homogenous particles with high dispersions and high level of control by chemical routes is a challenging task.[56,57] According to our view, ALD is highly interesting in model catalyst research, because it offers a methodology for mitigating particle size and compositional nonuniformities.

The ALD process that was previously used for deposition of Ga_2O_3 thin films was applied to COK-14 zeolite, an all-silica zeolite with OKO topology. This zeolite has

plate-like morphology with a 2D pore system running in the long direction. Without modification, COK-14 is catalytically inactive.[58] Regarding Ga-ALD, different precursor and co-reactant combinations have been explored which resulted in a wealth of ALD procedures that are available, *e.g.* combination of $Ga(acac)_3$ and water or ozone,[59] $((CH_3)_2GaNH_2)_3$ and oxygen plasma[60], $Ga_2(N(CH_3)_2)_6$ and water[61], gallium tri-isopropoxide (GTIP) and water[62], dimethylgallium isopropoxide (DMGIP) and water[63], trimethylgallium (TMGa) and ozone,[64] and tris(2,2,6,6-tetramethyl-3,5-heptanedionato gallium(III) ($Ga(TMHD)_3$) and O_2 plasma as reactant. The latter combination was used in this work for introducing acid sites in an all silica COK-14 zeolite. Ga-ALD for introduction of gallium onto zeolites has remained largely uninvestigated.

Platinum was deposited by ALD on ZSM-5. A commonly used Pt-ALD process implements alternating purges of (methylcyclopentadienyl)trimethylplatinum ($MeCpPtMe_3$) vapor and O_2 gas.[65–68] Besides O_2 gas, also O_2 plasma, O_3 gas, H_2 gas, H_2 plasma, N_2 plasma and NH_3 plasma have been used for Pt-ALD.[66,67,69–71] In recent years, Pt-ALD has been applied for catalyst design. It has been validated as a preparation method for catalysts with highly dispersed Pt nanoparticles and narrow size distributions. Various porous supports, such as carbon aerogel, carbon nanotubes, mesoporous silica gel, Si nanowires, titanium nitride nanowires, MOFs, *etc.*, were used and tested for various (electro)chemical reactions.[72–81] In the field of zeolite catalysis, Pt-ALD has been previously applied to ZSM-5 for hydrogenation of levulinic acid to valeric acid[82] and on zeolite beta for cinnamaldehyde hydrogenation.[83] Pt was also introduced to K-L zeolite by ALD and a high activity for n-heptane reforming to aromatics was observed.[84,85] Pt-ALD for preparing bifunctional catalysts for hydrocarbon conversion has further not yet been reported.

In Chapter 4, a different approach is used. Unsupported Pt nanostructures were synthesized by the hard templating method, consisting in deposition of platinum in the pores of a mesoporous oxide support followed by dissolution of the template. Pt-ALD was chosen for deposition of Pt in the pores and Zeotile-4 was the template.

Unsupported nanostructured high-surface area platinum catalysts are developed for specific applications. Pt nanostructures with open and porous structure are ideal candidates for applications that require both electron and mass transport.[14–16] They can excel in applications as battery electrodes, fuel cells, electronic devices, electrochemical sensors, neural stimulation electrodes and mechanical actuators.[86–88] When used for neural stimulation, the high surface area is highly advantageous for the signal to noise ratio, as the impedance at the interface between electrode and tissue is inversely related to the surface area. For bio-implantable electrode applications in general, a strong motivation for working with unsupported porous platinum is that platinum is very

noble with high biocompatibility and chemical stability.[88] In fuel cell applications, unsupported platinum electrocatalysts could be beneficial in comparison with conventional carbon-supported Pt nanoparticles. In the latter, corrosion of the support often leads to particle detachment and loss of electrical contact.[89]

In recent years, the Pt-ALD technique been used for uniformly coating of templates with porous features.[90–92] For preparation of a self-supporting porous Pt replica via the hard templating technique however, Pt-ALD has remained largely unexplored. Impregnation with a Pt complex is a common way to infiltrate the pores of a hard template.[93–107] Previously reported Pt replicas consist mostly of nanowire assemblies. In this work, ALD is applied for replication of the Zeotile-4 template, which is a mesoporous silica material with 3D accessible pores. This is an attractive strategy because the cyclic repetition of surface saturated reactions can lead to complete filling of the template. The method was proven suitable for synthesizing model monofunctional Pt catalysts. The structure was thoroughly characterized in detail with electron microscopy and tomography. The applicability of the Pt replica structure was demonstrated in electrocatalysis for the hydrogen evolution reaction (HER) and in biomedical sensing as microelectrode.

References

1 S. K. Haldar, in *Platinum-Nickel-Chromium Deposits Geology, Exploration and Reserve Base*, Elsevier, 2017, pp. 1–35.

2 W. Black, *The platinum group metals industry*, Woodhead Publishing Limited, 2000.

3 S. Mizuhashi, C. E. J. Cordonier, H. Honma and O. Takai, 2015, **162**, 497–502.

4 International Platinum Group Metals Association, *IPA Guidance Document: Chapter 3 – Production and Uses of Platinum Group Metals*, 2017.

5 Z. Peng and H. Yang, *Nano Today*, 2009, **4**, 143–164.

6 L. Gai, Y. K. Shin, M. Raju, A. C. T. Van Duin and S. Raman, *J. Phys. Chem. C*, 2016, **120**, 9780–9793.

7 N. K. Gopalan, S. Zhang, D. Du, P. Li and J. Ouyang, *ChemCatChem*, 2015, **7**, 422–426.

8 J. J. Bravo-suárez and R. V Chaudhari, in *Novel Materials for Catalysis and Fuels Processing*, eds. J. J. Bravo-Suárez, M. K. Kidder and V. Schwartz, 2013, pp. 1–68.

9 J. C. Védrine, in *Metal Oxides in Heterogeneous Catalysis*, Elsevier, 2018, pp. 1–41.

10 M. Bäumer, J. Libuda, K. M. Neyman, N. Rösch, G. Rupprechter and H. J. Freund, *Phys. Chem. Chem. Phys.*, 2007, **9**, 3541–3558.

11 F. Zaera, in *Encyclopedia of Inorganic and Bioinorganic Chemistry*, John Wiley & Sons, Ltd., 2014.

12 J. Libuda, S. Schauermann, M. Laurin, T. Schalow and H. J. Freund, *Monatshefte fur Chemie*, 2005, **136**, 59–75.

13 P. Serp, P. Kalck and R. Feurer, *Chem. Rev.*, 2002, **102**, 3085–3128.

14 H. Ataee-Esfahani, Y. Nemoto, L. Wang and Y. Yamauchi, *Chem. Commun.*, 2011, **47**, 3885.

15 M. Rück, A. Bandarenka, F. Calle-vallejo and A. Gagliardi, *Nanoscale Adv.*, 2019, **1**, 2901–2909.

16 E. Antolini and J. Perez, *J. Mater. Sci.*, 2011, **46**, 4435–4457.

17 F. C. Meunier, *ACS Nano*, 2008, **2**, 2441–2444.

18 J. Hoffmann, I. Meusel, J. Hartmann and J. Libuda, *J. Catal.*, 2001, **204**, 378–

392.

19 B. J. O'Neill, D. H. K. Jackson, J. Lee, C. Canlas, P. C. Stair, C. L. Marshall, J. W. Elam, T. F. Kuech, J. A. Dumesic and G. W. Huber, *ACS Catal.*, 2015, **5**, 1804–1825.

20 J. A. Dumesic, G. W. Huber and M. Boudart, in *Handbook of heterogeneous catalysis*, eds. G. Ertl, H. Knözinger, F. Schüth and J. Weitkamp, Wiley-VCH, Second., 2008, vol. 1.

21 O. Deutschmann, H. Knözinger, K. Kochloefl and T. Turek, in *Ullmann's Encyclopedia of Industrial Chemistry*, Wiley-VCH Verlag GmbH & Co. KGaA, 2009.

22 J. Hagen, in *Industrial Catalysis: A Practical Approach,* Wiley-VCH Verlag GmbH & Co. KGaA, 2006, pp. 99–222.

23 R. L. Augustine, *Heterogeneous Catalysis for the Synthetic Chemist*, Marcel Dekker, Inc., 1996.

24 H. J. Freund, H. Kuhlenbeck, J. Libuda, G. Rupprechter, M. Baumer and H. Hamann, *Top. Catal.*, 2001, **15**, 201–209.

25 B. C. Gates, *Top. Catal.*, 2001, **14**, 173–180.

26 C. Chizallet and P. Raybaud, *Catal. Sci. Technol.*, 2014, **4**, 2797–2813.

27 P. L. J. Gunter, J. W. H. Niemantsverdriet, F. H. Ribeiro and G. A. Somorjai, *Catal. Rev.*, 1997, **39**, 77–168.

28 F. Tao and P. A. Crozier, *Chem. Rev.*, 2016, **116**, 3487–3539.

29 E. Lundgren and H. Over, *J. Phys. Condens. Matter*, 2008, **20**, 180302.

30 G. A. Somorjai, R. L. York and J. Y. Park, *Phys. Chem. Chem. Phys.*, 2007, **9**, 3500–3513.

31 D. W. Goodman, *Surf. Sci.*, 1994, **299/300**, 837–848.

32 G. A. Somorjai and C. Aliaga, *Langmuir*, 2010, **26**, 16190–16203.

33 G. Rupprechter and C. Weilach, *J. Phys. Condens. Matter*, 2008, **20**, 184019.

34 K. Niesz, M. M. Koebel and G. A. Somorjai, *Inorganica Chim. Acta*, 2006, **359**, 2683–2689.

35 G. A. Somorjai and M. Yang, *Top. Catal.*, 2003, **24**, 61–72.

36 G. A. Somorjai, S. Habas, P. Yang, M. Grass, K. Niesz, R. M. Rioux, J. D. Hoefelmeyer and H. Song, *Top. Catal.*, 2006, **39**, 167–174.

37 S. Bernal, J. J. Calvino, M. A. Cauqui, J. M. Gatica, C. López Cartes, J. A. Pérez Omil and J. M. Pintado, *Catal. Today*, 2003, **77**, 385–406.

38 J. Y. Liu, *Microsc. Microanal.*, 2004, **10**, 55–76.

39 C. Detavernier, J. Dendooven, S. Pulinthanathu Sree, K. F. Ludwig and J. A. Martens, *Chem. Soc. Rev.*, 2011, **40**, 5242–5253.

40 J. Dendooven, R. K. Ramachandran, E. Solano, M. Kurttepeli, L. Geerts, G. Heremans, J. Rongé, M. M. Minjauw, T. Dobbelaere, K. Devloo-Casier, J. A. Martens, A. Vantomme, S. Bals, G. Portale, A. Coati and C. Detavernier, *Nat. Commun.*, 2017, **8**, 1074.

41 H. C. M. Knoops, S. E. Potts, A. A. Bol and W. M. M. Kessels, in *Handbook of Crystal Growth: Thin Films and Epitaxy: Second Edition*, ed. T. Kuech, Elsevier, 2015, pp. 1101–1134.

42 M. Ahonen, M. Pessa, T. Suntola and O. L. Ab, *Thin Solid Films*, 1980, **65**, 301–307.

43 S. M. George, *Chem. Rev.*, 2010, 111–131.

44 R. L. Puurunen, *J. Appl. Phys.*, 2005, **97**, 121301.

45 T. Suntola, J. Antson, Method for producing compound thin films, 4058430, 1977.

46 R. W. Johnson, A. Hultqvist and S. F. Bent, *Mater. Today*, 2014, **17**, 1369–7021.

47 V. Cremers, R. L. Puurunen and J. Dendooven, *Appl. Phys. Rev.*, 2019, **6**, 1–43.

48 H. Van Bui, F. Grillo, S. S. Kulkarni, R. Bevaart, N. Van Thang, B. Van Der Linden, J. A. Moulijn, M. Makkee, M. T. Kreutzer and J. R. Van Ommen, *Nanoscale*, 2017, **9**, 10802–10810.

49 E. Solano, J. Dendooven, R. K. Ramachandran, K. Van de Kerckhove, T. Dobbelaere, D. Hermida-Merino and C. Detavernier, *Nanoscale*, 2017, **9**, 13159–13170.

50 J. Provine, P. Schindler, J. Torgersen, H. J. Kim, H.-P. Karnthaler and F. B. Prinz, *J. Vac. Sci. Technol. A Vacuum, Surfaces, Film.*, 2016, **34**, 01A138.

51 M. J. Weber, A. J. M. MacKus, M. A. Verheijen, V. Longo, A. A. Bol and W.

M. M. Kessels, *J. Phys. Chem. C*, 2014, **118**, 8702–8711.

52 B. Zhang and Y. Qin, *ACS Catal.*, 2018, **8**, 10064–10081.

53 Z. Gao and Y. Qin, *Acc. Chem. Res.*, 2017, **50**, 2309–2316.

54 S. P. Sree, J. Dendooven, T. I. Koranyi, G. Vanbutsele, K. Houthoofd, D. Deduytsche, C. Detavernier and J. A. Martens, *Catal. Sci. Technol.*, 2011, 218–221.

55 S. P. Sree, J. Dendooven, J. Jammaer, K. Masschaele, D. Deduytsche, J. D. Haen, C. E. A. Kirschhock, J. A. Martens and C. Detavernier, *Chem. Mater.*, 2012, **24**, 2775–2780.

56 R. Fricke, H. Kosslick, G. Lischke and M. Richter, *Chem. Rev.*, 2000, **100**, 2303–2405.

57 B. A. T. Mehrabadi, S. Eskandari, U. Khan, R. D. White and J. R. Regalbuto, *A Review of Preparation Methods for Supported Metal Catalysts*, Elsevier Inc., 1st edn., 2017, vol. 61.

58 E. Verheyen, S. Pulinthanathu Sree, K. Thomas, J. Dendooven, M. De Prins, G. Vanbutsele, E. Breynaert, J. P. Gilson, C. E. A. Kirschhock, C. Detavernier and J. A. Martens, *Chem. Commun.*, 2014, **50**, 4610–4612.

59 M. Nieminen and E. Rauhalab, *J. Mater. Chem.*, 1996, **6**, 27–31.

60 F. K. Shan, G. X. Liu, W. J. Lee, G. H. Lee, I. S. Kim, F. K. Shan, G. X. Liu, W. J. Lee, G. H. Lee, I. S. Kim and B. C. Shin, *J. Appl. Phys.*, 2005, **98**, 023504.

61 C. L. Dezelah, J. Niinisto, K. Arstila, L. Niinisto and C. H. Winter, *Chem. Mater.*, 2006, **18**, 471–475.

62 D. Choi, K. Chung and J. Park, *Thin Solid Films*, 2013, **546**, 31–34.

63 B. H. Lee, K. Kim, J. Woo, D. Jun, Y. Park, Y. Kim, H. W. Lee and Y. J. Cho, *Chem. Vap. Depos.*, 2011, 191–197.

64 D. J. Comstock and W. J. Elam, *Chem. Mater.*, 2012, **24**, 4011–4018.

65 T. Aaltonen, M. Ritala, T. Sajavaara, J. Keinonen and M. Leskelä, *Chem. Mater.*, 2003, **15**, 1924–1928.

66 D. Longrie, K. Devloo-Casier, D. Deduytsche, S. Van den Berghe, K. Driesen and C. Detavernier, *ECS J. Solid State Sci. Technol.*, 2012, **1**, Q123–Q129.

67 H. C. M. Knoops, A. J. M. Mackus, M. E. Donders, M. C. M. van de Sanden, P.

H. L. Notten and W. M. M. Kessels, *Electrochem. Solid-State Lett.*, 2009, **12**, G34.

68 M. Filez, H. Poelman, R. K. Ramachandran, J. Dendooven, K. Devloo-Casier, E. Fonda, C. Detavernier and G. B. Marin, *Catal. Today*, 2014, **229**, 2–13.

69 J. Dendooven, R. K. Ramachandran, K. Devloo-Casier, G. Rampelberg, M. Filez, H. Poelman, G. B. Marin, E. Fonda and C. Detavernier, *J. Phys. Chem. C*, 2013, **117**, 20557–20561.

70 W. Setthapun, H. Feng, P. C. Stair, J. T. Miller, C. L. Marshall, W. D. Williams, F. H. Ribeiro, S. M. Kim, E. A. Stach, J. W. Elam, F. A. Rabuffetti and K. R. Poeppelmeier, *J. Phys. Chem. C*, 2010, **114**, 9758–9771.

71 L. Baker, A. S. Cavanagh, J. Yin, S. M. George, A. Kongkanand and F. T. Wagner, *Appl. Phys. Lett.*, 2012, **101**, 1–5.

72 J. Li, X. Liang, D. M. King, Y. B. Jiang and A. W. Weimer, *Appl. Catal. B Environ.*, 2010, **97**, 220–226.

73 J. S. King, A. Wittstock, J. Biener, S. O. Kucheyev, Y. M. Wang, T. F. Baumann, S. K. Giri, A. V Hamza, M. Baeumer and S. F. Bent, *Nano Lett.*, 2008, **8**, 2405–2409.

74 J. Zhang, C. Chen, S. Chen, Q. Hu, Z. Gao, Y. Li and Y. Qin, *Catal. Sci. Technol.*, 2017, **7**, 322–329.

75 C. Liu, C.-C. Wang, C.-C. Kei, Y.-C. Hsueh and T.-P. Perng, *Small*, 2009, **5**, 1535–1538.

76 M. Wang, Z. Gao, B. Zhang, H. Yang, Y. Qiao, S. Chen, H. Ge, J. Zhang and Y. Qin, *Chem. - A Eur. J.*, 2016, **22**, 8385.

77 A. Celebioglu, K. S. Ranjith, H. Eren, N. Biyikli and T. Uyar, *Sci. Rep.*, 2017, **7**, 1–10.

78 N. P. Dasgupta, C. Liu, S. Andrews, F. B. Prinz and P. Yang, *J. Am. Chem. Soc.*, 2013, **135**, 12932–12935.

79 C. M. Engelhardt, R. M. Kennedy, J. A. Enterkin, K. R. Poeppelmeier, D. E. Ellis, C. L. Marshall and P. C. Stair, *ChemCatChem*, 2018, **10**, 632–641.

80 K. Leus, J. Dendooven, N. Tahir, R. Ramachandran, M. Meledina, S. Turner, G. Van Tendeloo, J. Goeman, J. Van der Eycken, C. Detavernier and P. Van Der Voort, *Nanomaterials*, 2016, **6**, 45.

81 J. Sun, X. Wang, Y. Song, Q. Wang, Y. Song, D. Yuan and L. Zhang, *Chem.*

Commun., 2019, **55**, 13283–13286.

82 X. Gu, Z. Bin, H. Liang, H. Ge, H. Yang and Y. Qin, *J. Fuel Chem. Technol.*, 2017, **45**, 714–722.

83 M. Lashdaf, J. Lahtinen, M. Lindblad, M. Tiitta, T. Venäläinen and H. Österholm, *Stud. Surf. Sci. Catal.*, 2004, **154**, 1708–1713.

84 D. Xu, B. Wu, P. Ren, S. Wang, C. Huo, B. Zhang, W. Guo, L. Huang, X. Wen, Y. Qin, Y. Yang and Y. Li, *Catal. Sci. Technol.*, 2017, **7**, 1342–1350.

85 D. Xu, S. Wang, B. Wu, B. Zhang, Y. Qin, C. Huo, L. Huang, X. Wen, Y. Yang and Y. Li, *ACS Appl. Mater. Interfaces*, 2019, **11**, 29858–29867.

86 A. Takai, Y. Doi, Y. Yamauchi and K. Kuroda, *Chem. - An Asian J.*, 2011, **6**, 881–887.

87 P. K. Chen, N. C. Lai, C. H. Ho, Y. W. Hu, J. F. Lee and C. M. Yang, *Chem. Mater.*, 2013, **25**, 4269–4277.

88 A. Kloke, F. Von Stetten, R. Zengerle and S. Kerzenmacher, *Adv. Mater.*, 2011, **23**, 4976–5008.

89 B. Cai, S. Henning, J. Herranz, T. J. Schmidt and A. Eychmüller, *Adv. Energy Mater.*, 2017, **7**, 1–16.

90 H. S. Chen, P. H. Chen, S. H. Huang and T. P. Perng, *Chem. Commun.*, 2014, **50**, 4379–4382.

91 B. D. J. Comstock, S. T. Christensen, J. W. Elam, M. J. Pellin and M. C. Hersam, *Adv. Funct. Mater.*, 2010, **20**, 3099–3105.

92 S. Deng, Templated synthesis of porous materials via atomic layer deposition, Ghent University, Faculty of Sciences, Ghent, Belgium, 2015.

93 H. Wang, H. Y. Jeong, I. Masataka, L. Wang, L. Radhakrishnan, N. Fujita, T. Castle, O. Terasaki and Y. Yamauchi, *J. Am. Chem. Soc.*, 2011, **133**, 14526–14529.

94 Y. Song, R. M. Garcia, R. M. Dorin, H. Wang, Y. Qiu, E. N. Coker, W. A. Steen, J. E. Miller and J. A. Shelnut, *Nano Lett.*, 2007, **7**, 3650–3655.

95 A. Fukuoka, T. Higuchi, T. Ohtake, T. Oshio, J. I. Kimura, Y. Sakamoto, N. Shimomura, S. Inagaki and M. Ichikawa, *Chem. Mater.*, 2006, **18**, 337–343.

96 B. C. Yang, H. Sheu and K. Chao, *Adv. Funct. Mater.*, 2002, **300**, 143–148.

97 X.-J. Guo, C.-M. Yang, P.-H. Liu, M.-H. Cheng and K.-J. Chao, *Cryst. Growth Des.*, 2005, **5**, 33–36.

98 Y. Doi, A. Takai, Y. Sakamoto, O. Terasaki, Y. Yamauchi and K. Kuroda, *Chem. Commun.*, 2010, **46**, 6365–6367.

99 Y. Xu and B. Zhang, *Chem. Soc. Rev.*, 2014, **43**, 2439–2450.

100 R. Ryoo, C. H. Ko, M. Kruk, V. Antochshuk and M. Jaroniec, *J. Phys. Chem. B*, 2000, **104**, 11465–11471.

101 C. H. Ko and R. Ryoo, *Chem. Commun.*, 1996, **1**, 2467–2468.

102 F. Kleitz, S. H. Choi and R. Ryoo, *Chem. Commun.*, 2003, 2136–2137.

103 H. J. Shin, R. Ryoo, Z. Liu and O. Terasaki, *J. Am. Chem. Soc.*, 2001, **123**, 1246–1247.

104 H. J. Shin, C. H. Ko and R. Ryoo, *J. Mater. Chem.*, 2001, **11**, 260–261.

105 Z. Liu, Y. Sakamoto, T. Ohsuna, K. Hiraga, O. Terasaki, C. H. Ko, H. J. Shin and R. Ryoo, *Angew. Chemie - Int. Ed.*, 2000, **39**, 3107–3110.

106 A. Galarneau, H. Cambon, F. Di Renzo, R. Ryoo, M. Choi and F. Fajula, *New J. Chem.*, 2002, **27**, 73–79.

107 Y. Han, J. M. Kim and G. D. Stucky, *Chem. Mater.*, 2000, 2068–2069.

Chapter 1

Literature review of model platinum catalysts

1. Introduction

Industrial catalysts are not simple in terms of composition and structure.[1] They are generally multicomponent systems, consisting of metal or metal alloy nanoparticles, often with poisons or promotors, deposited on nanostructured porous metal-oxides.[2–6] In the past decades, it was found that it is this complexity that is imperative for the reactivity. Physical properties such as particle size and shape or chemical properties such as the nature of the support materials can have significant influences on the activity. Other complex features such as defects, impurities and interactions with the support can moreover considerably affect the performance.[4,7] When seeking more efficient catalysts, optimization of the parameters was mainly based on empirical grounds. Hence, the precise knowledge on the active sites and interplay between all the parameters are still not well understood.[1,2,4]

It is intrinsically difficult to relate properties of such samples to the activity because the individual contributions of each type of influencing parameter can be masked in the measured total activity. In an attempt to unravel the nature of the active sites, many investigations with simpler model catalysts have been performed.[8] They were mainly based on single-crystal surfaces or nanoparticles on planar supports in ultra-high vacuum surface science experiments.[4,8–10] Although many important insights with respect to the catalytic properties have been accumulated, *e.g.* structure sensitivity and promotor effects, model catalysts are far away from the analogous industrial catalyst.[7,10] The surfaces deviate significantly from the ideal surfaces obtained with surface-science techniques and the measurement conditions are very different from industrially relevant reactor conditions. Conditions at which real catalysts operate cover broad ranges of temperatures and pressures ranging from room temperature to hundreds of degrees Celsius and from millitorr to atmospheres.[11] Therefore, it is necessary to develop more sophisticated model systems that are closer to real world catalysts and that can be used in relevant reactor conditions.

Platinum is widely used for a multitude of applications due to its exceptional properties such as corrosion resistance, thermal stability and catalytic activity for many chemical reactions. Well-known applications include automotive catalysts for exhaust purification, sensors in medical applications and electrodes in fuel cells. It is also widely used as a catalyst for oxidation and (de)hydrogenation reactions that are important for manufacturing of petrochemical feedstocks and consumer products such as fertilizers, gasoline and plastics.[12–14] Observed from an industrial viewpoint, the high cost of platinum is a huge driving force for efficient use of the metal in new and improved types of catalyst systems.[15]

The focus of this literature review is platinum model catalyst systems. To master the complexity of catalyst systems, first, industrial catalyst designs and parameters affecting the performance will be discussed. Then, common model catalyst systems will be explained. Different model systems that are a simplified version of the complex industrial catalyst can be defined, however planar model systems, which covers a very broad research field, will not be described extensively. The cited examples are intended to give an idea on commonly applied designs. The review summarizes examples of 3D model catalysts and reveals that they remain limited. All the examples given in the different sections are narrowed to platinum catalysts to provide an in-depth review. The missing pieces in current model catalyst systems are discussed, as well as perspectives for design of new model catalysts.

2. Industrial catalysts

Heterogeneous catalysts are a vital component in a wide variety of processes in the chemical, petrochemical, biochemical and pharmaceutical industries. Since most of the present production routes for chemicals and fuels rely on heterogeneous catalysts, they have an immense economic impact.[5,16]

Heterogeneous materials can be used in unsupported form, but numerous catalysts use an additional material as support for the active phase.[17,18] Unsupported catalysts, of which the main component is the active material, are usually produced when the components are inexpensive.[6,19] Typical examples of unsupported catalysts are aluminosilicates and zeolites for cracking of petroleum fractions and alumina in the Claus process for sulfur recovery.[5,19,20] Unsupported platinum is only occasionally used in industry. An example is the platinum or platinum-alloy gauze for ammonia oxidation in the production of nitric acid whereby a gauze is used due to the highly exothermic reaction that requires small catalyst bed heights [5,21] The supported types are chosen depending on the requirements of the chemical process. Advantages such as high dispersion of the active phase, better diffusion through the reactor bed, better thermal conductivity and creation of bifunctional catalysts are a few among many reasons.[18] Two Pt examples include the well-known three-way catalyst consisting of Pt – Rh – Pd on Al_2O_3 modified by CeO_2 and Pt on chlorinated Al_2O_3 as bifunctional catalyst for catalytic reforming and for isomerization of petroleum fractions.[5]

(Co)Precipitation and impregnation/coating techniques are the most frequently applied methods to manufacture industrial catalysts.[22] Precipitation is mainly used for the production of unsupported oxidic catalysts and for the manufacture of pure support materials.[5,6] One or more metal salts, *e.g.* sulfates, chlorides and nitrates, are mixed in an aqueous solution and then (co)precipitated, often as hydroxides or carbonates.

The synthesis conditions can affect catalyst properties such as crystallinity, particle size, porosity and composition.[5,6]

For preparation of platinum based catalysts, that because of its high cost are mainly in supported form, impregnation is often used. The method involves impregnation of the porous support with platinum salts. The platinum precursor ions consist ligands, such as for example ammine for the common precursor $(NH_3)_4PtCl_2$, that need to be removed. To obtain platinum nanoparticles in zero-valent oxidation state, the impregnated and dried powder is typically converted in a calcination and/or reduction step.[23] The procedure usually results in a rather broad particle size distribution and nonuniform dispersion, due to the lack of interaction between the platinum precursor and the support.[23,24] More detailed information on the manufacturing of industrial catalysts, as well as some other procedures can be found elsewhere.[6,19]

Commercial catalysts can be used as a powder, however usually they are formed into larger shaped particles such as rings, spheres, tablets, and pellets depending on the end use.[6,19] The shape and size of the catalyst particles serve to enhance the catalytic activity, to control the mass transport properties through the catalyst bed, to influence the pressure drop and to increase mechanical strength and durability of the catalyst particles.[6] The decision to work with a particular shape and size is mainly based on the type of reactor. Commercially available coarse granules or fine powders can be shaped into larger bodies with the aid of binders and lubricants (*e.g.* stearic acid, graphite) and then be used in fixed bed reactors.[25,26] Spray-drying, extrusion, pelleting and granulation are the most important methods. Generally, spray-drying results in particles ranging in size from a few to a several hundred micrometers, while the other methods produce particles of a few millimeters.[6,27] For uses in fluidized beds or liquid phase, the catalyst is supplied as a powder.[19,25,26,28–31] In some cases, usually where conventional catalyst beds are restricting the gas flow, monoliths that consist of continuous structures with unidirectional parallel channels of varying shapes *e.g.* circular, hexagonal, square and triangular, are used. So far monoliths were mainly applied in exhaust purification.[26,32]

In summary, many industrial catalysts consist of nanometer sized nanoparticles, generally between 1 and 100 nm, dispersed in the pores of a high surface area support.[33–36] Supports with surface areas of 200 square meters per gram or more, and materials such as alumina, silica, zeolites or carbon are frequently used.[23,36,37] In general, the size of the support bodies varies between 10 μm and 1 cm and the morphology and porosity are usually marked on a (sub)micron scale.[38,39] The walls in a monolith exhibit a porosity between 15 and 40% and have pores with an average diameter of a few micrometers.[6] These scales are illustrated in figure 1.

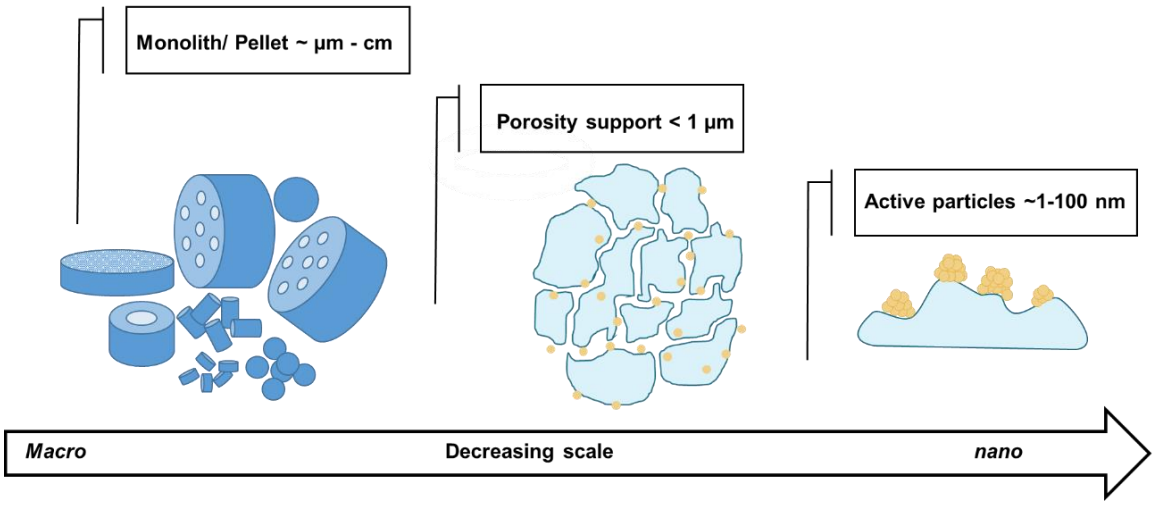

Figure 1. Hierarchical structure of a heterogeneous supported catalyst at various zoom-in levels. Industrial catalysts have features marked on macro- down to nanometer scale.

To uncover the factors important for catalytic activity and selectivity, commercial catalysts have limitations. They contain a combination of phases that can vary in stoichiometries, bulk and surface structures, particle shapes and sizes, defects, impurities, and interactions with the support. Usually supports themselves are also heterogeneous.[7] This complexity makes characterization inherently challenging for these materials.[4] Moreover, for such nonuniform samples, the contribution of each type of influencing parameter cannot be determined from the measured total activity. It is therefore necessary to design new experiments with simpler catalysts as model system.[8] Over the years, systematic studies with various types of well-defined model catalysts have been used to study activity and selectivity of catalytic reactions. The main aspects, including surface structure and support interaction, that exert influence on the performance are summarized in the next paragraphs.

3. Structure sensitivity

3.1 Particle size

Already in the 1960s the concept of structure sensitivity has been introduced, pointing out that the rate (and selectivity) of some catalytic reactions strongly depends on surface defects or crystallographic planes on the surface.[40–42] In the initial definition of Boudart, only the rate of the catalytic reaction is mentioned to be influenced by the surface structure, however cases where the selectivity changes with structure have been reported also. This structure sensitivity effect has been studied by investigating the size dependency of nanoparticles and by using single-crystal planes as model catalysts. The former approach is reasonable since the size of the particles influences the density

of under-coordinated atoms at corners or edges.[15,32,41,43] In general, the amount of kinks and edges on the surface of the nanoparticles increases with decreasing particle size.[41]

There are numerous examples of this size effect; most of these examples are correlations with the activity. The number of examples where selectivity could be related to size is lower.[44] Starting from the 1960s, several hydrocarbon reactions over platinum catalysts were shown to have an activity increase with decreasing particle size: isomerization of light alkanes (<C4), hydrogenolysis and dehydrocyclization of n-heptane to toluene.[41] Particle size was also shown to influence ethane hydrogenolysis and the regioselective hydrogenation reactions of quinoline.[45,46] More recent examples comprise oxidation of volatile organic compounds *e.g.* toluene oxidation on Pt/ZSM-5 [47] and on Pt/CeO_2 catalyst,[48] benzene oxidation Pt/Al_2O_3[49]. Numerous examples of the effect of size on the activity of various reactions, *e.g.* CO oxidation and methane oxidation, on supported Pt catalysts are reviewed elsewhere.[50] In electro- and photocatalytic technologies, multiple reactions display size-dependency: *e.g.* oxygen reduction reaction on Pt/carbon,[51,52] hydrogen evolution on Pt/TiO_2,[53] hydrogen oxidation and evolution on Pt/carbon particles,[54] CO reduction on hierarchical ordered TiO_2–SiO_2 porous material[55], *etc.* In some cases, the nanoparticles with larger particle sizes show better performance than smaller ones. This adverse effect was for example established for the hydrogen evolution reaction on Pt nanoparticles in the 1 - 3 nm range.[56]

An example of the influence of size on selectivity has been reported for n-butane hydrogenolysis and 1,3-butadiene hydrogenation.[57,58] Other examples of a shift in selectivity for platinum based catalysts include hydrogenation–dehydrogenation reactions of cyclohexene, isomerization of n-pentane, hydrogenation of α,β-unsaturated aldehydes and are reviewed elsewhere.[44,59,60]

3.2 Single crystals

In analogy with the under-coordinated atoms on small particles, fundamental studies on the single-crystal surfaces of bulk Pt have shown that high-index planes with open structures exhibit generally enhanced catalytic activity in comparison with low-index planes such as {111} and {100}.[15,61] For face-centered cubic (fcc) metals like platinum; the high-index planes, meaning that at least one of the Miller indices (hkl) is larger than one, are open-structure surfaces. They contain a high density of atomic steps and kinks.[15,37] To illustrate this, a unit stereographic triangle as shown in figure 2, is often used for platinum and other fcc metals. At the three vertices, the low-index planes, flat (111), flat (100) and stepped (110) are presented. Planes inside and at the sides of the triangle denote high-index planes with terrace-step structure.[62,63] The under-

coordinated atoms at these steps and kinks are believed to be the active sites for breaking the chemical bonds of the reactant molecule.[15,43]

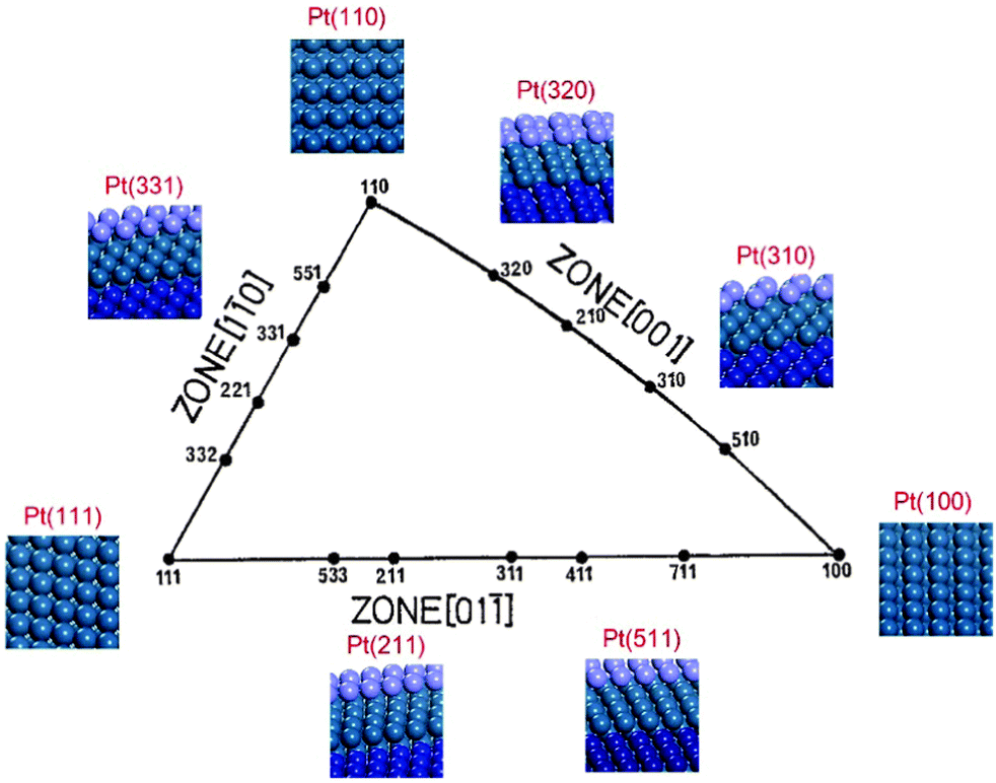

Figure 2. Unit stereographic triangle of Pt single-crystal surfaces and the corresponding model surface atomic arrangements. Reproduced from ref [62].

There are countless numbers of examples of platinum single crystal surface studies. They have been extensively studied in hydrocarbon conversion reactions and CO oxidation. A study by Somorjai *et al.* revealed that steps and kinks are the catalytic sites for C-C, C-H and H-H bond scissions during hydrocarbon reactions. They could establish a correlation between the activity of different crystal surfaces carrying out dehydrogenation and hydrogenolysis of cyclohexane to benzene and n-hexane, and surface structure/compositions.[64]

Besides activity, also the selectivity is dependent on the packing of atoms on the surface, however generalization is not simple. For example, in a study by Davis *et al.*, the structure dependence of n-hexane skeletal rearrangement was investigated on five different platinum single crystal surfaces Pt(100), Pt(111), Pt(332), Pt(13,1,1) and Pt(10,8,7). They have different density of terraces, steps, and kinks. In the aromatization of n-hexane to benzene, the rates and selectivities were structure dependent and highest for platinum surfaces with high concentrations of (111) microfacets, which are present on (111), (332), and (10,8,7). The rates of the competing reactions, isomerization, C_5-cyclization, and hydrogenolysis, exhibited little dependence on surface structure.

The hydrogenolysis products however were affected significantly by terrace structures. Selective hydrogenolysis of the internal and terminal C-C bond was favored by platinum surfaces with (100) terraces and surfaces with (111) terraces respectively.[65] Also, CO dissociation displayed structure sensitivity. It was found that CO dissociation requires different temperatures for the different planes ranked in increasing order of Pt(100) < Pt(557) and < Pt(111). The order is determined by the temperature at which the surface becomes more rough with steps and kinks due to formation of platinum carbonyls.[66]

Single crystals have also been applied in electrochemistry studies. For instance, the structure sensitivity was also investigated for the electrocatalytic CO oxidation on Pt single crystals: Pt(443), Pt(332), and Pt(322). The (111) terraces of these surfaces were found to be more reactive in comparison with (110) or (100) steps.[67] In the case of ethylene glycol oxidation, a higher activity on the (110) than on the (111) electrode was measured, however the best electrocatalytic properties have been reported for the (331) electrode, which was ascribed to the atomic arrangement and to the stability of this surface.[68] For CO_2 reduction, (210) planes with the highest density of kinks in their study, were the most active.[69] Density functional theory calculations predict activities in the following trend: (111) < (110) ~ (331) < (100) ~ (310) ~ (211) ~ (320) ~ (511) for ethanol electrocatalytic oxidation. A high selectivity toward CO_2 was only achieved with (110) and (331) step sites.[62] For other structure sensitivity effects of Pt single crystal electrodes in reactions as methanol, ethanol, ethylene glycol and formic acid oxidation and oxygen reduction, the reader is referred to the review by Sun and coworkers.[15]

3.3 Shape of nanoparticles

It is important to note that structure sensitivity not only involves the size of the active particles, but also comprises effects associated with distinct characteristics as their shape and structure.[42] In the past decades, tremendous progress in shape-controlled synthesis led to different polyhedral shapes that can be produced and employed as substitutes for metal single crystals.[15,43,44,70] Nanoparticles with controlled facets and morphology are most frequently synthesized through colloidal methods, consisting in reduction of a metal salt precursor with or without a stabilizing agent in solution, and are summarized in earlier reviews.[61,71,72] Various computational approaches, first mainly based on thermodynamics, later extended with kinetic driving forces, have been used to see which polyhedral shape the nanoparticles adopt and to predict the functional properties.[32,73–75] The most stable equilibrium shape of the Pt nanoparticle changes with the size.[76,77] For Pt nanoparticles, the relationship between shape and surface structure is documented. Different shapes expose different crystallographic planes.[15,43,61] To demonstrate the different crystal planes enclosing the Pt nanoparticles, a unit

stereographic triangle analogous to the one used for Pt single-crystals (Figure 2) is frequently used. This is illustrated in Figure 3.[37,78] For instance, a cube, octahedron and rhombic dodecahedron expose (100), (111) and (110) surfaces respectively.[15,43] The distribution of under-coordinated sites on edges, kinks, corners and terraces is controlled by the shape of the nanoparticle.[42]

There are many examples where the presence or absence of certain crystallographic facets associated with a particular shape, could be used to interpret the catalytic performance of different shapes.[79] Detailed size- and shape-dependent catalytic performances of metal nanoparticles may be found elsewhere.[37,50] With specific regard to Pt nanoparticles, the shape dependency has been investigated for several reactions. An example is the reaction between hexacyanoferrate (III) and thiosulfate ions in colloidal solution of Pt nanoparticles. The activity trend, multiarmed nanostar > tetrahedral-shaped Pt nanoparticles > cubic nanoparticles could be correlated with the fraction of surface atoms located on corners and edges.[80,81] The effect is also known for some heterogeneous gas-phase reactions such as the ethylene hydrogenation catalyzed by Pt nanoparticles supported on silicon wafers and mesoporous silica.[82,83] The shape also affects the reactivity for the oxidation of 2-propanol by Pt nanoparticles supported on γ-Al_2O_3.[84] Regarding the selectivity, the cis-trans isomerization of 2-butene has been reported to vary by using different Pt nanoparticle shapes supported on silica xerogel.[85] Also for benzene hydrogenations and pyrrole hydrogenations catalyzed by Pt nanoparticles, in the two reactions respectively supported on silicon wafers and mesoporous silica, the selectivity is strongly influenced by the shape.[86–88] The shape dependency is well-known in electrochemical investigations. Examples include the oxygen reduction reaction[89,90] and oxidation of formic acid and ethanol[91,92] In summary, the synthesis of nanoparticles with open surface structures could be a route towards tuning the selectivity and activity.

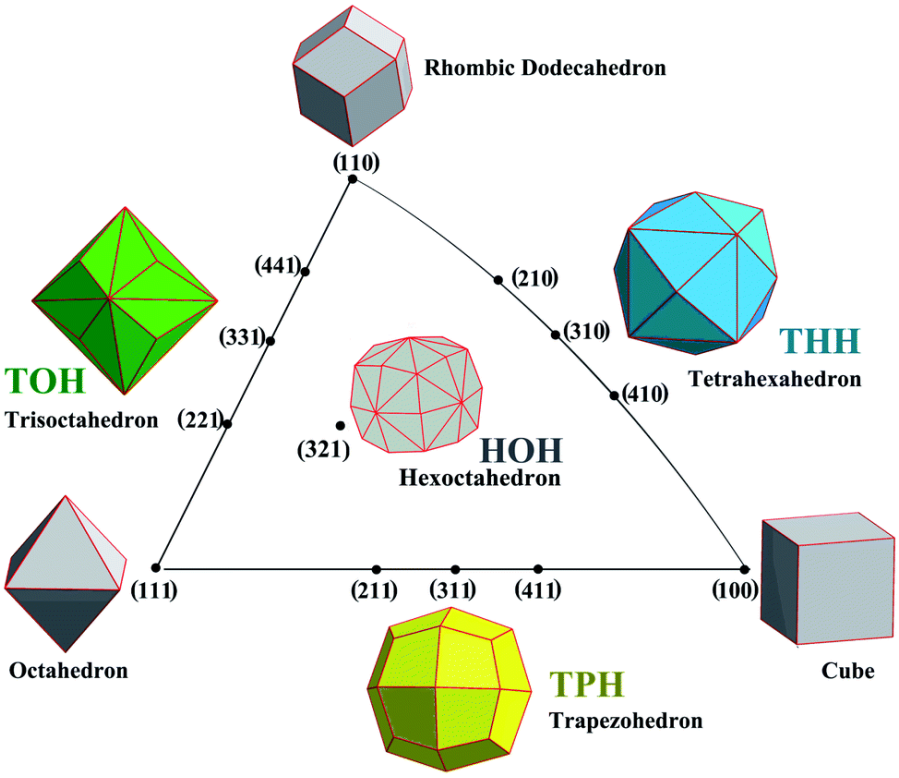

Figure 3. The unit triangle of the stereographic projection of polyhedral Pt nanoparticles enclosed by different crystal planes. Reproduced from ref [78].

4. Surface restructuring

4.1 Concept

The catalyst surface is dynamic and this complicates the study of individual contributions on the catalyst performance significantly. Its structure changes depending on the conditions and the active state of the catalyst can differ from the state of the fresh as-prepared catalyst.[88,93,94] Many techniques, *e.g.* (Ambient-Pressure) X-ray Photoelectron Spectroscopy (AP-)XPS, (High-Pressure) Scanning Tunneling Microscopy (HP-)STM, (in situ) Transmission Electron Microscope (in situ) TEM…, were developed to study the influence of reaction conditions at higher pressures and temperatures on the surface.[35,94–97] These developments were also an incentive in the field of computational catalysis to move from standard descriptive models at 0 K and low reactant concentrations (UHV) to more representative conditions. Theoretical studies are considered to be in situ when the calculations include practical conditions such as presence of reactant gases over a range of pressures, quasi-thermal equilibrium between gases and catalyst surface in terms of the chemical potential and stability of the surface under reaction conditions (*e.g.* oxidation of metal surfaces).[98] New methodologies towards in situ modeling that account for chemical environment, pressure and temperature comprise global optimization techniques, ab initio

constrained thermodynamics, biased molecular dynamics, microkinetic models of reaction networks and machine learning approaches and are summarized elsewhere.[99] The in situ experimental techniques and complementary computational simulations convey strong insight that the structure of metal catalyst surfaces is not rigid. Effects such as chemisorption and elevated temperatures induce restructuring of the surface.[93,96,100,101] Moreover a metallic surface has the tendency to become oxidized under oxygen pressure or carburized under carbon chemical potential.[1] The first examples presented here are Pt single-crystal studies in realistic gas pressures and temperatures. In the second set of examples, the effect of the gaseous environment, thermal treatment and catalytic reaction is discussed for supported Pt nanoparticle systems.

4.2 Single crystals

In the case of platinum, considerable efforts to study the surface reconstruction under reaction conditions have been undertaken. Reconstruction due to high temperatures or adsorption of gases is reported for low-index surfaces as {100} [101,102], {110} [103–106], and {111}[107,108]. Annealing leads to faceting of the Pt(113) surface with formation of terraces.[109] Much effort has been devoted to exploring this effect upon exposure to certain gases. In the presence of carbon monoxide, stepped single-crystal (557) and (332) surfaces were studied by HP-STM, AP-XPS and density functional theory (DFT) and found to be prone to extensive and reversible restructuring at pressures above 0.1 Torr. The terraces of Pt(557) and (332) break up into nanometer-sized clusters and return to the original morphology after removal of the CO gas.[11] Restructuring due to CO adsorption at 1.54 mbar and elevated temperatures was observed for a stepped (557) surface with AP-STM.[110] HP-STM and theoretical calculations revealed the atomic-scale restructuring of the Pt(100) surface is induced by CO at pressures up to several Torr.[101] In another study; density functional theory (DFT) calculations, Monte Carlo simulations and STM were applied to a Pt(110) surface at high gas pressures and temperatures. It was shown that CO binds strongly to under-coordinated Pt atoms, thereby breaking the Pt-Pt bonds and forming steps on the surface.[105] Besides CO, H_2 has also been shown to restructure Pt single crystal surfaces as studied by STM and sum frequency generation (SFG) vibrational spectroscopy.[111] Using SEM, DFT, X-ray diffraction (XRD) and STM, Pt restructuring was also observed during ammonia oxidation. The ammonia induced restructuring was further studied for single crystals of different orientation; (533), (443), (865), and (100), Pt gauzes and Pt foil, and the extent of restructuring relies on pressure, temperature and time.[112,113] Using theoretical modelling, oxygen adsorption on Pt(110)[114] and NO and NH_3 adsorption on Pt(100) surface was predicted to induce restructuring.[115]

Another factor leading to surface restructuring is the chemical reaction (oxidation, reduction, carbonization, *etc.*) between a reactant gas and a catalyst surface. The interactions with O_2 have been widely studied. The formation of bulk platinum oxide phases and thin oxide films on the Pt(111) surfaces has been investigated by means of ab initio thermodynamic calculations,[116] and with experimental techniques as on the Pt(100).[117] Oxidation of Pt(110) and Pt(332) surfaces and its effect on CO oxidation has been studied using DFT, STM and high resolution x-ray photoemission spectroscopy. Under oxidizing conditions the surfaces reconstruct into 1D oxide structures that are highly active for CO oxidation.[118] A recent study using in situ STM, shows that upon exposure of Pt(111) to oxidizing atmosphere, single-layer surface oxides with Pt oxide rows are formed.[119] The Pt(111) surface also reconstructs upon exposures to atomic oxygen.[120] In electrochemical environments, the surface can restructure due to, among others, the electrode potential, electrochemical adsorption of oxygen, hydrogen, electrolyte anions and the formation of surface oxides.[121–124] Figure 4 represents a schematic illustration of the flat surface which restructures in realistic reaction conditions.

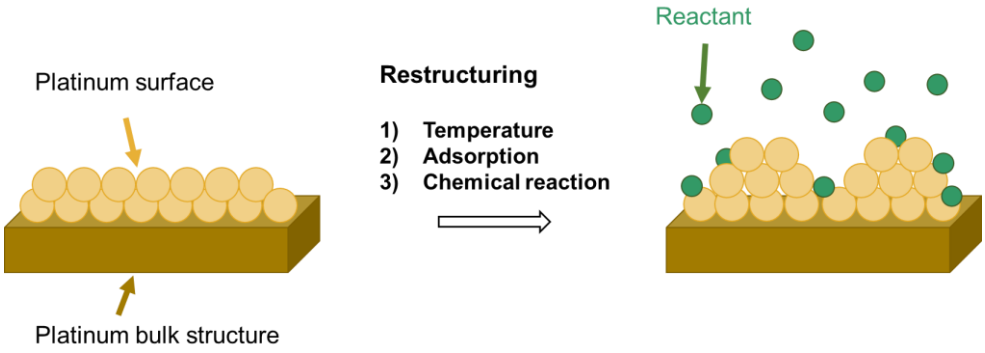

Figure 4. Schematic illustration of the flat surface of a platinum crystal prepared in UHV of which the surface reconstructs in realistic reaction conditions. Factors leading to restructuring are high temperature, gas adsorption or chemical reaction between reactant and catalyst surface.

4.3 Pt nanoparticles

For Pt nanoparticles, exposure to gaseous environment and thermal treatment during catalysis can lead to observable changes in size and shape.[81,125–130] A large number of studies are based on TEM techniques. For instance, using TEM, it was revealed that upon exposure to hydrogen sulfide in hydrogen, sulfur adsorbs and induces poisoning and restructuring of alumina supported Pt nanoparticles.[131] The effect of adsorbate and pretreatment conditions was studied using TEM for silica supported Pt nanoparticles. Particles mainly exposing the (111) faces were formed under reducing conditions (H_2 and vacuum). Rounded particles were formed after treatment in air at 923 K.[129]

Later, in an in situ ETEM study, large faceted Pt particles prepared in solution show reversible changes in morphology during oxidation in O_2 and reduction in H_2 at pressures of a few mbars.[125] Using ETEM, atomic reconstruction of {100} surfaces of Pt nanoparticles in oxygen environment could be observed.[96] Pt nanoparticles, supported on α-Al_2O_3, restructure and expose more undercoordinated steps, edges and corners upon CO oxidation reaction conditions as was shown using in situ diffuse reflectance Fourier transform infrared spectroscopy (DRIFTS).[132] Step formation from the NO reduction reaction with H_2 was investigated using in situ XRD and TEM. It was shown that Pt(110) surfaces reconstruct with extensive faceting and Pt nanoparticles become faceted in H_2 and spherical in NO.[133] Pt nanoparticles, prepared via colloidal synthesis, on a Si support were used for selective oxidation of methanol in the gas phase. Using XPS and diffuse reflectance infrared Fourier transform spectroscopy (DRIFTS), a size-dependent structure and oxidation state of the Pt nanoparticles was established. This resulted in high selectivity towards formaldehyde when the size of Pt nanoparticles was reduced to 1 nm.[134]

Also particle sintering and coarsening can change the crystallographic and electronic structure.[126] Using kinetic Monte Carlo simulations, the movement and diffusion of a platinum nanoparticle on different supports was studied. It changes with size, temperature, and adhesion on the support.[135] The sintering of Pt model catalysts on flat alumina and silica supports upon exposure to O_2 and NO_2 gases was studied under operating conditions using in situ indirect nanoplasmonic sensing (INPS).[136] The sintering of Pt nanoparticles on a planar SiO_2 and amorphous Al_2O_3 support was monitored during exposure to synthetic air at 650 °C by in situ TEM.[137,138] Annealing in H_2 at 800 °C induces sintering of Pt on planar SiO_2 as observed with in situ TEM.[139] Also on high surface area supports, in situ TEM can be used. Growth of Pt nanoparticles in reducing conditions, *i.e.* H_2 atmosphere and elevated temperatures, was revealed using the technique.[140] Agglomeration of Pt nanoparticles on carbon black at high temperatures was investigated using molecular dynamics simulations.[141] Particle coarsening was also studied using a model system of Pt nanoparticles on a single crystal Si wafer. Atomic layer deposition (ALD) was used to exert control over metal loading and Pt nanoparticle size and coverage. A series of samples with varying sizes and interparticle spacings was prepared and studied under different oxygen environments. The coarsening mechanism of the particles was studied with in situ grazing incidence small angle X-ray scattering (GISAXS). It was found that the as-deposited size and O_2 concentration were important parameters for the onset temperature of coarsening.[142]

Raybaud and coworkers were one of the first to describe the morphology of realistically sized platinum clusters supported on a γ-Al_2O_3 model which takes into account the operating conditions. Platinum clusters of 13 atoms, which have an estimated diameter of around 1 nm, were considered as a reasonable model for highly dispersed platinum catalysts. The influence of hydrogen pressure on the platinum particles was investigated by using periodic DFT calculations coupled to a thermodynamic model. They show that the Pt clusters are prone to a remarkable structural reconstruction upon H_2 exposure. The particles reach a higher hydrogen adsorption capacity than extended surfaces and form surface hydrides.[143] Later, in situ X-ray absorption near edge structure (XANES) recorded in high energy resolution fluorescence detection (HERFD) mode and density functional theory molecular dynamics (DFT-MD) of a similar system (nanometric platinum clusters supported on the two main surfaces of γ-alumina) were used for discrimination of different morphologies of nanoparticles and to quantify hydrogen coverage as a function of the temperature and hydrogen pressure.[144] The Pt clusters on γ-Al_2O_3 are also prone to restructuring during the dehydrogenation of methyl-cyclohexane reactions as was investigated using DFT-MD.[145] Using theoretical modeling on different Pt nanoparticles; sizes between 1-3 nm and shapes including octahedron, cuboctahedron and cubic, the size and shape effects on the uptake of atomic oxygen and hydrogen were investigated.[114]

In another study, H_2-TPD results support the changing structure of Pt nanoclusters during H_2 treatment and point out that restructuring needs to overcome activation barriers.[95] Besides morphological changes, understanding the electronic structure is also important for understanding the catalytic activity. In situ spectroscopic investigations (XANES and extended X-ray absorption) were conducted for supported Pt/γ-Al_2O_3 catalysts under partial pressures of H_2 and CO as well as at different temperatures. The data reveal a fluxional system where the changes in the electronic and metal-metal bonding structures show adsorbate and temperature dependencies.[146]

5. Support effects

5.1 Strong metal-support interaction (SMSI)

The support may play a distinct role in the overall catalytic performance. So called strong metal–support interaction (SMSI) effects have been the subject of many studies.[5,36,60,147–154] The term was first used in 1978 to explain the decrease in hydrogen and carbon monoxide sorption on group 8 noble metals supported on TiO_2 when reduced in H_2 at 500 °C.[148,149] SMSI effects were observed for other reducible oxides such as V_2O_3 and Nb_2O_5.[152,155–157] Several explanations were explored after these first observations, among which electronic and geometric effects. The latter was considered

the main effect; *i.e.* migration of (partially) reduced species from the support to the metal with blocking of the active sites as illustrated in Figure 5. Nevertheless, SMSI effects were in part ascribed to electronic effects.[5,26,152] The effect was reported to be less likely for less reducible oxides as SiO_2 and Al_2O_3.[36,158] SMSI behavior was also observed for combinations of reducible oxides and metals deposited on SiO_2 and Al_2O_3 supports.[156,157,159]

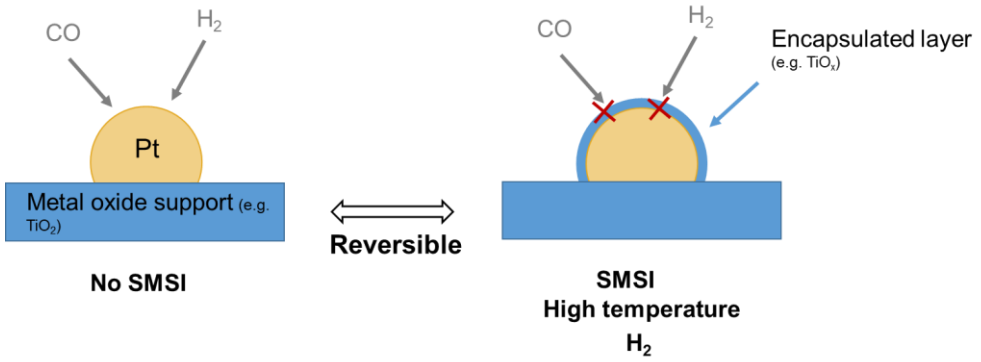

Figure 5. Schematic illustration of the geometric effect of the strong metal-support interaction (SMSI). In the SMSI state, CO and H_2 sorption is blocked.

SMSI has been repeatedly used to designate the geometric effect with migration of support species onto the active metal. However, more recently, SMSI has been used to refer to the broader concept of metal support interactions inducing changes in activity and selectivity. Generalizations are not straightforward, but SMSI can typically be expressed as 3 major effects: the geometric effect, the electronic interaction or in a bifunctional manner. Numerous examples, including Pt catalysts, of the 3 effects are reviewed elsewhere.[160] The change in the electronic properties of the metal catalyst is an implication of the strong interactions between the metal and the oxide support.[160] For example, the electronic interactions between platinum and a ceria support have been investigated and exploited for high catalytic activity in the water gas shift reaction.[161,162] In the bifunctional effect, SMSI generates active sites at the boundary between metal and support and involves migration or spillover of reaction species either from metal or support to the edge where the chemical reactions occur.[160] For example, the water gas shift reaction over Pt/TiO_2 catalysts occurs in a bifunctional manner.[163,164]

SMSI can have a major influence on the catalyst performance. Generally, catalytic activities of structure-sensitive reactions such as hydrogenolysis of hydrocarbons are suppressed by SMSI. An example is metylcyclopentane hydrogenolysis on Pt/TiO_2 that has no activity after high temperature reduction treatment.[165] On the other hand, on less structure-sensitive reactions such as dehydrogenation of hydrocarbons the effect is smaller.[152,154] Modification of catalytic properties by the SMSI effect has been explored

for Pt nanoparticles in a number of reactions supported on different oxide supports. Supported on TiO_2, CeO_2 and Nb_2O_5, enhanced activities and changed selectivities have been observed in hydrogenation reactions of molecules containing carbonyl bonds; *e.g.* CO[166,167], acetone[168], crotonaldehyde[169–172], cinnamaldehyde[173], benzaldehyde[174], acetophenone[175], acrolein[176],… The SMSI effect on TiO_2 has also been exploited for selective hydrogenation of nitrogroups in substituted aromatic molecules.[177] The increased performance for activating carbonyl and nitro groups can be attributed to stabilization of the group at metal-support interface.[169,170,177–180] Upon high temperature reduction, oxygen vacancies and cationic sites are generated at the interface. A correlation between the activity and Lewis acidity of the oxide was found, meaning that charge transfer between the carbonyl bond and cationic sites in the oxides occurs.[167,168,180–183] The oxygen vacancies can also interact with the oxygen atom of the group.[169] Pt supported on SMSI oxides have been studied in other hydrocarbon reactions. Supported on TiO_2, changed selectivities in the hydrogenolysis of alkanes[184] and methylcyclopentane[165] were observed. For n-heptane conversion, a high selectivity towards dehydrogenation with complete suppression of hydrogenolysis was observed.[155] A decrease in toluene hydrogenation was attributed to SMSI.[185] In the selective hydrogenation of lauric acid to n-dodecane, Pt on Nb_2O_5 has a higher activity than when supported on other supports.[186] In the hydrodeoxygenation of 1,6-hexanediol, a high selectivity to n-hexane was ascribed to SMSI effect.[187] On ZrO_2, the SMSI effect after high temperature hydrogen treatment was required for n-hexane conversion.[188] Atomic layer deposition has been used to deposit a metal oxide overcoating on the active material. This mimics the SMSI geometric effect and could also enhance the stability against sintering.[189,190] For example, a titania layer on Pt supported on $SrTiO_3$ has been used to enhance the selectivity to allyl alcohol in acrolein hydrogenation.[179] Atomic layer deposition has also been applied for improving the SMSI effect resulting from the metal–support interface. It has been exploited for improving of the activity for Pt on ZrC catalysts in the oxygen reduction reaction and for Pt on CeO_2 nanorods in the NO-CO reaction.[191,192]

Even after 4 decades of research, the origin of SMSI is being investigated. The geometric effect has been studied by imaging the encapsulated overlayer with transmission electron microscopy.[193–196] Using sum frequency generation (SFG) vibrational spectroscopy and DFT calculation, the molecular and electronic interactions were revealed in furfuraldehyde hydrogenation on Pt/TiO_2.[183] In an in situ infrared reflection adsorption spectroscopy on a model $TiO_x/Pt(111)$ surface, enhanced stability and activity for CO oxidation was attributed to the encapsulated layer of TiO_x.[197] Crotonaldehyde hydrogenation on Pt/TiO_2 was studied using in situ sum

frequency generation (SFG) vibrational spectroscopy.[182] XPS was used on Pt/yttria-stabilized zirconia catalysts and confirm charge transfer from support to the platinum.[198] The electronic support effect has also been extended for Pt supported on transition-metal carbides. Using DFT, a strong improved water gas shift reaction activity was demonstrated.[199] Small-angle X-ray scattering (SAXS), XRD and XPS was used to understand Pt/ceria-zirconia in the reduction of NO by propene in oxidizing conditions. The results were discussed in terms of the structural and electronic modifications induced by the SMSI effect.[200] The presence of S species on TiO_2 can suppress the geometric SMSI effect and improve the CO oxidation ability.[201]

SMSI examples for platinum on less reducible supports such as Al_2O_3 or SiO_2 remain much more limited. SMSI state of Pt/Al_2O_3 with reduced CO sorption capacity has been established by diffuse reflectance IR spectroscopic study.[202] Pt/SiO_2 reduced at high temperature showed an enhanced activity in propane dehydrogenation, which was ascribed to both electron and geometric SMSI effects.[203]

The examples so far, include SMSI after high temperature reduction. SMSI however can also be introduced through a mild reduction in $NaBH_4$ and HCHO solution.[181] Studies regarding SMSI under high temperature oxidation conditions, however, remain limited. SMSI between platinum group metals and hydroxyapatite on ZnO has been established resulting in increased stability in CO oxidation. The effect was explained by the encapsulated support, inhibiting metal leaching and aggregation.[204] LEED and STM on FeO_x/Pt was used to study the role of the encapsulation layer in the enhanced activity in CO oxidation in oxygen lean conditions.[205]

5.2 Other support effects

Discussed above are the more traditional examples of SMSI on oxide supports. However it is important to consider that the term can also be used in a more general sense by comprising the influence of the support on metal dispersion, spatial distribution, sintering and particle shape. Moreover, other supports, besides reducible oxides mentioned in the previous section, can induce metal-support interactions. This section briefly covers various examples, however it is not an exhaustive overview. The aim here is to illustrate that supports can have significant influence on metallic Pt nanoparticles. For a detailed overview the reader is encouraged to consult topical reviews.[206,207]

The shape of the metal particles can change with the support. As the shape influences the exposed crystallographic planes and the coordination number of surface metal atoms, the effect on catalytic performance can be significant.[88,207–209] In systems with strong interactions with the support, the particles spread over the support, which results

in flat so-called 'raft-like' structures.[26] Raft-like structures have been commonly reported on α- and γ-alumina.[210–212] For Pt_{13} clusters on γ-Al_2O_3 surfaces DFT calculations reveal that the hydroxylation of the support results in weaker metal adhesion, which influences particle shape. On the dehydrated (100) surface, flat particles were formed, while 3D morphologies were present on the hydroxyl groups of the (110) surface.[213] Related to this effect, is epitaxy of metal particles on the support surface, *i.e.* specific orientations and morphologies of nanoparticles can be favored on different oxide supports. By choosing a support that has strong epitaxy with platinum, specific orientation of the nanoparticle can be stabilized.[150] An example is Pt on $SrTiO_3$ cubical nanocrystals.[214] Strong interactions between Pt and the support can also protect against sintering.[206,215,216] For example, reduced sintering for Pt nanoparticles on γ-Al_2O_3 was revealed in situ after O_2 and H_2O treatment via Extended X-Ray Absorption Fine Structure spectroscopy (EXAFS) and ex situ via STEM.[217] The stability of the active particles can also be affected by surface poisoning during the reaction. For example, coke on Pt nanoparticles was formed at a higher rate when supported on Al_2O_3 than on CeO_2.[206]

Other supports besides reducible oxides can induce metal-support interactions. In comparison however, materials as carbon, graphite and zeolites exert a much weaker influence on the supported particles.[158] Pt–Pt interactions are usually much stronger than Pt–C interactions in carbon supports, however specific allotropes can exert larger influences. For example, it was revealed in a computational study that Pt_{13} clusters on carbon nanotube supports have higher stability than clusters on graphene.[218] Zeolites can induce steric constraints on the morphology of the nanoparticles and its acidity can have large effects on the electronic properties of Pt nanoparticles.[208,219,220] Early studies for investigating the electronic structure of Pt nanoparticles concentrated most on Y zeolites and the common explanation was that Pt particles were electron deficient on acid supports.[207,221] On the contrary, basic supports such as KL zeolite generate Pt particles with electron excess.[207] This can influence the activity of zeolite supported Pt catalysts in different reactions *e.g.* benzene hydrogenation, propane and neopentane hydrogenolysis and isomerization, and selectivity in reforming.[220,222,223] For example, the turnover frequency in neo-pentane conversion on Pt/Y zeolite was shown to change with metal–support interactions, while the selectivity towards hydrogenolysis increases with decreasing particle size.[222] By studying the trend in the competitive toluene/benzene hydrogenation on Pt/L-zeolites with different cations and thus varying acidity, it was shown that the support influences the Pt clusters via electronic interactions.[221]

6. Complexity of model catalysts

6.1 Concept model catalysts

The term modelling implies that a complex catalyst is substituted by a more simplified system, eliminating variations in particle size, shape and irregular defect structures of high surface area systems.[34,224] With the industrial-grade system too complicated for rigorous understanding; model catalysts, traditionally single crystal surfaces, were studied with surface science techniques. A shortcoming of this approach is the so-called materials and pressure gap.[2,8,10,35,98] Single crystal surfaces lack the complexity needed to study some important aspects.[35] In order to overcome this so-called materials gap between ideal and real catalyst systems, model catalysts with more complex features were developed.[2] The pressure gap originates from the discontinuity in pressure between model and real reaction conditions. Surface science studies are usually performed under ultrahigh-vacuum (UHV) conditions to exclude surface contamination and many techniques such as electron spectroscopies require high vacuum conditions. Closing the pressure gap between atomic-scale studies in UHV and real catalysis at pressures that are several orders of magnitude higher requires techniques covering the entire pressure range. They must be surface sensitive techniques that work in the presence of a gas phase. Examples include sum frequency generation (SFG) or polarization-modulation IR reflection absorption spectroscopy (PM-IRAS), high pressure photoelectron spectroscopy (HP-PES), environmental TEM (ETEM), scanning tunneling microscopy at high pressure (HP-STM), high pressure X-ray photoelectron spectroscopy (HP-XPS) in reactor cells. These techniques themselves will not be further discussed.[2,35,97,224–226]

Several strategies can be considered starting from the well-defined single crystal surface towards the industrially applied porous catalyst. Figure 6 shows some intermediates between the two extremes. Increased complexity in comparison with single crystals is obtained with thin films or nanoparticle arrays on planar supports. The next step to close the materials gap is 3D model catalyst systems with well-defined and uniform properties such as particle size, shape, surface structure and location of the Pt nanoparticles.

Zero-dimensional (0D) model catalysts refer to nanoparticles like quantum dots or clusters and also include nanoparticles in solution.[227,228] There are examples of unsupported 0D particles that are used for reaction studies in liquid phase [80,81,125] and gas phase [229–235]. However in most studies the particles are dispersed over a support.

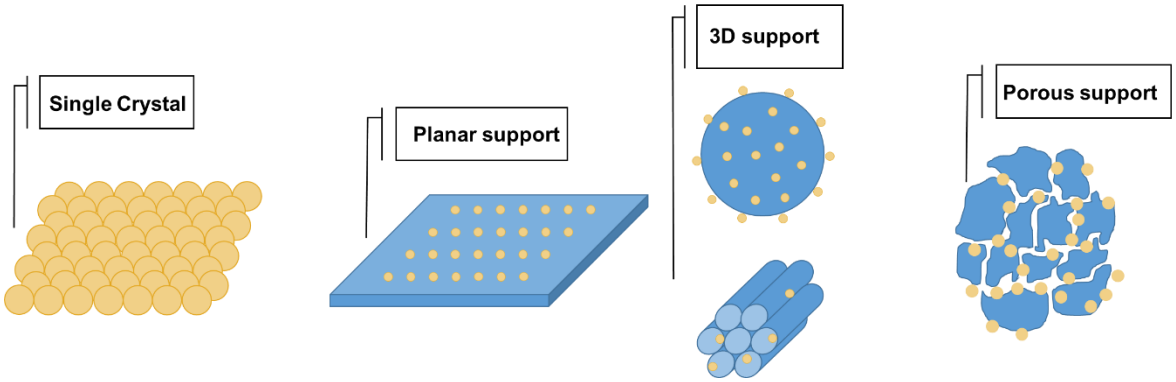

Figure 6. Several strategies exist for reducing the complexity of industrial porous catalyst systems: from single crystals to more complex 2D (planar support) and 3D model systems.

6.2 2D model catalysts

Traditional studies are based on single crystal or nanoparticle arrays on planar supports.[2,35,226] Using model single crystals and sum frequency generation (SFG), Somorjai's group could characterize several important reactions such as ethylene hydrogenation, propylene hydrogenation and dehydrogenation, cyclohexene hydrogenation and dehydrogenation, and carbon monoxide oxidation.[8,236] Other examples using single crystals are mentioned above in the structure sensitivity (§3.2) and structure restructuring paragraph (§4.2). Single crystal surfaces have provided many meaningful insights in model studies. Nonetheless, they are an oversimplification and neglect aspects such as defects, particle size and shape, presence of various orientations on the active particle, particle-support interactions,… For that reason, more complex two-dimensional and three-dimensional model catalysts are produced.[35,98,237]

Two-dimensional model catalysts are useful because surface science analytical methods can, due to the planarity and electrical/thermal conductivity, still be applied.[35,226] The catalyst supports that are most commonly used are single crystals of oxides or thin films of the oxides on metal supports.[238–240] The latter is used to avoid detrimental problems associated with the insulating character of bulk oxides, which appears as reduced intensity and/or resolution in techniques based on charged particle surface probes.[34,238,239] Many of the planar model catalysts are prepared by physical vapor deposition under UHV to prevent contamination.[2,4,226] However the technique produces particles with broad size distributions.[4,34] This can be overcome by mass-selected cluster beam deposition or atomic layer deposition.[4,34,241] Other preparation methods for model systems include for instance spin-coating of metal salt solutions, laser interference nanolithography, electron beam lithography, photolithography and Langmuir–Blodgett methods.[35,226,242] If similar wet chemical impregnation procedures as for the production of technical catalysts are used on a planar support, the chemical properties of the model system are closely related to the technical catalysts.[34] The main

shortcoming, however, is that structure and morphology of nanoparticles are more difficult to control.[34,238] In an additional step, more complex features can be introduced by surface modification or by addition of poisons or promoters.[2]

In the next paragraph, examples of 2D platinum model catalyst studies are listed. The cited examples are not a comprehensive list, but are intended to give an idea on commonly applied designs.

6.2.1 UHV techniques

Thin film and nanoparticle model catalysts were prepared by physical vapor deposition. For example, Pt deposited through evaporation on Ti foils was used for studying metal-support interactions and its influence on CO and H_2 chemisorption.[243] Sputtered platinum was used as model electrocatalyst for the oxygen reduction reaction.[244] On Al_2O_3 supports, evaporation of Pt leads to formation of nanoparticles. The model was used to study O_2 and H_2 treatment induced faceting and its effect on hydrogenolysis of methylcyclopentane and the isomerization of neopentane.[245] Nanocluster arrays deposited via electron beam evaporation on graphene on Rh(111) was used as model catalyst for the oxidation reaction of sulfur. The intrinsic Moiré pattern of graphene on Rh(111) served as template for narrow size distribution of the platinum nanoclusters. Using XPS, the difference with Pt(111) and stepped Pt(355) in the reaction kinetics were revealed and the effect of steps/edges and defects could not be neglected in oxidation catalysis.[246] Platinum was deposited through physical vapor deposition on a model planar Highly Oriented Pyrolytic Graphite support. XPS was used to study the oxidation state and activity for ethylene hydrogenation of Pt nanoparticles in NO_2.[247,248]

Narrow size distributions and small cluster sizes can be produced by size-selected cluster beam deposition. This method involves three steps: preparation of gas-phase metal clusters (*e.g.* through laser vaporization or magnetron sputtering), mass-separation in the gas phase and soft-landing on the support. In this approach, the number of atoms in the deposited clusters can be precisely controlled.[249,250]An example is the size dependency of CO oxidation and ethylene hydrogenation of Pt clusters supported on thin MgO(100) films.[251,252] In another study, CO oxidation on Pt/TiO_2 was studied in function of cluster morphology and reduction state of the support.[253,254]

Another successful approach consists in Atomic Layer Deposition (ALD). It is based on alternating exposures of a support to a gas-phase precursor of the chemical element and a co-reactant.[241,255–261] ALD is characterized by self-limited surface reactions resulting in atomic-level control, even on large surface area supports.[241,262] Pt-ALD

deposits nanoparticles in the first cycles according to a nucleation-controlled growth mechanism.[241,260,262,263] Pt-ALD uses often the platinum trimethyl(methylcyclopentadienyl) complex ($MeCpPtMe_3$) in combination with O_2 as co-reactant.[241,264] Other co-reactants are O_2 plasma, O_3 gas, H_2 gas, H_2 plasma, N_2 plasma and NH_3 plasma.[262,265–268] Moreover, through a two-step process with both O_2 and N_2 gas, the morphology of the Pt nanoparticles can be tuned, which can be valuable for creating model catalysts.[241] In a first step with O_2 gas, particle coverage can be controlled and in the second step with N_2 plasma, the particle size can be varied at constant coverage. This advantage has been exploited for creation of 2D Pt model catalysts for the hydrogen evolution reaction.[241] The impact of other ALD process parameters such as deposition temperature, co-reactant pressure, number of ALD cycles and passivation gases has been studied extensively.[269–272]

6.2.2 Non-UHV techniques

Examples for model catalysts on planar supports using colloidal synthesis methods were already discussed above in structure sensitivity paragraph §3.3.[86–88] Colloidal platinum nanoparticles can also be deposited by spin coating. Coverage and dispersion can be varied by concentration and spin speed. The effect of ligand removal conditions (H_2 or O_2) was studied for spin coated Pt on a silicon wafer.[273] To deposit 2D arrays of nanoparticles, the colloidal Pt nanoparticles can be distributed over the support using the Langmuir-Blodgett technique. The method consists of dispersing the solution on a liquid surface and then compressing at a given surface pressure on an oxide surface. [44,82,274] Using lithography, 2D arrays with high control of particle size and interparticle distance can be deposited.[275–277] Numerous lithography examples can be found for platinum catalysts. For example, electron beam lithography, size reduction lithography, and nanoimprint lithography have been demonstrated to produce platinum nanoparticles and nanowires on oxide films on SiO_2 and Al_2O_3 supports.[278,279] Patterns of Pt nanoparticles on SiO_2 and CeO_2 have been made by electron beam lithography in combination with lift-off techniques.[242] Research related to lithograpy techniques and variants thereof for model Pt catalysts is still ongoing: e.g scanning probe block copolymer lithography[280], colloidal lithography[281], displacement Talbot lithography (DTL) in combination with dry-etching techniques[282],…

7. 3D model catalysts

Model high surface area catalysts with a well-defined structure are unsuitable for surface science analysis tools, but can be used for reaction kinetic studies and characterization methods such as transmission infrared, Raman and x-ray absorption spectroscopy, ETEM,...[34,283] To reduce the complexity, the particle size, shape, surface structure and

location of the particles must be well-characterized and uniform.[83,237,284] The catalyst properties can then be varied systematically to find the correlation with the catalytic activity and selectivity.[83]

In this section, examples of 3D Pt model catalysts are reviewed. They are prepared through solution-phase methods, although a few examples of ALD were also reported. Most Pt deposition methods used for 2D model catalysts (planar support), *e.g.* PVD, lithography and cluster beam deposition (§6.2) are line-of-sight techniques and not applicable for preparation of 3D models with high surface area supports.[285,286]

7.1 Spherical supports

The most simple three-dimensional model system is where the porous support of the technical catalysts is substituted by a spherical nonporous one. This nonporous powder model catalyst can bridge between the high surface area industrial catalyst and the planar model catalyst.[287,288] This strategy was used before to facilitate observing metal particle size, shape and composition during TEM studies.[289–291]

Spherical model supports have been previously used in a few studies to examine particle morphology and metal-support interactions by transmission electron microscopy.[34] An example is Rh particles supported on nonporous SiO_2 and TiO_2 spheres, prepared by alkoxide hydrolysis and plasma synthesis respectively. Using TEM, the oxidation behavior of the Rh metal particles was studied.[289] In another study, palladium clusters grown by UHV vapor deposition on crystalline Al_2O_3 and TiO_2 microspheres were used to study the effect of support surface preparation on particle shape.[292] Furthermore, silica sphere supported cobalt catalysts were prepared using strong electrostatic adsorption (SEA), a wet impregnation method based on strong electrostatic interaction between precursor and surface by controlling the pH.[293] In the study, the monodisperse nonporous silica spheres were prepared by the Stöber method and considered as model support, well-suited for a TEM study.[291] In another study, oxide spherical supports, both commercial polydisperse silica and titania as synthesized monodisperse Stöber particles, have been employed as powder model catalyst support. Pt, Pd, Ag and Au nanoparticles were deposited by surface-mediated incipient wetness impregnation, followed by a thorough structural characterization by TEM focusing on crystallinity, lattice defects and surface stress of these metal nanoparticles.[294] With respect to in situ environmental TEM, an example of this approach using spherical model supports is nickel particles supported on Stöber silica spheres during oxidation of methane under high conversion conditions.[290] Another example where nonporous spheres are considered a 3D alternative of the flat model supports, is Fe

and FeMn nanoparticles on Stöber silica. The authors demonstrated their use for Fischer-Tropsch synthesis experiments.[295]

To the best of our knowledge, model studies under realistic conditions with well-defined Pt nanoparticles on a nonporous spherical support are missing. In one study, nonporous spherical oxide particles were synthesized by an aerosol-based chemical vapor synthesis (CVS) followed by sintering. Different model supports, silica, titania and alumina nanoparticles in the nanometer and submicrometer size range were prepared via this way. These particles were subsequently coated with Pt nanoparticles by a chemical vapor deposition method. The model catalysts were studied with wide-angle X-ray diffraction (WAXS or XRD) and small-angle X-ray scattering (SAXS) for investigation of morphology and structure.[296] Only one example can be considered as a model catalyst study, although not presented as one by the authors. Gao and coworkers used Pt nanoparticles with various sizes supported on amino-modified silica spheres in a systematic study of the relationship between catalytic performance and Pt particle size. A strong size effect of Pt nanoparticles on the regioselective hydrogenation of quinoline was established.[46] Spherical supports have been the subject of a number of studies, but they are not used as model catalyst *i.e.* not used for structure-activity relationships. They mainly include Pt supported on porous spheres.[297–301] Pt nanoparticles on Stöber silica spheres have been employed for testing and comparing analysis techniques.[302,303]

7.2 Ordered High Surface Area supports

The next step towards increasing complexity is using well-defined Pt nanoparticles supported on regular high surface area supports. High surface area model systems are still a reduction in complexity of real industrial catalysts, because several properties *i.e.*, metal particle size, surface structure, particle location within support, are well-characterized and can be controllably varied.[304]

Colloidal synthesis of nanoparticles is a suitable method for control of size and shape and thus for generation of model powder catalysts under realistic conditions.[72] Several synthetic methods for solution phase synthesis of monodispersed Pt nanoparticles supported on mesoporous oxides for three-dimensional model catalysts have already been reported by Somorjai and coworkers.[284] The Pt particles, ranging in size from 1 to 10 nm, were first synthesized in solution phase and then incorporated in the support. The different solution phase methods vary in choice of reducing agents, capping agents, reaction temperatures and solvents. Incorporation of the nanoparticles into the pores of the high surface area mesoporous oxides is done through sonication or direct synthesis of the oxide support around the particles. The supports were highly

ordered SBA-15 silica and Al_2O_3 and Ta_2O_5 with SBA-15 like structure.[284] A schematic illustration is given in Figure 7.

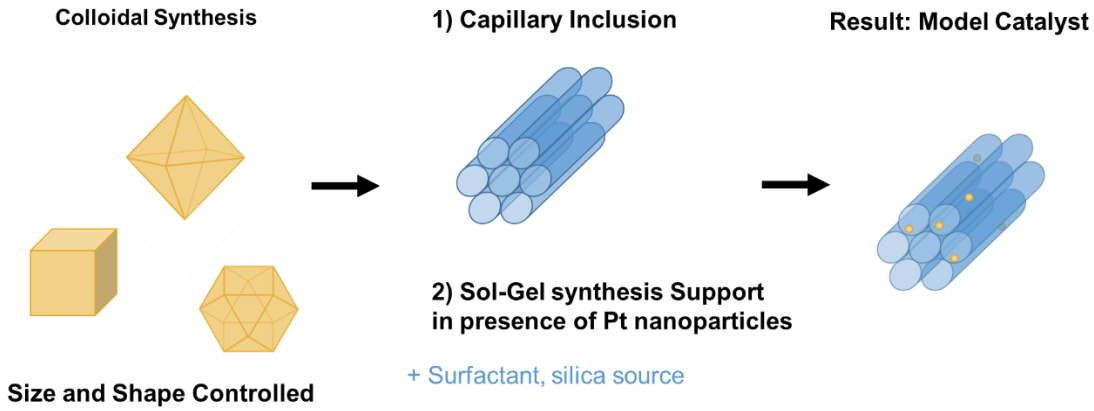

Figure 7. Schematic illustration of the preparation method of 3D model high surface area catalyst.

Coupling synthesis of monodisperse nanoparticles with studies of catalytic performance allows the deconvolution of the different structural properties involved in reactions.[44,72] Thorough studies using three-dimensional Pt model catalysts remain scarce. A few studies report the use of Pt nanoparticles supported on SBA-15. An example is the size effect of the ethylene hydrogenation and ethane hydrogenolysis. The Pt particles were prepared by alcohol reduction and incorporated during hydrothermal synthesis of SBA-15 or through sonication in SBA-15. It was found that ethylene hydrogenation rates were invariant with particle size, in contrast to ethane hydrogenolysis that shows structure sensitivity over the size range of 1-7 nm.[44,45] Another example by the same group involves synthesis of monodisperse Pt nanoparticles with well-defined shapes, and thus exposed facets, for ethylene hydrogenation. The synthesis of the Pt nanoparticles was achieved through a solution phase synthesis with silver ions and polyvinylpyrrolidone (PVP). Incorporation of the Pt nanoparticles in the support SBA-15 was done during the hydrothermal growth of the support. It was found that the rates of the reaction decreased with the amount of Ag present in the Pt nanoparticles after purification.[83]

Another successful approach is based on atomic layer deposition (ALD), which can be applied to large surface area supports. The uniform nanoparticle size and precise control of loading that characterizes ALD, could be exploited to obtain homogeneity required for model catalysts. Model catalysts have been created on high surface area $SrTiO_3$ nanocubes which are preferentially terminated by (100) facets. It was shown that the Pt nanoparticles on these support cubes adopt the most thermodynamically stable shape. The shape was also stable over a wide range of reaction conditions.[214,305] A similar model catalyst (on $Ba_xSr_{1-x}TiO_3$ nanocubes) was also used to study structure

sensitivity and SMSI effects in the acrolein hydrogenation.[150] Model Pt nanoparticles supported on graphene nanoplatelets, also deposited through Pt-ALD, were used for investigation of the size-dependent performance in propene oxidation. The performance could be related to the number of facet sites.[285] ALD has also been applied to study the size effect of Pt nanoparticles on carbon black in ethanol oxidation.[306]

Size-selected Pt clusters were also reported for 3D model catalysts. They were deposited on anodized aluminium oxide (AAO), however only 28% of the deposited clusters resides in the pores. They are tested in realistic conditions for oxidative dehydrogenation of propane. A high activity and selectivity towards formation of propylene over other products could be achieved. Corresponding quantum calculations reveal that the undercoordinated Pt atoms are responsible.[307] Chemical vapor deposition (CVD) of a Pt precursor has also been used for preparing model systems inside zeolite supports. Chemical vapor deposition was advantageous because no acidity is created in the reduction step. The model catalyst was used as a bifunctional catalyst in the conversion of methylcyclopentane to study the effect of support acidity.[308]

7.3 Other 3D models

Another strategy that was previously reported as a three dimensional powder model catalyst, is the use of unsupported highly dispersed platinum such as platinum black. Platinum black exposes polycrystalline facets, has a relatively high surface area and no support effects that can hamper spectroscopic investigations.[309–311] Pt black was investigated in n-hexane/H_2 environment between 483 and 663 K, followed by O_2 and H_2 exposure at 603 K. Surface composition changes with the exposed gas. Anisotropic recrystallization, favoring the more open (220) and (311) lattice planes, was observed upon H_2 treatment.[311] Another example of an unsupported model catalyst is PtSn powder for study of the effect of O_2 and H_2 treatment. The model catalyst was synthesized through direct reduction of a solution containing both H_2PtCl_6 and $SnCl_4$ using hydrazine.[312]

An alternative approach, also based on the cluster beam deposition technique, consists in cutting up of the substrate after nanoparticle deposition. This has already been reported for palladium nanoparticles. After deposition onto planar graphite tapes, microdicing of the tape was used to obtain the powder. A cluster size-dependent performance was observed in the vapor phase hydrogenation of 1-pentyne.[313]

The materials gap can also be tackled by using computational methods. For example, DFT calculations combined with kinetic Monte Carlo simulations were used to study

the catalytic CO oxidation of nanoparticles in the size range of 1 - 5 nm. The simulations were based on considering all sites on a truncated octahedral nanoparticle, which was cut in half to describe the geometry of a supported particle. It was revealed that depending on the reaction conditions different sites dominate the overall activity.[314] For NO reduction and oxidation, structure sensitivity (size effect) was studied using kinetic Monte Carlo simulations over 3D model Pt nanoparticles. The model Pt nanoparticles that were considered had sizes ranging from 2.3 to 4.6 nm and a truncated octahedral shape.[315] The kinetics of CO oxidation on nanometer supported catalysts in function of different facets and adsorption of reactants was modeled employing Monte Carlo simulations.[316] The model was also used for hydrogenation of alkenes.[317] In a DFT study of the oxidation of ethylene on Pt/MCM-41 models, the reaction pathway and the electronic effect of the silica support was studied. Several computational models were constructed to mimic distinct parts of the catalyst.[318] 3D nanoparticle structural models could be obtained from high-precision electron microscopy on Pt/carbon black and used in density functional theory for investigating the oxygen binding properties of Pt catalysts.[319] 3D numerical simulations are useful for detailed gas-phase and surface kinetics. This was demonstrated using Computational Fluid Dynamics (CFD) for high-temperature catalytic partial oxidation of methane over a platinum gauze.[320]

8. Summary and strategy of the research

The examples in this chapter clearly show the immense advancements that have been made during the past 40 years with respect to connecting model catalysts and technical real world catalysts.

8.1 Limitations planar model systems

Model systems with increasing complexity, from single crystals to nanoparticles on planar and 3D supports, were developed to understand the main features of a technical catalyst system. Each model system has its limitations and the level of complexity should be adjusted to the purpose of the study.[8]

Most studies have been content to single-crystal surfaces and well-defined nanoparticles with controlled size and morphology, and hence facets, on planar supports. Using these models, fundamental insights into kinetics, thermodynamics and chemisorption were acquired at the molecular scale. However, the complexity of a technical catalyst deviates significantly from these well-defined model surfaces. Many industrial catalysts consist of metal particles deposited on supports of which the pore structure is typically very complex with pore dimensions in the (sub)micron size range. Common support

materials are metal oxide, mixed-metal oxide and zeolite microcrystals which are usually arranged randomly with various orientations.[23,36,37,321] Catalysts can also have amorphous phases on the surface of the crystalline phases. In addition, catalyst crystals expose various crystal planes having defects such as kinks, edges and steps.[321] Thus, these model systems lack the complexity needed to understand the catalytic reactions on real catalyst surfaces. The heterogeneous nature of technical catalysts prevents direct translation of these insights to real world catalysts.[7,10] Furthermore, planar model catalysts expose only a very small amount of active sites, which makes them less suitable for activity measurements.[295] Additionally, they cannot easily be used in real environments as reactor set-ups for catalyst testing. Effects such as poor accessibility of active sites in the porous matrix and non-steady state kinetics in reactors cannot be studied using these planar model systems. To overcome these issues, developing 3D model catalysts systems, containing more features that resemble the technical catalyst, and testing them in a catalytic reactor could be very useful.[322]

8.2 Reactor level model catalyst

Planar model systems are thus very valuable for understanding of the impact of the catalyst structure on elementary processes at the active site *i.e.* the atomic/molecular level. However to be industrially relevant, complementary and equally necessary is the engineering/reactor level.

On this level, structural features including the distribution of active material in the catalyst granule, the specific surface area, morphology and pore structure can have large effects on the catalyst performance.[323,324] Examples of operating parameters that influence the performance are the reactor type (fixed bed, fluid bed, *etc.*), temperature, pressure, composition, flow rate and fluid management, agitation (in liquid phase batch reactors).[158,325] Complicating is that, at this level, the impact of properties of both catalyst and reactor are intertwined. Reactor level processes can affect the elementary processes on the porous catalyst material at the molecular level.[22,326] For example, the overall heat and mass transport phenomena in the reactor can have an impact on local concentrations and temperatures, which, in turn, can influence the structure and composition of a catalyst.

Different requirements apply to catalysts that are either used in a continuous flow or batch reactor. Catalyst in a fixed bed reactor are usually shaped in larger catalyst pellets to minimize pressure drop. With these larger pellets, however, diffusion limitations can exist. Batch and fluidized bed reactors generally use smaller particles so the catalyst can be easily suspended in the reaction medium.[19,25,26,28–31,158]

Flow models of different levels of complexity have been reported. They range from the simplest models based on ideal plug flow in packed bed reactors and perfect mixing in stirred batch to more elaborate models that include complex flow patterns inside porous media.[326,327] The condition for plug flow is that the radial velocity distribution is uniform without mixing in axial direction. Flow patterns in real reactor conditions however, do not satisfy this condition. For example, channeling might arise in a packed bed if there are variations in the packing density. Open channels with low flow resistance are formed and hence the local fluid velocity varies over the cross-section.[328] Another effect is formation of dead zones, *i.e.* stagnant zones where there is no fluid motion. Recirculation or secondary flows can also cause deviations from the ideal flow patterns.[327]

In practical applications, the catalyst is used in a chemical reactor. In catalyst design, it is thus important to include reactor operational parameters as heat and mass transfer. Hence, for meaningful kinetic data for practical applications, developing 3D model systems and evaluating its global reaction kinetics in realistic reactor setups is important. This doctoral research aims to contribute to this field.

8.3 Requirements 3D model systems

Selecting a suitable model system depends thus on the objectives of the research. Different objectives dictate different catalyst designs. In this work, synthesis techniques for preparation of 3D model catalyst systems that can be tested at the reactor level are presented. In this study, '3D model' refers to the entire catalyst system, thus including the support if one is used.

As discussed above, there only a few reports of 3D model catalysts systems and so far, they were mostly limited to size and shape-selected particles on channel-type supports. Therefore, it is useful to develop 3D model catalyst systems as they hold significant potential for understanding structure-activity relationships. Future directions should include synthesis, characterization and reaction studies with monodispersed metal nanoparticles supported on 3D model supports. Besides empirical research, computational studies are very important for further correlation between model systems and catalytic reactions at the atomic level. However this research focuses on experimental studies.

In reflection of the problems with previous planar model systems mentioned above, we will summarize the properties of an ideal 3D model catalyst system. An ideal model system has a low structural complexity with a high degree of uniformity regarding the support structure as well as the supported active particles. A model catalyst support has a simple and well-characterized geometry. The most simple is a monodisperse

nonporous support. The use of nonporous supports avoids complex intraparticle diffusion.[324,329] Another approach is the use of ordered porous supports of which the structure is fully characterized. In each case, whether a nonporous or porous model support is chosen, a precise and flexible control over all catalyst properties is essential. These properties are for example the size of the active particles, their shape, the presence of different facets, edges, corners, steps, poisons, promotors.[4,330] Furthermore, the catalyst system should be stable over the course of the experiment and should be reproducible.[9,330] For industrial purposes, metals are typically dispersed onto materials such as alumina, silica, zeolites, activated carbon, titania, zirconia or mixed oxides.[3] It would thus be very relevant to choose particles of these materials with a spherical morphology or with ordered porosity as a model catalyst support. Furthermore, working with well-defined unsupported high-surface area platinum catalysts is very relevant as they are interesting for specific applications requiring both electron and mass transport.[331–333]

This goal of this doctoral study was to demonstrate the significance of 3D model platinum catalyst systems and to find preparation routes for model systems for both supported and unsupported Pt catalysts, but with controllable properties. Well-defined nanoparticles and supports could enable a much better understanding of a number of important catalytic phenomena.

More specifically, this doctoral work presents 3 research directions. They are all related to achieving the goal of controlling the size, structure and distribution of the Pt nanoparticles. The 3 objectives are i) synthesis of a 3D spherical dense (alumina) model support and loading it with highly dispersed Pt nanoparticles, ii) evaluation of ALD for adding acid and metal functionality in zeolites in a controlled way and iii) finding a flexible method for the synthesis of ordered porous self-supporting Pt nanostructures. The latter was done by exploring ALD for replication of a mesoporous Zeotile-4 template. Zeotile-4 is an interesting choice because of the 3D pore accessibility. The inherent properties of the ALD process can lead to complete filling of the template.

A preliminary assessment of the performance in various model reactions is presented. These 3 objectives are summarized in figure 8. The following chapters 2-4 report each on one of these objectives.

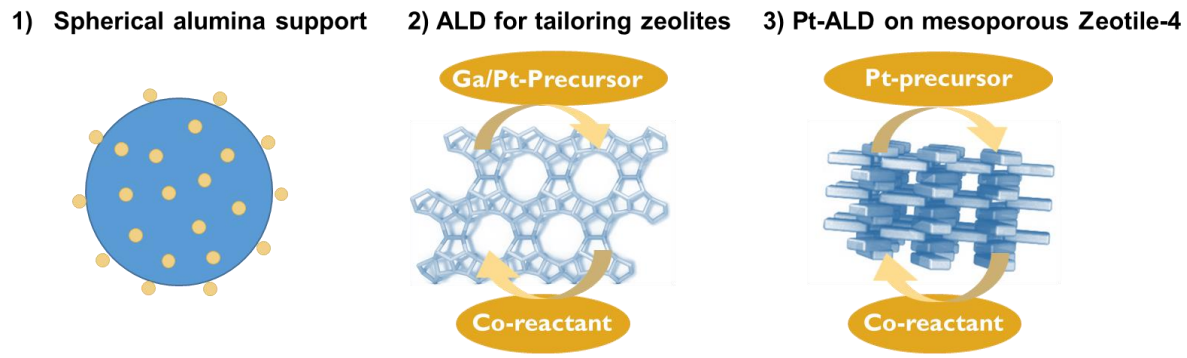

Figure 8. Research directions of this doctoral thesis.

Different characterization methods were used in this study, but one of the most extensively used methods was electron microscopy. In the following paragraph, the strengths and limitations of the technique are highlighted.

9. Electron microscopy

Numerous techniques are available for characterizing catalysts, however optical or X-ray technologies provide averaged information from a bulk volume. Electron microscopy on the other hand, can provide local information or information of individual supported nanoparticles, which is why the technique is indispensable in model catalyst research.[334,335] Electron microscopy encompasses a family of techniques such as scanning electron microscopy (SEM), transmission electron microscopy (TEM) and scanning transmission electron microscopy (STEM). In this study, a combination is used for a complete nanoscale investigation of the catalyst. The techniques that are employed include SEM, bright-field TEM (BF-TEM), (high-angle) annular dark-field scanning STEM (HAADF-STEM), selected area electron diffraction (SAED) and electron tomography. STEM is also combined with energy dispersive X-ray spectroscopy (EDX). Each techniques has its strengths and the decision to work with SEM or (S)TEM depends on the scale and type of the information that is needed (topography, morphology, structure or composition).

Electron microscopy is based on the interaction of an accelerated electron beam with the sample, which leads to emission of various electrons, X-rays and photons, as depicted in figure 9. Different detectors can gather different types of signals. As these detected signals result from different mechanisms of interaction with the sample, they contain different types of information.[336] When the sample is thin (< 100 nm), the electrons will pass the sample without (elastic scattering) and with energy loss (inelastic scattering). Elastically transmitted electrons are used by TEM and STEM to characterize the microstructure by imaging and diffraction.[336,337] Transmitted inelastically scattered electrons are used in electron energy-loss

spectroscopy (EELS) for determination of the chemical nature of the elements, the type of chemical bonds, and the atomic environment. X-ray photons are characteristic of the chemical elements in the sample and are analyzed using energy-dispersive spectrometry (EDX). An EDX can be installed in SEM, TEM and STEM.[336]

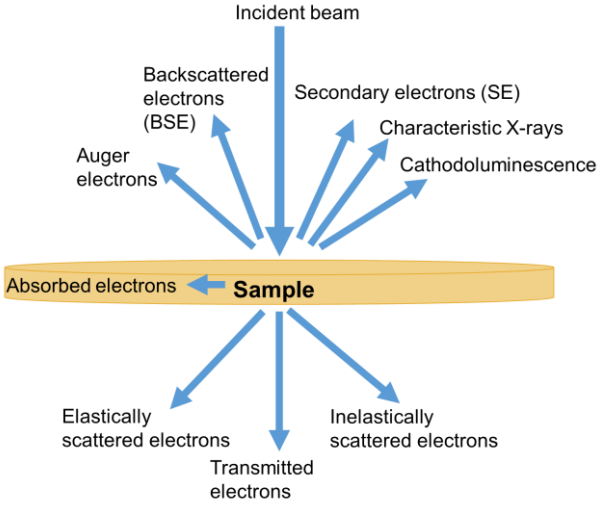

Figure 9. Various signals are generated upon interaction of an electron beam with a sample.

Information on size, morphology, topography and composition of a catalyst can be readily acquired by examination with SEM. In SEM, a narrow electron beam is scanned across the surface and the three types of emitted signals that are detected to construct images are secondary electrons (SE), backscattered electrons (BSE) and characteristic X-rays.[338] SE detectors are commonly used to show the topographic structure. Using BSE detectors, both compositional and topographical information can be retrieved. Elements separated by only 1 unit difference in atomic number give in general observable contrast. Furthermore by optimizing for a large depth-of-field, the three dimensional structure of a specimen can be perceived.[339] The resolution that can be achieved in SEM is around 1 nm at best measurement conditions.[340] SEM can be combined with and EDX to analyze the characteristic X-rays which allows elemental analysis and mapping.[338,341] In the case of Pt model catalysts, SEM can be very valuable for examination of the morphology, topography and pore entrances of the support material and to study the size, shape and distribution of Pt nanoparticles.

SEM equipped with advanced detectors and optics, namely a concentric backscattered detector (CBS) and a through-lens detector (TLD) in immersion mode and beam deceleration mode (BD), allows making images of improved resolution at very low accelerating voltages (down to 500 V).[338,339,342,343] A CBS detector can detect the backscattered electrons at high angles.[342] Immersion objective lenses, for which the sample is immersed in the objective lens field, in combination with through-lens detectors allows detection of secondary electrons for high resolution. The immersion

mode enables better focusing of the electron beam and efficient capture of the electrons.[344] The beam deceleration mode means biasing the sample stage by applying a negative voltage, which decelerates the beam when it arrives at the surface of the sample.[342] The above mentioned modes of image acquisition help in visualization of noble metal/metal oxide particles dispersed on non-conducting materials like zeolites, without the requirements of any special sample preparation such as sputtered Au, Au-Pd, Pt-Pd coatings. This is beneficial for understanding original features of these materials with high accuracy and clarity.[338,339] However when the Pt particles are very small, it is still difficult to visualize the particles because of the resolution limit. Also information on the crystallinity is difficult to obtain with SEM. TEM is then a better choice.[345]

In a conventional TEM, the sample is irradiated with a static electron beam which illuminates the entire sample at the same time. In STEM a convergent narrow electron beam scans the sample. TEM is often used for imaging and selected area diffraction (SAED). Bright-field (BF) and dark-field (DF) images can be constructed, which are formed by the direct beam and scattered beams respectively.[346] SAED is a TEM technique to generate diffraction patterns. The techniques is called 'selected area' because the microscopist can, by use of an aperture, select the area of the sample of which to obtain a diffraction pattern.[346] SAED is useful for investigation of the crystallinity of the sample and to identify crystal structures and defects.[336,346] Analogously to TEM imaging, STEM imaging can be done using two modes; bright-field and (annular) dark-field, BF and ADF, which collect transmitted and scattered electrons and only scattered electrons respectively. When the electrons scattered to the high angles are used to form the image (HAADF), a Z-contrast image, where the intensity depends on the atomic number of the atoms, is formed. This offers compositional sensitivity in the image.[336,347] The interpretation of image contrast in both SEM and TEM can be difficult. For more information of the underlying principles the reader is referred to textbooks.[339,346,347] For example, in TEM, the mechanism of formation of contrast can change with the magnification and microscopic condition.[345]

With TEM and STEM a spatial resolution on the order of 50 pm can be realized.[348,349] TEM is highly suitable for imaging crystal structures and for examining crystal size, morphology, crystal orientation, crystal defects, surface structures,… However, the images are only 2D projections and care should be taken when deriving 3D structural information from TEM.[345,350] However, for individual Pt nanoparticles either on or inside a support, distinguishing Pt particles with small diameter (< 2 nm) can be problematic. For such systems, STEM in (HA)ADF mode is superior to visualize the particles.[345] Using HAADF-STEM, even 0D individual metal atoms or clusters could

be located within the zeolite pores or on oxide supports.[351,352] Another great advantage of STEM is that it reduces the interaction between sample and beam, which results in less sample damage. This is beneficial for STEM-EDX. State-of-the-art aberration corrected EDX-STEM can accomplish elemental mapping at atomic resolution.[345]

TEM and STEM conventionally yield only two-dimensional (2D) projections of three-dimensional (3D) samples.[350]. Electron tomography can be used for 3D imaging of the sample.[353] The technique is based on recording and combining of multiple 2D (S)TEM images acquired along different tilt angles and then a mathematical algorithm is used for alignment and reconstruction of the 3D structure.[335,354] With this technique the interior of the sample can be computed. This can be useful when examining particles with core-shell structures or for location of supported particles in porous supports.[345] Elemental mapping as EDX or EELS collected with sample tilting can also be used for 3D reconstruction of materials.[335]

10. Conclusions

Literature reveals how valuable model platinum catalysts can be for progressing in the understanding of reaction mechanisms and active sites at the molecular scale. Shape-controlled synthesis of platinum metal single nanocrystals and model 2D platinum crystal planes have enabled investigation of structure sensitive catalysis and description of ensemble effects of active sites on catalytic activity and reaction selectivity. While these fields of research have been very successful, there has been less progress in the real world heterogeneous catalysis using extrudates carrying trace amounts of platinum because of the complex porosity and composition. Bridging the gap between the world of 0D and 2D investigations and the 3D real world catalysts is needed in order to be able to transfer knowledge and scientific insight from one field to the other. In this work such attempt is made by creating supported as well as non-supported 3D Pt catalysts using original synthesis approaches.

References

1 C. Chizallet and P. Raybaud, *Catal. Sci. Technol.*, 2014, **4**, 2797–2813.

2 M. Bäumer, J. Libuda, K. M. Neyman, N. Rösch, G. Rupprechter and H. J. Freund, *Phys. Chem. Chem. Phys.*, 2007, **9**, 3541–3558.

3 F. Zaera, in *Encyclopedia of Inorganic and Bioinorganic Chemistry*, John Wiley & Sons, Ltd., 2014.

4 J. Libuda, S. Schauermann, M. Laurin, T. Schalow and H. J. Freund, *Monatshefte fur Chemie*, 2005, **136**, 59–75.

5 O. Deutschmann, H. Knözinger, K. Kochloefl and T. Turek, in *Ullmann's Encyclopedia of Industrial Chemistry*, Wiley-VCH Verlag GmbH & Co. KGaA, 2009.

6 J. Hagen, in *Industrial Catalysis: A practical approach*, Wiley-VCH Verlag GmbH & Co. KGaA, 2015, pp. 211–238.

7 F. C. Meunier, *ACS Nano*, 2008, **2**, 2441–2444.

8 B. C. Gates, *Top. Catal.*, 2001, **14**, 173–180.

9 M. Boudart, *Top. Catal.*, 2000, **13**, 147–149.

10 D. W. Goodman, *Surf. Sci.*, 1994, **299/300**, 837–848.

11 F. Tao, S. Dag, L.-W. Wang, Z. Liu, D. R. Butcher, H. Bluhm, M. Salmeron and G. A. Somorjai, *Science*, 2010, **327**, 850–853.

12 S. Mizuhashi, C. E. J. Cordonier, H. Honma and O. Takai*, J. Electrochem. Soc,* 2015, **162**, 497–502.

13 International Platinum Group Metals Association, *IPA Guidance Document: Chapter 3 – Production and Uses of Platinum Group Metals*, 2017.

14 Z. Peng and H. Yang, *Nano Today*, 2009, **4**, 143–164.

15 N. Tian, Z.-Y. Zhou and S.-G. Sun, *J. Phys. Chem. C*, 2008, **112**, 19801–19817.

16 Y. Ozawa and K. Urashima, *Sci. Technol. Trends-Quarterly Rev.*, 2006, **19**, 63–76.

17 J. E. Bailie, G. J. Hutchings and S. O'Leary, in *Encyclopedia of Materials: Science and Technology*, 2001, pp. 8986–8990.

18 G. J. Hutchings and J. C. Vedrine, in *Basic Principles in Applied Catalysis*, ed. M. Baerns, Springer-Verlag Berlin Heidelberg GmbH, 2004, pp. 215–257.

19 R. J. Wijngaarden, A. Kronberg and K. R. Westerterp, in *Industrial Catalysis Optimizing Catalysts and Processes*, 1998, pp. 25–60.

20 S. Tong, I. G. D. Lana and K. T. Chuang, *Ind. Eng. Chem. Res*, 1997, **5885**, 4087–4093.

21 S. A. Axon, D. R. Coupland, J. R. Foy, J. Ridland, I. C. Wishart, Ammonia Oxidation Process, WO 2004/096703 A2, 2004, 21.

22 J. J. Bravo-suárez and R. V Chaudhari, in *Novel Materials for Catalysis and Fuels Processing*, eds. J. J. Bravo-Suárez, M. K. Kidder and V. Schwartz, 2013, pp. 1–68.

23 B. A. T. Mehrabadi, S. Eskandari, U. Khan, R. D. White and J. R. Regalbuto, in *Advances in Catalysis*, Elsevier Inc., 1st edn., 2017, vol. 61, pp. 1–35.

24 H. J. Freund, *Chem. - A Eur. J.*, 2010, **16**, 9384–9397.

25 I. Chorkendorff and J. W. Niemantsverdriet, in *Concepts of Modern Catalysis and Kinetics*, Wiley-VCH Verlag GmbH & Co. KGaA, 2003, pp. 167–214.

26 G. C. Bond, in *Metal-Catalysed Reactions of Hydrocarbons*, Springer Science_Business Media, Inc., 2005, pp. 35–91.

27 J. F. Le Page, in *Preparation of Solid Catalysts*, eds. G. Ertl, H. Knözinger and J. Weitkamp, Wiley-VCH Verlag GmbH, 1999, pp. 579–589.

28 D. Geldart, in *Mixing in the Process Industries*, eds. N. Harnby, M. F. Edwards and A. W. Nienow, Elsevier, 1992, pp. 62–78.

29 J. R. van Ommen, J. M. Valverde and R. Pfeffer, *J. Nanoparticle Res.*, 2012, **14**, 737.

30 N. Benamara, D. Assoua, L. Jaffeux, L. Vanoye, F. Simescu-Lazar, M. L. Zanota, F. Bornette, V. Meille and I. Pitault, *Processes*, 2018, **6**, 1–8.

31 F. Visscher, J. van der Schaaf, T. A. Nijhuis and J. C. Schouten, *Chem. Eng. Res. Des.*, 2013, **91**, 1923–1940.

32 K. Foger, in *Catalysis-Science and Technology*, eds. J. R. Anderson and M. Boudart, Springer-Verlag Berlin Heidelberg, 1984, pp. 227–305.

33 K. L. Fujdala, T. J. Truex, J. Cai, C. Sampara, Engine Exhaust Catalysts Containing Palladium-Gold, U.S. patent 8258070 B2, 2012.

34 P. L. J. Gunter, J. W. H. Niemantsverdriet, F. H. Ribeiro and G. A. Somorjai, *Catal. Rev.*, 1997, **39**, 77–168.

35 G. A. Somorjai, R. L. York and J. Y. Park, *Phys. Chem. Chem. Phys.*, 2007, **9**, 3500–3513.

36 S. J. Tauster, S. C. Fung, R. T. K. Baker and J. A. Horsley, *Science*, 1981, **211**, 1121–1125.

37 N. Tian, Y. H. Wen, Z. Y. Zhou and S. G. Sun, in *Complex-Shaped Metal Nanoparticles: Bottom-Up Syntheses and Applications*, eds. T. K. Sau and A. L. Rogach, Wiley-VCH, 2012, pp. 117–165.

38 U. Hanefeld and L. Lefferts, *Catalysis: An Integrated Textbook for Students*, Wiley VCH, 2017.

39 W. Liu, *China Particuology*, 2005, **3**, 383–394.

40 A. Sasahara, H. Tamura and K. Tanaka, *Catal. Letters*, 1994, **28**, 161–166.

41 G. A. Somorjai and J. Carrazza, *Ind. Eng. Chem. Fundam.*, 1986, **25**, 63–69.

42 F. Klasovsky and P. Claus, in *Metal Nanoclusters in Catalysis and Materials Science: The Issue of Size Control*, eds. B. Corain, G. Schmid and N. Toshima, Elsevier, 2008, pp. 167–181.

43 R. Huang, Y. H. Wen, Z. Z. Zhu and S. G. Sun, *J. Mater. Chem.*, 2011, **21**, 11578–11584.

44 R. M. Rioux, H. Song, P. Yang and G. A. Somorjai, in *Metal Nanoclusters in Catalysis and Materials Science: The Issue of Size Control*, 2008, pp. 149–166.

45 H. Song, R. M. Rioux, J. D. Hoefelmeyer, R. Komor, K. Niesz, M. Grass, P. Yang and G. A. Somorjai, *J. Am. Chem. Soc.*, 2006, **128**, 3027–3037.

46 L. Bai, X. Wang, Q. Chen, Y. Ye, H. Zheng, J. Guo, Y. Yin and C. Gao, *Angew. Chemie - Int. Ed.*, 2016, **55**, 15656–15661.

47 C. Chen, F. Chen, L. Zhang, S. Pan, C. Bian, X. Zheng, M. Xiangju and F.-S. Xiao, *Chem. Commun.*, 2015, **51**, 5936–5938.

48 R. Peng, S. Li, X. Sun, Q. Ren, L. Chen, M. Fu, J. Wu and D. Ye, *Appl. Catal. B, Environ.*, 2018, **220**, 462–470.

49 Z. Chen, J. Mao and R. Zhou, *Appl. Surf. Sci.*, 2019, **465**, 15–22.

50 S. Cao, F. F. Tao, Y. Tang, Y. Li and J. Yu, *Chem. Soc. Rev.*, 2016, **45**, 4747–4765.

51 J. Gan, W. Luo, W. Chen, J. Guo, Z. Xiang and B. Chen, *Eur. J. Inorg. Chem.*, 2019, 3210–3217.

52 M. Shao, A. Peles and K. Shoemaker, *Nano Lett.*, 2011, **11**, 3714–3719.

53 D. Wang, Z. Liu and W. Yang, *ACS Catal.*, 2018, **8**, 7270–7278.

54 C. M. Zalitis, A. R. Kucernak, J. Sharman and E. Wright, *J. Mater. Chem. A*, 2017, **5**, 23328–23338.

55 C. Dong, C. Lian, S. Hu, Z. Deng, J. Gong, M. Li, H. Liu, M. Xing and J. Zhang, *Nat. Commun.*, 2018, **9**, 1252.

56 T. L. Tan, L. L. Wang, J. Zhang, D. D. Johnson and K. Bai, *ACS Catal.*, 2015, **5**, 2376–2383.

57 J. R. Anderson and N. R. Avery, *J. Catal.*, 1966, **5**, 446–463.

58 W. D. Michalak, J. M. Krier, K. Komvopoulos and G. A. Somorjai, *J. Phys. Chem. C*, 2013, **117**, 1809–1817.

59 P. Gallezot and D. Richard, *Selective hydrogenation of a,β-unsaturated aldehydes*, 1998, vol. 40.

60 B. Coq, *Coord. Chem. Rev.*, 1998, **180**, 1753–1783.

61 Y. Xia, Y. Xiong, B. Lim and S. E. Skrabalak, *Angew. Chemie - Int. Ed.*, 2009, **48**, 60–103.

62 T. Sheng, W. F. Lin and S. G. Sun, *Phys. Chem. Chem. Phys.*, 2016, **18**, 15501–15504.

63 Z.-Y. Zhou, N. Tian, Z.-Z. Huang, D.-J. Chen and S.-G. Sun, *Faraday Discuss.*, 2008, **140**, 81–92.

64 G. A. Somorjai and D. W. Blakely, *Nature*, 1975, 487–488.

65 S. M. Davis, F. Zaera and G. A. Somorjai, *J. Catal.*, 1984, **85**, 206–223.

66 K. McCrea, J. S. Parker, P. Chen and G. Somorjai, *Surf. Sci.*, 2001, **494**, 238–250.

67 N. P. Lebedeva, A. Rodes, J. M. Feliu, M. T. M. Koper and R. A. Van Santen, *J. Phys. Chem. B*, 2002, **106**, 9863–9872.

68 S. G. Sun, A. C. Chen, T. S. Huang, J. B. Li and Z. W. Tian, *J. Electroanal. Chem.*, 1992, **340**, 213–226.

69 N. Hoshi, S. Kawatani, M. Kudo and Y. Hori, *J. Electroanal. Chem.*, 1999, **467**, 67–73.

70 M. Cargnello, *Chem. Mater.*, 2019, **31**, 576–596.

71 A. R. Tao, S. Habas and P. Yang, *Small*, 2008, **4**, 310–325.

72 P. Losch, W. Huang, E. D. Goodman, C. J. Wrasman, A. Holm, A. R. Riscoe, J. A. Schwalbe and M. Cargnello, *Nano Today*, 2019, **24**, 15–47.

73 Z. Yan, M. G. Taylor, A. Mascareno and G. Mpourmpakis, *Nano Lett.*, 2018, **18**, 2696–2704.

74 L. D. Marks and L. Peng, *J. Phys. Condens. Matter*, 2016, **28**, 053001.

75 B. Sun, H. Barron, G. Opletal and A. S. Barnard, *J. Phys. Chem. C*, 2018, **122**, 28085–28093.

76 A. Le Valant, C. Comminges, F. Can, K. Thomas, M. Houalla and F. Epron, *J. Phys. Chem. C*, 2016, **120**, 26374–26385.

77 C. Bréchignac, P. Houdy and M. Lahmani, Eds., *Nanomaterials and Nanochemistry*, Springer Berlin Heidelberg New York, 2006.

78 X. M. Zeng, R. Huang, G. F. Shao, Y. H. Wen and S. G. Sun, *J. Mater. Chem. A*, 2014, **2**, 11480–11489.

79 L. Xu, D. Liu, D. Chen, H. Liu and J. Yang, *Heliyon*, 2019, **5**, e01165.

80 R. Narayanan and M. A. El-Sayed, *Nano Lett.*, 2004, **4**, 1343–1348.

81 M. A. Mahmoud, C. E. Tabor, M. A. El-Sayed, Y. Ding and L. W. Zhong, *J. Am. Chem. Soc.*, 2008, **130**, 4590–4591.

82 H. Lee, S. E. Habas, S. Kweskin, D. Butcher, G. A. Somorjai and P. Yang, *Angew. Chemie - Int. Ed.*, 2006, **45**, 7824–7828.

83 G. A. Somorjai, S. Habas, P. Yang, M. Grass, K. Niesz, R. M. Rioux, J. D. Hoefelmeyer and H. Song, *Top. Catal.*, 2006, **39**, 167–174.

84 S. Mostafa, F. Behafarid, J. R. Croy, L. K. Ono, L. Li, J. C. Yang, A. I. Frenkel and B. R. Cuenya, *J. Am. Chem. Soc.*, 2010, **132**, 15714–15719.

85 I. Lee, R. Morales, M. A. Albiter and F. Zaera, *Proc. Natl. Acad. Sci.*, 2008, **105**, 15241–15246.

86 K. M. Bratlie, H. Lee, K. Komvopoulos, P. Yang and G. A. Somorjai, *Nano Lett.*, 2007, **7**, 3097–3101.

87 C. Aliaga, W. Huang, G. A. Somorjai, C.-K. Tsung, P. Yang, J. N. Kuhn and L.-I. Hung, *J. Am. Chem. Soc.*, 2009, **131**, 5816–5822.

88 B. Roldan Cuenya, *Acc. Chem. Res.*, 2012, **46**, 1682–1691.

89 C. M. Sánchez-Sánchez, J. Solla-Gullón, F. J. Vidal-Iglesias, A. Aldaz, V. Montiel and E. Herrero, *J. Am. Chem. Soc.*, 2010, **132**, 5622–5624.

90 R. Devivaraprasad, R. Ramesh, N. Naresh, T. Kar, R. K. Singh and M. Neergat, *Langmuir*, 2014, **30**, 8995–9006.

91 X. Huang, Z. Zhao, J. Fan, Y. Tan and N. Zheng, *J. Am. Chem. Soc.*, 2011, **133**, 4718–4721.

92 N. Tian, Z. Y. Zhou, S. G. Sun, Y. Ding and L. W. Zhong, *Science*, 2007, **316**, 732–735.

93 G. A. Somorjai, *Langmuir*, 1991, **7**, 3176–3182.

94 J. Dou, Z. Sun, A. A. Opalade, N. Wang, W. Fu and F. Tao, *Chem. Soc. Rev.*, 2017, **46**, 2001–2027.

95 O. A. Yakovina and A. S. Lisitsyn, *Langmuir*, 2016, **32**, 12013–12021.

96 H. Li, W. Yuan, Y. Jiang, Z. Zhang, Z. Zhang and Y. Wang, *Prog. Nat. Sci. Mater. Int.*, 2016, **26**, 308–311.

97 G. A. Somorjai and C. Aliaga, *Langmuir*, 2010, **26**, 16190–16203.

98 E. Lundgren and H. Over, *J. Phys. Condens. Matter*, 2008, **20**, 180302.

99 L. Grajciar, C. J. Heard, A. A. Bondarenko, M. V. Polynski, J. Meeprasert, E. A. Pidko and P. Nachtigall, *Chem. Soc. Rev.*, 2018, **47**, 8307–8348.

100 G. A. Somorjai, *Catal. Letters*, 1990, **7**, 169–182.

101 L.-W. Wang, Z. Liu, M. Salmeron, G. A. Somorjai, S. Dag, F. Tao and D. R. Butcher, *Nano Lett.*, 2009, **9**, 2167–2171.

102 Y. Y. Yeo, L. Vattuone and D. A. King, *J. Chem. Phys.*, 1996, **104**, 3810–3821.

103 G. L. Kellogg, *Phys. Rev. Lett.*, 1985, **55**, 2168–2171.

104 T. Zhu, S. G. Sun, R. A. Van Santen and E. J. M. Hensen, *J. Phys. Chem. C*, 2013, **117**, 11251–11257.

105 P. Thostrup, E. Christoffersen, H. T. Lorensen, K. W. Jacobsen and F. Besenbacher, *Phys. Rev. Lett.*, 2001, **87**, 2–5.

106 R. Koch, M. Sturmat and J. J. Schulz, *Surf. Sci.*, 2000, **454-456**, 543–551.

107 M. Hohage, T. Michely and G. Comsa, *Surf. Sci.*, 1995, **337**, 249–267.

108 S. R. Longwitz, J. Schnadt, E. K. Vestergaard, R. T. Vang, E. Lægsgaard, I. Stensgaard, H. Brune and F. Besenbacher, *J. Phys. Chem. B*, 2004, **108**, 14497–14502.

109 T. Yamanaka, Q. K. Xue, K. Kimura, T. Matsushima, Y. Hasegawa and T. Sakurai, *Japanese J. Appl. Physics,* 2000, **39**, 3562–3565.

110 J. Kim, M. C. Noh, W. H. Doh and J. Y. Park, *J. Am. Chem. Soc.*, 2016, **138**, 1110–1113.

111 G. A. Somorjai, K. S. Hwang and J. S. Parker, *Top. Catal.*, 2003, **26**, 87–99.

112 M. Baerns, R. Imbihl, V. A. Kondratenko, R. Kraehnert, W. K. Offermans, R. A. Van Santen and A. Scheibe, *J. Catal.*, 2005, **232**, 226–238.

113 R. Imbihl, A. Scheibe, Y. F. Zeng, S. Günther, R. Kraehnert, V. A. Kondratenko, M. Baerns, W. K. Offermans, A. P. J. Jansen and R. A. Van Santen, *Phys. Chem. Chem. Phys.*, 2007, **9**, 3522–3540.

114 L. Gai, Y. K. Shin, M. Raju, A. C. T. Van Duin and S. Raman, *J. Phys. Chem. C*, 2016, **120**, 9780–9793.

115 M. Rafti and J. L. Vicente, *Phys. Rev. E*, 2007, **75**, 061121.

116 N. Seriani, W. Pompe and L. C. Ciacchi, *J. Phys. Chem. B*, 2006, **110**, 14860–14869.

117 R. B. Shumbera, H. H. Kan and J. F. Weaver, *Surf. Sci.*, 2007, **601**, 235–246.

118 W. X. Li, *J. Phys. Condens. Matter*, 2008, **20**, 184022.

119 M. A. Van Spronsen, J. W. M. Frenken and I. M. N. Groot, *Nat. Commun.*, 2017, **8**, 429.

120 C. R. Parkinson, M. Walker and C. F. McConville, *Surf. Sci.*, 2003, **545**, 19–33.

121 A. Rodes and J. Clavilier, *J. Electroanal. Chem.*, 1993, **344**, 269–288.

122 I. T. McCrum, M. A. Hickner and M. J. Janik, *Langmuir*, 2017, **33**, 7043–7052.

123 D. M. Kolb, *Prog. Surf. Sci.*, 1996, **51**, 109–173.

124 D. V. Tripkovic, D. Strmcnik, D. van der Vliet, V. Stamenkovic and N. M. Markovic, *Faraday Discuss.*, 2008, **140**, 25–40.

125 R. Narayanan and M. A. El-Sayed, *J. Phys. Chem. B*, 2004, **108**, 5726–5733.

126 M. Cabié, S. Giorgio, C. R. Henry, M. R. Axet, K. Philippot and B. Chaudret, *J. Phys. Chem. C*, 2010, **114**, 2160–2163.

127 R. G. Nuzzo, J. Ciston, J. H. Kang, J. Li, S. I. Sanchez, D. D. Johnson, Q. Wang, L. Li, J. C. Yang, Z. Zhang, E. A. Stach, L.-L. Wang and A. I. Frenkel, *J. Am. Chem. Soc.*, 2013, **135**, 13062–13072.

128 T. Wang, C. Lee and L. D. Schmidt, *Surf. Sci.*, 1985, **163**, 181–197.

129 A. S. Ramachandran, S. L. Anderson and A. K. Datye, *Ultramicroscopy*, 1993, **51**, 282–297.

130 G. Rupprechter and H. J. Freund, *Top. Catal.*, 2001, **14**, 3–14.

131 P. J. F. Harris, *Nature*, 1986, **323**, 792–794.

132 M. J. Kale and P. Christopher, *ACS Catal.*, 2016, **6**, 5599–5609.

133 S. B. Roobol, W. G. Onderwaater, M. A. Van Spronsen, F. Carla, O. Balmes, V. Navarro, S. Vendelbo, P. J. Kooyman, C. F. Elkjær, S. Helveg, R. Felici, J. W. M. Frenken and I. M. N. Groot, *Phys. Chem. Chem. Phys.*, 2017, **19**, 8485–8495.

134 H. Wang, Y. Wang, Z. Zhu, A. Sapi, K. An, G. Kennedy, W. D. Michalak and G. A. Somorjai, *Nano Lett.*, 2013, **13**, 2976–2979.

135 L. Li, P. N. Plessow, M. Rieger, S. Sauer, R. S. Sánchez-Carrera, A. Schaefer and F. Abild-Pedersen, *J. Phys. Chem. C*, 2017, **121**, 4261–4269.

136 P. T. Z. Adibi, F. Mazzotta, T. J. Antosiewicz, M. Skoglundh, H. Grönbeck and C. Langhammer, *ACS Catal.*, 2015, **5**, 426–432.

137 S. B. Simonsen, I. Chorkendorff, S. Dahl, M. Skoglundh, J. Sehested and S. Helveg, *J. Catal.*, 2011, **281**, 147–155.

138 S. B. Simonsen, I. Chorkendorff, S. Dahl, M. Skoglundh, J. Sehested and S. Helveg, *J. Am. Chem. Soc.*, 2010, **132**, 7968–7975.

139 F. Behafarid, S. Pandey, R. E. Diaz, E. A. Stach and B. R. Cuenya, *Phys. Chem. Chem. Phys.*, 2014, **16**, 18176–18184.

140 S. Zhang, M. Cargnello, W. Cai, C. B. Murray, G. W. Graham and X. Pan, *J. Catal.*, 2016, **337**, 240–247.

141 S. Ban, K. Malek and C. Huang, *J. Power Sources*, 2013, **221**, 21–27.

142 E. Solano, J. Dendooven, R. K. Ramachandran, K. Van de Kerckhove, T. Dobbelaere, D. Hermida-Merino and C. Detavernier, *Nanoscale*, 2017, **9**, 13159–13170.

143 C. Mager-Maury, G. Bonnard, C. Chizallet, P. Sautet and P. Raybaud, *ChemCatChem*, 2011, **3**, 200–207.

144 A. Gorczyca, V. Moizan, C. Chizallet, O. Proux, W. Del Net, E. Lahera, H. Jean-Louis, P. Raybaud and Y. Joly, *Angew. Chemie - Int. Ed.*, 2014, **53**, 12426–12429.

145 W. Zhao, C. Chizallet, P. Sautet and P. Raybaud, *J. Catal.*, 2019, **370**, 118–129.

146 M. W. Small, S. I. Sanchez, N. S. Marinkovic, A. I. Frenkel and R. G. Nuzzo, *ACS Nano*, 2012, **6**, 5583–5595.

147 C. -S Chang, S. -J Jong and S. Cheng, *J. Chinese Chem. Soc.*, 1995, **42**, 31–36.

148 S. J. Tauster, S. C. Fung and R. L. Garten, *J. Am. Chem. Soc.*, 1978, **100**, 170–175.

149 S. J. Tauster, *Acc. Chem. Res.*, 1987, **20**, 389–394.

150 C. M. Engelhardt, R. M. Kennedy, J. A. Enterkin, K. R. Poeppelmeier, D. E. Ellis, C. L. Marshall and P. C. Stair, *ChemCatChem*, 2018, **10**, 632–641.

151 M. Bowker, P. Stone, P. Morrall, R. Smith, R. Bennett, N. Perkins, R. Kvon, C. Pang, E. Fourre and M. Hall, *J. Catal.*, 2005, **234**, 172–181.

152 G. L. Haller and D. E. Resasco, *Adv. Catal.*, 1989, **36**, 173–235.

153 R. T. K. Baker, E. B. Prestridge and R. L. Garten, *J. Catal.*, 1979, **59**, 293–302.

154 T. Uchijima, *Catal. Today*, 1996, **28**, 105–117.

155 D. A. G. Aranda, A. L. D. Ramos, F. B. Passos and M. Schmal, *Catal. Today*, 1996, **28**, 119–125.

156 E. I. Ko, R. Bafrali, N. T. Nuhfer and N. J. Wagner, *J. Catal.*, 1985, **95**, 260–270.

157 S. I. Ito, C. Chibana, K. Nagashima, S. Kameoka, K. Tomishige and K. Kunimori, *Appl. Catal. A Gen.*, 2002, **236**, 113–120.

158 R. L. Augustine, *Heterogeneous Catalysis for the Synthetic Chemist*, Marcel Dekker, Inc., 1996.

159 T. Beutel, O. S. Alekseev, Y. A. Ryndin, V. A. Likholobov and H. Knözinger, *J. Catal.*, 1997, **169**, 132–142.

160 C.-J. Pan, M.-C. Tsai, W.-N. Su, J. Rick, N. G. Akalework, A. K. Agegnehu, S.-Y. Cheng and B.-J. Hwang, *J. Taiwan Inst. Chem. Eng.*, 2017, **74**, 154–186.

161 C. T. Campbell, *Nat. Chem.*, 2012, **4**, 597–598.

162 A. Bruix, J. A. Rodriguez, P. J. Ramírez, S. D. Senanayake, J. Evans, J. B. Park,

D. Stacchiola, P. Liu, J. Hrbek and F. Illas, *J. Am. Chem. Soc.*, 2012, **134**, 8968–8974.

163 P. Panagiotopoulou and D. I. Kondarides, *J. Catal.*, 2004, **225**, 327–336.

164 C. M. Kalamaras, P. Panagiotopoulou, D. I. Kondarides and A. M. Efstathiou, *J. Catal.*, 2009, **264**, 117–129.

165 J. B. F. Anderson, R. Burch and J. A. Cairns, *J. Catal.*, 1987, **107**, 351–363.

166 M. A. Vannice and C. C. Twu, *J. Catal.*, 1983, **82**, 213–222.

167 M. A. Vannice and C. Sudhakar, *J. Phys. Chem.*, 1984, **88**, 2429–2432.

168 B. Sen and M. A. Vannice, *J. Catal.*, 1988, **113**, 52–71.

169 M. A. Vannice and B. Sen, *J. Catal.*, 1989, **115**, 65–78.

170 M. Englisch, A. Jentys and J. A. Lercher, *J. Catal.*, 1997, **166**, 25–35.

171 A. Dandekar and M. A. Vannice, *J. Catal.*, 1999, **183**, 344–354.

172 M. Abid, V. Paul-boncour and R. Touroude, *Appl. Catal. A Gen.*, 2006, **297**, 48–59.

173 A. B. Da Silva, E. Jordão, M. J. Mendes and P. Fouilloux, *Appl. Catal. A Gen.*, 1997, **148**, 253–264.

174 M. A. Vannice and D. Poondi, *J. Catal.*, 1997, **169**, 166–175.

175 S. D. Lin, D. K. Sanders and M. Albert Vannice, *Appl. Catal. A, Gen.*, 1994, **113**, 59–73.

176 H. Yoshitake and Y. Iwasawa, *J. Catal.*, 1990, **125**, 227–242.

177 A. Corma, P. Serna, P. Concepción and J. J. Calvino, *ACS Catal.*, 2015, **5**, 7114–7121.

178 H. Yoshitake and Y. Iwasawa, *J. Chem. Soc. Faraday. Trans*, 1992, **88**, 503–510.

179 R. M. Kennedy, L. A. Crosby, K. Ding, C. P. Canlas, A. Gulec, L. D. Marks, J. W. Elam, C. L. Marshall, K. R. Poeppelmeier and P. C. Stair, *Catal. Letters*, 2018, **148**, 2223–2232.

180 M. A. Vannice, *Top. Catal.*, 1997, **4**, 241–248.

181 Z. Rui, L. Chen, H. Chen and H. Ji, *Ind. Eng. Chem. Res.*, 2014, **53**, 15879–15888.

182 G. Kennedy, L. R. Baker and G. A. Somorjai, *Angew. Chemie - Int. Ed.*, 2014, **53**, 3405–3408.

183 L. R. Baker, G. Kennedy, M. Van Spronsen, A. Hervier, X. Cai, S. Chen, L. W. Wang and G. A. Somorjai, *J. Am. Chem. Soc.*, 2012, **134**, 14208–14216.

184 J. K. A. Clarke, R. J. Dempsey, T. Baird and J. J. Rooney, *J. Catal.*, 1990, **126**, 370–380.

185 N. A. Gaidai, R. V. Kazantsev, N. V. Nekrasov, Y. M. Shulga, I. N. Ivleva and S. L. Kiperman, *React. Kinet. Catal. Lett.*, 2002, **75**, 55–61.

186 K. Kon, W. Onodera, S. Takakusagi and K. Shimizu, *Catal. Sci. Technol.*, 2014, **4**, 3705–3712.

187 J. Jun, Y. Suh, D. Jin and Y. Lee, *Catal. Today*, 2018, **302**, 108–114.

188 D. L. Hoang and H. Lieske, *Catal. Letters*, 1994, **27**, 33–42.

189 B. Zhang and Y. Qin, *ACS Catal.*, 2018, **8**, 10064–10081.

190 J. Lu, B. Fu, M. C. Kung, G. Xiao, J. W. Elam, H. H. Kung and P. C. Stair, *Science*, 2012, **335**, 1205–1209.

191 N. Cheng, M. Norouzi Banis, J. Liu, A. Riese, S. Mu, R. Li, T. K. Sham and X. Sun, *Energy Environ. Sci.*, 2015, **8**, 1450–1455.

192 Q. Hu, K. Cao, Y. Lang, R. Chen, S. Chu, L. Jia, J. Yue and B. Shan, *Catal. Sci. Technol.*, 2019, **9**, 2664–2672.

193 X. Y. Shi, W. Zhang, C. Zhang, W. T. Zheng, H. Chen and J. G. Qi, *J. Microsc.*, 2016, **262**, 203–215.

194 S. Shaikhutdinov, *Catal. Letters*, 2018, **148**, 2627–2635.

195 S. Bernal, J. J. Calvino, M. A. Cauqui, J. M. Gatica, C. López Cartes, J. A. Pérez Omil and J. M. Pintado, *Catal. Today*, 2003, **77**, 385–406.

196 B. Zhang and D. S. Su, *ChemCatChem*, 2015, **7**, 3639–3645.

197 H. Li, X. Weng, Z. Tang, H. Zhang, D. Ding, M. Chen and H. Wan, *ACS Catal.*, 2018, **8**, 10156–10163.

198 S. Ntais, R. J. Isaifan and E. A. Baranova, *Mater. Chem. Phys.*, 2014, **148**, 673–679.

199 Y. Wang, X. Zhang, Z. Fu, Z. Lu and Z. Yang, *J. Phys. Condens. Matter*, 2019, **31**, 305201.

200 L. F. Liotta, A. Longo, A. Macaluso, A. Martorana, G. Pantaleo, A. M. Venezia and G. Deganello, *Appl. Catal. B Environ.*, 2004, **48**, 133–149.

201 J. Lee, I. Song and D. H. Kim, *ChemCatChem*, 2018, **10**, 1258–1262.

202 S. I. Abasov, V. Y. Borovkov and V. B. Kazansky, *Catal. Letters*, 1992, **15**, 269–274.

203 L. Deng, H. Miura, T. Shishido, S. Hosokawa, K. Teramura and T. Tanaka, *Chem. Commun.*, 2017, **53**, 6937–6940.

204 H. Tang, Y. Su, Y. Guo, L. Zhang, T. Li, K. Zang, F. Liu, L. Li, J. Luo, B. Qiao and J. Wang, *Chem. Sci.*, 2018, **9**, 6679–6684.

205 Y. N. Sun, Z. H. Qin, M. Lewandowski, S. Kaya, S. Shaikhutdinov and H. J. Freund, *Catal. Letters*, 2008, **126**, 31–35.

206 M. Ahmadi, H. Mistry and B. R. Cuenya, *J. Phys. Chem. Lett.*, 2016, **7**, 3519–3533.

207 A. Y. Stakheev and L. M. Kustov, *Appl. Catal. A Gen.*, 1999, **188**, 3–35.

208 B. Coq, in *Metal-Ligand Interactions in Chemistry, Physics and Biology*, eds. N. Russo and D. R. Salahub, Springer Science+Business Dordrecht, 2000, pp. 49–71.

209 K. Zhang, S. Shaikhutdinov and H.-J. Freund, *ChemCatChem*, 2015, **7**, 3725–3730.

210 K. Asakura, W. J. Chun, M. Shirai, K. Tomishige and Y. Iwasawa, *J. Phys. Chem. B*, 1997, **101**, 5549–5556.

211 B. Roldan Cuenya, J. R. Croy, S. Mostafa, F. Behafarid, L. Li, Z. Zhang, J. C. Yang, Q. Wang and A. I. Frenkel, *J. Am. Chem. Soc.*, 2010, **132**, 8747–8756.

212 M. Vaarkamp, J. T. Miller, F. S. Modica and D. C. Koningsberger, *J. Catal.*, 1996, **163**, 294–305.

213 C. H. Hu, C. Chizallet, C. Mager-Maury, M. Corral-Valero, P. Sautet, H. Toulhoat and P. Raybaud, *J. Catal.*, 2010, **274**, 99–110.

214 J. A. Enterkin, K. R. Poeppelmeier and L. D. Marks, *Nano Lett.*, 2011, **11**, 993–997.

215 S. Deng, C. Qiu, Z. Yao, X. Sun, Z. Wei, G. Zhuang, X. Zhong and J. guo Wang, *Wiley Interdiscip. Rev. Comput. Mol. Sci.*, 2019, **9**, 1–17.

216 K. Fujiwara, K. Okuyama and S. E. Pratsinis, *Environ. Sci. Nano*, 2017, **4**, 2076–2092.

217 J. Matos, L. K. Ono, F. Behafarid, J. R. Croy, S. Mostafa, A. T. Delariva, A. K. Datye, A. I. Frenkel and B. Roldan Cuenya, *Phys. Chem. Chem. Phys.*, 2012, **14**, 11457–11467.

218 N. T. Cuong, A. Fujiwara, T. Mitani and D. H. Chi, *Comput. Mater. Sci.*, 2008, **44**, 163–166.

219 D. Kubička, N. Kumar, T. Venäläinen, H. Karhu, I. Kubičková, H. Österholm and D. Y. Murzin, *J. Phys. Chem. B*, 2006, **110**, 4937–4946.

220 B. L. Mojet, M. J. Kappers, J. T. Miller and D. C. Koningsberger, *Stud. Surf. Sci. Catal.*, 1996, **101 B**, 1165–1174.

221 G. Larsen and G. L. Haller, *Catal. Letters*, 1989, **3**, 103–110.

222 D. C. Koningsberger, J. De Graaf, B. L. Mojet, D. E. Ramaker and J. T. Miller, *Appl. Catal. A Gen.*, 2000, **191**, 205–220.

223 S. Ramírez, P. Schacht, J. Ancheyta, I. Mexicano, E. Central, L. Cárdenas and D. F. México, *J. Mex. Chem. Soc.,* 2005, **49**, 271–278.

224 F. Tao and P. A. Crozier, *Chem. Rev.*, 2016, **116**, 3487–3539.

225 H. J. Freund, H. Kuhlenbeck, J. Libuda, G. Rupprechter, M. Baumer and H. Hamann, *Top. Catal.*, 2001, **15**, 201–209.

226 G. Rupprechter and C. Weilach, *J. Phys. Condens. Matter*, 2008, **20**, 184019.

227 E. Amayuelas, A. Fidalgo-Marijuán, B. Bazán, M. K. Urtiaga, G. Barandika and M. I. Arriortua, *CrystEngComm*, 2017, **19**, 7244–7252.

228 L. Mino, G. Agostini, E. Borfecchia, D. Gianolio, A. Piovano, E. Gallo and C. Lamberti, *J. Phys. D. Appl. Phys.*, 2013, **46**, 423001.

229 C. Kerpal, D. J. Harding, A. C. Hermes, G. Meijer, S. R. Mackenzie and A. Fielicke, *J. Phys. Chem. A*, 2013, **117**, 1233–1239.

230 D. J. Trevor, D. M. Cox and A. Kaldor, *J. Am. Chem. Soc.*, 1990, **112**, 3742–3749.

231 U. Achatz, C. Berg, S. Joos, B. S. Fox, M. K. Beyer, G. Niedner-Schatteburg and V. E. Bondybey, *Chem. Phys. Lett.*, 2000, **320**, 53–58.

232 T. Hanmura, M. Ichihashi and T. Kondow, *J. Phys. Chem. A*, 2002, **106**, 11465–11469.

233 K. Koszinowski, D. Schröder and H. Schwarz, *J. Phys. Chem. A*, 2003, **107**, 4999–5006.

234 C. Adlhart and E. Uggerud, *Chem. Commun.*, 2006, 2581–2582.

235 C. Adlhart and E. Uggerud, *Chem. - A Eur. J.*, 2007, **13**, 6883–6890.

236 G. A. Somorjai and K. R. McCrea, *Adv. Catal.,* 2004, **45**, 385–438.

237 G. A. Somorjai and M. Yang, *Top. Catal.*, 2003, **24**, 61–72.

238 M. Bäumer and H.-J. Freund, *Prog. Surf. Sci.*, 1999, **61**, 127–198.

239 D. W. Goodman, *Chem. Rev.*, 1995, **95**, 523–536.

240 T. P. St.Clair and D. W. Goodman, *Top. Catal.*, 2000, **13**, 5–19.

241 J. Dendooven, R. K. Ramachandran, E. Solano, M. Kurttepeli, L. Geerts, G. Heremans, J. Rongé, M. M. Minjauw, T. Dobbelaere, K. Devloo-Casier, J. A. Martens, A. Vantomme, S. Bals, G. Portale, A. Coati and C. Detavernier, *Nat. Commun.*, 2017, **8**, 1074.

242 S. Johansson, K. Wong, V. P. Zhdanov and B. Kasemo*, J. Vac. Sci. Technol A,* 1999, **17**, 297–302.

243 D. N. Belton, Y. M. Sun and J. M. White, *J. Phys. Chem.*, 1984, **88**, 1690–1695.

244 G. W. Sievers, A. W. Jensen, V. Brüser, M. Arenz and M. Escudero-Escribano, *Surfaces*, 2019, **2**, 336–348.

245 K. Hayek, *J. Mol. Catal.*, 1989, **51**, 347–359.

246 V. Schwaab, C. Papp, H.-P. Steinrück, F. Späth, F. Düll, P. Bachmann, J. Steinhauer and U. Bauer, *Chem. Phys. Lett.*, 2018, **708**, 165–169.

247 M. Y. Smirnov, A. V. Kalinkin, E. I. Vovk, P. A. Simonov, E. Y. Gerasimov, A. M. Sorokin and V. I. Bukhtiyarov, *Appl. Surf. Sci.*, 2018, **428**, 972–976.

248 A. M. Motin, T. Haunold, A. V. Bukhtiyarov, A. Bera, C. Rameshan and G. Rupprechter, *Appl. Surf. Sci.*, 2018, **440**, 680–687.

249 S. Vajda and M. G. White, *ACS Catal.*, 2015, **5**, 7152–7176.

250 N. Vandamme, E. Janssens, F. Vanhoutte, P. Lievens and C. Van Haesendonck, *J. Phys. Condens. Matter*, 2003, **15**, S2983–S2999.

251 U. Heiz, A. Sanchez, S. Abbet and W. D. Schneider, *J. Am. Chem. Soc.*, 1999, **121**, 3214–3217.

252 A. S. Crampton, M. D. Rötzer, C. J. Ridge, B. Yoon, F. F. Schweinberger, U. Landman and U. Heiz, *Surf. Sci.*, 2016, **652**, 7–19.

253 S. Bonanni, K. Aït-Mansour, W. Harbich and H. Brune, *J. Am. Chem. Soc.*, 2012, **134**, 3445–3450.

254 Y. Watanabe, X. Wu, H. Hirata and N. Isomura, *Catal. Sci. Technol.*, 2011, **1**, 1490–1495.

255 C. Detavernier, J. Dendooven, S. Pulinthanathu Sree, K. F. Ludwig and J. A. Martens, *Chem. Soc. Rev.*, 2011, **40**, 5242–5253.

256 H. C. M. Knoops, S. E. Potts, A. A. Bol and W. M. M. Kessels, in *Handbook of Crystal Growth: Thin Films and Epitaxy: Second Edition*, ed. T. Kuech, Elsevier, 2015, pp. 1101–1134.

257 M. Ahonen, M. Pessa, T. Suntola and O. L. Ab, *Thin Solid Films*, 1980, **65**, 301–307.

258 S. M. George, *Chem. Rev.*, 2010, 111–131.

259 R. L. Puurunen, *J. Appl. Phys.*, 2005, **97**, 121301.

260 B. J. O'Neill, D. H. K. Jackson, J. Lee, C. Canlas, P. C. Stair, C. L. Marshall, J. W. Elam, T. F. Kuech, J. A. Dumesic and G. W. Huber, *ACS Catal.*, 2015, **5**, 1804–1825.

261 T. Suntola, J. Antson, Method for producing compound thin films, 4058430, 1977.

262 W. Setthapun, H. Feng, P. C. Stair, J. T. Miller, C. L. Marshall, W. D. Williams, F. H. Ribeiro, S. M. Kim, E. A. Stach, J. W. Elam, F. A. Rabuffetti and K. R. Poeppelmeier, *J. Phys. Chem. C*, 2010, **114**, 9758–9771.

263 B. Sels and M. Van de Voorde, Eds., *Nanotechnology in Catalysis: Application in the Chemical Industry, Energy Development and Environment Protection*, Wiley VCH, 2017.

264 T. Aaltonen, M. Ritala, T. Sajavaara, J. Keinonen and M. Leskelä, *Chem. Mater.*, 2003, **15**, 1924–1928.

265 D. Longrie, K. Devloo-Casier, D. Deduytsche, S. Van den Berghe, K. Driesen and C. Detavernier, *ECS J. Solid State Sci. Technol.*, 2012, **1**, Q123–Q129.

266 H. C. M. Knoops, A. J. M. Mackus, M. E. Donders, M. C. M. van de Sanden, P. H. L. Notten and W. M. M. Kessels, *Electrochem. Solid-State Lett.*, 2009, **12**, G34.

267 J. Dendooven, R. K. Ramachandran, K. Devloo-Casier, G. Rampelberg, M. Filez, H. Poelman, G. B. Marin, E. Fonda and C. Detavernier, *J. Phys. Chem. C*, 2013, **117**, 20557–20561.

268 L. Baker, A. S. Cavanagh, J. Yin, S. M. George, A. Kongkanand and F. T. Wagner, *Appl. Phys. Lett.*, 2012, **101**, 1–5.

269 C. Wang, Y. Lin, L. Marks, L. Hu, K. Poeppelmeier and P. Stair, *J. Phys. D. Appl. Phys.*, 2017, **50**, 415301.

270 F. Grillo, H. Van Bui, D. La Zara, A. A. I. Aarnink, A. Y. Kovalgin, P. Kooyman, M. T. Kreutzer and J. R. Van Ommen, *Small*, 2018, **14**, 1800765.

271 F. Grillo, H. Van Bui, J. A. Moulijn, M. T. Kreutzer and R. J. van Ommen, *J. Phys. Chem. Lett.*, 2017, **8**, 975–983.

272 S. Xu, Y. Kim, J. Park, D. Higgins, S. J. Shen, P. Schindler, D. Thian, J. Provine, J. Torgersen, T. Graf, T. D. Schladt, M. Orazov, B. H. Liu, T. F. Jaramillo and F. B. Prinz, *Nat. Catal.*, 2018, **1**, 624–630.

273 Z. X. Chen, G. C. Smith, C. A. J. Putman and E. J. M. Ter Voert, *Catal. Letters*, 1998, **50**, 49–57.

274 H. Song, F. Kim, S. Connor, G. A. Somorjai and P. Yang, *J. Phys. Chem. B*, 2005, **109**, 188–193.

275 P. W. Jacobs, F. H. Ribeiro, G. A. Somorjai and S. J. Wind, *Catal. Letters*, 1996, **37**, 131–136.

276 J. Y. Park, Ed., *Current trends of surface science and catalysis*, Springer New York Heidelberg Dordrecht London, 2013, vol. 9781461487.

277 V. Komanicky, H. Lddir, K. C. Chang, A. Menzel, G. Karapetrov, D. Hennessy, P. Zapol and H. You, *J. Am. Chem. Soc.*, 2009, **131**, 5732–5733.

278 A. M. Contreras, J. Grunes, X. M. Yan, A. Liddle and G. A. Somorjai, *Catal. Letters*, 2005, **100**, 115–124.

279 A. M. Contreras, J. Grunes, X.-M. Yan, A. Liddle and G. A. Somorjai, *Top. Catal.*, 2006, **39**, 123–129.

280 L. Huang, P. C. Chen, M. Liu, X. Fu, P. Gordiichuk, Y. Yu, C. Wolverton, Y. Kang and C. A. Mirkin, *Proc. Natl. Acad. Sci. U. S. A.*, 2018, **115**, 3764–3769.

281 V. Komanicky, A. Barbour, M. Lackova, M. Zorko, C. Zhu, M. Pierce and H. You, *Nanoscale Res. Lett.*, 2014, **9**, 1–7.

282 H. Le-The, E. Berenschot, R. M. Tiggelaar, N. R. Tas, A. van den Berg and J. C. T. Eijkel, *Microsystems Nanoeng.*, 2018, **4**, 1–10.

283 S. Chaturvedi and P. N. Dave, *Microsc. Adv. Sci. Res. Educ.*, 2014, **1**, 813–818.

284 K. Niesz, M. M. Koebel and G. A. Somorjai, *Inorganica Chim. Acta*, 2006, **359**, 2683–2689.

285 H. Van Bui, F. Grillo, S. S. Kulkarni, R. Bevaart, N. Van Thang, B. Van Der Linden, J. A. Moulijn, M. Makkee, M. T. Kreutzer and J. R. Van Ommen, *Nanoscale*, 2017, **9**, 10802–10810.

286 W. Yu, M. D. Porosoff and J. G. Chen, *Chem. Rev.*, 2012, **112**, 5780–5817.

287 A. K. Datye, *Top. Catal.*, 2000, **13**, 131–138.

288 A. K. Datye and N. J. Long, *Ultramicroscopy*, 1988, **25**, 203–208.

289 A. David Logan, E. J. Braunschweig, A. K. Datye and D. J. Smith, *Ultramicroscopy*, 1989, **31**, 132–137.

290 S. Chenna, R. Banerjee and P. A. Crozier, *ChemCatChem*, 2011, **3**, 1051–1059.

291 C. K. Ling, N. A. M. Zabidi and C. Mohan, *J. Appl. Sci.*, 2011, **11**, 1436–1440.

292 G. Fuchs, D. Neiman and H. Poppa, *Langmuir*, 2005, **7**, 2853–2859.

293 B. A. T. Mehrabadi, S. Eskandari, U. Khan, R. D. White and J. R. Regalbuto, *A Review of Preparation Methods for Supported Metal Catalysts*, Elsevier Inc., 1st edn., 2017, vol. 61.

294 H. Hofmeister, P. Miclea, M. Steen and W. Mo, *Top. Catal.*, 2007, **46**, 11–21.

295 M. Dad, R. J. Lancee, M. Janse van Vuuren, J. van de Loosdrecht, J. W. H. Niemantsverdriet and H. O. A. Fredriksson, *Appl. Catal. A Gen.*, 2017, **537**, 83–92.

296 X. Guo, K. Gao, A. Gutsche, M. Seipenbusch and H. Nirschl, *Powder Technol.*, 2015, **272**, 23–33.

297 Y. Zhang, Z. Xue, J. Wang, X. Zhao, Y. Deng, W. Zhao and T. Mu, *RSC Adv.*, 2016, **6**, 51229–51237.

298 T. Kondo, T. Morimura, T. Tsujimoto, T. Aikawa and M. Yuasa, *Sci. Rep.*, 2017, **7**, 8651.

299 F. Yin, D. Wang, Z. Zhang, C. Zhang and Y. Zhang, *Mater. Lett.*, 2017, **207**, 225–229.

300 Y. Mei, G. Sharma, Y. Lu, M. Ballauff, M. Drechsler, T. Irrgang and R. Kempe, *Langmuir*, 2005, **21**, 12229–12234.

301 K. J. Lin, L. J. Chen, M. R. Prasad and C. Y. Cheng, *Adv. Mater.*, 2004, **16**, 1845–1849.

302 A. Sápi, A. Kéri, I. Kálomista, D. G. Dobó, A. Szamosvölgyi, K. L. Juhász, A. Kukovecz, Z. Kónya and G. Galbács, *J. Anal. At. Spectrom.*, 2017, **32**, 996–1003.

303 M. Zubko and A. Burian, *J. Appl. Crystallogr.*, 2018, **51**, 411–419.

304 R. M. Rioux, H. Song, J. D. Hoefelmeyer, P. Yang and G. A. Somorjai, *J. Phys. Chem. B*, 2005, **109**, 2192–2202.

305 J. A. Enterkin, R. M. Kennedy, J. Lu, J. W. Elam, R. E. Cook, L. D. Marks, P. C. Stair, C. L. Marshall and K. R. Poeppelmeier, *Top. Catal.*, 2013, **56**, 1829–1834.

306 R. S. Juang, C. Te Hsieh, J. Q. Hsiao, H. T. Hsiao, D. Y. Tzou and M. M. Huq, *J. Power Sources*, 2015, **275**, 845–851.

307 S. Vajda, M. J. Pellin, J. P. Greeley, C. L. Marshall, L. A. Curtiss, G. A. Ballentine, J. W. Elam, S. Catillon-Mucherie, P. C. Redfern, F. Mehmood and P. Zapol, *Nat. Mater.*, 2009, **8**, 213–216.

308 C. Dossi, R. Psaro, L. Sordelli, M. Bellatreccia and R. Zanoni, *J. Catal.*, 1996, **159**, 435–440.

309 Z. Paål, R. Schlögl and G. Ertl, *J. Chem. Soc. Faraday Trans.*, 1992, **88**, 1179–1189.

310 Z. Paál, M. Muhler and R. Schlögl, *Surf. Sci. Spectra*, 2002, **4**, 119–124.

311 J. Find, Z. Paál, R. Schlögl and U. Wild, *Catal. Letters*, 2000, **65**, 19–23.

312 Z. Paál, A. Wootsch, D. Teschner, K. Lázár, I. E. Sajó, N. Györffy, G. Weinberg, A. Knop-Gericke and R. Schlögl, *Appl. Catal. A Gen.*, 2011, **391**, 377–385.

313 V. Habibpour, M. Y. Song, Z. W. Wang, J. Cookson, C. M. Brown, P. T. Bishop and R. E. Palmer, *J. Phys. Chem. C*, 2012, **116**, 26295–26299.

314 M. Jørgensen and H. Gro, *ACS Catal.*, 2017, **7**, 5054–5061.

315 D. Mei, J. Du and M. Neurock, *Ind. Eng. Chem. Res.*, 2010, **49**, 10364–10373.

316 V. P. Zhdanov and B. Kasemo, *Phys. Rev. B - Condens. Matter Mater. Phys.*, 1997, **55**, 4105–4108.

317 A. S. McLeod, *Catal. Today*, 1999, **53**, 289–302.

318 R. Miyazaki, N. Nakatani, S. V. Levchenko, T. Yokoya, K. Nakajima, K. Hara, A. Fukuoka and J. Y. Hasegawa, *J. Phys. Chem. C*, 2019, **123**, 12706–12715.

319 J. Aarons, L. Jones, A. Varambhia, K. E. MacArthur, D. Ozkaya, M. Sarwar, C. K. Skylaris and P. D. Nellist, *Nano Lett.*, 2017, **17**, 4003–4012.

320 R. Quiceno, J. Pérez-Ramírez, J. Warnatz and O. Deutschmann, *Appl. Catal. A Gen.*, 2006, **303**, 166–176.

321 J. T. Gleaves, G. Yablonsky, X. Zheng, R. Fushimi and P. L. Mills, *J. Mol. Catal. A Chem.*, 2010, **315**, 108–134.

322 Y. Suchorski and W. Drachsel, *Top. Catal.*, 2007, **46**, 201–215.

323 K. Cheng, M. Virginie, V. V. Ordomsky, C. Cordier, P. A. Chernavskii, M. I. Ivantsov, S. Paul, Y. Wang and A. Y. Khodakov, *J. Catal.*, 2015, **328**, 139–150.

324 S. T. Sie, *Chem. Eng. J. Biochem. Eng. J.*, 1993, **53**, 1–11.

325 National Research Council, *Catalysis Looks to the Future*, Washington, DC: The National Academies Press, 1992.

326 A. Bruix, J. T. Margraf, M. Andersen and K. Reuter, *Nat. Catal.*, 2019, **2**, 659–670.

327 J. M. Winterbottom and M. B. King, *Reactor Design for Chemical Engineers*, Routledge, Taylor & Francis group, 1999.

328 F. J. Navarro-Brull and R. Gómez, *Ind. Eng. Chem. Res.*, 2018, **57**, 84–92.

329 Y. N. Zhitnev, E. A. Tveritinova, F. M. Spiridonov and V. V. Lunin, *Russ. J. Phys. Chem. A*, 2010, **84**, 1127–1131.

330 F. Schweinberger, *Supported Size-Selected Clusters as Sophisticated Model Catalyst Systems at Applied Reaction Conditions*, Elsevier, 2018.

331 H. Ataee-Esfahani, Y. Nemoto, L. Wang and Y. Yamauchi, *Chem. Commun.*, 2011, **47**, 3885.

332 M. Rück, A. Bandarenka, F. Calle-vallejo and A. Gagliardi, *Nanoscale Adv.*, 2019, **1**, 2901–2909.

333 E. Antolini and J. Perez, *J. Mater. Sci.*, 2011, **46**, 4435–4457.

334 Y. Zhu, M. Xu and W. Zhou, *Chinese Phys. B*, 2018, **27**, 056804.

335 O. Ersen, I. Florea, C. Hirlimann and C. Pham-Huu, *Mater. Today*, 2015, **18**, 395–408.

336 J. Ayache, L. Beaunier, J. Boumendil, G. Ehret and D. Laub, *Sample Preparation Handbook for Transmission Electron Microscopy*, Springer Science+Business Media, LLC 2010, 2010.

337 B. Kwiecińska, S. Pusz and B. J. Valentine, *Int. J. Coal Geol.*, 2019, **211**, 103203.

338 Jeol, *Application note: Scanning Electron Microscope A to Z*, No.1101B972C(Ks), https://www.jeol.co.jp/en/applications/pdf/sm/sem_atoz_all.pdf.

339 J. I. Goldstein, D. E. Newbury, J. R. Michael, N. W. M. Ritchie, J. H. J. Scott and D. C. Joy, *Microscopy and X-Ray Microanalysis*, Springer Science+Business Media LLC, 2018.

340 FEI, *Nova NanoSEM 50 Series Excellent Performance for the Widest Range of Samples*, http://www.fei.co.jp/_documents/NovaNanoSEMDatasheet.pdf.

341 E. Prestat, M. A. Kulzick, P. J. Dietrich, M. M. Smith, M. E. P. Tien, M. G. Burke, S. J. Haigh and N. J. Zaluzec, *ChemPhysChem*, 2017, **18**, 2151–2156.

342 L. Zarraoa, M. U. González and Á. S. Paulo, *Sci. Rep.*, 2019, **9**, 1–11.

343 FEI, *Appl. Note: Information from Every Angle Directional BSE Detector for Next-Level Imaging,* 2013, http://emc.missouri.edu/wp-content/uploads/2016/03/FEI-Information-for-Every-Angle-DBS-Detector.pdf.

344 Q. Xing, *Scanning*, 2016, **38**, 864–879.

345 W. Zhou and H. F. Greer, *Eur. J. Inorg. Chem.*, 2016, **2016**, 941–950.

346 D. B. Williams and C. B. Carter, *Transmission electron microscopy: A textbook for materials science*, Springer Science+Business Media, LLC, 2009.

347 B. Fultz and J. M. Howe, *Transmission Electron Microscopy and Diffractometry of Materials*, Springer-Verlag Berlin Heidelberg, 2008.

348 K. W. Urban, *Nat. Mater.*, 2009, **8**, 260–262.

349 C. Kisielowski, B. Freitag, M. Bischoff, H. Van Lin, S. Lazar, G. Knippels, P. Tiemeijer, M. Van Der Stam, S. Von Harrach, M. Stekelenburg, M. Haider, S. Uhlemann, H. Müller, P. Hartel, B. Kabius, D. Miller, I. Petrov, E. A. Olson, T. Donchev, E. A. Kenik, A. R. Lupini, J. Bentley, S. J. Pennycook, I. M. Anderson, A. M. Minor, A. K. Schmid, T. Duden, V. Radmilovic, Q. M. Ramasse, M. Watanabe, R. Erni, E. A. Stach, P. Denes and U. Dahmen, *Microsc. Microanal.*, 2008, **14**, 469–477.

350 P. A. Midgley and R. E. Dunin-Borkowski, *Nat. Mater.*, 2009, **8**, 271–280.

351 B. Qiao, A. Wang, X. Yang, L. F. Allard, Z. Jiang, Y. Cui, J. Liu, J. Li and T. Zhang, *Nat. Chem.*, 2011, **3**, 634–641.

352 W. Zhang and W. T. Zheng, *Phys. Chem. Chem. Phys.*, 2015, **17**, 14461–14469.

353 P. A. Midgley and M. Weyland, *Ultramicroscopy*, 2003, **96**, 413–431.

354 W. van Aarle, W. J. Palenstijn, J. De Beenhouwer, T. Altantzis, S. Bals, K. J. Batenburg and J. Sijbers, *Ultramicroscopy*, 2015, **157**, 35–47.

Chapter 2

Spherical core-shell alumina support particles for model platinum catalysts

Prepared as full article for submission in peer-reviewed journal: Lisa Geerts, Hannelore Geerts-Claes, Alexander Skorikov, Julie Vermeersch, Gina Vanbutsele, Vladimir Galvita, Denis Constales, C. Vinod Chandran, Sambhu Radhakrishnan, Jin Won Seo, Eric Breynaert, Sara Bals, Sreeprasanth Pulinthanathu Sree, Johan A. Martens

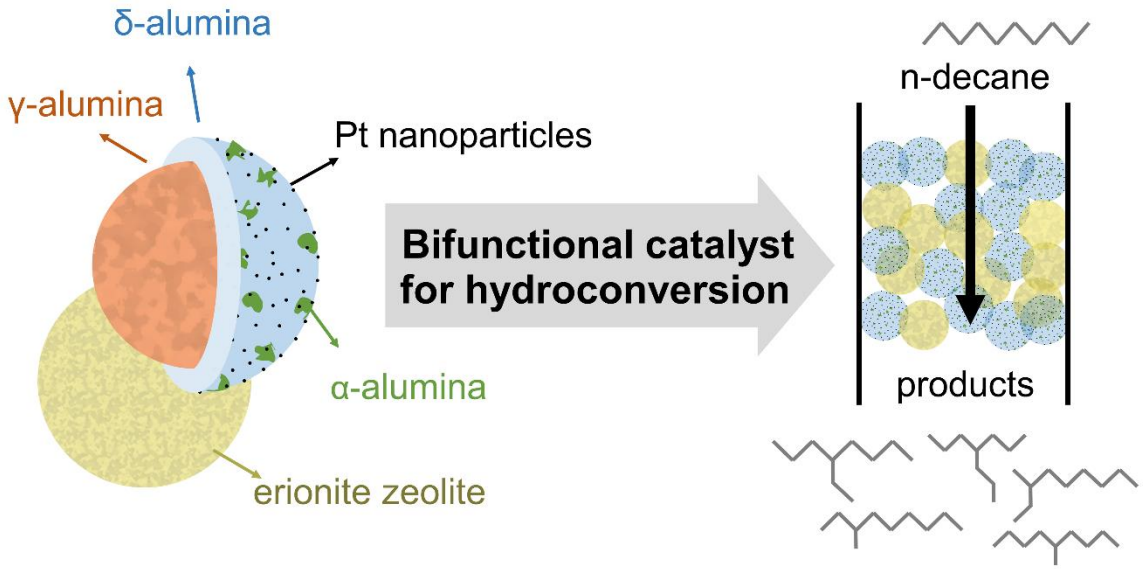

This work was conducted at:

KU Leuven, Center for Surface Chemistry and Catalysis: Characterization and Application Team, Celestijnenlaan 200F, 3001 Leuven, Belgium

University of Antwerp, Electron Microscopy for Materials Science, Groenenborgerlaan 171, 2020 Antwerp, Belgium

KU Leuven, Department of Materials Engineering, Kasteelpark Arenberg 44, bus 2450, 3001 Leuven, Belgium

Ghent University, Laboratory for Chemical Technology, Technologiepark 125, 9052, Zwijnaarde, Belgium

Ghent University, Department of Electronics and information systems, Krijgslaan 281 S8, 9000, Ghent, Belgium

Contributions:

L. Geerts and Prof. J. Martens designed the research. L. Geerts performed material synthesis, performed (S)TEM and EDX characterization, analyzed the data and wrote the article. J. Vermeersch assisted with the material synthesis. STEM, electron tomography and EDX was done by A. Skorikov. S. P. Sree performed SEM characterization. The hydroisomerization experiments were done by G. Vanbutsele and J. Vermeersch. NMR was done by C. Vinod Chandran. All of the authors contributed to the finalization of the article. J. Martens helped with data interpretation and writing.

γ- and δ-alumina are popular catalyst support materials. Using a hydrothermal synthesis method starting from aluminum nitrate and urea in diluted solution spherical core-shell particles with uniform particle size of about 1 μm were synthesized. Upon calcination at 1000 °C, the particles adopted a core-shell structure with γ-alumina core and δ-alumina shell as evidenced with 2D and 3D electron microscopy and ^{27}Al magic angle spinning nuclear magnetic resonance spectroscopy. The spherical alumina particles were loaded with Pt nanoparticles with an average size of 1 nm using strong electrostatic adsorption method. Electron microscopy and energy dispersive X-ray spectroscopy revealed a homogeneous platinum dispersion over the alumina surface. These platinum loaded alumina spheres were used as model catalyst for bifunctional catalysis. Physical mixtures of Pt/alumina spheres and spherical zeolite particles are equivalent to catalysts with platinum deposited on the zeolite itself facilitating investigation of the catalyst components individually.

Introduction

Heterogeneous catalysts are generally very complex materials consisting of multiple components. Many catalysts consist of metal nanoparticles deposited on porous metal oxides.[1–3] Deriving intrinsic kinetic data from kinetic experiments on heterogeneous catalysts is complicated by the involvement of multicomponent diffusion and adsorption in the porous matrix and the presence of temperature gradients.[3–6] This complexity motivates the use of model catalysts for investigating reaction mechanisms and kinetics.[3,4] One approach consists of using single-crystal surfaces and nanoparticles on planar supports in ultra-high vacuum surface science experiments.[3,4,7,8] This approach generated important insight in catalysis, *e.g.* molecular description of active sites and reaction intermediates, and it revealed structure sensitivity and promotor effects. The translation of these surface science concepts to real world fully formulated catalysts is not trivial.[8,9] Dense, spherical support particles of which the surface can be loaded uniformly with the active metal phase may bridge between the two research fields. Examples of this type of model catalysts are Rh, Co and Ni particles on SiO_2 spheres and Pd on Al_2O_3 spheres.[10–13] Monodisperse silica particles made with the Stöber process, have been used as model catalyst support for Pt, Pd, Ag and Au nanoparticles.[14]

Alumina is commonly used as catalyst support, next to adsorbent, ceramic, abrasive and filter.[15–19] Many particle shapes such as rods, fibrous structures, flakes and spheres have been reported.[18,20–26] Alumina spheres can be synthesized using sol–gel processes and hydrothermal procedures, from micro-emulsion, or using spray drying, spray

pyrolysis or via other ways.[21,27–35] Among the methods, precipitation is a simple, fast method suitable for upscaling.[36,37] The sphere sizes are in the range from nanometre to millimetre. The interior can be hollow, porous or dense. Only rarely documented are spheres with a core-shell architecture, with core and shell being a different alumina phase. The original alumina phase is converted upon calcination in transition alumina phases, and ultimately the fully dehydroxylated most stable α-alumina phase is obtained.[38] The transformation is influenced by the starting material, the particle size, relative humidity, alkalinity, heating rate, pressure and bed depth.[39]

Alumina spheres can be prepared in various ways. Submicrometre particles were obtained by polymerization using acetic acid [30] and lauric acid.[40] Larger microspheres with size from 500 to 1500 μm and mesoporous alumina spheres of 2 mm diameter have been obtained by combination of drop-generation and sol–gel methods.[27,34] Chitosan has been used as porogen.[41] The sol-emulsion-gel method comprises gelation of an emulsion of an aqueous sol and organic reagents, with or without surfactant.[42–44] Similarly, mesoporous alumina spheres with nonuniform size distribution of 100-200 nm to several μm have been synthesized using the microemulsion method.[32] Controlled hydrolysis of aluminum alkoxides is an alternative method.[45] Hydro-/solvothermal processes have also been frequently applied.[21,46–48] Precipitation by thermal decomposition of urea is another common approach.[16,19,26,49–53] The obtained alumina particle sizes vary from 200 nm to 120 μm. An alternative route to spherical alumina particles with diameters of 0.3 to 1.7 μm is direct thermal decomposition of aluminum isopropoxide.[17] Heating aluminum generates spherical particles with size between 5-100 nm.[54] Spray pyrolysis can also be used for spherical particles.[31,55–58] Mesoporous spheres have been obtained in organic solvents in the presence of an amphiphilic triblock copolymer.[59,60] Hollow spheres having a permeable shell composed of aggregated nanoplatelets/nanoparticles have been prepared using hydrothermal and solvothermal methods.[61–63] Sizes of up to a few micrometer were obtained in presence of urea and/or trisodium citrate.[15,28,62,64–67] Spray pyrolysis has been used to prepare nanosized hollow alumina nanospheres with a porous shell.[68] Hard templating is another method for synthesis of porous hollow spheres.[69–71] Sol-gel chemistry has also been applied for synthesis of hollow spheres.[72,73] In another procedure, hollow alumina spheres and solid spheres were synthesized with water in oil in water (W/O/W) emulsions.[74] In a synthesis departing from $Al(NO_3)_3$ in water/acetone solution, by adjusting the reaction time the properties of the obtained alumina spheres were tuneable from uniformly solid to core–shell and hollow.[61]

In the present work core-shell spherical alumina particles were synthesized via alumina precipitation with urea followed by calcination up to 1000 °C to provoke the

transformation to transition alumina. The synthesis of alumina spheres with urea precipitation is challenging because pH, nature of salts and bases, and their addition sequence matter and need to be meticulously controlled.[49,51,52] Perfectly spherical particles with narrow size distribution have been rarely reported, and the characterization of obtained core-shell particles remained limited. Here the presence of core-shell structures is investigated using (scanning) transmission electron microscopy and electron tomography. The transition alumina phases were identified and quantified using ^{27}Al magic angle spinning (MAS) nuclear magnetic resonance (NMR) spectroscopy.[39] The core-shell alumina particles were used as support for platinum. Deposition of H_2PtCl_6 precursor by strong electrostatic adsorption on the alumina surface in acidic conditions followed by reduction with hydrogen leads to high dispersion and uniform platinum deposition. The platinum loaded core shell particles were used as hydrogenation-dehydrogenation catalyst and admixed with acid erionite zeolite agglomerate particles of similar size to prepare bifunctional catalysts. The platinum loaded core-shell alumina particles were found useful for investigating bifunctional catalysis and the positioning of Pt metal with respect to zeolite acid sites.

Experimental

Preparation of the alumina spheres

All chemicals and reagents were analytical grade and used without further purification. 1.065 g aluminum nitrate ($Al(NO_3)_3.9H_2O$, Chem-Lab) was dissolved in 1000 g MilliQ water in a 1 l Schott bottle. 0.4757 g ammonium sulfate (RPL, UCB) and 6.006 g urea (Sigma-Aldrich) were sequentially added. The mixture was vigorously stirred at room temperature. When dissolution was complete, the bottle was sealed and transferred to an oven at 90 °C. The precipitation of the alumina particles was provoked by the temperature-induced decomposition of urea which increased the pH.[50,75,76] The bottle was left 24 h in the oven. After cooling to room temperature, the suspension was centrifuged and successively washed with deionized water, ethanol (technical grade) and deionized water. The wet precipitate was dried at 60 °C for 12 h. Finally, the resulting powder was calcined in air at 1000 °C for 4 h with a ramp rate of 2 °C/min.

Preparation of erionite zeolite

The erionite zeolite was synthesized according to a modified procedure reported by Lee *et al.*[77] The synthesis mixture was prepared using tetraethylammonium hydroxide solution (Aldrich, 35% by weight in water), aluminum-sec-butoxide (Fluka analytical), Ludox AS-40 colloidal silica (Aldrich), hexamethoniumbromide (Sigma) and potassium chloride (Chem-Lab). The first step of the gel preparation consisted of dissolution of

0.988 g aluminum-sec-butoxide in 43.88 g tetraethylammonium hydroxide solution. 19.27 g of Ludox was subsequently added dropwise and under stirring. After homogenization, 5.82 g hexamethoniumbromide was added to the mixture, and next to it a solution of 0.8735 g potassium chloride in 29.16 g water. The gel was stirred at room temperature for 24 h. The gel was then transferred to a 120 mL stainless steel autoclave. The autoclave was placed in an oven at 100 °C and agitated by tumbling for 14 days. The solid product was recovered by centrifugation at 12,000 rpm, washed with deionized water and dried overnight at 60 °C. The zeolite powder was subjected to 2 consecutive ion exchanges in 0.5 M ammonium chloride (Chem-Lab) solution (1 g of zeolite in 100 ml solution) under reflux conditions for 4 h each. Finally, the zeolite powder was calcined at 550 °C for 8 h with heating rate of 1 °C/min to obtain the acid form. Further characterization of this zeolite is provided in supplementary information (Figure S1 and S2).

Platinum deposition

A strong electrostatic adsorption method[78,79] adapted from Zečević *et al.*[80] was used for Pt deposition on the alumina spheres. First, 0.5 g of the alumina powder was suspended in 152 ml of MilliQ water and stirred for 1 h. Then, a 0.1 M HCl solution was added dropwise until a pH of 2.6 was reached. An amount of $H_2PtCl_6{\cdot}6H_2O$ (Aldrich) salt was dissolved in 16.9 ml MilliQ water, corresponding to 1 wt% of Pt of the alumina support. This solution was added dropwise to the alumina suspension under stirring. After 3 h of stirring, the sample was filtered and washed with deionized water and dried at 60 °C. The sample was then reduced under hydrogen flow at 600 °C for 3.5 h with a ramp rate of 5 °C/min. For preparation of erionite zeolite containing 1 wt% platinum, incipient wetness impregnation with $Pt(NH_3)_4Cl_2$ (Alfa Aesar) complex was performed. 0.0186 g platinum tetraamine complex was dissolved in 0.9424 g of MilliQ water and then 0.100 g of zeolite was added to 0.0980 g of this solution. The slurry was mixed thoroughly by hand and dried overnight in an oven at 60 °C. The sample was pretreated at 400 °C (5 °C/min): first an oxidation for 1 h under oxygen flow, followed by reduction for 1 h under hydrogen flow.

Electron microscopy

High resolution scanning electron microscopy (HR-SEM) images were obtained on a Nova NanoSEM450 (FEI, Eindhoven). Using carbon tape, the powder samples were mounted on aluminum stubs and directly imaged without any further sample modification. Bright-field TEM (BF-TEM) and high-angle annular dark-field scanning TEM (HAADF-STEM) were performed using JEOL ARM200F electron microscope operated at acceleration voltage of 200 kV. Images in high-angle annular dark-field

scanning TEM mode (HAADF-STEM) and energy-dispersive X-ray spectroscopy (EDX) elemental maps were acquired using a probe-corrected FEI Titan^3 operated at 300 kV and equipped with a four-quadrant EDX detector (Super-X). TEM samples were prepared by dispersing the powder in 2-propanol and placing a few drops of the solution onto the copper TEM grids covered with lacey carbon film (Pacific Grid Tech). Tomographic tilt series were acquired over a ±75° angular arrange with a 3° step interval using Fischione Model 2020 tomography sample holder. After aligning the images in the tilt series by a cross-correlation based algorithm, 3D reconstructions were obtained using expectation maximization (EM) method as implemented in ASTRA Toolbox.[81]

Nitrogen physisorption

N_2 physisorption isotherms were recorded on a Micromeritics TriStar 3000 instrument at liquid nitrogen temperature. The sample was pretreated at 400 °C in N_2 flow for 12 h before measurement.

X-ray diffraction

Powder X-ray diffraction was performed on a STOE STADI P Combi diffractometer with focusing Ge(111) monochromator (Cu Kα1 radiation) in transmission geometry with 140°-curved image plate position sensitive detector (IP PSD) with an internal IP PSD resolution of 0.03°.

Thermogravimetric analysis

Thermogravimetric analysis (TGA) was performed using a TA instrument Q500 under N_2 flow with a heating rate of 5 °C/min.

^{27}Al solid-state NMR

^{27}Al magic-angle spinning (MAS) NMR experiments were carried out on a Bruker 500 Avance III spectrometer operating at 11.74 T, with ^{27}Al Larmor frequency of 130.52 MHz. The alumina sample was packed in a 4 mm zirconia rotor and spun in triple-resonance 4 mm MAS probe up to a rotation frequency of 15 kHz. A radio-frequency (RF) pulse of 125 kHz strength with a flip-angle of 15 degree was used to record the ^{27}Al spectrum. ^{1}H decoupling at RF strength of 60 kHz was achieved by robust SW_f-SPINAL sequence.[82] 1024 transients were collected with a recycle delay of 2 s. The ^{27}Al chemical shifts were referenced against 1M solution of aluminium nitrate (at 0 ppm). The spectral decomposition was carried out with the help of DMFit program.[83]

Catalysis

Bifunctional catalysts were prepared by combining the zeolite powder with the Pt-loaded alumina spheres and by Pt loaded on zeolite powder diluted with inert alumina coated silica spheres. The mixing of powders was done at equal weight ratio. The catalysts are denoted as Pt-Al_2O_3/ERI and Pt-ERI/Al_2O_3. In Pt-Al_2O_3/ERI Pt is located on the alumina component, whereas in Pt-ERI/Al_2O_3, Pt is located on the zeolite . The powder mixtures were compressed to pellets with diameters between 125 and 250 μm. n-Decane (Acros) hydroconversion was performed in high-throughput fixed-bed continuous-flow reactor.[84,85] 50 mg of catalyst was loaded in the microreactor tubes with an internal diameter of 2 mm. The reactor was operated at a total pressure of 0.45 MPa and a molar ratio of H_2 to n-decane of 214. The space time at the reactor entrance, W/F, was 1.400 kg s mol^{-1}. Before the reaction, the catalyst was pretreated at 400 °C under hydrogen flow for 2 h. The reactor was cooled to 120 °C and n-decane/H_2 mixture admitted. The reaction temperature was increased stepwise with 5 °C. Reaction products were sampled at the reactor outlet after equilibration at a given temperature for 1 h. Reaction product analysis was achieved using an automated online GC equipped with a non-polar capillary column (HP-1, Agilent) and flame ionization detector.

Results and discussion

HR-SEM, TEM and STEM images of the uncalcined alumina particles are shown in Figure 1. The particles had spherical morphology with typical diameters of 0.98 - 1.20 μm. Small amounts of impurities with irregular shape and elongated features were also present (Figure 1c upper left corner). Most of the particles exhibited a perfect spherical shape with a denser shell region, which can be observed in the HAADF-STEM image of an individual particle (Figure 1d). TEM and HAADF-STEM images revealed the presence of a denser shell region with thickness of about 100 nm.

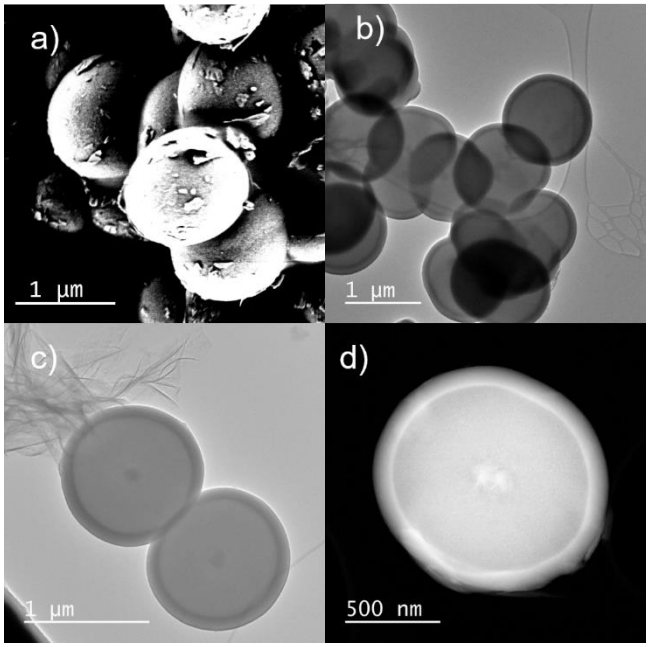

Figure 1. Electron microscopic characterization of the precursor spheres (a) HR-SEM (b-c) TEM and (d) HAADF-STEM image.

To reveal the phase of the core-shell precursor particles, ^{27}Al solid-state NMR experiments were performed (Figure 2). The ^{27}Al MAS NMR spectrum exhibits three distinct signals. According to literature, the isotropic chemical shifts (δ_{iso}) in the range between 60 to 80 ppm, 30 to 50 and -20 to 20 ppm can be assigned to tetra-, penta- and hexa-coordinated Al sites, respectively. The uncalcined precursor was mainly composed of hexa-coordinated Al, typical of crystalline aluminum hydroxide and oxyhydroxide phases. The tetra- and penta-coordinated Al are characteristic of an amorphous phase.[39]

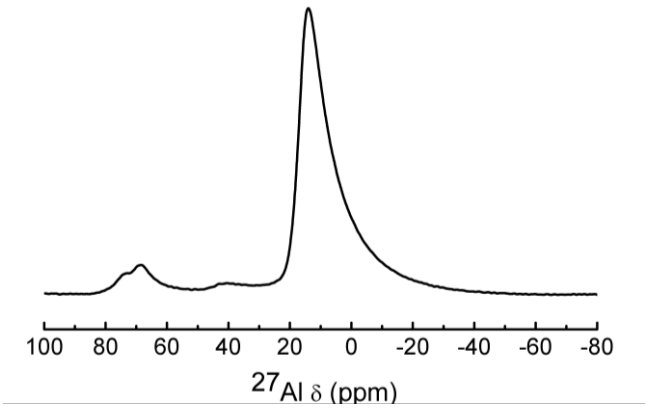

Figure 2. ^{27}Al MAS NMR of the uncalcined alumina precipitate.

The thermal transformation was investigated by thermogravimetric analysis (Figure 3). The significant weight loss upon heating is due to dehydroxylation and elimination of residual nitrate, if any.[49] Around 950 °C, there was a step in the weight loss where after the weight remained almost constant. The total weight loss corresponded to *ca.* 36.5%.

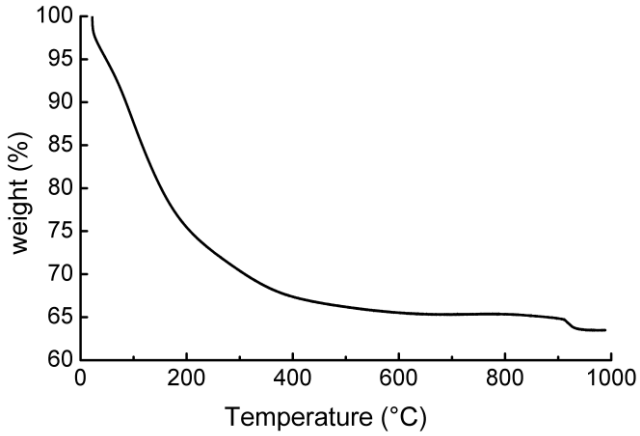

Figure 3. TGA curve of the precipitated Al spheres

TEM and STEM revealed that despite the significant weight loss upon calcination (Figure 3), the particles showed little shrinkage upon calcination at 1000 °C (Figure 4). The size of the calcined spheres was ranging from 0.96 to 1.18 μm. The shell underwent shrinkage up to *ca.* 80 nm after calcination.

The internal structure of the spheres was revealed by electron tomography. The tomography experiment was performed on 2 individual particles. Figure 5 shows 2D slices and cuts through the 3D reconstructions of the particles. Movies of the 3D reconstructions can be found in the supplementary information (supplementary movie S1 and S2). Figures 5a and b show a particle with a dense shell and a less dense core, whereby the shell and core are separated by a void. In the center of the core, a denser part can be discriminated. In the 3D reconstruction of the second particle (Figure 5c and d) the void between core and shell is absent and the central dense core has a smaller size.

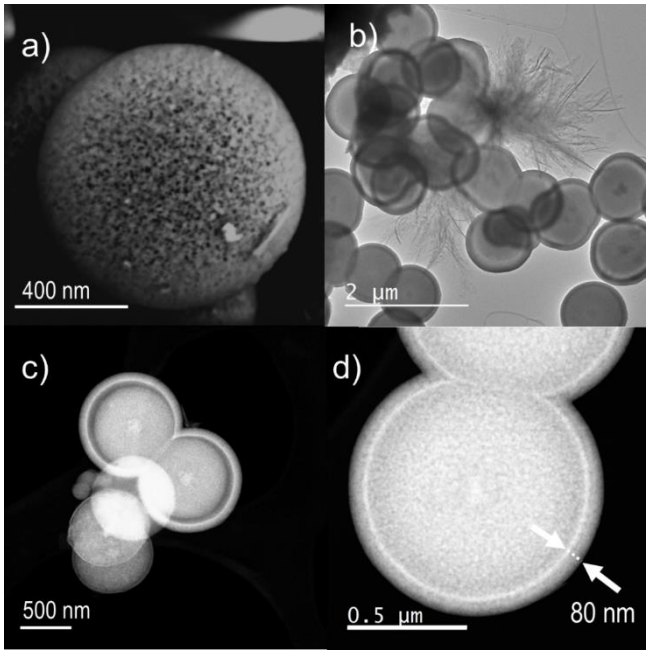

Figure 4. (a) HR-SEM (b) TEM and (c-d) HAADF-STEM image of the calcined alumina spheres.

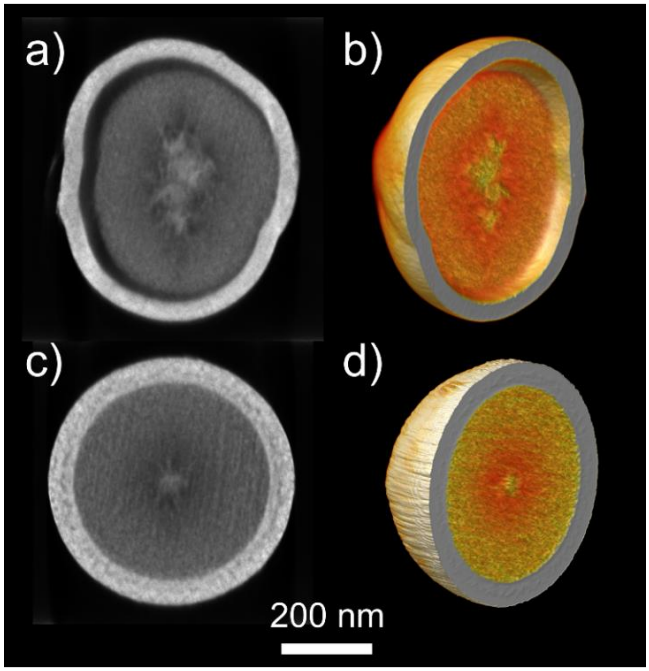

Figure 5. (a,c) Orthoslices and (b,d) cuts through 3D visualizations of HAADF-STEM tomographic reconstructions of two alumina particles after calcination at 1000 °C (supplementary movies S1 and S2).

Between the temperatures of dehydroxylation of the aluminium (oxy)hydroxides and the alpha-alumina transformation, a number of transition alumina structures are formed. Typical temperatures that are reported are between 450 and 700 °C for *γ*-Al_2O_3 and 750 °C – 900 °C for *δ*-Al_2O_3. Further increasing of the temperature to 1000 °C and 1100 °C can lead to *θ*-Al_2O_3 and *a*-Al_2O_3 respectively.[39,86,87] Prediction of the phases based on the transformation temperature is difficult as it can vary significantly with the starting material, the particle size, relative humidity, alkalinity, heating rate, pressure and bed depth.[39,86] For example, mechanical grinding of *γ*-Al_2O_3 lowers the temperature needed to reach *a*-Al_2O_3. From ground *γ*-Al_2O_3, a temperature of 600-800 °C resulted in a mixture of *γ*-Al_2O_3 and *a*-Al_2O_3, while from the unground sample, a temperature of 1000 °C led to *δ*-Al_2O_3.[88] In this study, 1000 °C was used as calcination temperature and these phases, *i.e.* *γ*-Al_2O_3, *δ*-Al_2O_3, *θ*-Al_2O_3, *a*-Al_2O_3, or a mixture thereof, can thus be expected.

The nature of the transition alumina phases of the calcined core-shell particles was investigated using ^{27}Al solid-state NMR. ^{27}Al MAS and 3QMAS NMR spectra of the alumina spheres are shown in Figure 6. The 3QMAS experiment rendered high-resolution in the ^{27}Al spectrum. Seven different aluminum species were identified. The ^{27}Al spectrum shows two distinct sets of peaks centered at around chemical shifts of 12 ppm and 70 ppm corresponding to hexa and tetra-coordinated sites, respectively.[89] The ^{27}Al NMR spectrum was decomposed using the information from the 3QMAS experiment and the fitting parameters (chemical shift δ_{iso}, quadrupolar coupling constants C_Q, asymmetry parameter η_Q and relative fractions of the phases) are presented in Table 1. The identification of the alumina phases based on solid-state NMR parameters was carried out using the strategy published in a recent review.[39] 36% of the calcined alumina sample is attributed to δ-alumina, 46% to γ-alumina, and 17% to amorphous phase. About 1% of the alumina is present in an α-alumina phase.

The amorphous phase in the calcined sample detected with NMR was considered to be present outside of the core-shell particles. It was assumed to be present in the extraneous material observed after synthesis (Figure 4b). This leads to a composition of the core-shell particles of 55% γ-alumina, 43% δ-alumina, and 2% α-alumina phase. Based on the particle diameter and the shell thickness averaged over 5 particles and measured with HAADF-STEM, volume fractions of the shell and core were estimated at 40% and 60%, respectively (as explained in the supporting information). From the phase composition according to NMR and the volumetric composition according to HAADF-STEM, it appears that the shell could consist of δ-alumina, and the core of γ-alumina. This interpretation is consistent with the contrast in (S)TEM images (Figures 4 and 5). The sequence of formation of transition alumina phases at increasing

temperatures corresponds to γ-$Al_2O_3 \rightarrow \delta$-$Al_2O_3 \rightarrow \theta$-$Al_2O_3 \rightarrow \alpha$-$Al_2O_3$.[39] The density of the phases increases in this order. The shell has the highest intensity in HAADF-STEM, in agreement with the presence of the δ-Al_2O_3 , while the core is less dense and composed of γ-Al_2O_3. The α-alumina is assumed to be present as islands on the surface of the particles. The formation of α-alumina requires the highest temperature. In calcination processes, α-alumina grows from the surface towards the core of the particle.[53,89–91] A schematic representation of the proposed composition of the core-shell alumina particles is shown in Figure 7.

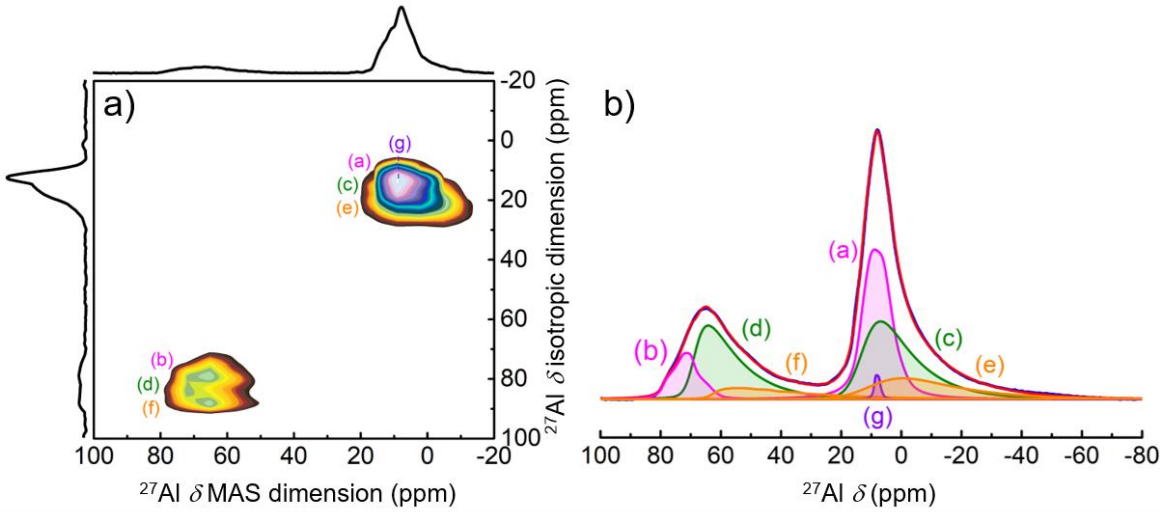

Figure 6. (a) ^{27}Al 3QMAS and (b) MAS NMR of the calcined alumina spheres (1000 °C). The blue and red lines respectively correspond to the experimentally obtained and simulated spectrum. The other colors (marked a-g) show the individual simulated signals.

Table 1. ^{27}Al solid-state NMR simulation parameters (chemical shift δ_{iso}, quadrupolar coupling constants C_Q and asymmetry parameter η_Q) of the alumina phases. The letters correspond to the NMR signals in Figure 6.

	C_Q (MHz)	δ_{iso} (ppm)	η_Q	Δ_{CS} (ppm)	Sites	Assignment	Content (%)
(a)	4.20	14.50	0.42	0.00	AlO_6	δ-alumina	36
(b)	4.40	79.50	0.70	0.00	AlO_4		
(c)	5.58	13.50	0.61	8.95	AlO_6	γ-alumina	46
(d)	5.42	69.40	0.61	5.30	AlO_4		
(e)	7.16	10.95	0.61	16.70	AlO_6	amorphous	17
(f)	7.90	63.30	0.61	3.50	AlO_4		
(g)	1.88	9.18	0.00	0.00	AlO_6	α-like islands on the surface	1

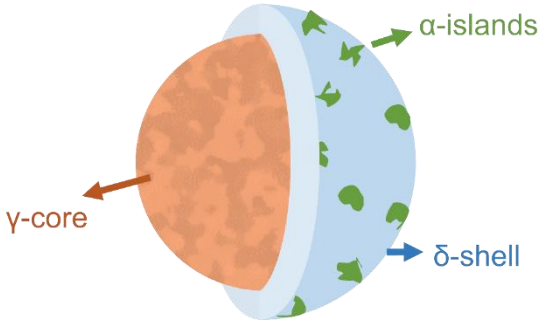

Figure 7. Schematic arrangement of transition alumina phases in the core-shell alumina particles.

The porous structure and texture of the particles were investigated with N_2 adsorption porosimetry. Nitrogen adsorption-desorption isotherms, t-plot and the corresponding pore-size distribution curves of the sample after calcination at 1000 °C are included in the supplementary information (Figure S3). The Brunauer–Emmett–Teller (BET) specific surface area estimated by using the multipoint BET method using the adsorption data in the relative pressure range of 0.05-0.1 was 76 m^2/g. This value is too large for spherical particles measuring around 1 micrometer. The corrugated external surface observed in SEM and TEM (Figures 4 and 5) and the presence of mesopores with diameters from 6 and 20 nm and a volume of 0.12 ml/g explains the larger surface area.

The core-shell alumina particles were loaded with platinum using the strong electrostatic adsorption of chloroplatinate on the protonated surface.[78,80] Figure 8 e-f shows a typical EDX elemental map of an individual alumina sphere loaded with platinum. The distributed Pt signal indicates that Pt particles are homogeneously spread. Figure 8 a-c displays high magnification HAADF-STEM images of the Pt loaded alumina spheres. The images confirm the high dispersion with Pt particles isolated from each other and uniformly distributed on the support. The size of the Pt particles was estimated at about 1 nm. The imaging revealed the limited penetration of the platinum into the particles. This size range of the Pt particles corresponds to the size of highly dispersed Pt catalysts supported on alumina used experimentally and industrially, and its location on the outer surface eliminates the potential occurrence of diffusional limitation of the catalyzed reaction.[92–98]

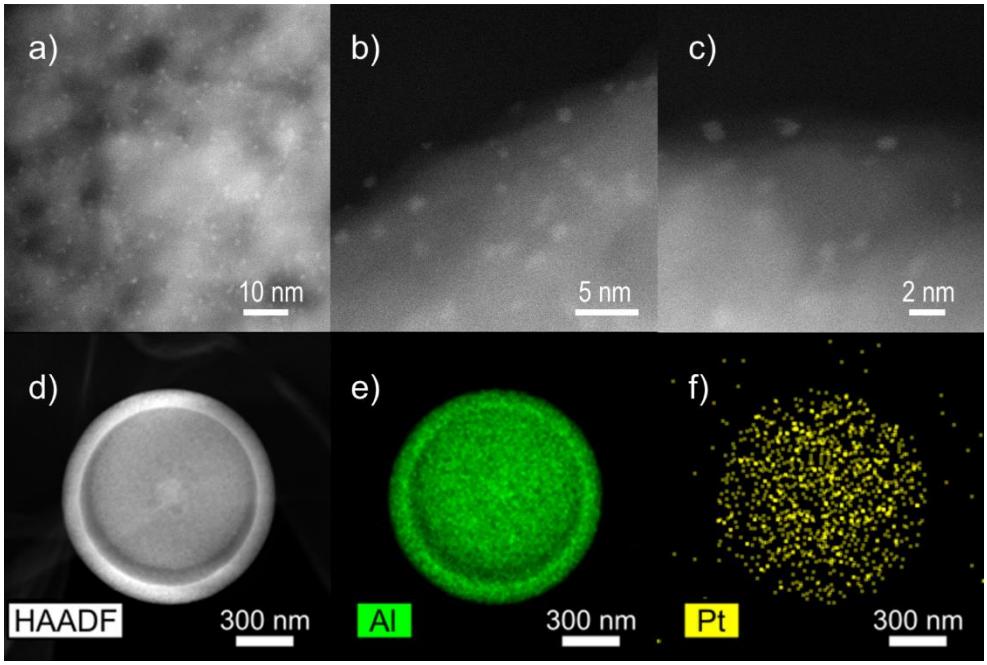

Figure 8. (a-c) High magnification HAADF-STEM images of the Pt decorated alumina spheres. (d) HAADF-STEM image and EDX elemental mapping of (e) Al and (f) Pt on an individual alumina sphere, proving the uniform distribution of the Pt nanoparticles on the alumina support.

To reveal the relevance of the platinum-loaded core-shell alumina particles, the spheres were combined with powder of acid erionite zeolite with a similar spherical morphology and size (Figure 9). Such combination of a platinum catalyst with an acid zeolite can serve as bifunctional catalyst for isomerization and hydrocracking of hydrocarbons. Pt was also deposited on the ERI zeolite and mixed with inert material (alumina coated silica spheres). Figure 9 c-f shows the ERI spheres after Pt deposition. The Pt nanoparticles are homogeneously distributed and have sizes in the range from 1.6 nm to 7.7 nm.

n-Decane is a model molecule which often has been used to evaluate the bifunctional catalytic properties of zeolites.[99–103] The physical mixture of acid zeolite with Pt loaded core-shell alumina, and the zeolite loaded with platina, diluted with inert spheres were loaded in a fixed bed continuous flow reactor, having in both cases the same amount of acid zeolite and platinum.

Combining the Pt-loaded alumina spheres with a zeolite was done in order to provide acid sites that are required in bifunctional hydroconversion catalysts. The erionite zeolite was chosen because of its spherical morphology. In the bifunctional conversion of n-decane, n-decane is first dehydrogenated on the metal site. Protonation of alkene intermediates on acid functions leads to alkylcarbenium ions that undergo isomerization and cracking reactions. The isomerized and cracked carbocations are then finally desorbed from the acid sites and hydrogenated on the metal site.[80,100,104,105]

The kinetics and the sequence of reactions depends on the diffusion of intermediates between acid and metal sites and hence optimizing the distance between the sites is very important. Recently it was shown that closest proximity between metal and acid sites can be disadvantageous for selectivities.[80] When Pt is located on the alumina spheres, the metal function is more distant from the acid sites in the zeolite in comparison with Pt located on the zeolite with metal-acid sites in more intimate contact.

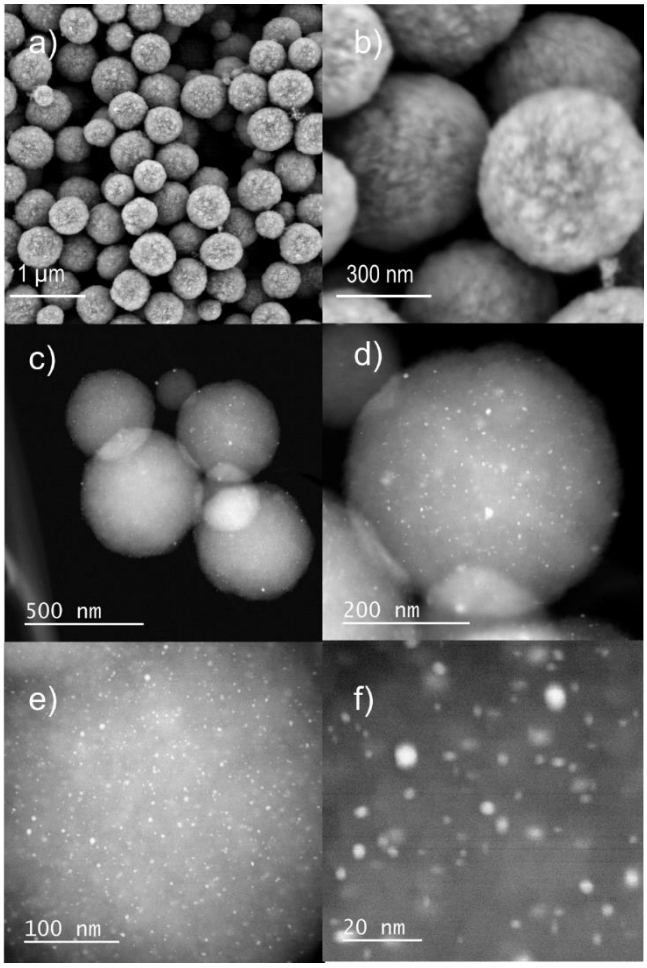

Figure 9. (a, b) HR-SEM image of the erionite zeolite. (c-f) HAADF-STEM image of the Pt loaded erionite spheres at different magnifications.

The two catalysts were equally active as the decane conversion versus reaction temperature coincided (Figure 10). Decane is converted to branched skeletal isomers, and cracked products. Also the yield of isomers and cracked products on both catalysts were very similar. These results reveal that the platinum-loaded core-shell alumina spheres are suitable for investigations of bifunctional catalysis. Acid zeolites can be admixed with Pt/alumina spheres and evaluated without the need of loading the platinum on the zeolite itself. This is advantageous because high Pt dispersions using conventional impregnation methods is difficult to achieve on a zeolite.[106] Furthermore,

the platinum loaded core-shell alumina particles can serve as model catalysts for investigating the spatial organization of the two sites in further studies. The Pt/alumina spheres could be combined with any zeolite and used as a bifunctional model catalyst.

A detailed analysis of the C10 skeletal isomers was made as shown in Figure 11 and 12. On both catalysts, the monobranched isomers were the primary reaction products (Figure 11). Di- and tribranched isomers can only be formed consecutive to monobranched products.[99,100,105,107]

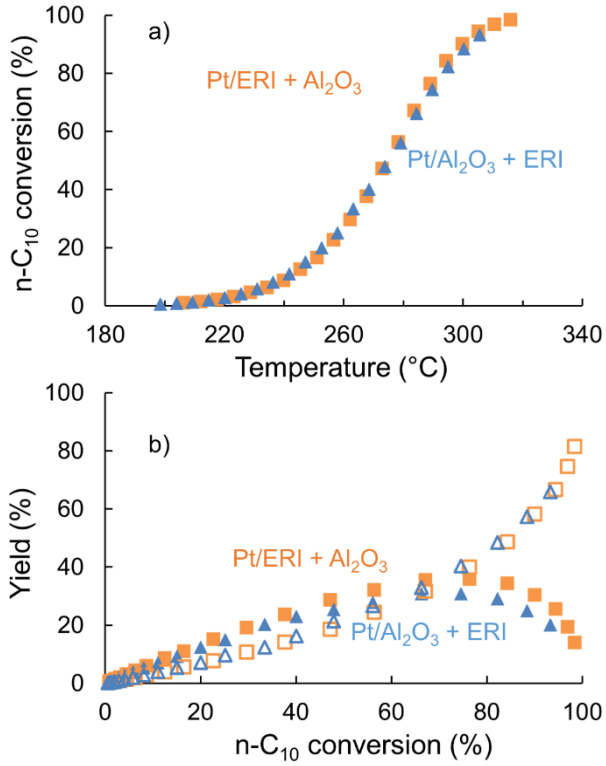

Figure 10. (a) n-decane conversion against reaction temperature on two catalysts: physical mixture of platinum-loaded core-shell alumina and acid erionite zeolite (Pt/Al_2O_3 + ERI) and platinum-loaded acid erionite zeolite diluted with Al_2O_3 spheres ($Pt/ERI + Al_2O_3$; (b) yield of isomerization (closed symbols) and cracked products (open symbols) against n-decane conversion over both catalysts.

The evolution of the distribution of the methylnonanes was comparable for the two catalyst mixtures (Figure 12). Among the four methylnonane isomers, 2-methylnonane, 3-methylnonane, 4-methylnonane were formed in similar amounts. They were formed preferentially in comparison with 5-methylnonane. On zeolites without shape selective effects, alkylcarbenium ion chemistry predicts low amounts of 2-methylbranched nonanes, comparable to the amount of 5-methylbranched isomers.[99,107] The higher amount of 2-methylnonane in comparison with 5-methylnonane can be interpreted as an indication for steric restrictions of bulky transition states in the pores of a zeolite.

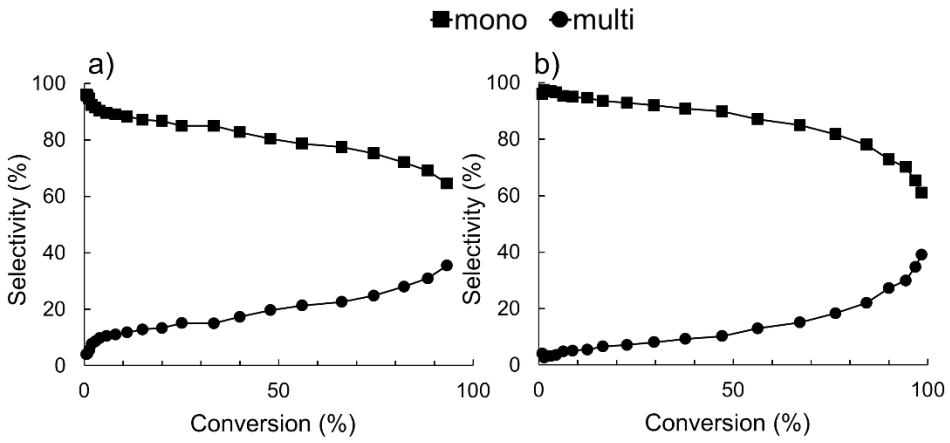

Figure 11. Distribution of C10 skeletal isomers (mono- and multibranched) obtained by hydroconversion on (a) Pt/Al_2O_3 + ERI (b) Pt/ERI + Al_2O_3. The contribution of tribranched isomers to the multibranched isomers was below 0.6%.

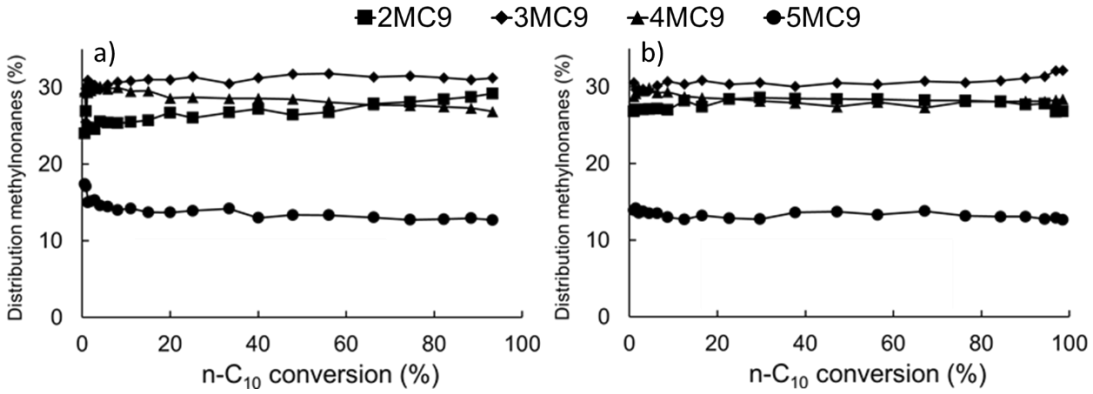

Figure 12. Distribution of methylnonane skeletal isomers obtained on (a) Pt/Al_2O_3 + ERI (b) Pt/ERI + Al_2O_3.

Table 2 summarizes three product characteristics of the n-decane test that can be used to reveal the pore structure of a zeolite. The numerical values indicate whether there are deviations from the ideal hydrocracking mechanism and can be used to probe steric constraints in the pores as well as pore-mouth catalysis.[99,100,105] The steric restriction is also reflected in the refined constraint index (CI*), which is defined as the product ratio of 2-methylnonane and 5-methylnonane at 5% isomerization yield (Table 2).[99,101] Without steric restrictions, the CI* index is expected to be equal to one. 12-membered ring (MR) zeolites typically have CI* values between 1.0 and 2.2. Higher CI* values are found for 10-MR zeolites with constraints for isomerization. For cage zeolites limited by 8-MR rings, CI* values overlap between those of the 12-MR and 10-MR zeolites.[99–101] A value of 2.5 has been reported for the erionite zeolite.[108] The second parameter, *i.e.* the relative quantities of ethyloctanes in the monobranched feed isomers at 5% isomerization conversion, is zero for zeolites with 10-MR pores.[99] The third parameter, the yield of isopentane expressed in mol/100 mol n-decane cracked at 35%

cracking yield is larger than 35 for 12-MR zeolites.[109] Combination of the three product characteristics classifies the zeolite among the 8-MR cage zeolites.

Table 2. Product characteristics of the n-decane bifunctional conversion.

	Pt/Al_2O_3 + ERI	**Pt/ERI + Al_2O_3**	**Assignment**
CI* 2MC9/5MC9 at 5% isomerization	1.8	2	12-MR or 8 MR + cage
% ethyloctanes in monobranched isomers at 5% isomerization	7.8	4.6	12-MR pore or 8 MR + cage
isopentane (mol/100 mol C10 cracked) at 35% cracking	15	12	10 MR or 8 MR + cage

Cracked products (C4, C5 and C6) are grouped into branched and linear fragments and its relative amounts at 35% hydrocracking yield are summarized in Table 3. The composition obtained on the 2 catalysts is comparable. Linear isomers dominate in these fractions, which means the molecules undergo substantial cracking. We note that methane and ethane, which can only be ascribed to hydrogenolysis, were also formed. This can be explained by the easy accessibility of the Pt metal being located at the external surface in combination with the limited accessibility of the acid sites in the pores of the zeolite.[99]

Table 3. Composition of C4, C5 and C6 cracked product fraction at 35% hydrocracking yield. Branched and linear products are denoted here as i and n.

	Pt/Al_2O_3 + ERI		**Pt/ERI + Al_2O_3**	
	i	**n**	**i**	**n**
C4	45	55	43	57
C5	36	64	33	67
C6	34	66	28	71

Conclusions

Spherical 1 μm sized core-shell alumina particles with a narrow size distribution were synthesized by the urea based precipitation method. Electron microscopy and tomography reconstruction were used to characterize the core-shell nanostructure of the calcined particles and to locate the transition alumina phases quantified with ^{27}Al NMR spectroscopy. The particles have δ-alumina shell with small islands of α-alumina, and γ-alumina core. This organization reflects the temperatures that were reached in the calcination process, being higher outside than inside. Homogeneous loading of

uniformly sized Pt nanoparticles on the alumina core-shell particles was obtained by strong electrostatic interaction of chloroplatinate precursor with the protonated surface of the particles, limiting the penetration of the platinum inside the particles. The excellent accessibility of the Pt particles was confirmed in bifunctional catalysis experiments; in the isomerization and hydrocracking of n-decane a same catalytic performance was obtained with platinum on alumina spheres admixed with acid zeolite and acid zeolite loaded with platinum itself. It reveals the potential of the core-shell alumina spheres to serve as model catalyst support.

Supporting Information in appendix 1.

XRD and N_2 sorption data: Figure S1-S3

Acknowledgments

This work is supported by Research Foundation Flanders (G0A5417N, G038116N) and the Flemish Government through Long-term structural funding (Methusalem). It was also supported by the Flemish Hercules Foundation (AKUL/13/19).

References

1 M. Bäumer, J. Libuda, K. M. Neyman, N. Rösch, G. Rupprechter and H. J. Freund, *Phys. Chem. Chem. Phys.*, 2007, **9**, 3541–3558.

2 F. Zaera, in *Encyclopedia of Inorganic and Bioinorganic Chemistry*, John Wiley & Sons, Ltd., 2014.

3 J. Libuda, S. Schauermann, M. Laurin, T. Schalow and H. J. Freund, *Monatshefte fur Chemie*, 2005, **136**, 59–75.

4 B. C. Gates, *Top. Catal.*, 2001, **14**, 173–180.

5 C. Chizallet and P. Raybaud, *Catal. Sci. Technol.*, 2014, **4**, 2797–2813.

6 J. Hoffmann, I. Meusel, J. Hartmann and J. Libuda, *J. Catal.*, 2001, **204**, 378–392.

7 M. Boudart, *Top. Catal.*, 2000, **13**, 147–149.

8 D. W. Goodman, *Surf. Sci.*, 1994, **299/300**, 837–848.

9 F. C. Meunier, *ACS Nano*, 2008, **2**, 2441–2444.

10 P. L. J. Gunter, J. W. H. Niemantsverdriet, F. H. Ribeiro and G. A. Somorjai, *Catal. Rev.*, 1997, **39**, 77–168.

11 C. K. Ling, N. A. M. Zabidi and C. Mohan, *J. Appl. Sci.*, 2011, **11**, 1436–1440.

12 B. A. T. Mehrabadi, S. Eskandari, U. Khan, R. D. White and J. R. Regalbuto, *A Review of Preparation Methods for Supported Metal Catalysts*, Elsevier Inc., 1st edn., 2017, vol. 61.

13 S. Chenna, R. Banerjee and P. A. Crozier, *ChemCatChem*, 2011, **3**, 1051–1059.

14 H. Hofmeister, P. Miclea, M. Steen and W. Mo, *Top. Catal.*, 2007, **46**, 11–21.

15 W. Cai, J. Yu and S. Mann, *Microporous Mesoporous Mater.*, 2009, **122**, 42–47.

16 X. J. Xu, X. D. Sun, Y. Q. Liang and W. Qiu, *Appl. Mech. Mater.*, 2013, **341–342**, 100–104.

17 W. Yang, H. Wang, X. Cheng, Z. Xie and L. An, *J. Am. Ceram. Soc.*, 2008, **91**, 2732–2735.

18 Y. Xie, D. Kocaefe, Y. Kocaefe, J. Cheng and W. Liu, *Nanoscale Res. Lett.*, 2016, **11**, 259.

19 J. Kong, B. Chao, T. Wang and Y. Yan, *Powder Technol.*, 2012, **229**, 7–16.

20 C. Bousquet, F. Cansell, C. Elissalde, M. Maglione and C. Aymonier, https://pdfs.semanticscholar.org/efeb/a2291b2bd20c2cda932b2328dd82380611be.pdf.

21 R. R. Manesh, M. Kohnehpoushi, M. Eskandari, Z. Fakhroueian and B. A. Nejand, *Mater. Res. Express*, 2017, **4**, 095025.

22 S. Liu, R. J. Wehmschulte and C. M. Burba, *J. Mater. Chem.*, 2003, **13**, 3107–3111.

23 V. Piriyawong, V. Thongpool, P. Asanithi and P. Limsuwan, *J. Nanomater.*, 2012, **5**, Article ID 819403, 1-6.

24 C. B. Reid, J. S. Forrester, H. J. Goodshaw, E. H. Kisi and G. J. Suaning, *Ceram. Int.*, 2008, **34**, 1551–1556.

25 M. Shojaie-Bahaabad and E. Taheri-Nassaj, *Mater. Lett.*, 2008, **62**, 3364–3366.

26 H. I. Ul, K. Akhtar and Z. U. Khan, *High. Temp. Mater. Proc.*, 2015, **34**, 325–332.

27 N. Dilsiz and G. Akovali, *Mater. Sci. Eng.*, 2002, **332**, 91–96.

28 J. Zhou, L. Wang, Z. Zhang and J. Yu, *J. Colloid Interface Sci.*, 2013, **394**, 509–514.

29 R. Brace and E. Matijevic, *J. inorg. nucl. Chem.*, 1973, **35**, 3691–3705.

30 F. Liu, X. Zheng, J. Chen and L. Jiang, *RSC Adv.*, 2015, **5**, 93917–93925.

31 S. Arita, N. Aoyagi, K. Ohshita, Y. Tsubota and T. Ogihara, *J. Ceram. Soc. Japan*, 2017, **125**, 539–542.

32 Q. Chang, X. Wang, J. Zhou and Y. Wang, *Adv. Mater. Res.*, 2012, **412**, 199–202.

33 P. Liu, J. Feng, X. Zhang, Y. Lin, D. G. Evans and D. Li, *J. Phys. Chem. Solids*, 2008, **69**, 799–804.

34 A. Islam and Y. Hui, *J. Porous Mater.*, 2012, **19**, 807–817.

35 S. Cottrino, Y. Jorand, J. Adrien and C. Olagnon, *Powder Technol.*, 2013, **237**, 586–593.

36 L. Wang and N. Zhang, *Adv. Mater. Res.*, 2014, **1079–1080**, 62–65.

37 S. A. Hassanzadeh-Tabrizi and E. Taheri-Nassaj, *Mater. Lett.*, 2009, **63**, 2274–2276.

38 C. Pecharromán, I. Sobrados, J. E. Iglesias, T. González-Carreño and J. Sanz, *J. Phys. Chem. B*, 1999, **103**, 6160–6170.

39 C. V. Chandran, C. E. A. Kirschhock, S. Radhakrishnan, F. Taulelle, J. A.

Martens and E. Breynaert, *Chem. Soc. Rev.*, 2019, **48**, 134–156.

40 Q. Fu, T. He, Y. Chai and C. Liu, *J. Nat. Gas Chem.*, 2010, **19**, 557–559.

41 H. V. Fajardo, A. O. Martins, R. M. De Almeida, L. K. Noda, L. F. D. Probst, N. L. V. Carreño and A. Valentini, *Mater. Lett.*, 2005, **59**, 3963–3967.

42 M. Chatterjee, M. K. Naskar, B. Siladitya and D. Ganguli, *J. Mater. Res.*, 2000, **15**, 176–185.

43 M. Rajendran and A. K. Bhattacharya, *Mater. Sci. Eng.*, 1999, **60**, 217–222.

44 H. Yang, Y. Xie, G. Hao, W. Cai and X. Guo, *New J. Chem.*, 2016, **40**, 589–595.

45 T. Ogihara, H. Nakajima, T. Yanagawa, N. Ogata, K. Yoshida and N. Matsushita, *J. Am. Ceram. Soc.*, 1991, **74**, 2263–2269.

46 H. Liu, G. Lu, Y. Guo, Y. Wang and Y. Guo, *Cent. Eur. J. Chem.*, 2009, **7**, 794–802.

47 X. Song, P. Yang, C. Jia, L. Chen and K. Matras-Postolek, *RSC Adv.*, 2015, **5**, 33155–33162.

48 I. Saptiama, Y. V. Kaneti, Y. Suzuki, K. Tsuchiya, N. Fukumitsu, T. Sakae, J. Kim, Y. M. Kang, K. Ariga and Y. Yamauchi, *Small*, 2018, **14**, 1–14.

49 H. S. Potdar, K. Jun, J. W. Bae, S. Kim and Y. Lee, *Appl. Catal. Gen. A*, 2007, **321**, 109–116.

50 J. W. Geus and R. J. Stol, *J. Colloid Interface Sci.*, 1975, **51**, 449–458.

51 W. Zhou, S. Xiangqian and J. Maoxiang, *Adv. Mater. Res.*, 2014, **936**, 145–148.

52 K. Ada, Y. Sarıkaya and T. Alemdarog, *Ceram. Int.*, 2003, **29**, 513–518.

53 D. S. Tucker, *J. Am. Ceram. Soc.*, 1985, **68**, 163–164.

54 S. Iijima, *Jpn. J. Appl. Phys.*, 1984, **23**, L347–L350.

55 M. I. Martín, L. S. Gómez, O. Milosevic and M. E. Rabanal, *Ceram. Int.*, 2010, **36**, 767–772.

56 M. I. Martín, M. E. Rabanal, L. S. Gómez, J. M. Torralba and O. Milosevic, *J. Eur. Ceram. Soc.*, 2008, **28**, 2487–2494.

57 J. H. Kim, K. Y. Jung, K. Y. Park and S. B. Cho, *Microporous Mesoporous Mater.*, 2010, **128**, 85–90.

58 J. H. Kim, K. Y. Jung and K. Y. Park, *J. Ind. Eng. Chem.*, 2012, **18**, 344–348.

59 L. Qian, L. Li, X. Zhi-yuan and Z. Dong-yuan, *Chem. Res. Chinese Univ.*, 2001, **17**, 143–147.

60 C. Boissière, L. Nicole, C. Gervais, F. Babonneau, M. Antonietti, H. Amenitsch, C. Sanchez and D. Grosso, *Chem. Mater*, 2006, **18**, 5238–5243.

61 L. Zhang, W. Lu, R. Cui and S. Shen, *Mater. Res. Bull.*, 2010, **45**, 429–436.

62 W. Cai, S. Chen, J. Yu, Y. Hu, C. Dang and S. Ma, *Mater. Chem. Phys.*, 2013, **138**, 167–173.

63 G. Xue, X. Huang, N. Zhao, F. Xiao and W. Wei, *RSC Adv.*, 2015, **5**, 13385–13391.

64 X. Wu, B. Zhang, D. Wang and Z. Hu, *Mater. Lett.*, 2012, **70**, 128–131.

65 X. Wu, D. Wang, Z. Hu and G. Gu, *Mater. Chem. Phys.*, 2008, **109**, 560–564.

66 L. Nie, A. Meng, J. Yu and M. Jaroniec, *Sci. Reports - Nat.*, 2013, **3**, 3215.

67 W. Cai, J. Yu, B. Cheng, B. L. Su and M. Jaroniec, *J. Phys. Chem. C*, 2009, **113**, 14739–14746.

68 Y. Hu, H. Ding and C. Li, *Particuology*, 2011, **9**, 528–532.

69 J. Tian, P. Tian, H. Pang, G. Ning, R. F. Bogale, H. Cheng and S. Shen, *Microporous Mesoporous Mater.*, 2016, **223**, 27–34.

70 J. Tian, P. Tian, H. Pang and G. Ning, *Mater. Lett.*, 2018, **210**, 35–38.

71 Y. Wang and W. J. Tseng, *J. Am. Ceram. Soc.*, 2009, **92**, 32–37.

72 M. Chatterjee, D. Enkhtuvshin, B. Siladitya and D. Ganguli, *J. Mater. Sci.*, 1998, **33**, 4937–4942.

73 H. Wang, F. Wang, Q. Liao and X. Li, *Ceram. Int.*, 2015, **41**, 4959–4965.

74 L. M. Zhang, L. Han, H. Zhang, S. S. Shen and W. C. Lu, *Appl. Mech. Mater.*, 2011, **110–116**, 997–1002.

75 X. Jin, Q. Qi, W. Ye, Z. Feng, C. Yan-bin, L. Jie and L. Ye-xiang, *J. Cent. South Univ. Technol.*, 2007, **14**, 773–778.

76 L. Yan-hui, P. Cheng, Z. Wei, B. Ming-Min and R. Ping-Gen, *J. Inorg. Mater.*, 2014, **29**, 1115–1120.

77 J. H. Lee, M. B. Park, J. K. Lee, H. Min and M. K. Song, *J. Am. Chem. Soc.*, 2010, **132**, 12971–12982.

78 H. Cho and J. R. Regalbuto, *Catal. Today*, 2015, **246**, 143–153.

79 B. A. T. Mehrabadi, S. Eskandari, U. Khan, R. D. White and J. R. Regalbuto, in *Advances in Catalysis*, Elsevier Inc., 1st edn., 2017, vol. 61, pp. 1–35.

80 J. Zecevic, G. Vanbutsele, K. P. de Jong and J. A. Martens, *Nature*, 2015, **528**, 245–248.

81 W. van Aarle, W. J. Palenstijn, J. De Beenhouwer, T. Altantzis, S. Bals, K. J. Batenburg and J. Sijbers, *Ultramicroscopy*, 2015, **157**, 35–47.

82 C. V. Chandran and T. Bräuniger, *J. Magn. Reson.*, 2009, **200**, 226–232.

83 D. Massiot, F. Fayon, M. Capron, I. King, S. Le Calvé, B. Alonso, J. O. Durand, B. Bujoli, Z. Gan and G. Hoatson, *Magn. Reson. Chem.*, 2002, **40**, 70–76.

84 G. Burnens, C. Bouchy, E. Guillon and J. A. Martens, *J. Catal.*, 2011, **282**, 145–154.

85 W. Huybrechts, P. A. Jacobs and J. A. Martens, *Appl. Catal. A Gen.*, 2003, **243**, 1–13.

86 G. Busca, *Adv. Catal.*, Elsevier Inc., 1st edn., 2014, **57**, 319-404.

87 P. S. Santos, H. S. Santos and S. P. Toledo, *Mater. Res.*, 2000, **3**, 104–114.

88 K. J. D. MacKenzie, J. Temuujin, M. E. Smith, P. Angerer and Y. Kameshima, *Thermochim. Acta*, 2000, **359**, 87–94.

89 E. Romanova, M. Shari, D. Freude, M. Wark, P. Heitjans and M. Wilkening, *J. Phys. Chem. C*, 2011, **115**, 22770–22780.

90 B. Bbguin, E. Garbowski and M. Primet, *Appl. Catal.*, 1991, **75**, 119–132.

91 P. Burtin, J. P. Brunelle, M. Pijolat and M. Soustelle, *Appl. Catal.*, 1987, **34**, 225–238.

92 J. H. Kang, L. D. Menard, R. G. Nuzzo and A. I. Frenkel, *J. Am. Chem. Soc.*, 2006, **128**, 12068–12069.

93 J. Singh, R. C. Nelson, B. C. Vicente, S. L. Scott and J. A. van Bokhoven, *Phys. Chem. Chem. Phys.*, 2010, **12**, 5668–5677.

94 E. Yoo, T. Okata, T. Akita, M. Kohyama, J. Nakamura and I. Honma, *Nano Lett.*, 2009, **9**, 2255–2259.

95 C. Shakthivel, L. Keerthana and I. Prabha, *Johnson Matthey Technol. Rev.*, 2019, **63**, 122–133.

96 J. G. Irwin and R. L. Moss, *J. Chem. Technol. Biotechnol.*, 1980, **30**, 657–666.

97 L. Spenadel and M. Boudart, *J. Phys. Chem.*, 1960, **64**, 204–207.

98 A. Gholidoust, A. Naderifar, M. Rahmani and S. Sahebdelfar, *Int. J. Mod. Phys. Conf. Ser.*, 2012, **05**, 168–176.

99 J. A. Martens, M. Tielen, P. A. Jacobs and J. Weitkamp, *Zeolites*, 1984, **4**, 98–107.

100 J. A. Martens and P. A. Jacobs, *Zeolites*, 1986, **6**, 334–348.

101 W. Souverijns, L. Rombouts, J. A. Martens and P. A. Jacobs, *Microporous Mater.*, 1995, **4**, 123–130.

102 W. Souverijns, W. Verrelst, G. Vanbutsele, J. A. Martens and P. A. Jacobs, *J. Chem. Soc., Chem. Commun.*, 1994, 14, 1671–1672.

103 C. Zschiesche, D. Himsl, R. Rakoczy, A. Reitzmann, J. Freiding, N. Wilde and R. Gläser, *Chem. Eng. Technol.*, 2018, **41**, 199–204.

104 J. E. Samad, J. Blanchard, C. Sayag, C. Louis and J. R. Regalbuto, *J. Catal.*, 2016, **342**, 213–225.

105 J. A. Martens, R. Parton, L. Uytterhoeven, P. A. Jacobs and G. F. Froment, *Appl. Catal.*, 1991, **76**, 95–116.

106 C. Dai, A. Zhang, C. Song and X. Guo, *Adv. Catal.*, 2018, **63**, 75–115.

107 E. Verheyen, C. Jo, M. Kurttepeli, G. Vanbutsele, E. Gobechiya, T. I. Korányi, S. Bals, G. Van Tendeloo, R. Ryoo, C. E. A. Kirschhock and J. A. Martens, *J. Catal.*, 2013, **300**, 70–80.

108 P. A. Jacobs and J. A. Martens, *Pure Appl. Chem.*, 1986, **58**, 1329–1338.

109 J. A. Martens, E. Benazzi, J. Brendlé, S. Lacombe and R. Le Dred, *Stud. Surf. Sci. Catal.*, 2000, **130**, 293–298.

Chapter 3

Creation of gallium acid and platinum metal sites in bifunctional zeolite hydroisomerization and hydrocracking catalysts by atomic layer deposition

Prepared as full article for submission in peer-reviewed journal: Lisa Geerts, Ranjith K. Ramachandran, Jolien Dendooven, Sambhu Radhakrishnan, Jin Won Seo, Christophe Detavernier, Johan Martens and Sreeprasanth Pulinthanathu Sree

This work was conducted at:

KU Leuven, Center for Surface Chemistry and Catalysis: Characterization and Application Team, Celestijnenlaan 200F, 3001 Leuven, Belgium

Ghent University, Department of Solid State Sciences, CoCooN, Krijgslaan 281/S1, 9000 Ghent, Belgium

KU Leuven, Department of Materials Engineering, Kasteelpark Arenberg 44, 3001 Leuven, Belgium.

Contributions:

L. Geerts, S. P. Sree and J. Martens conceived the idea. L. Geerts performed (S)TEM and analyzed the catalytic data. L. Geerts wrote the article and adapted the manuscript based on the critical comments of S. P. Sree, J. M. Martens, J. Dendooven and R. K. Ramachandran. S. P. Sree performed SEM characterization. J. W. Seo assisted with the STEM characterization. The hydroisomerization experiments were done by G. Vanbutsele. ALD was performed by R. K. Ramachandran.

Atomic Layer Deposition (ALD) is a vacuum technology serving the deposition of a small number of atoms on surfaces. Its use in catalysis is growing. Here we explored the use of ALD for introducing acid and metal sites in zeolites for performing bifunctional catalysis. Plasma-enhanced ALD involving cyclic exposures of the sample to tris(2,2,6,6-tetramethyl-3,5-heptanedionato) gallium ($Ga(TMHD)_3$) vapor and O_2 plasma (Ga-ALD) was used for introducing acid sites. Interestingly, Ga-ALD was found to cause a preferential deposition of Pt nanoparticles on the edges of the COK-14 crystal plates, in contrast to previously published results on Al-ALD. Benefiting from the optimum proximity between the Ga acid and Pt metal sites, it is shown here that Ga-ALD is a way to introduce sufficient acidity in all-silica zeolite COK-14 for obtaining bifunctional catalytic behavior. Hydrogenation-dehydrogenation activity in bifunctional catalysts is typically provided by trace amounts of platinum dispersed on the zeolite. Pt-ALD was applied for finely dispersing platinum on ZSM-5 zeolite. The Pt-ALD involved alternating exposure to trimethyl(methylcyclopentadienyl) platinum (IV) ($MeCpPtMe_3$) precursor and ozone. Pt-ALD method proved to be an efficient way to uniformly disperse ultra-small Pt nanoparticles onto the zeolite. The bifunctional catalytic behavior of ALD-functionalized zeolites was confirmed in the hydroconversion of n-decane model molecule.

Introduction

Atomic Layer Deposition (ALD) is a self-limited growth process that is characterized by alternating exposures of a support to a volatile precursor of the chemical element and a co-reactant.[1–8] The conversion of the precursor to the desired phase can be done by hydrolysis, oxidation or reduction, *etc.*[3] ALD can be used to deposit thin layers of oxides, nitrides, sulfides and metals on various supports.[1–8] Advantages imparted by the self-limiting surface chemistry in each cycle, are the outstanding thickness control, uniformity and conformality.[7,9,10] Beside flat surfaces, ALD can be used for functionalizing porous materials for specific catalytic applications.[1,11] Moreover, by making use of the initial island growth mode often observed for metal ALD processes, ALD can be applied to deposit metal nanoparticles instead of films.[2,7,9]

Hydroconversion reactions of hydrocarbons require bifunctional catalysts having two types of catalytic sites, *viz.* metal and acid. Noble metals provide the (de)hydrogenation function, while the acid function catalyzes isomerization and cracking reactions via alkylcarbenium ion chemistry.[12,13] In this catalysis, the spatial arrangement of the two

types of active sites and their intimacy is critical.[12,13] The control over the ALD deposition can be used for customized synthesis of complex catalysts.[7]

Introduction of acid sites in nanoporous materials by ALD through sequential exposure to trimethylaluminum (TMA) precursor and H_2O (Al-ALD) has already been demonstrated.[1,11,14,15] This Al-ALD process has first been applied to ultrastable Y zeolite and ordered mesoporous Zeotile-4 silica material.[1] The beneficial effect of Al-ALD on the catalysts was revealed in the isomerization and hydrocracking of n-decane.[15] Using Al-ALD, all-silica zeolite COK-14 was rendered active in isomerization and hydrocracking.[16] Enhanced activity upon application of Al-ALD has also been demonstrated for desilicated ZSM-5.[11]

Gallium containing zeolites, with gallium incorporated in the framework or deposited as separate oxide phase have been widely investigated. Ga-based zeolites, mostly ZSM-5, have been reported to be active for alkylation, isomerization, and disproportionation of aromatics, which are acid catalyzed reactions.[17] Gallium-loaded ZSM-5 zeolite catalyst has been used for the dehydrogenation of propane[18], ethane[19] and for the aromatization of n-butane[20]. Furthermore, gallium-loaded ZSM-5 catalyst performs the reduction of NO_x by methane and higher hydrocarbons.[21,22] Incorporation of gallium in zeolites is usually achieved by wet chemical methods such as impregnation and ion exchange.[17] Chemical vapor deposition (CVD) of $GaCl_3$ resulting in the formation of GaO^+ ions and Ga_2O_3 particles in ZSM-5 has been demonstrated.[23] ALD of Ga_2O_3 (Ga-ALD) has previously been applied for depositing thin films. Different precursor and co-reactant combinations have been explored and a wealth of ALD procedures are available, *e.g.* the combination of $Ga(acac)_3$ and water or ozone,[24] $((CH_3)_2GaNH_2)_3$ and oxygen plasma[25], $Ga_2(N(CH_3)_2)_6$ and water[26], gallium tri-isopropoxide (GTIP) and water[27], dimethylgallium isopropoxide (DMGIP) and water[28], trimethylgallium (TMGa) and ozone,[29] and tris(2,2,6,6-tetramethyl-3,5-heptanedionato gallium(III) ($Ga(TMHD)_3$) and O_2 plasma as reactant.[30] Ga-ALD for introduction of gallium onto zeolites has remained largely unexplored.

Pt-ALD is also relevant to bifunctional catalysts. Pt-ALD is attractive to catalysis because nanoparticles are formed instead of a continuous layer according to a nucleation-controlled growth mechanism.[2,7] Islands are formed during the first cycles.[9] Pt-ALD has the advantage to provide atomic-level control and to enable production of well-defined nanoparticles with narrow size distributions.[2,31] The most frequently applied Pt-ALD process uses trimethyl(methylcyclopentadienyl)platinum ($MeCpPtMe_3$) as precursor and O_2 as co-reactant.[2,32] Besides O_2 gas, also O_2 plasma, O_3 gas, H_2 gas, H_2 plasma, N_2 plasma and NH_3 plasma have been described for Pt-ALD.[31,33–36] Co-reactants with relatively short lifetimes such as O_3 gas and plasma

enhance the conversion of the precursor at deposition temperatures below 300 °C.[3,33,37] The choice of the co-reactant will have an impact on the Pt nanoparticle morphology as it influences the nucleation and island growth behavior.[2] O_2 gas provokes stronger lateral growth compared to N_2 plasma, due to a higher tendency for diffusion-driven coalescence processes.[2] The impact of other ALD process parameters such as deposition temperature, co-reactant pressure and number of ALD cycles is well documented.[38–40]

In recent years, Pt-ALD has been applied for catalyst design. Pt-ALD was applied in hard template replication for obtaining a hydrogen evolution electrocatalyst for water electrolysis.[41] A Pt electrocatalyst for electro-oxidation of ethanol and for the hydrogen evolution reaction has been created by Pt-ALD on TiO_2 nanotubes.[42] Another example in electrocatalysis is the synthesis of Pt nanotubes by coating of an anodized aluminum template for polymer electrolyte fuel cell electrodes.[43] Pt nanoparticles on carbon aerogels were prepared to achieve high catalytic activity for the oxidation of CO.[44] Pt nanoparticles on carbon nanotubes were prepared for hydrolysis of ammonia borane,[45] and for proton-exchange membrane fuel cells.[46] Pt catalysts confined in Al_2O_3 nanotubes with an ultrathin coat of Al_2O_3, made by sequential Al- and Pt-ALD on carbon nanocoils followed by removal of the carbon template, have improved activity for hydrogenation of 4-nitrophenol.[47] Another example is Pt nanoparticles on a polymeric (polyacrylonitrile (PAN)) nanofibrous web which has been shown to have a good activity for the reduction of 4-nitrophenol to 4-aminophenol.[48] Pt-ALD on p-type Si nanowire was used for photoelectrochemical water reduction.[49] Pt-ALD has also been applied to MOFs such as MIL-101 and used for the hydrogenation of olefins.[50] In the field of zeolite catalysis, Pt-ALD has been applied on ZSM-5 for hydrogenation of levulinic acid to valeric acid[51] and on zeolite beta for cinnamaldehyde hydrogenation.[52] Pt-ALD has also been applied into K-L zeolite and an excellent activity for n-heptane reforming to aromatics was observed.[53,54] Pt-ALD for preparing bifunctional catalysts for hydrocarbon conversion has further not been reported.

In this work, we investigate the suitability of ALD for introduction of both acid and metal sites in zeolites. The obtained catalysts were evaluated in n-decane isomerization and hydrocracking. Inspired by the approach of Al-ALD for introduction of acid sites, we attempted activation of all-silica COK-14 zeolite by Ga-ALD using $Ga(TMHD)_3$ precursor and O_2 plasma. Without modification, the COK-14 loaded with platinum is inactive in n-decane hydroconversion, owing to a lack of Brønsted acid sites.[16] An increase in activity would confirm the efficacy of the Ga-ALD process. COK-14 possesses 10- and 12-membered ring intersecting channels, which renders it highly interesting for (selective) catalysis in reactions of industrial relevance.[55–58]

Pt-ALD is applied for depositing Pt nanoparticles on acid ZSM-5 zeolite using the low-temperature $MeCpPtMe_3/O_3$ ALD process.[34] ZSM-5 zeolite with a three-dimensional 10-membered ring pore system has been chosen as zeolite support. This is considered an appropriate choice because it has been widely used in several petrochemical reactions due to its high catalytic activity and shape selective properties.[59–64]

Experimental

Preparation of catalysts

All silica zeolite COK-14 (OKO topology) was synthesized according to a reported protocol[65] which involves treatment of as-synthesized IM-12 zeolite (UTL topology) in 12 M HCl solution (VWR Chemicals) in proportions of 50 g HCl solution for 1 g of IM-12 at 95 °C for 48 h followed by filtration, washing with distilled water and drying at 60 °C.

Atomic Layer Deposition of Ga_2O_3 on to COK-14

Ga-ALD was carried out in a home built cold wall ALD chamber using the $Ga(TMHD)_3$ and O_2 plasma process.[30] For each deposition, 300 mg of COK-14 powder was loaded in the ALD reactor and kept at 200 ˚C under vacuum for 2 h. $Ga(TMHD)_3$- vapor and O_2 plasma were alternately introduced to the ALD chamber at pressures of *ca.* 1 Pa. Twenty cycles of ALD were performed, each cycle comprising exposure to $Ga(TMHD)_3$ for 30 s, evacuation under vacuum, and exposure to O_2 plasma for 20 s followed by evacuation. The sample is further named **Ga-ALD-COK-14**.

Platinum incipient wetness impregnation on Ga-ALD-COK-14

Creation of bifunctionality to the Ga-ALD-COK-14 was realized by introducing 0.5 wt% platinum by incipient wetness impregnation using aqueous solution of $Pt(NH_3)_4Cl_2$. Then the zeolite impregnated with the Pt complex was filled into microreactor tubes made of quartz. The sample was subjected to an oxidation via heating at 400 ˚C under O_2 followed by reduction using H_2 at the same temperature. The sample after Pt deposition is denoted as **Pt-IW-Ga-ALD-COK-14**.

Pt-ALD on ZSM-5

Commercial NH_4-ZSM-5 zeolite (CBV 8014 Zeolyst) was used to perform Pt-ALD. The commercial ZSM-5 was calcined in static air at 550 ˚C and is denoted as parent ZSM-5. Pt-ALD was carried out in a home built cold wall ALD chamber, using an ozone-based Pt-ALD process.[34] The Pt precursor used for ALD was trimethyl(methylcyclopentadienyl) platinum (IV) ($MeCpPtMe_3$). 400 mg of parent

ZSM-5 sample was loaded in a molybdenum sample cup, placed on the heated copper block. The sample heated to 200 ˚C was allowed to outgas and thermally equilibrate for at least 1 h under vacuum. A static exposure mode was applied during both ALD half-cycles. The pulse time of the $MeCpPtMe_3$ precursor was 10 s, after which the valves to the pumping system were kept closed for another 20 s, resulting in a total exposure time of 30 s. The same pulse time and exposure time were used for the O_3 also. During the precursor and reactant exposures, the pressure in the chamber increased to *ca.* 50 Pa and 100 Pa, respectively. Twenty cycles were performed. The as-deposited sample was named as **AD-Pt-ALD-ZSM-5.** The as-deposited sample was then exposed to oxidation reduction atmospheres (O_2/H_2) in the quartz reactor tubes at 400 ˚C and referred to as **Pt-ALD-ZSM-5**. For comparison purposes, the same Pt loading, *i.e.* 0.7 wt% platinum as determined using X-ray fluorescence measurements, was introduced via incipient wetness impregnation of $Pt(NH_3)_4Cl_2$ to a part of parent ZSM-5 zeolite followed by oxidation reduction at 400 ˚C. This sample was named as **Pt-IW-ZSM-5.**

Characterization

X-ray fluorescence (XRF) was performed using a Mo X-ray source (at an angle of 45˚ with sample surface) and a silicon drift detector placed at an angle of 52˚ with the sample surface. The fluorescence signal was integrated over a period of 100 s. Quantification of Pt-content of the zeolites was performed by subjecting zeolites impregnated with different amounts of Pt to XRF measurements. Plotting XRF counts against Pt content yielded a linear calibration curve. The successful deposition of Ga_2O_3 was confirmed by XRF measurements.

High resolution scanning electron microscopy (HR-SEM) images were made using a Nova NanoSEM450 (FEI Eindhoven). Zeolite powder was mounted on Al stubs and imaging was performed without any further sample modification. HR images were obtained at very low voltages (<2 kV) by employing a Concentric Backscattered (CBS) detector combined with beam deceleration. Transmission electron microscopy (BF-TEM) and annular dark-field scanning transmission electron microscopy (ADF-STEM) was performed with a probe-corrected transmission electron microscope (ARM200F cold-FEG, JEOL) operated at acceleration voltage of 200 kV. The samples were prepared by dispersing the powder in 2-propanol and placing a few drops of the solution onto the copper TEM grids covered with lacey carbon film (Pacific Grid Tech).

N_2 physisorption isotherms were measured on a Micromeritics TriStar 3000 instrument at liquid nitrogen temperature. The sample was pretreated at 150 °C in N_2 flow for 12 h before measurement.

Powder X-ray diffraction was performed on a STOE STADI P Combi diffractometer with focusing Ge(111) monochromator (Cu Kα1 radiation) in transmission geometry with 140°-curved image plate position sensitive detector (IP PSD) with an internal IP PSD resolution of 0.03°.

Catalytic tests

Hydroisomerization and hydrocracking tests were carried out in a high-throughput reactor with automated online gas chromotography for product analysis. 50 mg of catalyst was loaded in quartz microreactor tubes with an internal dimeter 2 mm. n-decane hydroconversion was carried out over the catalysts at 0.45 MPa pressure. The H_2/n-decane molar ratio in the feed was 214 and the space time, W/F, was 1400 kg s mol^{-1}.

Results and discussion

*Catalytic activation of COK-14 with Ga-*ALD

COK-14 is an all-silica zeolite with thin plate crystal morphology. SEM images reveal the typical dimensions of the plates of several micrometers and thicknesses around 100 nm (Figure 1). The plates generally exhibit rather smooth surfaces with surface terraces. Without modification, COK-14 is catalytically inactive.[16] In the past, COK-14 has been activated using Al-ALD.

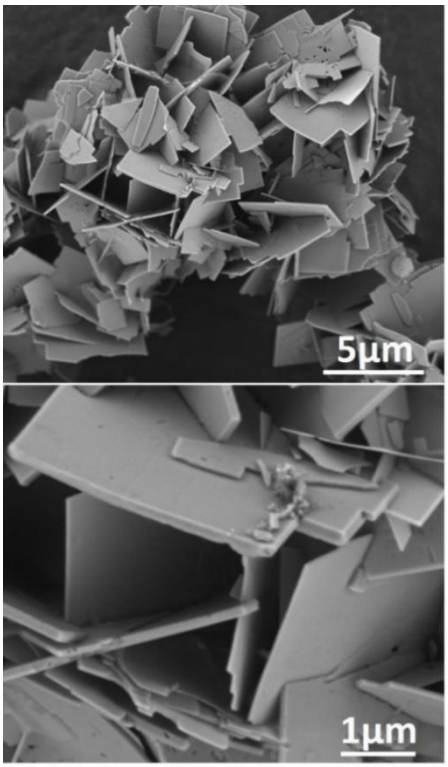

Figure 1. HR-SEM images of COK-14 zeolite.

Ga-ALD was performed to introduce acidity. Subsequently, the sample was loaded with platinum by impregnation with $Pt(NH_3)_4Cl_2$ solution followed by oxidation and reduction to spread platinum particles over the zeolite. The dispersion of Pt particles on the Pt-IW-Ga-ALD-COK-14 sample was investigated via HR-SEM (Figure 2). Interestingly, Pt particles were preferentially positioned at the rim of the zeolite crystals and also at some irregularities and terraces on the surface of the plates (Figure 2). In COK-14, the zeolite micropores run in two directions, both parallel to the plane of the crystal. Only the borders of the plates give access to the intracrystalline pore system. According to SEM (Figure 2) Pt particles are located preferentially close to pore entrances, which is further confirmed by TEM (Figure 3).

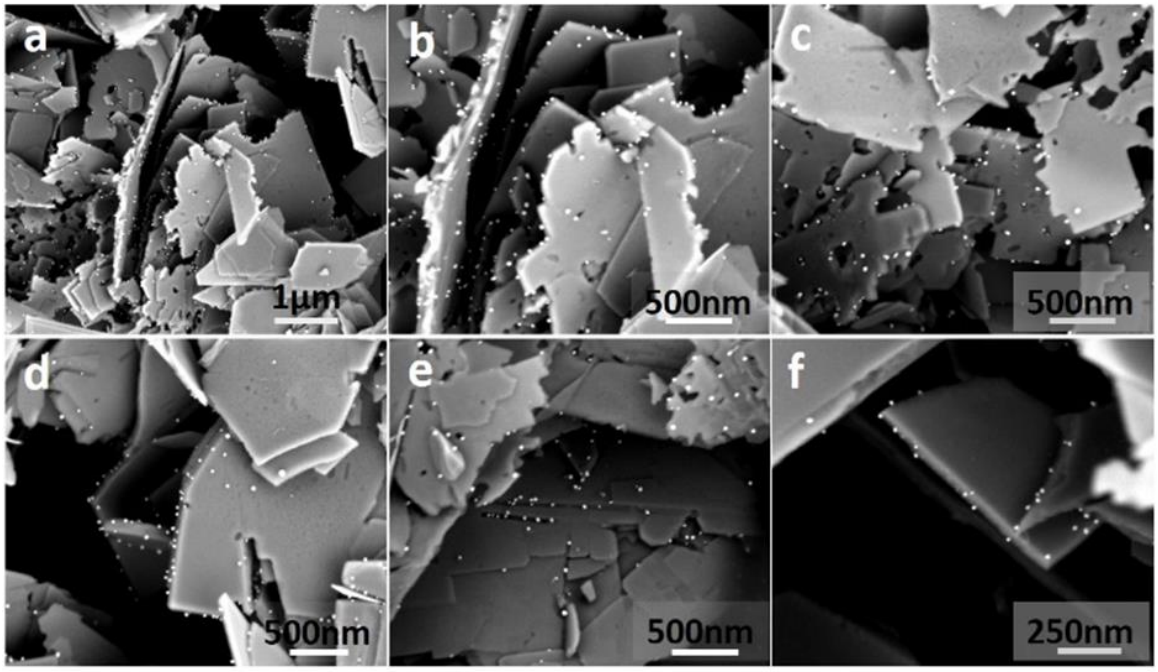

Figure 2. (a-f) HR-SEM of Pt-IW-Ga-ALD-COK-14 catalyst revealing the distribution of Pt particles.

In previous work on activation of COK-14 through alumination with aluminum isopropoxide during milling and Al-ALD, the Pt nanoparticles were uniformly spread over the plates.[16,56] In that work, a thin layer of alumina was spread over the entire surface, serving as anchoring point for Pt nanoparticles. Figure 4 shows SEM images of COK-14 after Al-ALD and Pt IW, prepared as reported in ref [16]. The Pt particles were distributed uniformly on the external surface of the zeolite crystals. In Ga-ALD, SEM images suggest such anchoring points are missing on the large surfaces of the plates. For elemental mapping of the distribution of Ga using energy dispersive X-ray spectroscopy in scanning transmission electron microscopy (STEM-EDS), the loading was below the detection limit. N_2 physisorption performed after Ga-ALD and Pt impregnation showed no notable difference in the total BET surface area and total pore

volume when compared to parent COK-14. This suggests that the catalyst preparation steps, Ga-ALD and Pt impregnation, induced no pore blocking. XRD confirmed structural stability of the catalyst after catalyst preparation and reaction.

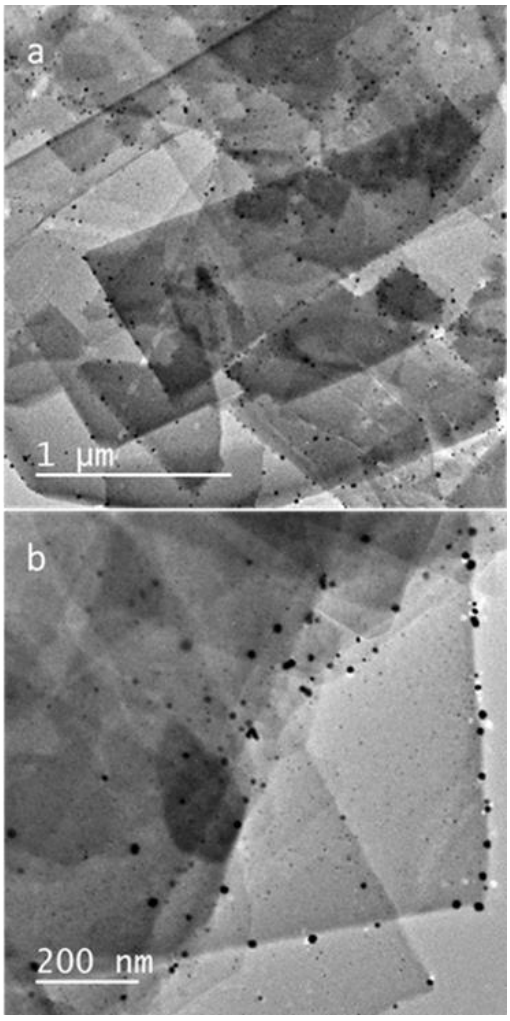

Figure 3. TEM of Pt-IW-Ga-ALD-COK-14 catalyst revealing the distribution of Pt particles.

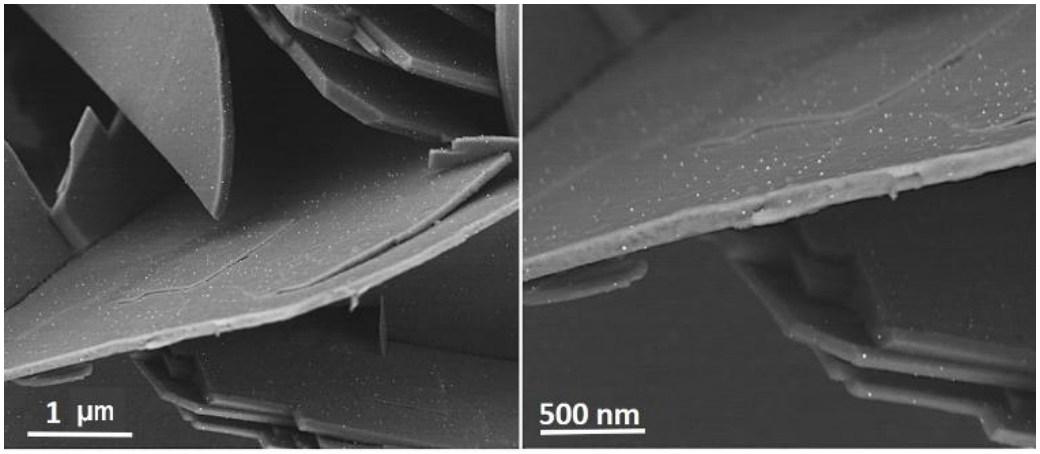

Figure 4. HR-SEM of COK-14 after Al-ALD and Pt IW.

In bifunctional catalysis, the platinum metal particles catalyze dehydrogenation of alkanes to alkenes, which upon adsorption on Brønsted acid sites become alkylcarbenium ions which undergo skeletal rearrangements and β-scission reactions. Isomerized and cracked alkylcarbenium ions are desorbed from the acid sites and thus obtained alkenes are hydrogenated on the metal sites. As a result, because of the presence of large amounts of hydrogen, all reaction products are saturated. This is summarized as a schematic (Figure 5).

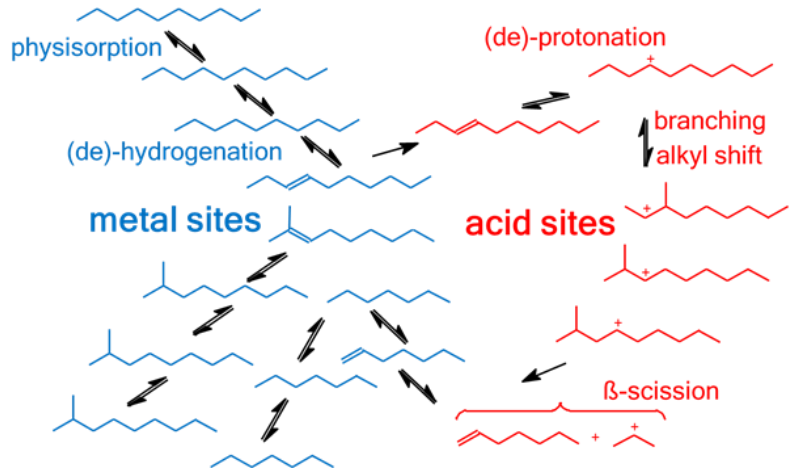

Figure 5. Scheme of reactions in the hydroisomerization and hydrocracking of n-decane on a bifunctional catalyst.

Hydroconversion of n-decane over Pt-IW-Ga-ALD-COK-14 catalyst was performed in a fixed bed reactor with stepwise increasing temperature at constant contact time. The conversion of n-decane is plotted against reaction temperature in Figure 6a. Parent siliceous COK-14 loaded with platinum is inactive in n-decane hydroconversion under these reaction conditions, owing to a lack of Brønsted acid sites.[16] Ga-ALD rendered COK-14 active (Figure 6a). The onset temperature of catalytic activity was 220 °C and full conversion of n-decane was reached at 320 °C (Figure 6a). In a previous publication, COK-14 activated with Al-ALD showed a very similar n-decane conversion curve, with conversion setting in around 205 °C and reaching completion around 310 °C. [16] In the modification with aluminum, it was found that a very low concentration of strong Brønsted acid sites, retaining pyridine at 200 °C of 5 μmol/g was sufficient to reach such activity.[16] The present results show that such traces of acidity can also be introduced using Ga-ALD. The penetration of the metalorganic $Ga(TMHD)_3$ precursor in the micropores of COK-14 is expected to be very limited, and deposition most likely occurs on the external surface and near the pore openings.

A normal alkane like n-decane undergoes skeletal branching as primary reaction. The more branchings introduced, the more the molecule is sensitive to cracking via β-scission of alkylcarbenium ions. Skeletal isomerization and cracking are consecutive

reactions. Consequently, the yield of skeletal isomers from n-decane plotted against conversion of the feed passes through a maximum. High yields of feed isomers are indicative of a well-balanced bifunctional catalyst.[12] The yield of C_{10} skeletal isomers and cracked products is presented in Figure 6b. A maximum isomerization yield of *ca.* 70% was achieved at *ca.* 80% conversion, which is quite high compared to other large pore zeolites, like ultrastable Y zeolite, which do not surpass 60% isomerization yield in n-decane hydroconversion under similar reaction conditions.[66–69] The remarkable activity and selectivity for hydroconversion of n-decane in ALD-modified samples can be explained by the optimum proximity of acid sites and Pt metal sites, both located at the edges of the crystals exposing the micropore openings.[12]

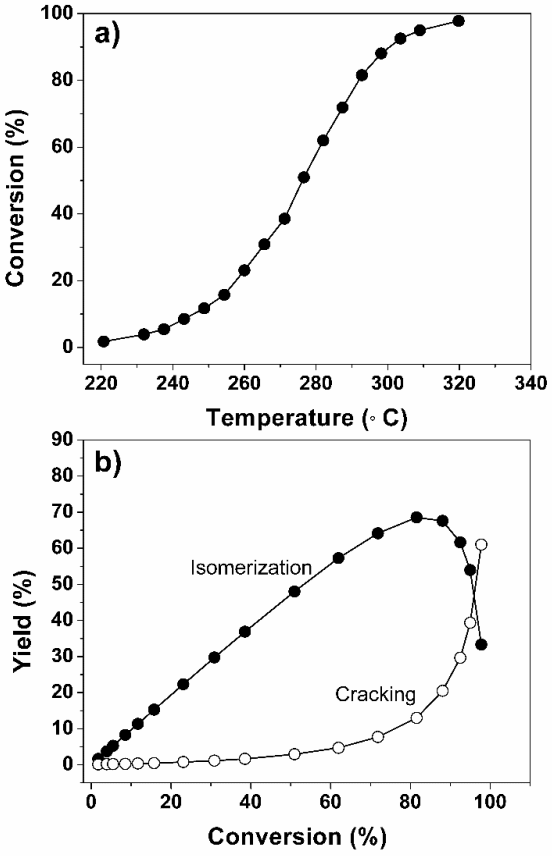

Figure 6. (a) n-decane conversion against reaction temperature on Pt-IW-Ga-ALD-COK-14 and (b) C_{10} isomerization yield (closed symbols) and cracking products yield (open symbols) against n-decane conversion.

Among the isomers, monobranched C_{10} isomers and multi-branched C_{10} isomers were formed in consecutive reactions (Figure 7a). In the reaction product fraction of monomethyl branched isomers, 3-methylnonane and 4-methylnonane were preferentially formed initially (Figure 7b). Kinetic suppression of 2-methylnonane formation is characteristic of alkylcarbenium ion chemistry in absence of shape selectivity, while this isomer is preferentially formed in medium pore zeolites such as

ZSM-22 and ZSM-5.[67,70] The refined constrained index (CI°) calculated from the ratio of 2-methylnonane to 5-methylnonane yield at 5% n-decane conversion, probes the presence of shape selectivity. CI° of COK-14 modified with Ga-ALD was 1.1, which is a typical value for large pore zeolites.[71,72] Similar CI° values were obtained with COK-14 samples activated with Al-ALD and with aluminum isopropoxide. [16,56] COK-14 has a pore system with intersecting 10- and 12-membered ring channels. Apparently, the catalytic activity is concentrated in the largest micropores and the smaller channel system does not contribute. It seems difficult to introduce acid sites using ALD in 10-MR pores, as observed earlier for Silicalite-1, a siliceous zeolite with MFI framework type.[73]

Hydrocracking to lower molecular weight products is a consecutive reaction to isomerization. The yield of cracked products according to carbon numbers at 35% hydrocracking is depicted in Figure 7c. This distribution of yields of cracked products divided according to carbon number on molar basis is fairly symmetric, showing that molecules are cracked only once. The formation of some C1, C2, C8 and C9 products can be explained by hydrogenolysis on the platinum metal. It confirms the catalyst has an excess of noble metal compared to acidity.

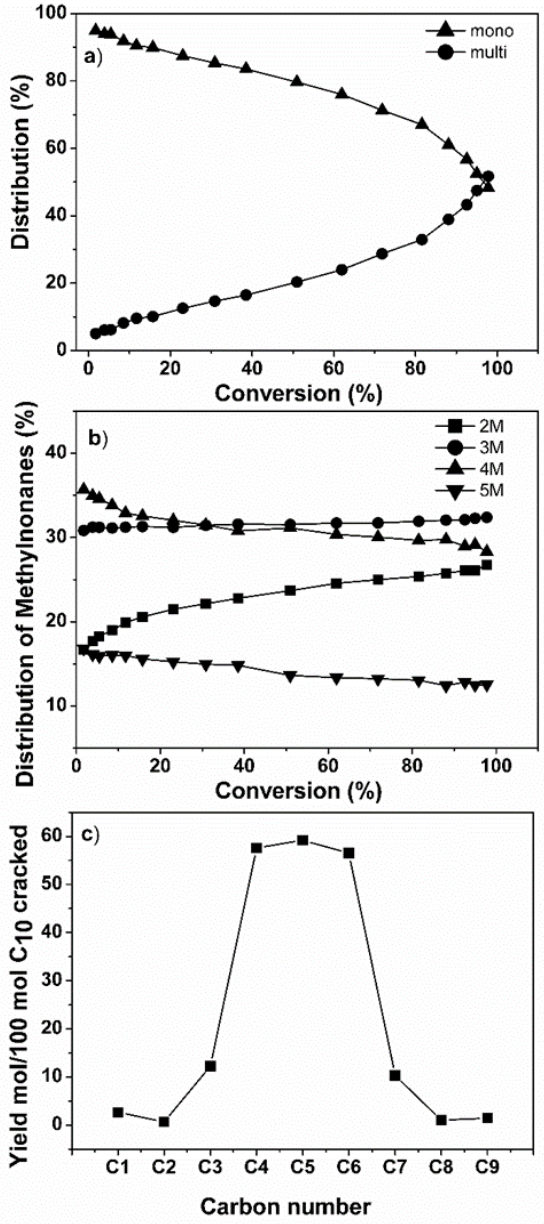

Figure 7. (a) Distribution of C_{10} skeletal isomers according to the number of branchings in n-decane hydroconversion on Pt-IW-Ga-ALD-COK-14; (b) Distribution of methylnonane isomers against n-decane conversion ; (c) Molar yields of carbon number fractions per 100 mol of n-decane cracked at 35% n-decane hydrocracking

Catalytic activation of ZSM-5 with Pt-ALD

The use of Pt-ALD for preparing bifunctional catalysts was explored on another type of zeolite: ZSM-5. The parent commercial ZSM-5 sample with Si/Al atomic ratio of 40 was in NH_4-form. The sample was subjected to 20 ALD cycles using $MeCpPtMe_3$ precursor and ozone (O_3). The final Pt content of the sample, estimated with XRF, amounted to 0.7 wt%. HR-SEM of the as-deposited sample (AD-Pt-ALD-ZSM-5) showed hardly any presence of Pt on the smooth surfaces of the aggregated zeolite crystals at magnifications around 350 k (Figure 8a). When observed under annular dark-field STEM (ADF-STEM) at three times higher magnification, uniform and homogeneously dispersed Pt particles on the zeolite particles were visualized. In Figure 8b and c, bright dots represent Pt particles and the grey area presents the zeolite. These Pt particles were in the size range of 1-2 nm. For catalytic testing, pretreatment at higher temperature is needed to desorb ammonia from the acid sites. A typical pretreatment is by oxidation with molecular oxygen and reduction with hydrogen at 400 °C. The sample, referred to as Pt-ALD-ZSM-5, showed the presence of Pt nanoparticles in HR-SEM as well as ADF-STEM. Figure 9 a-d reveals the presence of dispersed Pt particles having sizes larger than the as-deposited sample. The size of Pt particles on Pt-ALD-ZSM-5 sample is in the range of 2-4 nm. The coarsening of ALD-grown Pt nanoparticles induced by oxidation and reduction treatments was investigated before by Solano *et al.*[74]

For comparison, parent ZSM-5 was loaded with platinum using incipient wetness impregnation of $Pt(NH_3)_4Cl_2$ complex, followed by oxidation and reduction at 400 °C. The sample was named Pt-IW-ZSM-5. HR-SEM, TEM and ADF-STEM (Figure 10) revealed rather inhomogeneous deposition of Pt with large particle sizes up to 15-20 nm.

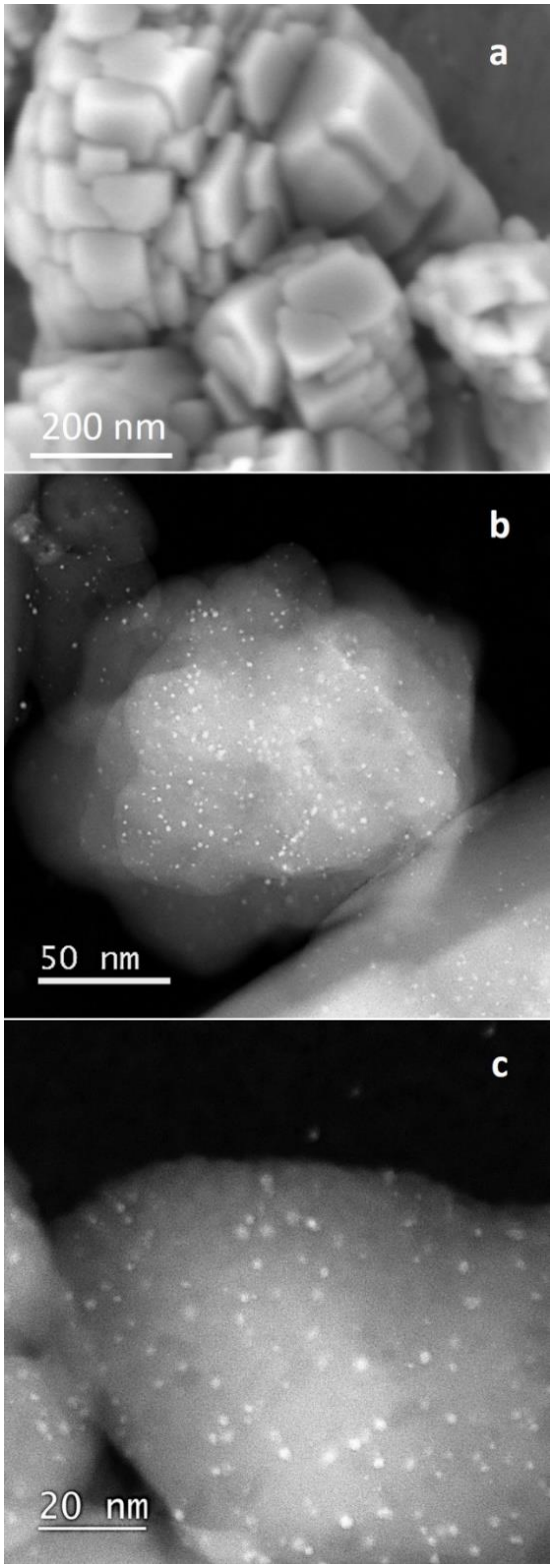

Figure 8. (a) HR-SEM and (b,c) ADF-STEM of as-deposited AD-Pt-ALD-ZSM-5 samples at different magnifications. (a) at 350k and (b,c) at 1000k and 2000k.

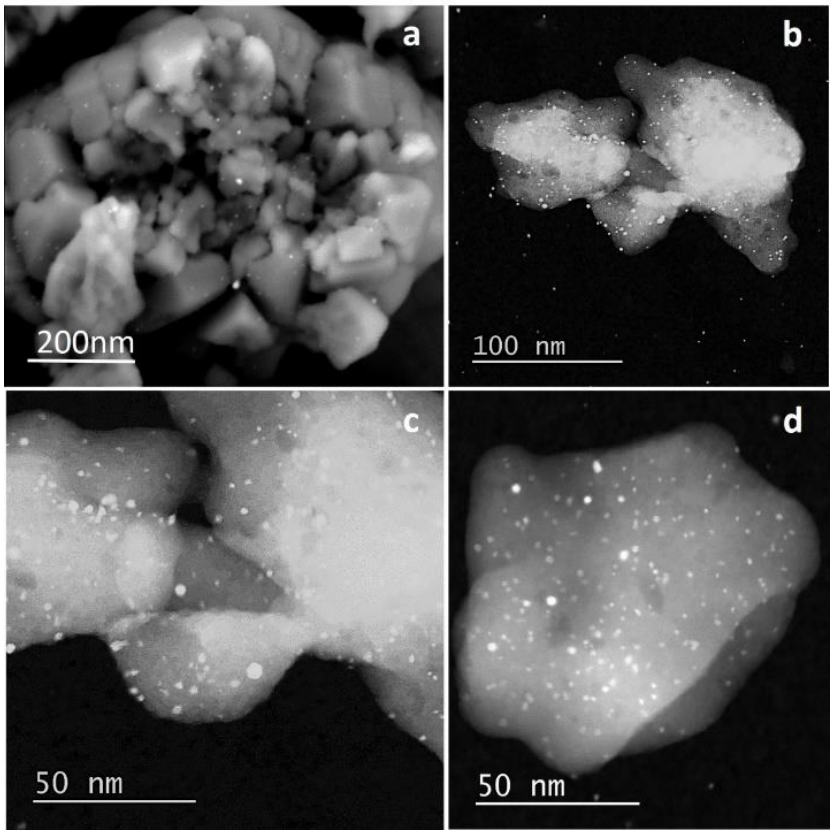

Figure 9. (a) HR-SEM and (b,c,d) ADF-STEM of Pt-ALD-ZSM-5 samples at different magnifications (a) at 350k and (b) 800k (c,d) at 1500k.

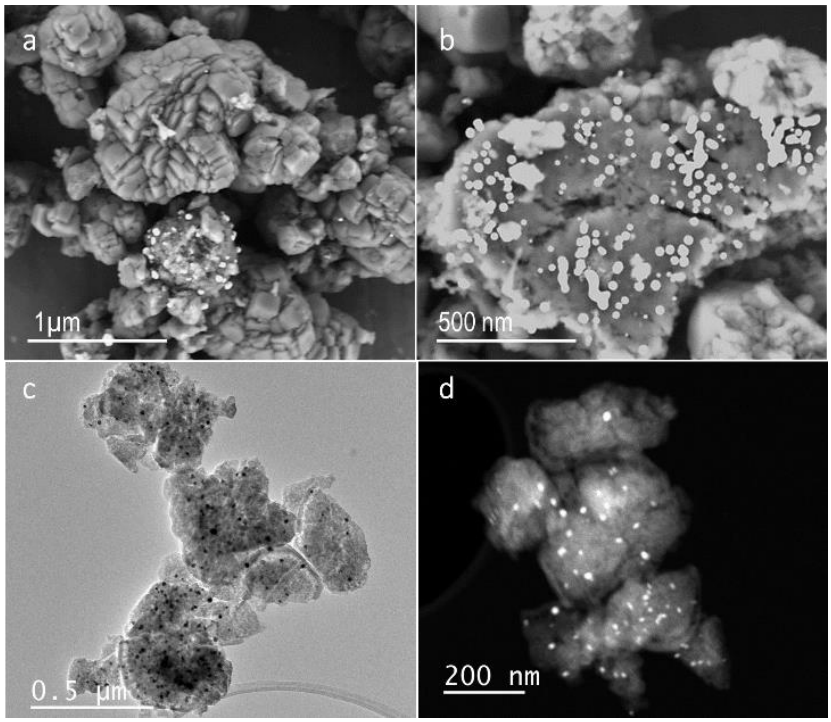

Figure 10. HR-SEM of Pt-IW-ZSM-5 samples at different magnifications of (a) 100k and (b) 200k. (c) TEM image at 12k and (d) ADF-STEM image at 200k on similar regions as shown in (a-b).

Two different configurations of detectors were used to study the position of the nanoparticles in the ZSM-5 zeolite. STEM images using ADF detectors probing the entire particles are shown in Figure 11a and 11c. Figure 11b and 11d show images obtained using secondary electrons (SE) detectors to reveal the surface topography of the sample. Visibility of Pt nanoparticles in the SE image indicates they are on or very near the surface. Nanoparticles were observed to move and agglomerate upon beam exposure, as shown in Figure 12. Movement and coalescence has been observed before for platinum clusters deposited on a thin single crystalline γ-Al_2O_3 film grown by oxidation of NiAl(110) and for Pt particles prepared by colloidal methods on an amorphous carbon grid.[75,76]

The characterization with electron microscopy revealed Pt-ALD to be superior to impregnation for dispersing platinum on this commercial ZSM-5 zeolite sample.

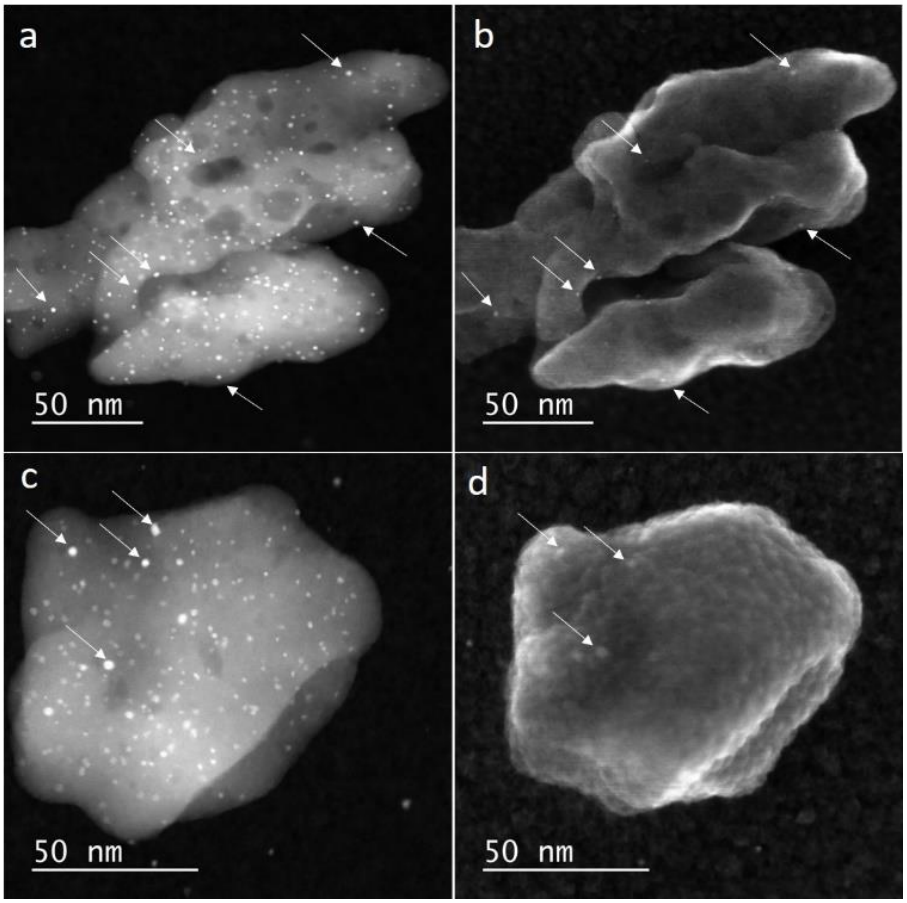

Figure 11. (a,c) ADF-STEM of the as-deposited AD-Pt-ALD-ZSM-5 and Pt-ALD-ZSM-5 and (b,d) Secondary electron images (SEI) images of the same crystals respectively.

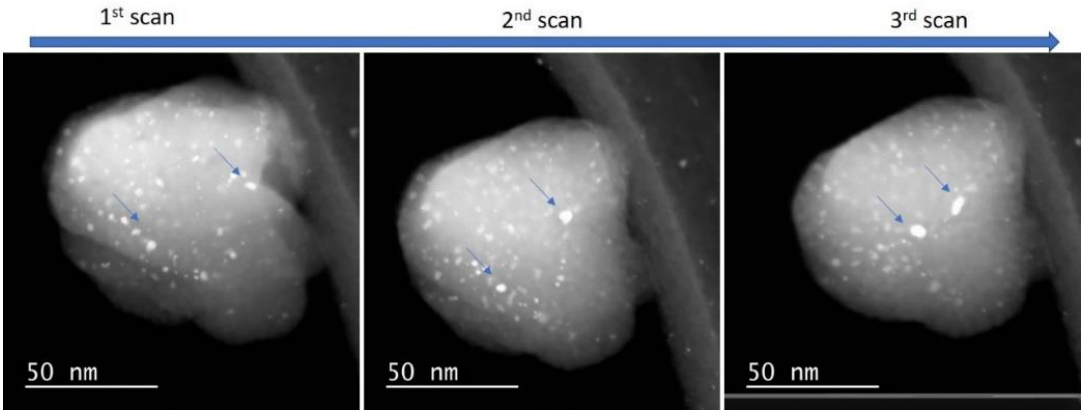

Figure 12. ADF-STEM of Pt-ALD-ZSM-5 in three consecutive scans showing migration and clustering of Pt particles under the influence of electron beam.

n-Decane isomerization and hydrocracking was performed on bifunctional ZSM-5 catalyst activated with Pt-ALD and incipient wetness impregnation. Pt-ALD-ZSM-5 was slightly more active than Pt-IW-ZSM-5 as it converted more n-decane at the same reaction temperature (Figure 13a). Pt-ALD-ZSM-5 also exhibited a slightly higher hydroisomerization yield compared to Pt-IW-ZSM-5 (Figure 13b). ZSM-5 is a medium-pore zeolite which exhibits shape selective effects in hydroisomerization/hydrocracking of long-chain n-alkanes.[67,70,77–79] One pronounced shape selectivity effect is the preferential formation of 2-methylnonane among the monomethylbranched skeletal isomers of n-decane (Figure 14). The sample prepared with Pt-ALD showed a higher selectivity for 2-methylnonane compared to the incipient wetness impregnated sample and the refined constraint index, CI° was higher, *viz.* 9.9, compared to 7.2.

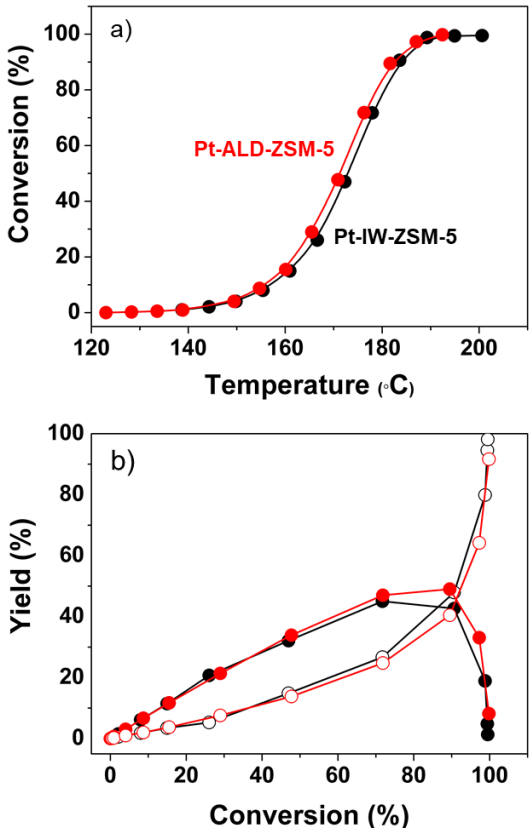

Figure 13. (a) n-decane conversion against reaction temperature on Pt-IW-ZSM-5 and Pt-ALD-ZSM-5. (b) Isomerization yield (closed symbols) and cracking yield (open symbols) against n-decane conversion on the same catalysts.

The molar distribution of cracked product yields according to carbon numbers (Figure 15) displays the characteristic "M" shape, with a suppression of central cracking of the C10 molecules into C5 fragments. This was similar for the two catalysts. Among the cracking patterns, formation of C4 and C6 prevailed over formation of C5 fragments and C3 plus C7 fragments. These n-decane isomerization and hydrocracking experiments confirmed that Pt-ALD is an adequate method for loading platinum on aluminosilicate zeolites for performing bifunctional catalysis.

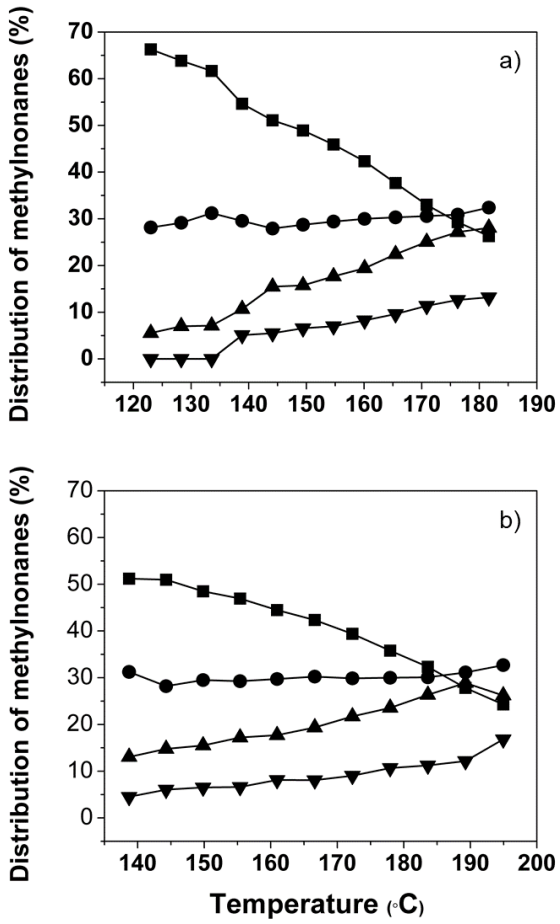

Figure 14. Distribution of methylnonane isomers obtained from n-decane skeletal isomerization on, (a) Pt-ALD-ZSM-5 and (b) Pt-IW-ZSM-5 (top to bottom: 2-methyl, 3-methyl, 4-methyl and 5-methylnonane).

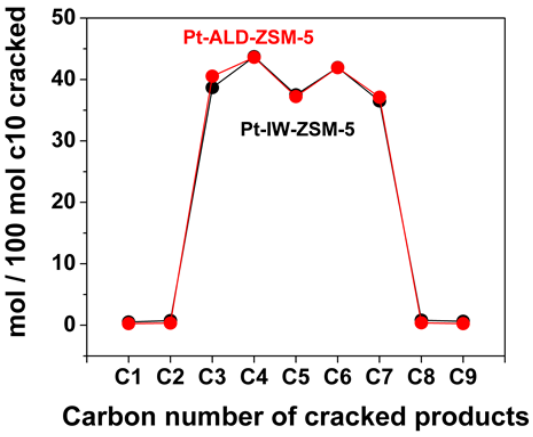

Figure 15. Carbon number distribution of cracked products at 35% n-decane hydroconversion on Pt-IW-ZSM-5 (black) and Pt-ALD-ZSM-5 (red).

Conclusions

ALD is an efficient tool to create catalytically active acid sites and to deposit finely dispersed platinum on zeolites. Ga-ALD, using $Ga(TMHD)_3$ and O_2 plasma, is shown to introduce acid sites in COK-14, an all-silica zeolite that originally lacks acid sites. Gallium was most likely deposited on the external surface and edges of the zeolite particles and created preferential sites for platinum deposition at the edges. This resulted in optimum proximity of metal and acid sites, which was beneficial for the activity and selectivity in the hydroconversion of n-decane. The maximum isomerization yield of *ca.* 70% exceeds that of other large pore zeolites. Pt-ALD using $MeCpPtMe_3$ and ozone was applied to engineer Pt sites on ZSM-5 zeolite and resulted in finely dispersed Pt nanoparticles of 1-2 nm. After heat treatment under oxidation and reduction conditions, the Pt nanoparticles were in the range of 2-4 nm due to thermal sintering. The Pt-ALD-ZSM-5 sample has been proven to be an excellent catalyst for n-decane hydroisomerization. A ZSM-5 catalyst with Pt deposited via incipient wetness impregnation was equally active and selective. The ALD method demonstrated here can be extended to many other catalysts of academic and industrial significance.

Acknowledgements

This work is supported by Research Foundation Flanders (G0A5417N) and the Flemish Government through Long-term structural funding (Methusalem). It was also supported by the Flemish Hercules Foundation (AKUL/13/19), and the Special Research Fund of Ghent University (01G01019). J.D. and R.K.R. acknowledge the Research Foundation Flanders for a personal fellowship.

References

1 C. Detavernier, J. Dendooven, S. Pulinthanathu Sree, K. F. Ludwig and J. A. Martens, *Chem. Soc. Rev.*, 2011, **40**, 5242–5253.

2 J. Dendooven, R. K. Ramachandran, E. Solano, M. Kurttepeli, L. Geerts, G. Heremans, J. Rongé, M. M. Minjauw, T. Dobbelaere, K. Devloo-Casier, J. A. Martens, A. Vantomme, S. Bals, G. Portale, A. Coati and C. Detavernier, *Nat. Commun.*, 2017, **8**, 1074.

3 H. C. M. Knoops, S. E. Potts, A. A. Bol and W. M. M. Kessels, in *Handbook of Crystal Growth: Thin Films and Epitaxy: Second Edition*, ed. T. Kuech, Elsevier, 2015, pp. 1101–1134.

4 M. Ahonen, M. Pessa, T. Suntola and O. L. Ab, *Thin Solid Films*, 1980, **65**, 301–307.

5 S. M. George, *Chem. Rev.*, 2010, 111–131.

6 R. L. Puurunen, *J. Appl. Phys.*, 2005, **97**, 121301.

7 B. J. O'Neill, D. H. K. Jackson, J. Lee, C. Canlas, P. C. Stair, C. L. Marshall, J. W. Elam, T. F. Kuech, J. A. Dumesic and G. W. Huber, *ACS Catal.*, 2015, **5**, 1804–1825.

8 T. Suntola, J. Antson, Method for producing compound thin films, 4058430, 1977.

9 B. Sels and M. Van de Voorde, Eds., *Nanotechnology in Catalysis: Application in the Chemical Industry, Energy Development and Environment Protection*, Wiley VCH, 2017.

10 V. Cremers, R. L. Puurunen and J. Dendooven, *Appl. Phys. Rev.*, 2019, **6**, 1–43.

11 S. P. Sree, J. Dendooven, P. C. M. M. Magusin, K. Thomas, J. P. Gilson, F. Taulelle, C. Detavernier and J. A. Martens, *Catal. Sci. Technol.*, 2016, **6**, 6177–6186.

12 J. Zecevic, G. Vanbutsele, K. P. de Jong and J. A. Martens, *Nature*, 2015, **528**, 245–248.

13 J. E. Samad, J. Blanchard, C. Sayag, C. Louis and J. R. Regalbuto, *J. Catal.*, 2016, **342**, 213–225.

14 Y. Wu, Z. Lu, L. Emdadi, S. C. Oh, J. Wang, Y. Lei, H. Chen, D. T. Tran, I. C. Lee and D. Liu, *J. Catal.*, 2016, **337**, 177–187.

15 S. P. Sree, J. Dendooven, T. I. Koranyi, G. Vanbutsele, K. Houthoofd, D. Deduytsche, C. Detavernier and J. A. Martens, *Catal. Sci. Technol.*, 2011, 218–221.

16 E. Verheyen, S. Pulinthanathu Sree, K. Thomas, J. Dendooven, M. De Prins, G. Vanbutsele, E. Breynaert, J. P. Gilson, C. E. A. Kirschhock, C. Detavernier and J. A. Martens, *Chem. Commun.*, 2014, **50**, 4610–4612.

17 R. Fricke, H. Kosslick, G. Lischke and M. Richter, *Chem. Rev.*, 2000, **100**, 2303–2405.

18 Z. Shen, J. Liu, H. Xu, Y. Yue, W. Hua and W. Shen, *Appl. Catal. A Gen.*, 2009, **356**, 148–153.

19 J. Wang, F. Zhang, W. Hua, Y. Yue and Z. Gao, *Catal. Commun.*, 2012, **18**, 63–67.

20 R. Le Van Mao, J. Yao, L. A. Dufresne and R. Carli, *Catal. Today*, 1996, **31**, 247–255.

21 J. N. Armor, *Catal. Today*, 1996, **31**, 191–198.

22 E. Kikuchi, M. Ogura, I. Terasaki and Y. Goto, *J. Catal.*, 1996, **161**, 465–470.

23 B. S. Kwak and W. M. H. Sachtler, *J. Catal.*, 1994, 145, 456–463.

24 M. Nieminen and E. Rauhalab, *J. Mater. Chem.*, 1996, **6**, 27–31.

25 F. K. Shan, G. X. Liu, W. J. Lee, G. H. Lee, I. S. Kim, F. K. Shan, G. X. Liu, W. J. Lee, G. H. Lee, I. S. Kim and B. C. Shin, *J. Appl. Phys.*, 2005, **98**, 023504.

26 C. L. Dezelah, J. Niinisto, K. Arstila, L. Niinisto and C. H. Winter, *Chem. Mater.*, 2006, **18**, 471–475.

27 D. Choi, K. Chung and J. Park, *Thin Solid Films*, 2013, **546**, 31–34.

28 B. H. Lee, K. Kim, J. Woo, D. Jun, Y. Park, Y. Kim, H. W. Lee and Y. J. Cho, *Chem. Vap. Depos.*, 2011, 191–197.

29 D. J. Comstock and W. J. Elam, *Chem. Mater.*, 2012, **24**, 4011–4018.

30 R. K. Ramachandran, J. Dendooven, J. Botterman, S. Pulinthanathu Sree, D. Poelman, J. A. Martens, H. Poelman and C. Detavernier, *J. Mater. Chem. A*, 2014, **2**, 19232–19238.

31 W. Setthapun, H. Feng, P. C. Stair, J. T. Miller, C. L. Marshall, W. D. Williams, F. H. Ribeiro, S. M. Kim, E. A. Stach, J. W. Elam, F. A. Rabuffetti and K. R. Poeppelmeier, *J. Phys. Chem. C*, 2010, **114**, 9758–9771.

32 T. Aaltonen, M. Ritala, T. Sajavaara, J. Keinonen and M. Leskelä, *Chem. Mater.*, 2003, **15**, 1924–1928.

33 H. C. M. Knoops, A. J. M. Mackus, M. E. Donders, M. C. M. van de Sanden, P. H. L. Notten and W. M. M. Kessels, *Electrochem. Solid-State Lett.*, 2009, **12**, G34.

34 J. Dendooven, R. K. Ramachandran, K. Devloo-Casier, G. Rampelberg, M. Filez, H. Poelman, G. B. Marin, E. Fonda and C. Detavernier, *J. Phys. Chem. C*, 2013, **117**, 20557–20561.

35 L. Baker, A. S. Cavanagh, J. Yin, S. M. George, A. Kongkanand and F. T. Wagner, *Appl. Phys. Lett.*, 2012, **101**, 1–5.

36 D. Longrie, K. Devloo-Casier, D. Deduytsche, S. Van den Berghe, K. Driesen and C. Detavernier, *ECS J. Solid State Sci. Technol.*, 2012, **1**, Q123–Q129.

37 L. Baker, A. S. Cavanagh, D. Seghete, S. M. George, A. J. M. Mackus, W. M. M. Kessels, Z. Y. Liu and F. T. Wagner, *J. Appl. Phys.*, 2011, **109**, 084333.

38 C. Wang, Y. Lin, L. Marks, L. Hu, K. Poeppelmeier and P. Stair, *J. Phys. D. Appl. Phys.*, 2017, **50**, 415301.

39 F. Grillo, H. Van Bui, D. La Zara, A. A. I. Aarnink, A. Y. Kovalgin, P. Kooyman, M. T. Kreutzer and J. R. Van Ommen, *Small*, 2018, **14**, 1800765.

40 F. Grillo, H. Van Bui, J. A. Moulijn, M. T. Kreutzer and R. J. van Ommen, *J. Phys. Chem. Lett.*, 2017, **8**, 975–983.

41 S. Pulinthanathu Sree, J. Dendooven, L. Geerts, R. K. Ramachandran, E. Javon, F. Ceyssens, E. Breynaert, C. E. A. Kirschhock, R. Puers, T. Altantzis, G. Van Tendeloo, S. Bals, C. Detavernier and J. A. Martens, *J. Mater. Chem. A*, 2017, **5**, 19007–19016.

42 L. Assaud, J. Schumacher, A. Tafel, S. Bochmann, S. Christiansen and J. Bachmann, *J. Mater. Chem. A*, 2015, **3**, 8450–8458.

43 S. Galbiati, A. Morin and N. Pauc, *Electrochim. Acta*, 2014, **125**, 107–116.

44 J. S. King, A. Wittstock, J. Biener, S. O. Kucheyev, Y. M. Wang, T. F. Baumann, S. K. Giri, A. V Hamza, M. Baeumer and S. F. Bent, *Nano Lett.*, 2008, **8**, 2405–2409.

45 J. Zhang, C. Chen, S. Chen, Q. Hu, Z. Gao, Y. Li and Y. Qin, *Catal. Sci. Technol.*, 2017, **7**, 322–329.

46 C. Liu, C.-C. Wang, C.-C. Kei, Y.-C. Hsueh and T.-P. Perng, *Small*, 2009, **5**, 1535–1538.

47 M. Wang, Z. Gao, B. Zhang, H. Yang, Y. Qiao, S. Chen, H. Ge, J. Zhang and Y. Qin, *Chem. - A Eur. J.*, 2016, **22**, 8385.

48 A. Celebioglu, K. S. Ranjith, H. Eren, N. Biyikli and T. Uyar, *Sci. Rep.*, 2017, **7**, 1–10.

49 N. P. Dasgupta, C. Liu, S. Andrews, F. B. Prinz and P. Yang, *J. Am. Chem. Soc.*, 2013, **135**, 12932–12935.

50 K. Leus, J. Dendooven, N. Tahir, R. Ramachandran, M. Meledina, S. Turner, G. Van Tendeloo, J. Goeman, J. Van der Eycken, C. Detavernier and P. Van Der Voort, *Nanomaterials*, 2016, **6**, 45.

51 X. Gu, Z. Bin, H. Liang, H. Ge, H. Yang and Y. Qin, *J. Fuel Chem. Technol.*, 2017, **45**, 714–722.

52 M. Lashdaf, J. Lahtinen, M. Lindblad, M. Tiitta, T. Venäläinen and H. Österholm, *Stud. Surf. Sci. Catal.*, 2004, **154**, 1708–1713.

53 D. Xu, B. Wu, P. Ren, S. Wang, C. Huo, B. Zhang, W. Guo, L. Huang, X. Wen, Y. Qin, Y. Yang and Y. Li, *Catal. Sci. Technol.*, 2017, **7**, 1342–1350.

54 D. Xu, S. Wang, B. Wu, B. Zhang, Y. Qin, C. Huo, L. Huang, X. Wen, Y. Yang and Y. Li, *ACS Appl. Mater. Interfaces*, 2019, **11**, 29858–29867.

55 T. Willhammar, J. Sun, W. Wan, P. Oleynikov, D. Zhang, X. Zou, M. Moliner, J. Gonzalez, C. Martínez, F. Rey and A. Corma, *Nat. Chem.*, 2012, **4**, 188–194.

56 M. De Prins, E. Verheyen, G. Vanbutsele, S. P. Sree, K. Thomas, J. P. Gilson, J. Vleugels, C. E. A. Kirschhock and J. A. Martens, *Catal. Today*, 2019, **334**, 3–12.

57 R. Simancas, D. Dari, N. Velamazan, M. T. Navarro, A. Cantí, J. L. Jordá, G. Sastre, A. Corma and F. Rey, *Science*, 2010, **330**, 1219–1223.

58 D. L. Dorset, S. C. Weston and S. S. Dhingra, *J. Phys. Chem. B*, 2006, **110**, 2045–2050.

59 Y. Ji, H. Yang and W. Yan, *Catalysts*, 2017, **7**, 367.

60 L. Zoubida and B. Hichem, in *Nanocrystals and Nanostructures*, ed. C. M. Simonescu, 2018, p. 62.

61 S. Inagaki, S. Shinoda, S. Hayashi, T. Wakihara, H. Yamazaki, J. N. Kondo and Y. Kubota, *Catal. Sci. Technol.*, 2016, **6**, 2598–2604.

62 L. Tan, X. Guo, X. H. Gao and N. Tsubaki, *Catalysts*, 2019, **9**, 17.

63 G. T. Kokotailo, P. Chu, S. L. Lawton and W. M. Meirer, *Nature*, 1978, **275**, 119–120.

64 L. Meng, X. Zhu, W. Wannapakdee, R. Pestman, M. G. Goesten, L. Gao, A. J. F. van Hoof and E. J. M. Hensen, *J. Catal.*, 2018, **361**, 135–142.

65 E. Verheyen, L. Joos, K. Van Havenbergh, E. Breynaert, N. Kasian, E. Gobechiya, K. Houthoofd, C. Martineau, M. Hinterstein, F. Taulelle, V. Van Speybroeck, M. Waroquier, S. Bals, G. Van Tendeloo, C. E. A. Kirschhock and J. A. Martens, *Nat. Mater.*, 2012, **11**, 1059–1064.

66 J. A. Martens, E. Benazzi, J. Brendlé, S. Lacombe and R. Le Dred, *Stud. Surf. Sci. Catal.*, 2000, **130**, 293–298.

67 J. A. Martens, R. Parton, L. Uytterhoeven, P. A. Jacobs and G. F. Froment, *Appl. Catal.*, 1991, **76**, 95–116.

68 R. Parton, L. Uytterhoeven, J. A. Martens and P. A. Jacobs, *Appl. Catal.*, 1991, **76**, 131–142.

69 G. F. Froment, *Catal. Today*, 1987, 455–473.

70 J. Weitkamp, P. A. Jacobs and J. A. Martens, *Appl. Catal.*, 1983, **8**, 123–141.

71 W. Souverijns, L. Rombouts, J. A. Martens and P. A. Jacobs, *Microporous Mater.*, 1995, **4**, 123–130.

72 J. A. Martens and P. A. Jacobs, *Zeolites*, 1986, **6**, 334–348.

73 S. P. Sree, J. Dendooven, T. I. Korányi, G. Vanbutsele, K. Houthoofd, D. Deduytsche, C. Detavernier and J. A. Martens, *Catal. Sci. Technol.*, 2011, **1**, 218–221.

74 E. Solano, J. Dendooven, R. K. Ramachandran, K. Van de Kerckhove, T. Dobbelaere, D. Hermida-Merino and C. Detavernier, *Nanoscale*, 2017, **9**, 13159–13170.

75 S. A. Nepijko, M. Klimenkov, H. Kuhlenbeck and H. J. Freund, *J. Vac. Sci. Technol. a-Vacuum Surfaces Film.*, 1999, **17**, 577–583.

76 N. J. Long, R. F. Marzke, M. Mckelvy and W. S. Glaunsinger, *Ultramiscroscopy*, 1986, **20**, 15–20.

77 J. A. Martens, M. Tielen, P. A. Jacobs and J. Weitkamp, *Zeolites*, 1984, **4**, 98–107.

78 P. A. Jacobs, E. Derouane and J. Weitkamp, *J.C.S. Chem. Comm.*, 1981, 591–593.

79 K. Park and S. Ihm, *Appl. Catal. A Gen.*, 2000, **203**, 201–209.

Chapter 4

3D porous nanostructured platinum prepared using atomic layer deposition

This text was published as: Sreeprasanth Pulinthanathu Sree,‡ Jolien Dendooven,‡ Lisa Geerts,‡ Ranjith K. Ramachandran, Elsa Javon, Frederik Ceyssens, Eric Breynaert, Christine E. A. Kirschhock, Robert Puers, Thomas Altantzis, Gustaaf Van Tendeloo, Sara Bals, Christophe Detavernier and Johan A. Martens, 3D porous nanostructured platinum prepared using atomic layer deposition, Journal of Materials Chemistry A, 2017, 5, 19007-19016. (‡Joint first author)

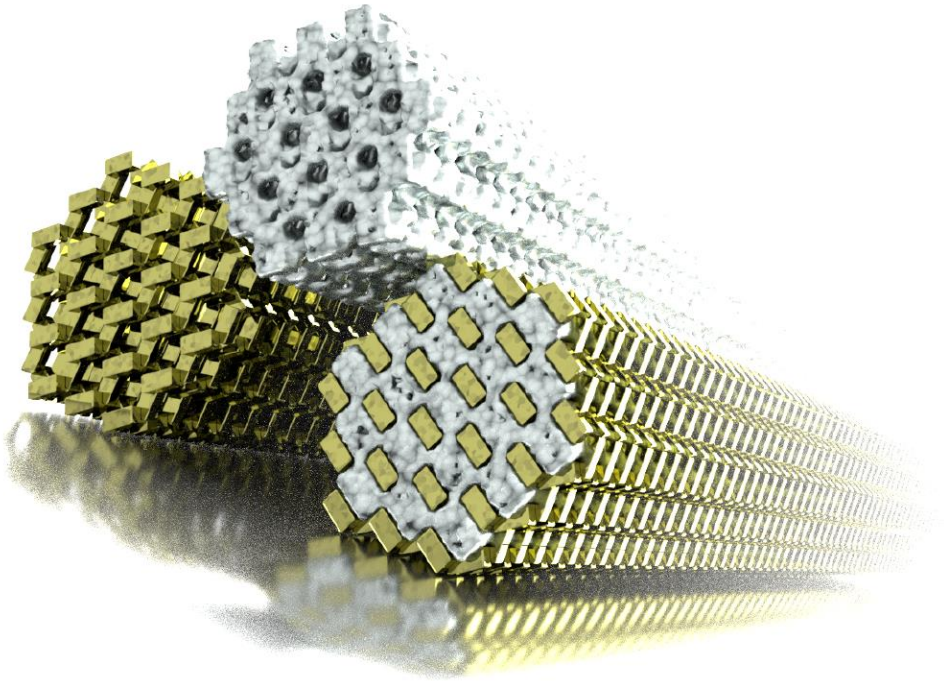

Electronic supplementary information (ESI) available: Movies showing the 3D porous structure of the Zeotile-4 and corresponding replica, demonstrating the replication of the pore system of host matrix by platinum along with tomography sequences of Pt replica. See DOI: 10.1039/c7ta03257a

This work was conducted at:

KU Leuven, Center for Surface Chemistry and Catalysis: Characterization and Application Team, Celestijnenlaan 200F, 3001 Leuven, Belgium

Ghent University, Department of Solid State Sciences, CoCooN, Krijgslaan 281/S1, 9000 Ghent, Belgium

University of Antwerp, Electron Microscopy for Materials Science, Groenenborgerlaan 171, 2020 Antwerp, Belgium

KU Leuven, Department of Electrical Engineering (ESAT), Kasteelpark Arenberg 10, B- 3001 Leuven, Belgium

Contributions:

L. Geerts and S. P. Sree partly conceived the idea, wrote the article and performed material synthesis. SEM characterization was done by S. P. Sree. The electrocatalysis experiments (hydrogen evolution reaction) were done by L. Geerts. J. Dendooven and R. K. Ramachandran contributed to the part on atomic layer deposition. E. Javon and T. Altantzis collected the HAADF-STEM images, electron tomography series and performed selected area electron diffraction (SAED). C. E. A. Kirschhock helped with the data interpretation and made Movie 4 in the ESI. F. Ceyssens performed the experiments with the microelectrodes. All of the authors contributed to the finalization of the article. J. Martens reviewed and supervised the work.

A robust and easy to handle 3D porous platinum structure was created via replicating the 3D channel system of an ordered mesoporous silica material using atomic layer deposition (ALD) over micrometer distances. After ALD of Pt in the silica material, the host template was digested using hydrogen fluoride (HF). A fully connected ordered Pt nanostructure was obtained with morphology and sizes corresponding to that of the pores of the host matrix, as revealed with high-resolution scanning transmission electron microscopy and electron tomography. The Pt nanostructure consisted of hexagonal Pt rods originating from the straight mesopores (11 nm) of the host structure and linking features resulting from Pt replication of the interconnecting mesopore segments (2-4 nm) present in the silica host structure. Electron tomography of partial replicas, made by incomplete infilling of Zeotile-4 material with Pt, provided insight in the connectivity and formation mechanism of the Pt nanostructure by ALD. The Pt replica was evaluated for its potential use as electrocatalyst for the hydrogen evolution reaction, one of the half-reactions of water electrolysis, and as microelectrode for biomedical sensing. The Pt replica showed high activity for the hydrogen evolution reaction and electrochemical characterization revealed a large impedance improvement in comparison with reference Pt electrodes.

Introduction

Platinum nanostructures exposing large surface area are required for miniaturized sensing and electronic devices.[1] The synthesis of platinum nanostructures is challenging as the high surface energy of platinum metal favors low rather than high specific surface area. Platinum nanoparticles with desired size and shape can be obtained via colloidal chemistry approaches using capping agents to achieve steric or electrostatic stabilization.[2,3] These nanoparticles can be fixed at surfaces or assembled to generate larger features. An early means to achieve porous platinum nanostructures is de-alloying, whereby the less noble metal is selectively leached from a bimetallic alloy via an electrochemical or chemical process.[1,4,5] Another strategy for achieving platinum nanostructures makes use of the soft templating approach where surfactant self-assembly generates ordered platinum structures constituting walls separating regular voids holding the soft template such as *e.g.* a lyotropic liquid crystal (LLC) phase of octaethylene glycol monohexadecyl ether[6,7] or diblock copolymer[8–10]. Various morphologies were prepared by electrochemical or chemical reduction of the platinum precursor and removal of the surfactant.[7,9] Synthesis of porous platinum with large mesocages using electrodeposition templated by poly(styrene-b-ethylene oxide) block copolymer has been demonstrated.[10] Platinum nanoballs, containing 50-80 nm

mesodomains of connected nanowires, were generated by use of giant hexagonal mesophases with cetyl trimethyl ammonium bromide as soft template.[9]

Another efficient methodology to realize mesostructured Pt is hard templating, which is based on the deposition of the metal in the pores of a mesoporous oxide matrix followed by dissolution of the hard template to liberate the metallic replica.[1] Electrodeposition of platinum in the pores of anodic aluminum oxide (AAO) templates resulted in solid nanowires with diameters according to the AAO pore size.[11–14] Deposition on the walls of AAO pores resulted in the formation of hollow platinum nanotubes. An alternative attractive robust hard template is ordered mesoporous silica.[1,15–17] Replicas of many ordered mesoporous silica matrices have been reported, most appearing like networks of polycrystalline nanowires.[18–24] Olive shaped porous Pt metal bodies of 150 to 230 nm with an internal structure of interconnected Pt nanorods were created using SBA-15 template.[25] Formation of single-crystal platinum nanorods by glycol-assisted one step vacuum impregnation of SBA-15 template was reported. Depending on the Pt precursor concentration, either individual nanorods or interconnected nanorod bundles were obtained.[26] Gyroid Pt nanowire networks were obtained by replication of the pores of MCM-48.[27] The double gyroid structure of KIT-6 was replicated to form an inverse gyroid structure with average particle sizes of 50 nm to a few hundred nanometers.[17,28]

Impregnation of a Pt complex in the pores of a hard template followed by chemical or electrochemical reduction and template dissolution is the most common pore replication method.[1,17,29–33,18–24,28] Photoreduction is an alternative to (electro)chemical reduction.[15,16] Atomic Layer Deposition (ALD) is a technique which proved its efficiency in introducing metal and metal oxides into mesoporous silica matrices,[34–36] but ALD of platinum for the creation of porous nanostructures has scarcely been reported. For instance, nanostructured films composed of Pt/Ir nanowires (~ 70 nm diameter) via ALD into AAO membrane have been reported.[37] In that study, after ALD of Pt and Ir, the AAO membrane was epoxy-bonded to a polycarbonate substrate whereafter the hard AAO template was etched in alkaline solution to liberate the Pt/Ir film. Also a low temperature ozone-based Pt-ALD process was demonstrated, by which anodized alumina pores with an average diameter of 23 nm and mesoporous silica films with a much smaller average pore diameter of 4 nm could be coated conformally.[38] Applying the same process on ordered multi-walled carbon nanotubes followed by removal of CNTs created a 3D network of self-supporting Pt nanowires.[39] Further, ALD was used to investigate the growth of Pt nanostructures on highly ordered pyrolytic graphite model carbon surface forming laterally aligned Pt nanowires.[40]

Nanostructured platinum materials fire the imagination of designs for tailor-made metal catalysts, electronics, non-linear optics and magnetic devices.[41] Efforts are reported in literature where the purpose of making a Pt replica was mainly to reveal the pore architecture of the hard template material, as Pt nanostructures are conveniently imaged via electron microscopy.[18–20] The existence of connecting micropores between mesopores of SBA-15 material was revealed using a Pt replica.[24] Platinum nanowires and nanoparticles templated on FSM-16 and HMM-1 have been tested for the preferential oxidation of CO in H_2 excess, which is important in fuel cells, where trace amounts of residual CO can poison the electrodes. A high activity and selectivity has been reported for the nanowires and particles in FSM-16.[16] Moreover, a high catalytic performance for the water gas shift reaction has been demonstrated on Pt wires templated inside FSM-16 pores.[42] Pt nanowires made in AAO membranes have been reported to function well in hydrogen peroxide detection.[11] Nanowire arrays, fabricated using the electrochemical deposition of PtCu alloy nanowires onto AAO templates followed by de-alloying of the Cu component, have been investigated for ethanol electro-oxidation, a half-reaction of ethanol fuel cell.[43] Skeletal Pt nanostructures, prepared through the chemical reduction by ethylene glycol vapor of a Pt precursor in presence of $(NH_4)_2CO_3$, exhibit high activity for the electrochemical oxidation of methanol.[44]

Reported Pt nanostructures are mostly nanowire assemblies, made using channel type host matrices. Also with the current methods it appears very difficult to replicate the hard porous template over lengths exceeding a micrometer. Such larger structures are desired for electrode and sensor applications. Here we report the fabrication of large skeletal platinum structures by replication of an ordered mesoporous 3D mosaic structure called Zeotile-4. It is formed by tiling of pre-fabricated rectangular silica particles, designated as nanoslabs (4 x 8 x 2 nm^3), in a hexagonal pattern.[45–47] The unique skeletal 3D porous mosaic Pt structure was confirmed with electron tomography. Electrochemical characterization revealed exceptional properties.

Experimental

Synthesis of Zeotile-4

Zeotile-4 powder was synthesized following a recipe reported in ref [47]. This involved the preparation of a clear solution of silicalite precursors otherwise called silica nanoslabs and combining it with Pluronic 123 followed by aging at high temperature. The clear solution was prepared by mixing tetra-ethylorthosilicate (TEOS) with tetrapropylammonium hydroxide (TPAOH) under vigorous stirring facilitating the hydrolysis of TEOS. Then water was added to the suspension and stirred for another

24 h. The molar ratio of TEOS : TPAOH : H_2O was maintained to be 25 : 9 : 400. 18 g of this clear solution was added to 9 g HCl (5M) and mixed with 24 g of aqueous Pluronic P123 solution (10 wt%) which has been already acidified using 8 g of 5 M HCl. The mixture was kept at 95 °C for 96 h in a polypropylene bottle. The solid precipitate formed was recovered, washed, dried and calcined at 350 °C for 12 h using a heating ramp of 0.5 °C min^{-1}.

Atomic Layer Deposition

Pt-ALD was carried out in a home built cold wall ALD chamber.[38] The powder sample was loaded in a molybdenum sample cup, which was then transferred into the ALD reactor through the load-lock and was placed on a heater block. The sample was then allowed to outgas and thermally equilibrate for at least 1 h under vacuum. The solid $MeCpPtMe_3$ precursor (99% Strem Chemicals), kept in a stainless steel container, was heated above its melting point (30 °C), and the delivery line to the chamber was heated to 60 °C. Argon was used as a carrier gas for the Pt precursor. O_3 was produced from a pure O_2 flow with an OzoneLabTM OL100 ozone generator, resulting in an O_3 concentration of 175 μg ml^{-1}. A static exposure mode was applied during both ALD half-cycles. The pulse time of the MeCpPtMe3 precursor was 10 s, after which the valves to the pumping system were kept closed for another 20 s, resulting in a total exposure time of 30 s. The same pulse time and exposure time was used for the O_3 also. For the creation of the full replica (Fig. 3), the $MeCpPtMe_3$ precursor exposure was repeated 3 times for one O_3 exposure during each ALD cycle. For the creation of the micron-long mesoporous Pt tubes (Fig. 6), only one precursor pulse was applied during each ALD cycle. In both cases, 250 ALD cycles were applied. During the precursor and reactant exposures, the pressure in the chamber increased to *ca.* 0.5 mbar and 1 mbar, respectively. After ALD, the silica of the host material was digested using 0.5 M HF solution at 60 °C for 3 h to create the Pt replica.

HR-SEM

HR-SEM images of all samples were obtained on a Nova NanoSEM450 (FEI, Eindhoven). The powder samples were mounted on aluminium stubs using carbon tape and directly imaged without any further sample modification.

STEM/tomography

HAADF-STEM images, electron tomography series and selected area electron diffraction (SAED) patterns were acquired by using an aberration corrected 'cubed' FEI Titan electron microscope operated at 200 and 300 kV. Electron tomography series acquisition was performed in STEM mode by using a Fischione model 2020 single tilt

tomography holder. The series was reconstructed by using the simultaneous iterative reconstruction technique (SIRT) implemented in the Inspect3D software from FEI.[48,49]

N_2 physisorption

N_2 physisorption measurements were performed on a Quantachrome Autosorb-1. The samples were pretreated at 120 °C under vacuum for 12 h. The N_2 adsorption isotherms were analyzed using Brunauer−Emmett−Teller (BET) and *t*-plot methods.

Synthesis of hydrogen evolution electrode

N-type silicon wafers (Cemat Silicon, 4" unpolished) with a thickness of 525-575 μm were used as substrates for the Pt deposited Zeotile-4. RCA cleaning was performed and followed by a wet oxidation at 1100 °C for 2 h which resulted in an insulating layer of SiO_2. Thin film layers were sputtered with a Balzers BAE 370 sputtering tool. A Ti/W ($Ti_{10}W_{90}$ target, 99.95%) was sputtered at 2 x 10^{-3} mbar and 150 W for 1 min as an adhesion layer for the platinum metal. Pt (Pt target, 99.95%) was then sputtered at 100 W for 3 min under Ar atmosphere at 2 x 10^{-3} mbar. Subsequently a conducting wire was soldered on the electrode by use of silver paint (RS, US) and the contact was sealed with epoxy coating (Hysol 9466, Henkel). Geometric surface areas were determined by making a picture of the electrodes and using the software ImageJ to calculate the area. Prior to deposition, the substrate was cleaned in milliQ water and ethanol. To make a catalyst ink, the powder with Pt (0.0114 g) was dispersed in 2 ml ethanol with 0.0209 g polyvinyl alcohol (Sigma-Aldrich) and 30 μl Nafion solution (5% Quintech). The solution was intensively vortexed to become a homogenous solution. The replica was deposited on precleaned platinum support by use of a micropipette. 6 times 5 μl was pipetted on the surface. The electrodes were then air-dried for 60 ± 10 min.

Electrocatalytic activity for the hydrogen evolution reaction

Current-voltage curves were recorded without IR compensation at ambient temperature using a VersaSTAT 4 potentiostat (Princeton Applied Research) in a one-compartment electrochemical cell with electrolyte content of approximately 600 ml. Experiments were performed in 0.5 M H_2SO_4 and the electrolyte (Fisher Scientific, 95%) was diluted at 0.5 M concentration using Milli-Q water (18 MΩ cm). A platinum ring served as auxiliary electrode and an Ag/AgCl (3M KCl saturated with AgCl, Radiometer Analytical) was used as reference electrode. Scan rate was set at 2 mV s^{-1} and H_2 was purged through the solution prior to measurements to saturate the solution.

Fabrication of multi-electrode array

A multi-electrode array of flat circular test electrodes with 0.019 cm^2 surface area was fabricated by lithography on a glass substrate. A two-layer lift-off resist layer (LOR10B + S1818) was applied by spin coating and patterned by UV contact lithography and development in 0.26N NaOH. 10 nm thick TiW adhesion layer and a 120 nm thick Pt layer were sputtered with a Balzers BAE 370 sputtering tool, after which the remaining lift-off resist was removed in N-methylpyrrolidone. Next, a 5 μm thick film polyimide (Dupont PI-2611) was applied by spin coating and cured at 350 °C to serve as insulation layer. A reactive ion etch using a thick ma-p 1275HV resist layer as mask, was used to open the polyimide layer, thereby releasing the platinum layer and defining the size and shape of the electrodes.

The tubular Pt Zeotile-4 replica was dispersed in demineralized water at a concentration of 3 wt% and mixed by sonication. The resulting suspension was deposited on the test electrodes (heated to 90 °C to accelerate drying) by micropipetting 1 μl drops five times per electrode. The resulting layer was then annealed for 5 hours at a temperature between 250 and 575 °C (in Ar from 450 °C on, to protect the polyimide from oxidation).

Impedance and charge injection capacity of multi-electrode array

Testing was performed in phosphate buffered saline water (Invitrogen Gibco, pH 7.2) using a platinum counter electrode and an Ag/AgCl electrode (3M KCl saturated with AgCl, Radiometer Analytical) as reference. The readout electronics consisted of a Solartron SI 1255 frequency response analyser and a SI 1287 electrochemical interface. For impedance testing, a 0.1 V amplitude sine waveform was scanned between 0.1 and 1MHz. For cyclic voltammetry, a scan rate of 100 mV s^{-1} was employed.

Results and discussion

Zeotile-4 is an ordered mesoporous material with parallel straight channels in hexagonal arrangement, interconnected systematically via slit-like voids left open between the stapled nanoslabs. The architecture of this nano-mosaic has been demonstrated earlier by electron tomography.[47] Zeotile-4 synthesis starts with the preparation of a suspension of nanoslabs from tetraethylorthosilicate (TEOS) and tetrapropyl ammonium (TPA) hydroxide.[45] Mesostructuring of the nanoslabs subsequently is achieved using triblock copolymer, Pluronic P123 surfactant. The organics are conveniently removed by calcination to evacuate the pores.

Zeotile-4 particles were investigated by scanning electron microscopy (SEM). Hereby, a concentric backscattered detector, combined with beam deceleration at accelerating voltages down to 500 V was used. The particles were found to adopt an hexagonal cylindrical morphology, with typical sizes of 2-3 μm by 0.5-1 μm (Fig. 1). The systematic presence of two types of pore openings is revealed: (i) openings of ~11 nm in an hexagonal arrangement observed at the end and ascribed to the apertures of straight mesopores running according to the long direction of the particles and (ii) sideways perforation ascribed to the termination of the slit pores. A movie in the ESI shows the idealized topology of Zeotile-4 and the resulting replica (ESI Movie 1).

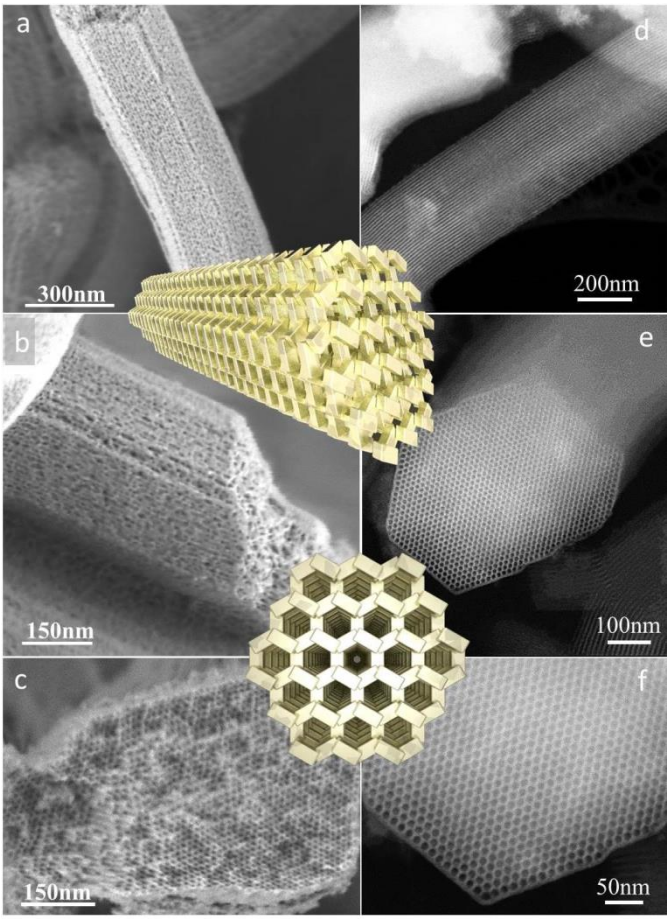

Figure 1. HR-SEM images of calcined Zeotile-4 sample: (a and b) lateral view showing the presence of slit like entrances allowing sideways access to the porosity and (c) axial view which presents hexagonally ordered mesopores of ~11 nm. HAADF-STEM images of calcined Zeotile-4 particles: (d) lateral view and (e and f) view perpendicular to the main mesopores (~11 nm) at different magnifications. Overlaid is the schematic of Zeotile-4 structure, (top) the lateral view and (bottom) the axial view.

Zeotile-4 hard template with its 3D mesoporosity is particularly suited for ALD, as demonstrated previously for TiO_2 deposition.[36,47] In this work, Pt-ALD was performed on Zeotile-4 powder using alternating exposure to (methylcyclopentadienyl-) trimethylplatinum ($MeCpPtMe_3$) vapor and O_3 gas at 200 °C.[38] Large precursor

exposures were used to enhance the deposition in the inner portions of the Zeotile-4 material (see Methods Section). After 250 ALD cycles, the silica of the Zeotile-4 host material was dissolved using 0.5 M HF solution at 60 °C for 3 h to liberate the Pt replica. HAADF-STEM imaging confirmed the uniform dispersion of Pt on the Zeotile-4 powder particles (Fig. 2a). Fig. 2b shows an HR-SEM image of the Pt replica after dissolution of the hard template material. Comparison of Fig. 2a, where the silica matrix is still present, with Fig. 2b confirmed that the as-deposited structure is retained after removal of the template. Fig. 2c and d show the orthoslices of the tomography sequences (ESI Movies 2 and 3). The successful replication of the porous structure over micron lengths is demonstrated by the HR-SEM images in Fig. 2 e and f. BET-analysis of the N_2 physisorption isotherms yielded a specific surface area of 20 $m^2 g^{-1}$, confirming the formation of an open, accessible interior void structure. Values of 53 $m^2 g^{-1}$ and 38 $m^2 g^{-1}$ have been obtained respectively with unsupported Pt-nanowire networks based on a soft template,[29] and with inverse gyroid structures templated from KIT-6.[17] The Pt replica of Zeotile-4 was quite robust and survived mechanical processes like sonication, indicating firm connectivity of the rods and struts of the Pt nanostructure. No visible changes of the Pt morphology were observable in SEM after annealing of the Pt structure.

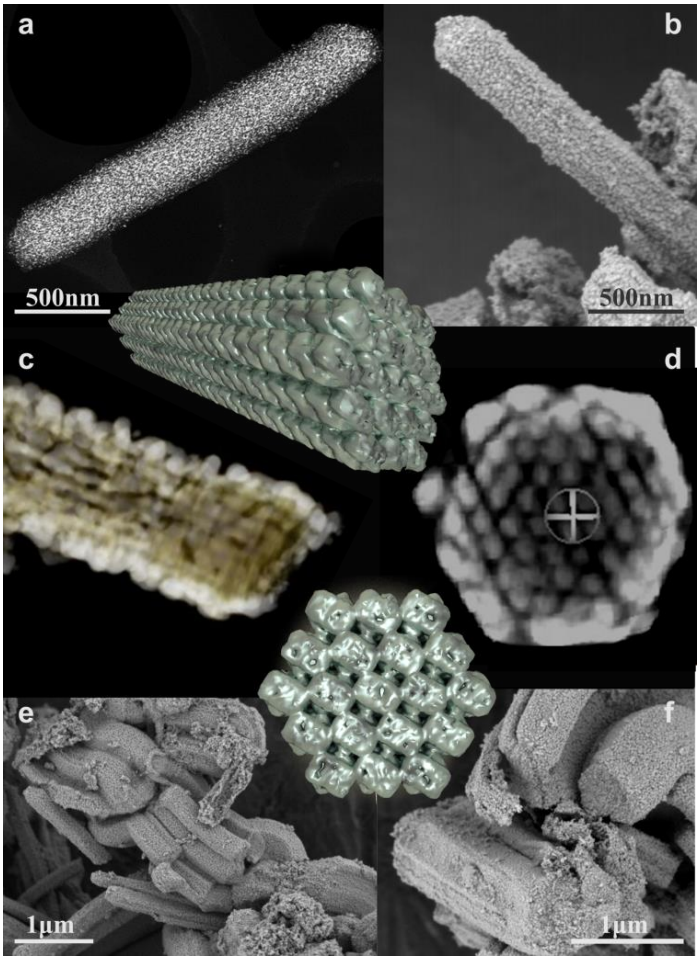

Figure 2. (a) HAADF-STEM image of Zeotile-4 filled with Pt and (b, e and f) HR-SEM images of Pt Zeotile-4 replica at different magnifications. (c and d) Orthoslices of tomography sequences of the Pt replica (ESI Movies 2 and 3). Overlaid is the schematic of Pt replica structure, (top) the lateral view and (bottom) the axial view.

HAADF-STEM images of the Pt Zeotile-4 replica (Fig. 3) allowed a more detailed characterization of the morphology of the obtained Pt nanostructure. The plan view images in Fig. 3a and b revealed the formation of Pt rods along the long direction of the Zeotile-4 template as a consequence of the successful ALD filling of the straight Zeotile-4 mesopores with Pt. Moreover, these images evidenced the arrangement of Pt struts connecting the main rods. The cross sectional view of the Pt replica in Fig. 3c provided confirmation of the hexagonal shape of the Pt rods and of the overall hexagonal organization originating from the pore arrangement in the Zeotile-4 template. The diameter of the Pt rods of the replica and the pores of the silica host material were identical, *viz.* 11 nm (Fig. 1f).

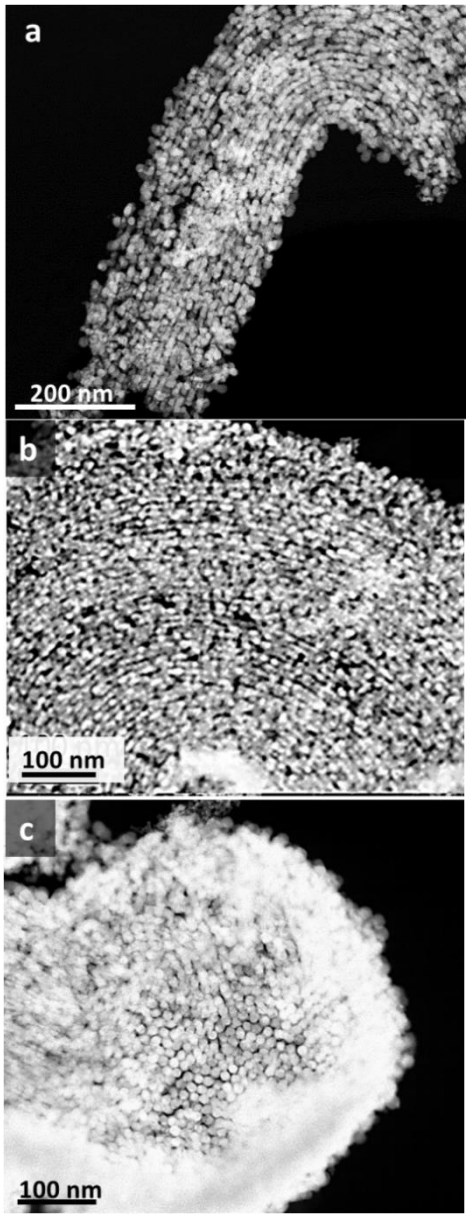

Figure 3. HAADF-STEM image corresponding to (a and b) plan view of the replica showing the struts of Pt and (c) cross-section of Pt replica after removing the silica with HF indicating the conservation of organization.

To explore the matching of the embedded platinum nanostructure and the Zeotile-4 template, both phases need to be mapped during a same tomography series. Unfortunately, due to the large difference in atomic number for Pt and Si it was not possible to map the silica of Zeotile-4 by HAADF-STEM when the material is filled with Pt. Therefore, powder particles with reduced Pt loading via ALD were characterized with HAADF-STEM tomography. This study (Fig. 4) revealed the formation of Pt aggregates, owing to the nucleation-controlled growth mode of the Pt-ALD process.[38] Fig. 4a and b present two different orientations of the volume rendering of the 3D reconstruction, and Fig. 4c shows a slice though the reconstruction.

In Fig. 4a, the hexagonal organization of Zeotile-4 (red color) is recognized. Aggregates of Pt which are highlighted by a bright and yellow color are localized at different places. In this orientation the main channels of Zeotile-4 are interspaced with stacks of nanoslabs with slits in between them. Many of the smallest aggregates such as those shown by the white arrows, are observed inside the stacking of nanoslabs, indicative of Pt nucleation on the accessible nanoslab surfaces inside the small slits. Other small aggregates are localized in the large hexagonal pores created by the nanoslab organization, indicating that platinum particle growth can also start at the sides of the nanoslabs. Large aggregates such as those highlighted with black circles in the Fig. 4a, are systematically located in the main channels. From the view in perpendicular direction (Fig. 4b) it is also clear that these aggregates are elongated in the direction of the pores. A movie is available in the ESI, observing one large aggregate seen under different orientations (ESI Movie 4). The orthoslice shown in Fig. 4c corresponds to a real section in the center of the sample. The lower contrast corresponds to the silica of Zeotile-4 and the highest contrast to the aggregates of Pt. Since it does not correspond to a projection, the orthoslice confirms the location of the large aggregates of Pt in the large channels of zeotile-4. Based on these results, we propose the following nucleation and growth mechanism for the Pt-ALD process in Zeotile-4 material. The presence of small Pt aggregates within the stacking of the slabs and along the walls of the main channels suggests that the nucleation of Pt particles can start anywhere on a nanoslab surface, and even more likely on the largest surface, which means inside the nanoslab stacking. Nucleation in the slit-like openings seems not be hindered by the limited size (2 to 4 nm) compared to the large straight channels (~11 nm). However, continued Pt deposition gives rise to bigger agglomerates that need larger space and only fit in the main channels of Zeotile-4. When the silica is removed by HF treatment in order to obtain the replica, rods of Pt grown in the main channels are held together by platinum struts formed by virtue of the nucleation of Pt nanoparticles in the nanoslab stacks. The robustness of the Pt replica is explained by this growth mechanism where there are no boundaries between Pt grown in the two types of pores.

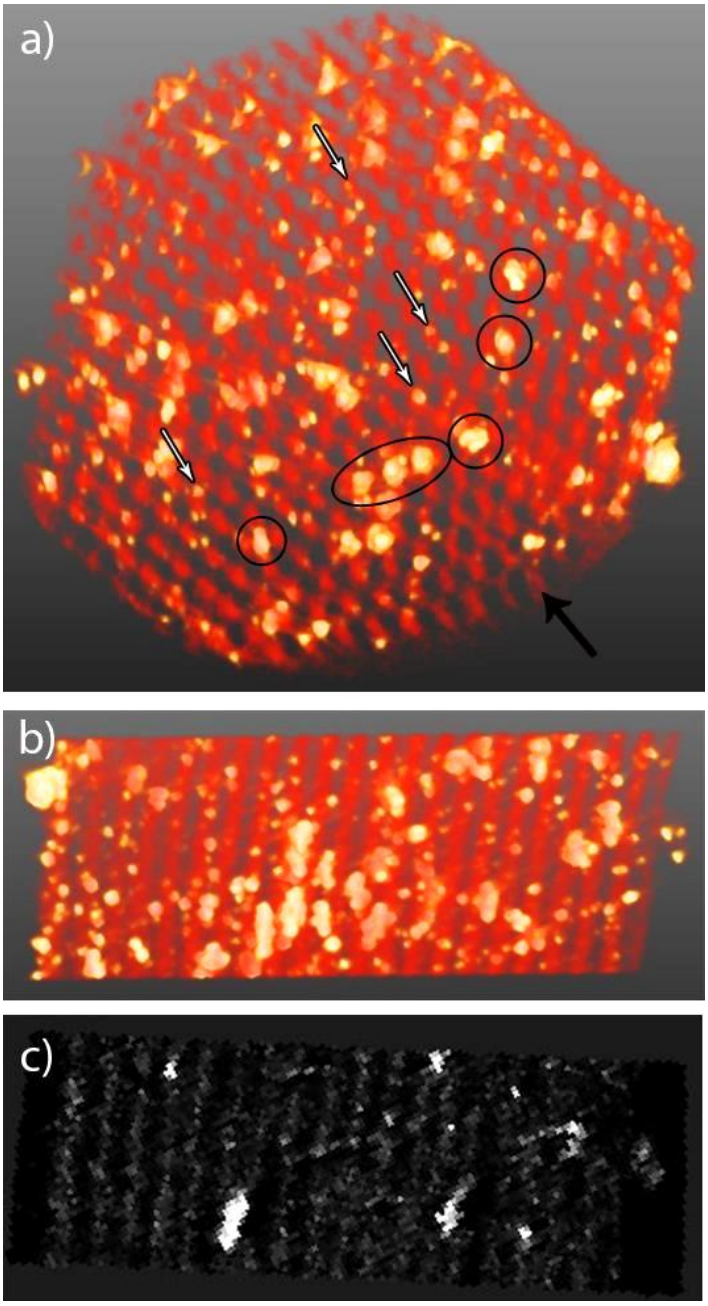

Figure 4. (a and b) Volume rendering of the tomography reconstruction displayed along two directions. White arrows show the small aggregates of Pt localized between the slabs and black circles highlight large aggregates of Pt localized in the main mesopores. The black arrow indicates the direction along which the second orientation (b) is visualised. (c) Orthoslice showing localization of the large aggregates of Pt in the mesopores of the Zeotile-4.

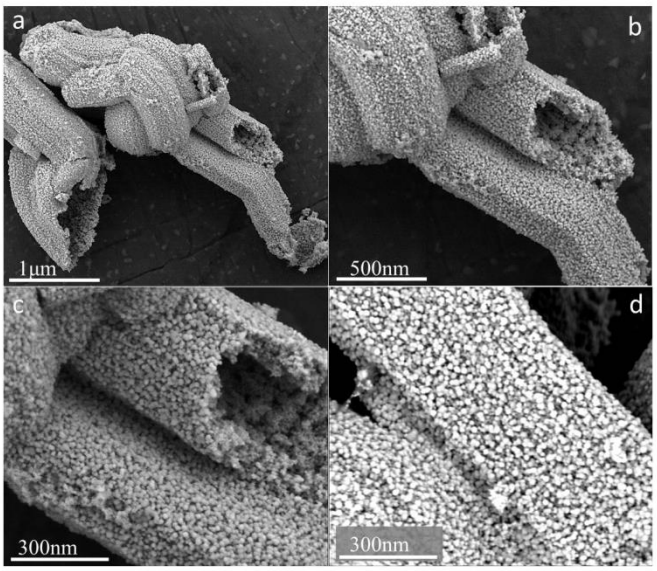

Figure 5. HR-SEM of Pt Zeotile-4 replica created via less time of exposure of the Pt precursor.

This growth model is further supported by High Resolution STEM on a completely filled sample (Fig. 6b and c). It can clearly be seen that the platinum replica is composed of partially coalesced nanocrystallites, which presumably nucleated initially on the silica surface and grew during subsequent ALD cycles. Owing to the mild conditions of ALD with temperatures not higher than 200 °C the nanocrystallites did not fully merge into one solid structure but preserved their almost spherical habit. According to the corresponding electron diffraction these nanocrystallites are randomly oriented and do not show any significant alignment with respect to the original pore direction of the Zeotile, which also indicates the original orientation of each crystallite is preserved after nucleation, growth and coalescence with neighboring Pt particles. Interestingly the nanoparticles are stable in the porous silica matrix for at least 2-3 years and after silica removal, observed to be stable for months of storage at ambient conditions.

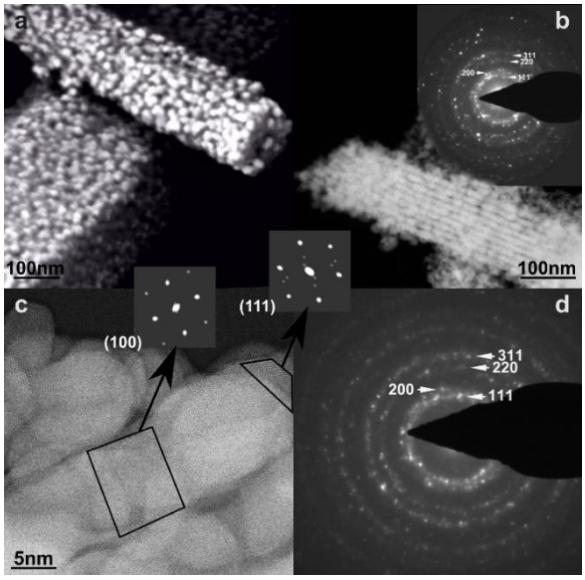

Figure 6. (a) HR-SEM of Pt Zeotile-4 replica. (b and c) HR-STEM of similar regions as shown in (a). (d) and inset in (b) show the electron diffraction patterns of (c) and (b) respectively. Small insets show contrast enhanced Fourier transforms with tentative assignment of the respective crystal facets of the regions indicated in (c).

In previous work on TiO_2-ALD in Zeotile-4 powder particles, the TiO_2 deposition was concentrated in the rim of the Zeotile-4 particles by decreasing the exposure time of the Ti-precursor.[36] This could be understood based on the diffusion limited nature of the ALD process which leads to the progressive penetration of deposition fronts in all directions of the Zeotile-4 material with increasing exposure time. This property was exploited to create micron-sized mesoporous Pt tubes, which could be of interest for application. The penetration depth of the Pt precursor was limited by applying an ALD protocol with a three times shorter exposure time for the Pt precursor. The obtained Pt nanostructures liberated after silica dissolution in SEM had a nanoscopic appearance similar to the full replica (Fig. 5). The large void in the middle of the replica confirmed the limited penetration depth of the ALD process in this instance. SEM (Fig. 5b and c) evidenced the creation of Pt tubes of *ca.* 2 μm by 0.5 μm with a wall of thickness 150 nm and an inner diameter of ~200 nm. The wall thickness of the tube reflects the platinum deposition depth in the Zeotile-4 particles.[36] The presence of an open channel in the center of mesoporous Pt structure could be very beneficial to enhance the accessibility of the inner surfaces of the Pt structure. Using the diffusion-limited nature of ALD, the diameter of the open channel can be precisely tuned by changing the Pt precursor exposure time.

To illustrate the applicability of the Pt replica structure, proof-of-concept experiments were performed, being the application in electrocatalysis for the hydrogen evolution reaction (HER) and in biomedical sensing as microelectrode. Electrocatalysis is expected to take advantage of the large surface area offered by the Pt structure.

The activity of the Pt electrode was investigated for the HER, one of the half-reactions of water electrolysis. To date, platinum is acknowledged as the most active HER catalyst with lowest overpotential.[50–52] Nanostructuring is a way to reduce the platinum content of electrodes.[50–53] A Pt electrode was prepared by depositing Pt deposited-powder on a 2.1 cm^2 flat platinum support *via* dropcasting (80 μg cm^{-2}). All electrochemical measurements were performed in 0.5 M H_2SO_4 at room temperature (21 °C) using a one-compartment three-electrode electrochemical cell. Fig. 7 shows the HER activity of the bare platinum support in comparison with the Pt-coated electrode.

The nanostructured Pt occluded in the Zeotile matrix has a significant catalytic activity towards the HER. Compared with the flat Pt support, the Pt replica coated electrode exhibits a higher current density and this was achieved with a loading of Pt on Zeotile-4 of *ca.* 80 μg cm^{-2}, representing *ca.* 55 μg cm^{-2} platina. Typical loadings for the cathode side vary between 0.5 and 1 mg cm^{-2}.[54] The platinum replica coated electrode requires an overpotential of 120 mV necessary to drive the current density to 10 mA cm^{-2}, which is 45 mV less than for the flat Pt support. This significant enhancement indicates a very high mass activity of the Pt nanostructure. Furthermore the electrode showed a stability as seven cyclic voltammograms were recorded and the hydrogen evolution current density shows negligible change.

Single-crystal model experiments and computational studies revealed (electro)catalytic activity to be strongly dependent of atomic organization at the surface.[55–59] Close-packed low-index crystal planes such as (111) and (100) planes exhibit lower reactivity in comparison with (110) planes and planes with higher indices.[57–60] Increased reactivity was observed by the presence of steps, kinks and defects on these more open crystal surfaces. The mild temperature (200°) of the Pt-ALD process as well as the structure being composed of partially coalesced nanoparticles might explain why less stable crystal facets, like (100) are preserved (Fig. 6). For very small Pt-nanoparticles it is known that energetically less stable faces than (111) can be expressed to minimize exposed surface by assuming an almost spherical rounded shape.[61]

In literature, colloidal synthesis has been applied for platinum particle synthesis with high index facets.[62,63] Nanosized cubes, tetrahedra and octahedra have been obtained.[59,64] Using multi-walled carbon nanotube support, Pt nanoparticles with higher fractions of high-index facets have been synthesized.[65] Electrochemical methods have been used for synthesis of particles with high-index facets by starting from conventional Pt nanocrystals and subjecting them to square-wave voltammetry.[66] After colloidal synthesis methods, ligands must generally be eliminated prior to use as electrocatalyst and this often results in altered size and shape. In this respect,

impregnation of a template with a precursor, followed by gas- or liquid phase reduction is easier, but size and dispersion are more difficult to control.[65]

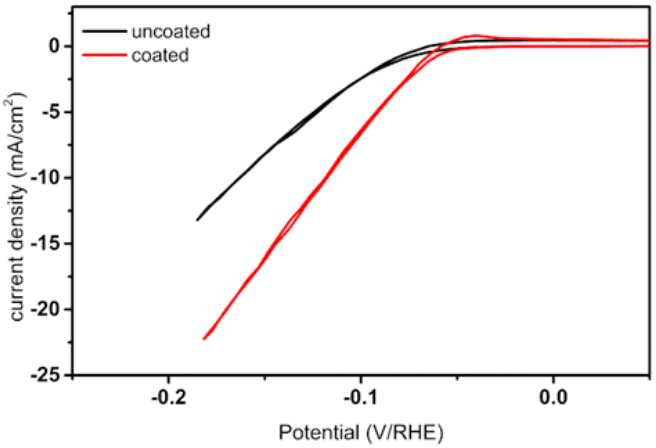

Figure 7. Cyclic voltammograms of the bare platinum support and Pt Zeotile-4 coated electrode. The potential (V/RHE) is the potential of the working electrode with respect to the reversible hydrogen electrode. The current density (mA cm^{-2}) is normalized to the geometric surface area. Scan rate was set at 2 mV s^{-1}.

The hierarchical nature of the Pt nanostructure is expected to be beneficial to electrode impedance at relevant frequencies and charge injection capacity, two parameters that are important in the design of neural stimulation and recording implants. Pt replica powder was used to fabricate a platinum microelectrode. A planar platinum multi-electrode array of which each electrode has an area of 1.9 mm^2, was fabricated using standard lithography and thin film deposition techniques. Glass was used as substrate. Above, Pt was sputterdeposited and the microelectrodes were structured in a lift-off process. The process is detailed in the Methods section. An amount of 15 μg of Pt replica powder was deposited from suspension by micropipetting on each 1.9 mm^2 electrode, followed by heat treatment. Inspection by SEM confirmed the replica structure was preserved. Impedance spectroscopy and cyclic voltammetry in phosphate buffered electrolyte (pH 7.2) were used to assess performance and to compare to other Pt electrodes. Impedance spectroscopy (Fig. 8a) shows that deposition of Pt replica reduces impedance in the low frequency (capacitively-dominated) part of the spectrum with three orders of magnitude. It had at least 5 times lower impedance than porous platinum electrodes based on platinum black from literature that were prepared *via* electroplating. This confirms the vastly enlarged accessible surface area. [67–69]

Cyclic voltammetry is used for determining the charge injection capacity, which is the time integral of the current at a certain sweep rate. Such a measurement on the 1.9 mm^2 Pt replica coated electrode showed 230 times increased charge storage capacity compared to flat Pt support (Fig. 8b). This leads to the conclusion that Pt replica of

Zeotile is a promising material for the fabrication of sensitive platinum electrodes, with potential biomedical applications such as neuro stimulation. Existing technologies include the use of porous platinum,[67,68] porous iridium oxide (deposited as such or electrochemically created in a smooth layer by anodization),[70] TiN,[68,71] carbon-based electrodes such as CNTs[72] or conductive polymer based electrodes such as PEDOT[73]. Platinum replica of Zeotile-4 realized *via* ALD adds a new promising method.

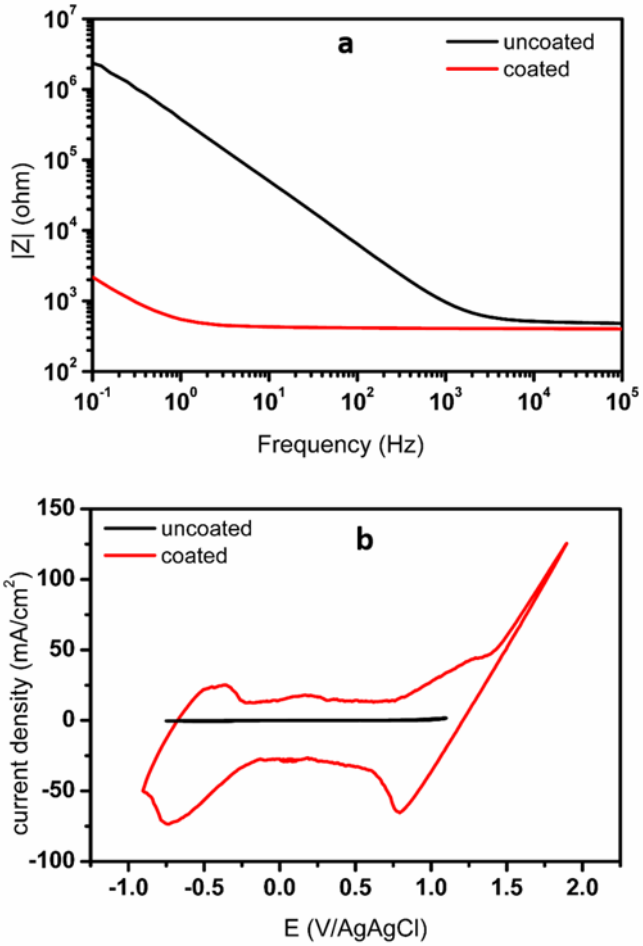

Figure 8. (a) Impedance spectra of Pt electrode (0.019 cm^2 surface area) with and without Pt replica deposited. Deposition of the Pt replica reduces the impedance in the low frequency region. (b) Cyclic voltammetry was performed at 100 mV s^{-1}. The potential is calibrated against the Ag/AgCl reference electrode and current density is normalized to geometric surface area. Charge storage capacity was increased by a factor of 230.

Conclusions

Synthesis of interconnected hexagonal Pt nanorods by replicating the voids of a mesoporous Zeotile-4 template using atomic layer deposition was achieved. The Pt nanostructure measuring typically 2-3 μm by 0.5-1 μm consists of hexagonal Pt rods, matching with the straight pores of Zeotile-4 and linking features ascribed to Pt replication of interconnecting slits. The unique skeletal 3D porous mosaic Pt structure

was confirmed with electron tomography. We developed a method that can replicate the hard porous template over lengths exceeding a micrometer, which is convenient for electrode and sensor applications. This structure has been shown to have a high activity for the hydrogen evolution reaction and to be promising for low impedance coatings for neural recording and stimulation electrodes, due to its large impedance improvement and high charge injection capacity. These enhanced properties could be attributed to the three-dimensional, ordered, mesoporous structure with large surface area, which can offer advantages in a wide range of applications. Future efforts can be devoted to the replication of other Zeotiles and mesoporous silica thin films.[46,74]

Acknowledgements

This work was supported by the Flemish government through long-term structural funding (Methusalem) to J.A.M. and FWO for a research project (G0A5417N). J.D., T.A. and F.C. acknowledge Flemish FWO for a post-doctoral fellowship. S.B. acknowledges funding from ERC Starting Grant COLOURATOMS (335078).

References

1 Y. Xu and B. Zhang, *Chem. Soc. Rev.*, 2014, **43**, 2439–2450.

2 B. Escobar Morales, S. A. Gamboa, U. Pal, R. Guardian, D. Acosta, C. Magana and X. Mathew, *Int. J. Hydrogen Energy*, 2010, **35**, 4215–4221.

3 Z. Peng and H. Yang, *Nano Today*, 2009, **4**, 143–164.

4 M. Oezaslan, M. Heggen and P. Strasser, *J. Am. Chem. Soc.*, 2012, **134**, 514–524.

5 S. Tominaka, M. Shigeto, H. Nishizeko and T. Osaka, *Chem. Commun.*, 2010, **46**, 8989–8991.

6 G. S. Attard, J. M. Corker, C. G. Göltner, S. Henke and R. H. Templer, *Angew. Chemie Int. Ed. English*, 1997, **36**, 1315–1317.

7 G. S. Attard, P. N. Bartlett, N. R. B. Coleman, J. M. Elliott, J. R. Owen and J. H. Wang, *Science*, 1997, **278**, 838–840.

8 S. C. Warren, L. C. Messina, L. S. Slaughter, M. Kamperman, Q. Zhou, S. M. Gruner, F. J. DiSalvo and U. Wiesner, *Science*, 2008, **320**, 1748–1752.

9 G. Surendran, L. Ramos, B. Pansu, E. Prouzet, P. Beaunier, F. Audonnet and H. Remita, *Chem. Mater.*, 2007, **19**, 5045–5048.

10 Y. Yamauchi, A. Sugiyama, R. Morimoto, A. Takai and K. Kuroda, *Angew. Chemie - Int. Ed.*, 2008, **47**, 5371–5373.

11 D. Ruan, F. Gao and Z. Gu, *J. Electrochem. Soc.*, 2014, **161**, 666–671.

12 Y. Su, H. Liu, Z. Yan, M. Feng, J. Tang and H. Du, *Electrochim. Acta*, 2015, **164**, 182–186.

13 S. Garbarino, A. Ponrouch, S. Pronovost, J. Gaudet and D. Guay, *Electrochem. commun.*, 2009, **11**, 1924–1927.

14 L. Liu, E. Pippel, R. Scholz and U. Gösele, *Nano Lett.*, 2009, 6876–6877.

15 Y. Sakamoto, A. Fukuoka, T. Higuchi, N. Shimomura, S. Inagaki and M. Ichikawa, *J. Phys. Chem. B*, 2004, **108**, 853–858.

16 A. Fukuoka and M. Ichikawa, *Top. Catal.*, 2006, **40**, 103–109.

17 Y. Doi, A. Takai, Y. Sakamoto, O. Terasaki, Y. Yamauchi and K. Kuroda, *Chem. Commun.*, 2010, **46**, 6365–6367.

18 R. Ryoo, C. H. Ko, M. Kruk, V. Antochshuk and M. Jaroniec, *J. Phys. Chem. B*,

2000, **104**, 11465–11471.

19 C. H. Ko and R. Ryoo, *Chem. Commun.*, 1996, **1**, 2467–2468.

20 F. Kleitz, S. H. Choi and R. Ryoo, *Chem. Commun.*, 2003, 2136–2137.

21 H. J. Shin, R. Ryoo, Z. Liu and O. Terasaki, *J. Am. Chem. Soc.*, 2001, **123**, 1246–1247.

22 H. J. Shin, C. H. Ko and R. Ryoo, *J. Mater. Chem.*, 2001, **11**, 260–261.

23 Z. Liu, Y. Sakamoto, T. Ohsuna, K. Hiraga, O. Terasaki, C. H. Ko, H. J. Shin and R. Ryoo, *Angew. Chemie - Int. Ed.*, 2000, **39**, 3107–3110.

24 A. Galarneau, H. Cambon, F. Di Renzo, R. Ryoo, M. Choi and F. Fajula, *New J. Chem.*, 2002, **27**, 73–79.

25 H. Wang, M. Imura, Y. Nemoto, S.-E. Park and Y. Yamauchi, *Chem. - An Asian J.*, 2012, **7**, 802–808.

26 H. Liu, D. Ma and X. Bao, *Dalton Trans.*, 2009, 1894–1896.

27 O. Terasaki, Z. Liu, T. Ohsuna, H. J. Shin and R. Ryoo, *Microsc. Microanal.*, 2002, **8**, 35–39.

28 H. Wang, H. Y. Jeong, I. Masataka, L. Wang, L. Radhakrishnan, N. Fujita, T. Castle, O. Terasaki and Y. Yamauchi, *J. Am. Chem. Soc.*, 2011, **133**, 14526–14529.

29 Y. Song, R. M. Garcia, R. M. Dorin, H. Wang, Y. Qiu, E. N. Coker, W. A. Steen, J. E. Miller and J. A. Shelnut, *Nano Lett.*, 2007, **7**, 3650–3655.

30 Y. Han, J. M. Kim and G. D. Stucky, *Chem. Mater.*, 2000, 2068–2069.

31 A. Fukuoka, T. Higuchi, T. Ohtake, T. Oshio, J. I. Kimura, Y. Sakamoto, N. Shimomura, S. Inagaki and M. Ichikawa, *Chem. Mater.*, 2006, **18**, 337–343.

32 B. C. Yang, H. Sheu and K. Chao, *Adv. Funct. Mater.*, 2002, **300**, 143–148.

33 X.-J. Guo, C.-M. Yang, P.-H. Liu, M.-H. Cheng and K.-J. Chao, *Cryst. Growth Des.*, 2005, **5**, 33–36.

34 C. Detavernier, J. Dendooven, S. Pulinthanathu Sree, K. F. Ludwig and J. A. Martens, *Chem. Soc. Rev.*, 2011, **40**, 5242–5253.

35 S. P. Sree, J. Dendooven, T. I. Koranyi, G. Vanbutsele, K. Houthoofd, D. Deduytsche, C. Detavernier and J. A. Martens, *Catal. Sci. Technol.*, 2011, 218–

221.

36 S. P. Sree, J. Dendooven, J. Jammaer, K. Masschaele, D. Deduytsche, J. D. Haen, C. E. A. Kirschhock, J. A. Martens and C. Detavernier, *Chem. Mater.*, 2012, **24**, 2775–2780.

37 B. D. J. Comstock, S. T. Christensen, J. W. Elam, M. J. Pellin and M. C. Hersam, *Adv. Funct. Mater.*, 2010, **20**, 3099–3105.

38 J. Dendooven, R. K. Ramachandran, K. Devloo-Casier, G. Rampelberg, M. Filez, H. Poelman, G. B. Marin, E. Fonda and C. Detavernier, *J. Phys. Chem. C*, 2013, **117**, 20557–20561.

39 S. Deng, M. Kurttepeli, S. Deheryan, D. J. Cott, P. M. Vereecken, J. A. Martens, S. Bals, G. van Tendeloo and C. Detavernier, *Nanoscale*, 2014, **6**, 6939–6944.

40 H. Lee, S. H. Baeck, T. F. Jaramillo and S. F. Bent, *Nano Lett.*, 2013, **13**, 457–463.

41 A. Chen and P. Holt-hindle, *Chem. Rev.*, 2010, **110**, 3767–3804.

42 A. Fukuoka, N. Higashimoto, Y. Sakamoto, M. Sasaki, N. Sugimoto, S. Inagaki, Y. Fukushima and M. Ichikawa, *Catal. Today*, 2001, **66**, 23–31.

43 X. Zhang, W. Lu, J. Da, H. Wang, D. Zhao and P. a Webley, *Chem. Commun.*, 2009, 195–197.

44 N. K. Gopalan, S. Zhang, D. Du, P. Li and J. Ouyang, *ChemCatChem*, 2015, **7**, 422–426.

45 C. E. A. Kirschhock, S. P. B. Kremer, J. Vermant, G. Van Tendeloo, P. A. Jacobs and J. A. Martens, *Chem. - A Eur. J.*, 2005, **11**, 4306–4313.

46 J. A. Martens, J. W. Thybaut, J. F. . Denayer, S. P. Sree, A. Aerts, M. F. Reyniers, V. Van Speybroeck, M. Waroquier, A. Buekenhoudt, I. Vankelecom, W. Buijs, J. Persoons, G. V. Baron, S. Bals, G. Van Tendeloo, G. B. Marin, P. A. Jacobs and C. E. A. Kirschhock, *Catal. Today*, 2011, **168**, 17–27.

47 S. Bals, K. J. Batenburg, D. Liang, O. Lebedev, G. Van, A. Aerts, J. A. Martens and C. E. a Kirschhock, *J. Am. Chem. Soc*, 2009, **131**, 4769–4773.

48 B. Goris, T. Roelandts, K. J. Batenburg, H. Heidari Mezerji and S. Bals, *Ultramicroscopy*, 2013, **127**, 40–47.

49 W. van Aarle, W. J. Palenstijn, J. De Beenhouwer, T. Altantzis, S. Bals, K. J.

Batenburg and J. Sijbers, *Ultramicroscopy*, 2015, **157**, 35–47.

50 W. Liu, E. Hu, H. Jiang, Y. Xiang, Z. Weng, M. Li, Q. Fan, X. Yu, E. I. Altman and H. Wang, *Nat. Commun.*, 2016, **7**, 10771.

51 A. Kiani and S. Hatami, *Int. J. Hydrogen Energy*, 2010, **35**, 5202–5209.

52 D. V. Esposito, S. T. Hunt, A. L. Stottlemyer, K. D. Dobson, B. E. McCandless, R. W. Birkmire and J. G. Chen, *Angew. Chemie - Int. Ed.*, 2010, **49**, 9859–9862.

53 Y. Cao, Y. Yang, Y. Shan, C. Fu, N. Viet Long, Z. Huang, X. Guo and M. Nogami, *Nanoscale*, 2015, **7**, 19461–19467.

54 M. Carmo, D. L. Fritz, J. Mergel and D. Stolten, *Int. J. Hydrogen Energy*, 2013, **38**, 4901–4934.

55 M. T. M. Koper, *Nanoscale*, 2011, **3**, 2054–2073.

56 E. Skulason, V. Tripkovic, M. E. Bjorketun, S. Gudmundsdottir, G. Karlberg, J. Rossmeisl, T. Bligaard, H. Jonsson and J. K. Norskov, *J. Phys. Chem. C*, 2010, **114**, 18182–18197.

57 J. H. Barber and B. E. Conway, *J. Electroanal. Chem.*, 1999, **461**, 80–89.

58 N. M. Marković, B. N. Grgur and P. N. Ross, *J. Phys. Chem. B*, 1997, **101**, 5405–5413.

59 C. Burda, X. Chen and R. Narayanan, *Chem. Rev.*, 2005, **105**, 2–5.

60 B. E. Conway and B. V Tilak, *Electrochim. Acta*, 2002, **47**, 3571–3594.

61 L. C. Gontard, R. E. Dunin-Borkowski and D. Ozkaya, *J. Microsc.*, 2008, **232**, 248–259.

62 S. E. F. Kleijn, S. C. S. Lai, M. T. M. Koper and P. R. Unwin, *Angew. Chemie - Int. Ed.*, 2014, **53**, 3558–3586.

63 J. M. Petroski, Z. . l. Wang, T. . C. Green and M. A. El-Sayed, *J. Phys. Chem. B*, 1998, **102**, 3316–3320.

64 Y. Xia, Y. Xiong, B. Lim and S. E. Skrabalak, *Angew. Chemie - Int. Ed.*, 2009, **48**, 60–103.

65 Y. T. Kim, K. Ohshima, K. Higashimine, T. Uruga, M. Takata, H. Suematsu and T. Mitani, *Angew. Chemie - Int. Ed.*, 2006, **45**, 407–411.

66 N. Tian, Z.-Y. Zhou and S.-G. Sun, *J. Phys. Chem. C*, 2008, **112**, 19801–19817.

67 S. A. Desai, J. D. Rolston, L. Guo and S. M. Potter, *Front. Neuroeng.*, 2010, **3**, 1–5.

68 A. Norlin, J. Pan and C. Leygraf, *Biomol. Eng.*, 2002, **19**, 67–71.

69 W. Franks, I. Schenker, P. Schmutz and A. Hierlemann, *IEEE Trans. Biomed. Eng.*, 2005, **52**, 1295–1302.

70 S. F. Cogan, J. Ehrlich, T. D. Plante, A. Smirnov, D. B. Shire, M. Gingerich and J. F. Rizzo, in *Conf Proc IEEE Eng Med Biol Soc.*, 2004, vol. 6, pp. 4153–4156.

71 J. D. Weiland, D. J. Anderson and M. S. Humayun, *IEEE Trans. Biomed. Eng.*, 2002, **49**, 1574–1579.

72 E. W. Keefer, B. R. Botterman, M. I. Romero, A. F. Rossi and G. W. Gross, *Nat. Nanotechnol.*, 2008, **3**, 434–439.

73 K. A. Ludwig, J. D. Uram, J. Yang, D. C. Martin and D. R. Kipke, *J. Neural Eng.*, 2006, **3**, 59–70.

74 S. P. Sree, J. Dendooven, D. Smeets, D. Deduytsche, A. Aerts, K. Vanstreels, M. R. Baklanov, J. W. Seo, K. Temst, A. Vantomme, C. Detavernier and J. A. Martens, *J. Mater. Chem.*, 2011, **21**, 7692.

General conclusions and perspectives

This study was intended to demonstrate the significance of 3D model platinum catalysts for kinetic studies under reaction conditions that are relevant for industrial practice. It was an attempt to bridge the materials gap in model catalyst systems between ideally characterized quantum dots and model 2D surfaces, and the 3D materials used in electro- and heterogeneous catalysis. The aim was to provide a comprehensive study integrating synthesis, characterization and kinetic evaluation to offer the scientific community 3D model systems.

Despite the large variety of techniques that are available to prepare Pt model catalysts, well-defined 3D model catalysts, that were investigated under realistic reactor conditions, have only been reported sparsely. A review of the literature revealed the materials gap between the well-characterized 0D nanoparticles synthesized in solution, the 2D model surfaces exposing various crystal planes of Pt metal and the real world catalyst extrudates supporting a platinum phase used in industrial heterogeneous catalysis. The art in model catalyst design is to adapt the design according to the needs and objectives of the research, which can be understanding at the atomic/molecular level or the engineering/reactor level. This work adds to the progress that has been made on connecting model catalyst and complex real-world catalysts.

The focus of this doctoral work was on synthesis techniques for preparation of 3D model catalyst systems that can be tested at the reactor level. In this study, '3D model' refers to the entire catalyst system, thus including the support if one is used. The 3D models can be useful for acquiring insights in the interplay of kinetics, diffusion and hydrodynamics.

The most important property characterizing an ideal 3D model catalyst was defined as uniformity. This applies to the support structure as well as the supported active particles. The most simple 3D model catalyst is a monodisperse nonporous support, because intraparticle diffusion is then avoided.[1,2] Another approach is the use of ordered porous supports of which the structure is fully characterized. In each case, whether a nonporous or porous model support is chosen, a precise and flexible control over all catalyst properties is desired.

This doctoral work presents 3 research directions. They are all related to achieving the goal of controlling the size, structure and distribution of the Pt nanoparticles. The model catalyst systems that have been synthesized and investigated are:

Pt nanoparticles supported by alumina spheres, Pt nanoparticles supported by zeolites and a Pt porous unsupported nanostructure. In this work three different approaches were successfully followed to construct model catalysts: (i) synthesis of uniform spherical dense alumina particles; (ii) deposition of platinum via atomic layer deposition and (iii) hard replication of ordered mesoporous silica material. Electron microscopy techniques have contributed significantly in the characterization of the model catalysts.

Alumina is a very popular catalyst support material. A first model catalyst was obtained by synthesizing uniform spherical alumina particles without pores, such that platinum nanoparticles are deposited solely on the outer surface of alumina and thus all have the same environment. The urea based precipitation method was successfully used to create spherical 1 μm sized alumina particles with a narrow size distribution. The thickness of the shell was 80 nm. Using 2D and 3D electron microscopy and ^{27}Al magic angle spinning nuclear magnetic resonance spectroscopy, the core-shell structure was fully characterized. The different phases recognized with electron microscopy and tomography reconstruction could be related to the transition alumina phases quantified with ^{27}Al NMR spectroscopy. The particles have δ-alumina shell with small islands of α-alumina, and γ-alumina core. Perfectly spherical particles with narrow size distribution have been rarely reported before and in comparison with other reports in literature, we performed a more detailed characterization of the obtained particles with assignments of the phases present in the particles. In future work, the hydrothermal method could be explored for precise control of size, porosity and phases of the alumina particles by tuning parameters as reactant concentration, time, hydrothermal treatment temperature and calcination conditions. Depending on the calcination temperature, the phase present at the surface can be tuned.

Strong electrostatic interaction of the chloroplatinate precursor with the protonated surface of the alumina particles, followed by drying and reduction with H_2 flow, was used to deposit Pt nanoparticles. As evidenced in HAADF-STEM, this procedure generates an excellent dispersion of 1 nm sized Pt nanoparticles. The Pt nanoparticles are homogeneously distributed on the alumina surface and have narrow size distribution. The accessibility of the Pt nanoparticles was demonstrated in bifunctional catalysis experiments. A same catalytic performance was reached with platinum located on alumina spheres admixed with acid zeolite and acid zeolite loaded with platinum itself in the isomerization and hydrocracking of n-decane. This work exemplifies the potential of studying core-shell alumina spheres in model catalyst studies.

(S)TEM 2D-projection images were insufficient to understand the core-shell structure of the alumina particles and electron tomography was needed. It revealed essential information on the internal structure of the alumina particles *i.e.* core-shell

structure instead of hollow spheres. Moreover in HR-TEM, it was difficult to image the small Pt nanoparticles on the micrometer sized alumina spheres. Therefore, STEM-based high-angle annular dark-field imaging was used to visualize the nanoparticles. A much clearer contrast was obtained which allowed determination of the size and distribution of the small Pt nanoparticles. Similar to TEM, the interpretation of the observed contrast becomes challenging in thicker regions *i.e.* the center of the alumina particle. Therefore additional analysis of the Pt-alumina particles by EDX spectroscopy was performed, which provided evidence that the Pt nanoparticles were homogeneously distributed.

Detailed characterization of the Pt nanoparticle structure itself was not yet achieved. The simple geometry of this support with Pt nanoparticles located on the external surface could be advantageous for observing the metal particles in profile by HR-TEM.[3–5] Moreover the model catalyst was now only demonstrated in combination with a zeolite as a bifunctional catalyst. The spherical support could also be useful for creation of monofunctional Pt catalysts and tested for other reactions as well. It would also be interesting to investigate the strong electrostatic adsorption method and other methods for preparation of different Pt nanoparticles sizes and shapes for obtaining structure-function relationships. And finally, the spherical support strategy could also be extended to other popular catalysts supports such as silica.

Another achievement of this work was the uncovering of the potential of ALD as a technique for preparing model catalysts. Platinum was successfully deposited on zeolites and made catalytically active. The ambition was even higher and the idea was to create catalytically active acid sites in addition to the platinum sites using ALD. Two examples of Pt-based catalysts with emphasis on electron microscopy characterization were presented. The catalytic properties were examined by studying hydroisomerization and hydrocracking of decane.

In the first example, Ga-ALD, using $Ga(TMHD)_3$ and O_2 plasma, was used on COK-14, an all-silica zeolite, followed by Pt deposition via incipient wetness impregnation with $Pt(NH_3)_4Cl_2$. Ga-ALD for introduction of gallium onto zeolites had remained largely unexplored. In this work, it was shown that Ga-ALD is an efficient tool for introduction of trivalent elements in the silicate framework generating acid sites and most likely also sites for anchoring Pt precursors. SEM revealed preferential location of the Pt nanoparticles on the edges of the zeolite particles. The consequent optimum proximity of metal and acid sites was highly beneficial for the catalytic performance. The maximum isomerization yield of *ca.* 70% surpassed that of other large pore zeolites.

In the second example, Pt-ALD with $MeCpPtMe_3$ and ozone was applied for incorporation of Pt nanoparticles on ZSM-5 zeolite. To give a comprehensive description of the catalyst, the structural information obtained from ADF-STEM was supplemented with topology information by secondary electron imaging. Finely dispersed Pt nanoparticles of 1-2 nm were achieved with Pt-ALD. After heat treatment under oxidation and reduction conditions, HAADF-STEM revealed a change in size. It is thus essential to include characterization of the samples after treatment, because as-deposited samples may not be representative of the active form of the catalyst. It was also observed that small Pt nanoparticles (~1 nm) move under the electron beam to form larger Pt particles. In TEM-related studies, it is thus important to consider the morphology changes of particles induced by irradiation of the electron beam. The Pt-ALD-ZSM-5 sample has been proven to be an excellent catalyst for n-decane hydroisomerization.

In conclusion, ALD has been demonstrated to be an effective way for tuning zeolites as model catalyst material. Highly dispersed nanoparticles with narrow size distribution can be deposited uniformly on the support. In future work, the technique can be created to prepare a series of model catalysts with increasing Pt nanoparticle size at a constant coverage as demonstrated on a flat support in ref [6]. Moreover, variation of ALD parameters can be used to control the concentration and position of acid and metal nanoparticles with respect to the catalyst support, which will help in our understanding of bifunctional catalysts. ALD holds, due to its ability to precisely control catalyst features, along with a large choice of elements that can be deposited, significant potential for designing catalysts for virtually any chemistry.

Hard templating in combination with ALD was found to be an elegant way for creating a stable porous 3D nanostructure. Using this approach Pt replication of Zeotile-4, a hierarchically ordered mesoporous silica system, was successful over micrometer distances. After dissolution of the silicate scaffold, a free standing nanomosaic of Pt nanoparticles was obtained. A full replication of the pores of the Zeotile-4 template over micrometer lengths was possible through use of the Pt-ALD process with $MeCpPtMe_3$ and ozone. TEM and STEM images of the platinum replica obtained after dissolution of the Zeotile-4 template show that the resulting structure consisted of interconnected hexagonal Pt nanorods. The open accessible structure of the Pt replica was confirmed by BET-analysis of the N_2 physisorption isotherms which yielded a high value, 20 $m^2 g^{-1}$, for the specific surface area. With electron tomography, the structure was thoroughly characterized. This structure had a high activity for the hydrogen evolution reaction. Moreover it is highly promising for use in coatings for neural recording and stimulation electrodes, due to its low impedance and high charge

injection capacity. These enhanced properties could be attributed to the three-dimensional, ordered, mesoporous structure with large surface area. The replica shows unprecedented structural properties in terms of stability and robustness. As evidenced with SEM, the high surface area structure was preserved up to temperatures of 500 °C and after electrochemical reactions. Moreover the Pt nanostructure is unique in terms of the micrometer lengths. Such larger structures are useful in electrode and sensor applications.

This replica method using ALD could be considered a generic approach for synthesis of well-defined Pt catalysts with uniform structure and can easily be extended to other metals as well. In future work, other Zeotiles and mesoporous silica thin films could be replicated for specific applications. For application in model catalyst studies, the replica method could be helpful for synthesizing model particles with systematically altered properties. If the synthesis is then supplemented with a full characterization of the structure as demonstrated here, it enables understanding the effect of structure on the performance.

In summary, a new collection of well-defined 3D model Pt catalysts was successfully prepared and characterized. The specific goal of creating uniformity in the catalyst system was achieved. Uniform alumina spheres could be coated with homogeneously distributed Pt nanoparticles. Another approach was ALD, which proved to be an efficient tool for fine-tuning the homogeneity in the sample. Moreover the Pt nanoparticles exhibited the ideal size and excellent dispersions were reached. The desired flexible control over all catalyst properties such as size and shape of the Pt nanoparticles could be further explored in future work. The kinetic experiments in various reactions (hydroisomerization, hydrocracking, hydrogen evolution reaction) reveal the value of these model catalysts for reaction kinetic studies. The approaches presented in this thesis (dense alumina support spheres, ALD and hard replication) can provide as a guideline and inspiration for design of other model metal catalysts.

Using the knowhow gained in this doctoral work, a variety of 3D model catalyst systems is available. In future work for instance, combining the strategies presented in the different chapters can yield interesting catalysts. The spherical supports as discussed in chapter 2, namely the alumina and erionite spheres, can be loaded with Pt using the Pt-ALD process discussed in chapter 3. The Pt/alumina spheres can be combined with various zeolites and used as a bifunctional zeolite.

As discussed above, 3D model catalyst systems should be tested at the reactor-level. In this work, preliminary reactions were performed. In future work, a detailed analysis of the kinetics of these catalysts obtained in relevant reactor conditions is needed to

address the important issues specifically related to operation in a reactor. These are both structural features of the catalyst, such as the distribution of active material in the catalyst granule, morphology and pore structure, as well as operating parameters such as mass and heat transfer, pressure, flow rate and fluid management.[2,7–9]

In future work, the flexibility of the ALD process can also be exploited for controlling the position of Pt nanoparticles with respect to various catalyst supports. This is useful for investigations of the influence of the spatial distribution of the active material in catalyst particles in many reactions. For example, in a porous material with sufficiently large pores, *i.e.* larger than the effective diameter of the $MeCpPtMe_3$ molecule of ~0.96 nm[10], different diffusion times of the Pt precursor in an ALD cycle, could enable Pt nanoparticles being located solely on the exterior rim of the catalyst or in the interior and exterior of particles.[2] At the reactor-level, uniform spreading of active material in catalyst pellets is not always the best catalyst. This may vary depending on the hydrodynamics, diffusion and kinetics of the reaction. Pellets with the active metal concentrated in a layer inside the pellet, but at a definite distance from the pellet surface have been reported to show superior performance.[2] In the investigation of this effect, combination of atomic-resolution spectroscopy (EDX or EELS) with tomography could help in revealing the 3D structure with the location of the imbedded particles.[11,12] Although STEM-HAADF tomography can reach atomic resolution in 3D due to improvements of instrumentation and reconstruction algorithms, identification of the spatial distribution of Pt particles in the support is still difficult.

Furthermore, it would also be relevant to use *in situ* (S)TEM experiments, at elevated temperatures and/or in gas phase. The technique would enable direct visualization of the nanoscale behavior of the Pt nanoparticles in reaction conditions and provide a direct link between structure and performance.[13–15]

References

1 Y. N. Zhitnev, E. A. Tveritinova, F. M. Spiridonov and V. V. Lunin, *Russ. J. Phys. Chem. A*, 2010, **84**, 1127–1131.

2 S. T. Sie, *Chem. Eng. J. Biochem. Eng. J.*, 1993, **53**, 1–11.

3 A. K. Datye and N. J. Long, *Ultramicroscopy*, 1988, **25**, 203–208.

4 A. K. Datye, *Top. Catal.*, 2000, **13**, 131–138.

5 A. David Logan, E. J. Braunschweig, A. K. Datye and D. J. Smith, *Ultramicroscopy*, 1989, **31**, 132–137.

6 J. Dendooven, R. K. Ramachandran, E. Solano, M. Kurttepeli, L. Geerts, G. Heremans, J. Rongé, M. M. Minjauw, T. Dobbelaere, K. Devloo-Casier, J. A. Martens, A. Vantomme, S. Bals, G. Portale, A. Coati and C. Detavernier, *Nat. Commun.*, 2017, **8**, 1074.

7 K. Cheng, M. Virginie, V. V. Ordomsky, C. Cordier, P. A. Chernavskii, M. I. Ivantsov, S. Paul, Y. Wang and A. Y. Khodakov, *J. Catal.*, 2015, **328**, 139–150.

8 National Research Council, *Catalysis Looks to the Future*, Washington, DC: The National Academies Press, 1992.

9 R. L. Augustine, *Heterogeneous Catalysis for the Synthetic Chemist*, Marcel Dekker, Inc., 1996.

10 H. Yan, Y. Lin, H. Wu, W. Zhang, Z. Sun, H. Cheng, W. Liu, C. Wang, J. Li, X. Huang, T. Yao, J. Yang, S. Wei and J. Lu, *Nat. Commun.*, 2017, **8**, 1–10.

11 Y. Zhu, M. Xu and W. Zhou, *Chinese Phys. B*, 2018, **27**, 056804.

12 S. M. Collins and P. A. Midgley, *Ultramicroscopy*, 2017, **180**, 133–141.

13 D. Su, *Green Energy Environ.*, 2017, **2**, 70–83.

14 J. Wu, H. Shan, W. Chen, X. Gu, P. Tao, C. Song, W. Shang and T. Deng, *Adv. Mater.*, 2016, **28**, 9686–9712.

15 T. Altantzis, I. Lobato, A. De Backer, A. Béché, Y. Zhang, S. Basak, M. Porcu, Q. Xu, A. Sánchez-Iglesias, L. M. Liz-Marzán, G. Van Tendeloo, S. Van Aert and S. Bals, *Nano Lett.*, 2019, **19**, 477–481.

Appendices

Supporting information of chapter 2

Characterization of the ERI zeolite

The powder XRD pattern of the as-synthesized product obtained after 14 days of crystallization at 100 °C is given in Figure S1. The XRD pattern corresponds to the calculated pattern for ERI structure type according to IZA Structure Commission.[1]

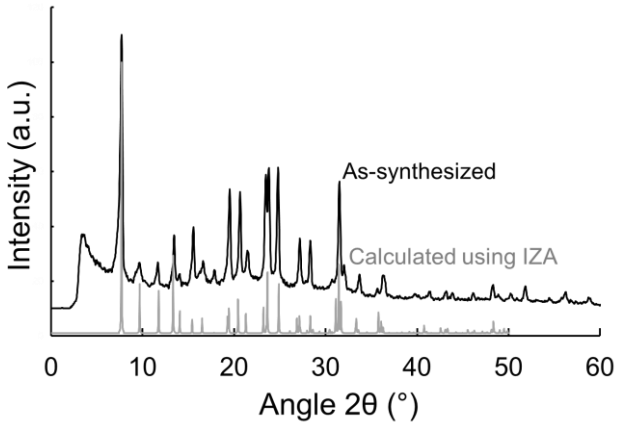

Figure S1. XRD pattern of the as-synthesized erionite zeolite and the calculated pattern in the International Zeolite Association (IZA) tabulation.[1]

The ERI spheres are also characterized by nitrogen physiorption. The isotherm is a reversible Type I isotherm (shown in Fig S2) and proves the material contains micropores.[2] The BET surface area, calculated with the multipoint BET method using the adsorption data in the relative pressure range of 0.05-0.32, amounts to 468 m^2/g.

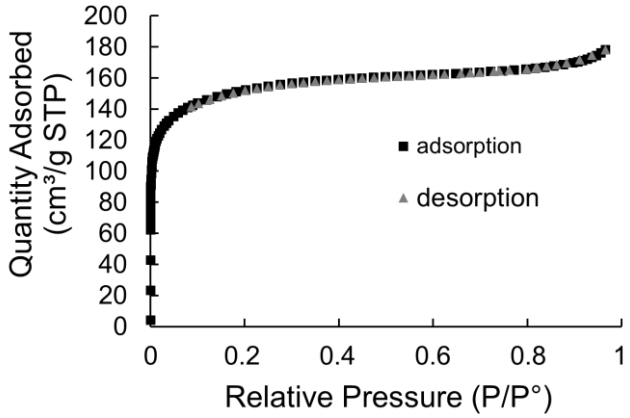

Figure S2. Nitrogen adsorption-desorption isotherm of the erionite zeolite spheres after ammonium exchange and calcination at 550 °C.

Characterization of the alumina spheres

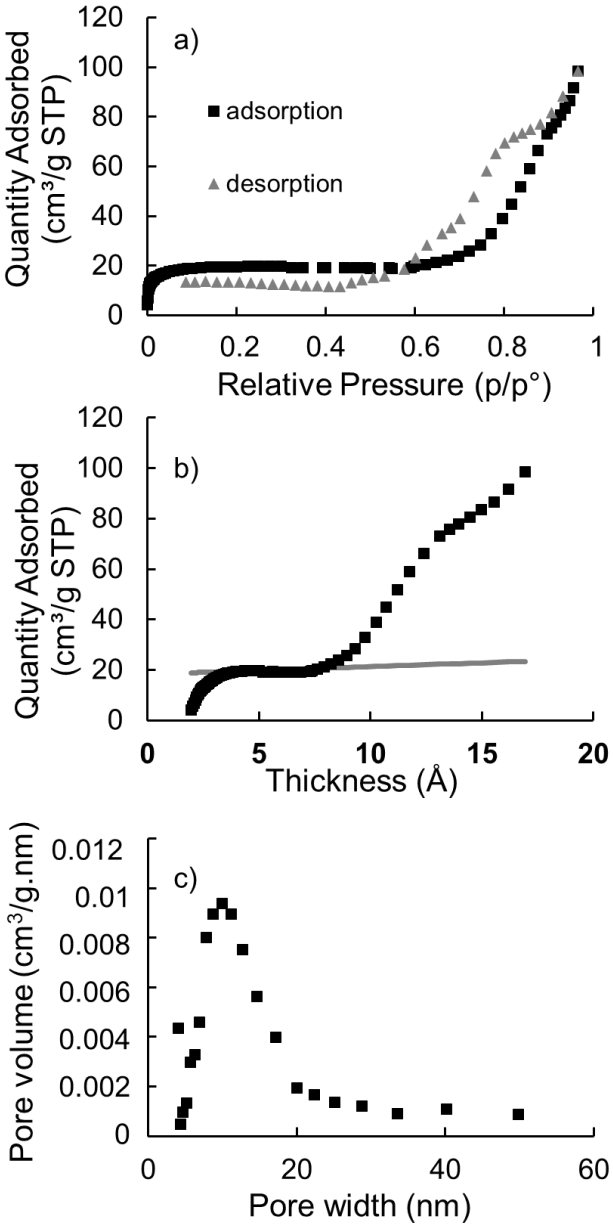

Figure S3. (a) Nitrogen adsorption-desorption isotherm (b) corresponding t-plot and (c) BJH pore size distributions for the alumina spheres after calcination at 1000 °C. For the t-plot, the intercept of the lower linear curve represents the microporous volume. The nitrogen adsorption volume at the relative pressure of 0.967 was used to determine the total pore volume because no linear curve could be fitted in the high statistical thickness region. The pore size distribution was derived from the adsorption branch by using the BJH method and shows a broad size distribution of mesopores between 6 and 20 nm.

References

1 C. Baerlocher and L. B. McCusker, Database of Zeolite Structures, http://www.iza-structure.org/databases/.

2 M. Thommes, K. Kaneko, A. V Neimark, J. P. Olivier, F. Rodriguez-reinoso, J. Rouquerol and K. S. W. Sing, *Pure Appl. Chem.*, 2015, **87**, 1051–1069.

List of publications

1. Sreeprasanth Pulinthanathu Sree,‡ Jolien Dendooven,‡ **Lisa Geerts,‡** Ranjith K. Ramachandran, Elsa Javon, Frederik Ceyssens, Eric Breynaert, Christine E. A. Kirschhock, Robert Puers, Thomas Altantzis, Gustaaf Van Tendeloo, Sara Bals, Christophe Detavernier and Johan A. Martens, 3D porous nanostructured platinum prepared using atomic layer deposition, Journal of Materials Chemistry A, 2017, 5, 19007-19016. **(‡Joint first author)**

2. **Lisa Geerts**, Salvatore Cosentino, Ting-Wei Liao, Anupam Yadav, Pin-Cheng Lin, Vyacheslav S. Zharinov, Kuo-Juei Hu, Alessandro Longo, Lino M. C. Pereira, Didier Grandjean, Jan Rongé, Peter Lievens and Johan A. Martens, Highly Active Oxygen Evolution Reaction Model Electrode based on supported Gas-Phase NiFe Clusters, Catalysis Today, 334, 59-67.

3. Tom Bosserez, **Lisa Geerts,** Jan Rongé, Frederik Ceyssens, Sophia Haussener, Robert Puers, Johan Martens, Minimization of Ionic Transport Resistance in Porous Monoliths for Application in Integrated Solar Water Splitting Devices, Journal of Physical Chemistry C, 2016, 120, 38, 21242-21247.

4. Frederik Ceyssens, Sreeprasanth Pulinthanathu Sree, **Lisa Geerts**, Johan Martens, Robert Puers, In-situ growth of platinum with hierarchical porosity for low impedance biomedical microelectrode fabrication, Procedia Engineering, 168, 2016, 1122 – 1126.

5. Tom Bosserez, Jan Rongé, **Lisa Geerts**, Christos Trompoukis, Johan A. Martens, Integrated solar hydrogen devices: cell design and nanostructured components in liquid and vapour phase water splitting, In Nanotechnology in Catalysis: Applications in the Chemical Industry, Energy Development, and Environment Protection, eds. Marcel Van de Voorde and Bert Sels, 2017, Chapter 34, 907-938, Wiley-VCH Verlag GmbH & Co. KGaA.

6. Jolien Dendooven, Ranjith K. Ramachandran, Eduardo Solano, Mert Kurttepeli, **Lisa Geerts**, Gino Heremans, Jan Rongé, Matthias Minjauw, Thomas Dobbelaere, Kilian Devloo-Casier, Johan A. Martens, André Vantomme, Sara Bals, Giuseppe Portale, Allesandro Coati, Christophe Detavernier, Independent tuning of size and coverage of supported Pt nanoparticles using atomic layer deposition, Nature Communications, 2017, 8,1074.

7. James Redfern, **Lisa Geerts**, Jin Won Seo, Joanna Verran, Lubomira Tosheva, Lik Hong Wee, Toxicity and antimicrobial properties of ZnO@ZIF-8 embedded silicone against planktonic and biofilm catheter-associated pathogens, ACS Applied Nanomaterials, 2018, 1, 4, 1657-1665.